Miniaturised wireless and battery-free systems for physiological monitoring and stimulation

Zhangyu Xu

A thesis submitted in fulfillment
of the requirements of the degree of
Doctor of Philosophy

School of Biomedical Enegineering
Faculty of Engineering
The University of Sydney

Submitted January 2025;

Declaration

This is to certify that, to the best of my knowledge, the content of this thesis is my own work. This thesis has not been previously submitted for any degree. I certify that the intellectual content of this thesis has been declared. The thesis is the product of my own work, and all the assistance received in preparing this thesis and sources have been acknowledged.

Chapter 3 of this thesis is published as Xu et al. (2023).

For this work, I conceived the idea, designed the study, performed experiments, analysed data, produced the figures and drafted the manuscript. My mentor and co-author, Dr Nhan Duy Truong, helped me revise the manuscript for publication. My co-authors and supervisors, Professors Omid Kavehei and Armin Nikpour, supervised this work and mentored me during the conceptualisation, methodology development, data analysis and result gathering.

Chapter 4 of this thesis is published as Xu et al. (2024).

For this work, I conceived the idea with my supervisor, Professor Omid Kavehei. My co-author, Dr Majid Khazaee had direct engagement during the conceptualisation. I co-designed the experiments with my co-author Dr Majid Khazaee. I coordinated the study with my lead supervisor Omid Kavehei. I performed experiments, analysed data, produced most of the figures and drafted the manuscript. My co-authors, Dr Nhan Duy Truong and Dr Arman Ahnood helped me revise the manuscript for publication alongside my supervisors. My co-authors and supervisors, Professors Omid Kavehei and Armin Nikpour, supervised this work and mentored me during the conceptualisation, methodology development, data analysis and result gathering.

Chapter 5 of this thesis was submitted to Nature Communication Engineering for publication and is currently under peer review.

For this work, I conceived the idea, designed the study, performed experiments, analysed data, produced the figures and drafted the manuscript. My co-authors, Dr Nhan Duy Truong and Dr Arman Ahnood helped me revise the manuscript for publication. My co-authors and supervisors, Professors Omid Kavehei and Armin Nikpour, supervised this work and mentored me during the conceptualisation, methodology development, data analysis and result gathering.

Chapter 6 of this thesis is an idea developed by my lead supervisor, Professor Omid Kavehei. The idea is filed as a Provisional Patent Application (HAIR-LIKE DEVICE AND METHOD OF IMPLANTING SAME, patent number 2024-059-PRO-0). All the intellectual properties of this work belong to the inventor, Professor Omid Kavehei. For this work, I performed and designated experiments, collected and analysed data, produced the figures and drafted reports.

In addition to the statements above, in cases where I am not the corresponding author of a published item, permission to include the published material has been granted by the corresponding author.

Jan 2025

As the supervisor for the candidature upon which this thesis is based, I can confirm that the authorship attribution statements above are correct.

Supervisor Name: Omid Kavehei

Jan 2025

Abstract

This thesis explores the development of miniaturised wireless and battery-free systems for physiological monitoring and their possible applications in stimulation. It addresses critical challenges in power delivery, energy harvesting, data communication, device miniaturisation, lowering implantation potential risks, and improving end-user comfort. This thesis includes a comprehensive literature review that establishes the groundwork by identifying gaps and opportunities in the field. The research introduces a high-bandwidth optical telemetry system for brain signal sensing, which achieved 108 Mbit/s and 54 Mbit/s back telemetry data rates for tissue thicknesses of 3 mm and 8 mm, respectively, with a power consumption of 1.57 mW, resulting in an energy efficiency of 14.5 pJ/bit. This provides a foundation for wireless monitoring technologies. This is extended with a novel integration of optical telemetry and focused ultrasound power transfer, creating a complete system for endovascular applications that eliminates long wires and enhances clinical applicability, especially for fragile or pediatric patients. The experiments shows data transmission speeds of over 2 Mbit/s and deliver delivers up to 10 mW of power through the scalp(6 mm), skull(10 mm), and subdural space(5 mm), adhering to safety limits. Further contributions include a groundbreaking wireless power transfer system designed to deliver sufficient energy directly to standard stents for monitoring and stimulation applications without modifying its structure, achieving high efficiency and safety compliance. The experiments shows the system achieved 7.26% DC-to-DC efficiency and can deliver over 45 mW of power without exceeding safety limits. The thesis also presents a novel sensing electrode for a wireless ambulatory electroencephalogram (EEG) using hair-like conductive material implanted in the skin layer, combining biocompatibility, comfort, aesthetics, and reliable signal capture for long-term brain monitoring. Together, these advancements represent a significant step forward in wireless and battery-free biomedical systems, offering practical and innovative solutions for diagnostics, therapy, and research while addressing key limitations in current technologies.

Acknowledgements

The research reported in this thesis was supported by the Australian Research Council under Project DP230100019 and also supported by the award of a Faculty of Engineering Research Scholarship to the PhD Candidate.

This thesis uses a LaTeX template created and publicly shared by the Australian Centre for Field Robotics School of Aerospace, Mechanical and Mechatronic Engineering.

This thesis is dedicated to my beloved wife, whose unwavering support and sacrifices have been my anchor throughout this journey. Your steadfast encouragement, endless patience, and unconditional love have been my greatest strength. While I immersed myself in the demands of my research, you shouldered the responsibility of nurturing our son, Joe, with grace and devotion. You ensured our family remained whole, even when my focus was elsewhere. This accomplishment would not have been possible without your resilience and belief in me. For this, I am profoundly grateful.

I also wish to express my deepest apologies to my dear parents. Being overseas for such an extended period meant I could not provide the companionship and care you deserved. The distance has been a source of great sorrow, and I regret that my academic pursuits took me away from you during moments when my presence might have brought you comfort. Your advice, love, and sacrifices have laid the foundation for all I have achieved. Please know that, despite the physical separation, you have always been in my thoughts and heart.

To my wife, son, and parents, this work is as much yours as it is mine. It stands as a testament to your love, understanding, and support.

Thank you for walking this path with me.

Contents

List of Figures

List of Tables

Nomenclature

List of Acronyms

AC	Alternating Current
AD2	Analog Discovery 2
ADC	Analog-to-Digital Converter
APD	Avalanche Photodiode
API	Application Programming Interface
ASIC	Application-Specific Integrated Circuit
AI	Artificial Intelligence
BCI	Brain-Computer Interface
BER	Bit Error Rate
CSF	Cerebrospinal Fluid
CT	Computed Tomography
DC	Direct Current
DUT	Device Under Test
EAP	Extracellular Action Potential
eBCIs	Endovascular Brain-Computer Interfaces
ECoG	Electrocorticography
EEG	Electroencephalogram
endoECoG	Endovascular Electrocorticography
ENOB	Effective Number of Bits
ESD	Electrostatic Discharge
fNIRS	Functional Near-Infrared Spectroscopy
FPGA	Field Programmable Gate Arrays
FUS	Focused Ultrasound
FWHM	Full Width at Half Maximum
I/O	Input/Output
IoT	Internet of Things
IR-UWB	Impulse-Radio Ultra-Wideband
KVL	Kirchhoff's Voltage Law
LED	Light-Emitting Diode
LFP	Local Field Potential
MCU	Microcontroller

MRI	Magnetic Resonance Imaging
NFC	Near-Field Communication
OFDM	Orthogonal Frequency-Division Multiplexing
OOK	On Off Keying
PC	Personal Computer
PCB	Printed Circuit Board
PDM	Pulse-Density Modulation
PMU	Power Management Unit
PWM	Pulse Width Modulation
RF	Radio-Frequency
RTT	Radiation Transfer Theory
SAR	Specific Absorption Rate
SNR	Signal-to-Noise Ratio
SSS	Superior Sagittal Sinus
SymPy	Python's Symbolic Mathematics Solver
TIA	Trans-Impedance Amplifier
VCSEL	Vertical-Cavity Surface-Emitting Laser
VNA	Vector Network Analyser
WPT	Wireless Power Transfer

Chapter 1

Introduction

1.1 Problem definition

Miniaturized wireless and battery-free systems for physiological monitoring and stimulation face numerous challenges that must be overcome to realise their transformative potential in healthcare and biomedical research fully. A primary challenge lies in the trade-offs between functionality, power consumption and size Zhang et al. (2023a). Making the physiological monitoring and stimulation device wireless is highly complex, as these systems require a reliable power supply and continuous streaming data for sensing. These power transfer and data communication solutions face the challenge of biological tissue attenuation, energy losses and body movement Stuart et al. (2021). At the same time, these wireless solutions need to meet safety standards and not cause damage to surrounding tissues. Miniaturization necessitates the development of compact and lightweight designs that can be seamlessly integrated into or onto the body, whether for wearable or implantable applications Nair et al. (2023). However, this size reduction inherently limits the capacity for energy storage, computational power, and data communication, which are critical for achieving high-performance physiological monitoring and stimulation.

Physiological monitoring often requires high-bandwidth data transmission to capture signals with higher resolution and higher sampling rates for diagnostics, decoding

and real-time feedback. For example, monitoring neural activities demands high-resolution data as it requires over 10 bits of resolution to cover the dynamic range and a sampling rate over 250 Hz, and normally, multiple channels will be needed to identify the different regions of the activity Moore et al. (2021a). These requirements increase the burden on wireless telemetry systems, especially when power consumption and the transmitter's volume are limited. At the same time, in endovascular implants, such as stent-based smart devices, the shape and volume are highly restricted, which makes wireless power transfer very hard. The balance between more powerful functions and maintaining low power consumption to avoid overheating or tissue damage is hard to achieve, and existing solutions often fail to meet these dual requirements effectively.

Another critical challenge for Physiological monitoring and stimulation devices is achieving long-term stability and reliability in harsh and often dynamically changed biological environments Kim et al. (2024). When the implanted or wearable system has a lead wire or cable, it must withstand movement, varying tissue conditions, and potential drag force over extended periods. Making the system wireless is the way to solve these long-term related challenges. Additionally, by removing the cable or lead wire, we can minimise the invasiveness of the system and reduce the risks and discomfort for the patient. Over the years, we have seen substantial engineering efforts to make this system wireless. Still, due to the limited transceiver size, power budget and bandwidth requirement, it is hard to address these requirements simultaneously, leaving critical gaps in their applicability to achieve the device's full potential.

Addressing these challenges is of principal importance, as miniaturized wireless and battery-free systems hold immense promise for revolutionizing the healthcare industry. They have the potential to enable minimal or non-invasive diagnostics, real-time feedback mechanisms, and personalized therapies, which can improve patient outcomes and reduce healthcare costs. For instance, wearable systems could continuously monitor chronic conditions, such as epilepsy or neurodegenerative diseases, enabling timely interventions and reducing the burden on healthcare facilities. Implantable devices could offer targeted therapies, such as deep brain stimulation or pain management, with minimal discomfort or disruption to the patient's daily life.

Furthermore, these systems could open new frontiers in biomedical research by enabling precise, long-term monitoring and stimulation of biological processes, providing deeper insights into complex physiological mechanisms.

Multidisciplinary advancements in materials science, electronics, bioengineering, and data science are required to bridge the existing gaps. Innovations in ultra-low-power electronics, energy harvesting, and wireless communication technologies will be pivotal in overcoming size and power constraints. Additionally, integrating advanced biocompatible materials and adaptive algorithms for real-time data processing will enhance these systems' usability, stability, and safety. By addressing these challenges, miniaturized wireless and battery-free systems can become scalable, reliable, and impactful solutions that redefine modern healthcare, offering new possibilities for diagnostics, therapy, and research.

1.2 The approach

This thesis employs a comprehensive and systematic approach to address the research questions related to miniaturized wireless and battery-free physiological monitoring and stimulation systems. The investigation begins with an extensive literature review to provide a broad and detailed perspective on the field's current state, identifying key challenges and opportunities. Building on this foundation, the research initially focuses on developing wireless data communication technology designed explicitly for brain signal sensing. Wireless data communication is the critical entry point for creating miniaturized systems, addressing the fundamental need for efficient and reliable data transmission.

The work then progresses to integrate wireless data communication with innovative wireless power solutions, advancing the field toward a comprehensive solution for physiological monitoring systems. This integration enhances system functionality and lays the groundwork for developing complete miniaturized and battery-free platforms. The thesis introduces and evaluates a novel power transfer technology capable of delivering sufficient energy directly to a standard stent to address the constraints

imposed by volume, size, implantation position, and stringent safety requirements. This solution meets the demanding power requirements for monitoring and stimulation applications, demonstrating its viability for practical use.

Additionally, the research explores innovative electrode designs to create a fully wireless, ambulatory EEG system that satisfies signal quality, comfort and aesthetic requirements. These novel electrodes enhance user experience while maintaining high-quality signal acquisition, making the system suitable for extended use in real-world settings. Together, these efforts represent a multidisciplinary approach to overcoming this field's technical and practical challenges, paving the way for advanced solutions in biomedical monitoring and therapeutic systems.

1.3 Contributions

This thesis makes significant contributions to the development of miniaturized wireless and battery-free systems for physiological monitoring and stimulation, addressing key challenges in power delivery, data communication, device miniaturization, and user comfort. The research begins with an extensive review of the current state of the field, providing a comprehensive understanding of existing gaps and opportunities. A major contribution lies in the development of a novel wireless optical telemetry system for high-bandwidth brain signal sensing, which serves as a foundation for miniaturized monitoring systems. This work is further extended by integrating wireless power solutions, creating a comprehensive system capable of both data transmission and power delivery. Another notable contribution is the design of a cutting-edge wireless power transfer technology that delivers sufficient energy to a typical stent, meeting the stringent requirements for size, implantation position, and safety while enabling both monitoring and stimulation functionalities. Additionally, this thesis introduces a novel hair-electrode design for EEG monitoring, transforming conventional systems into fully wireless, comfortable, and aesthetically acceptable devices suitable for long-term use. Figure 1.1 illustrates the main contributions of this thesis and how these works can benefit biomedical devices. These contributions advance the state of the

art in wireless and battery-free biomedical systems, paving the way for innovative applications in diagnostics, therapy, and research and addressing critical challenges in healthcare and biomedical engineering.

Chapter 3 reports a proof-of-concept optical telemetry module that uses a single LED as the transducer. It demonstrates achieving a small, reliable, and reasonably high bit-rate data uplink between a neural implant and its proximal wirelessly connected external unit. This chapter presents the design of a subdermal optical telemetry module that balances high data rate, high power efficiency, and low volume. The proposed design, implemented with discrete components and tested with animal tissue, achieves a 108 Mbit/s data rate through 3 mm of tissue, tolerating misalignment up to 5 mm and $\pm 15°$. The module's power consumption is below 1.57 mW, with a data transmission efficiency of 14.5 pJ/bit. The transducer's volume is less than 1 mm^3, demonstrating excellent potential for miniaturization and diverse applications. When integrated with an Application-Specific Integrated Circuit (ASIC), this small (in size) telemetry module nominally supports 1,000 channels of neural recordings, each sampled at 9 kSps at 12-bit resolution.

Chapter 4 introduces a groundbreaking optical wireless telemetry module combined with a Focused Ultrasound (FUS) power transfer system designed for integration within an endovascular stent. This innovation addresses the critical limitations of current Endovascular Brain-Computer Interfaces (eBCIs), such as the Stentrode™, by eliminating the need for long wires connecting stent electrodes to encapsulated electronics. Our approach enhances the clinical applicability of eBCIs for patients with fragile or weak blood vessels and presents a viable solution for pediatric applications. The proposed system demonstrates high-speed data transmission (over 2 Mbit/s, supporting 41 Electrocorticography (ECoG) channels at a 2 kHz sampling rate and 24-bit resolution) and efficient power transfer (up to 10 mW) within safety limits. Proof-of-concept experiments using fresh bovine tissues confirm the system's effectiveness, laying the groundwork for future advancements in neuroscience, engineering, and medical technology.

Chapter 5 presents significant advancements in developing minimally invasive, fully

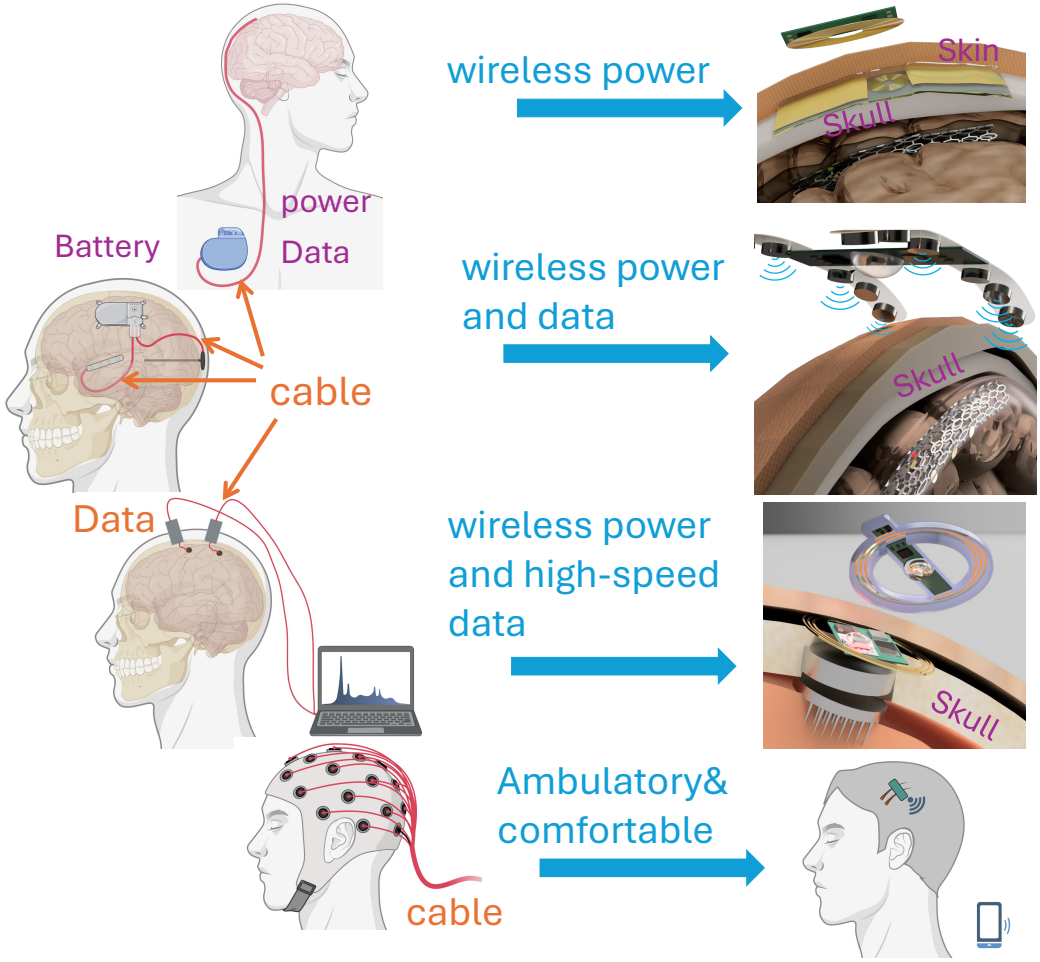

Figure 1.1 – Topic introduction, conceptual illustration of the potential benefits of miniaturized, wireless, and battery-free systems for physiological monitoring and stimulation in biomedical devices. The left panel highlights various existing devices and technologies that have achieved significant physiological monitoring and stimulation milestones. These devices rely on cables for power or data transmission. Some of these devices incorporate implantable batteries as their energy source, and some of these devices use cables to send high-speed data out of the body. The top left depicts an endovascular stent-based monitoring device with a chest companion and a long cable that travels through the vessel to connect the two parts. The second top left illustrates a closed-loop deep brain stimulation device powered by an implantable battery featuring subcutaneous sensing electrodes and electronics. All electrodes are connected via lead wires to a bulky hermetic package housing the battery and circuitry. The second bottom left showcases a Utah array device, a high-performance Brain-Computer Interface (BCI) system that requires a bulky cable for high-speed data transmission to an external computer. The bottom left presents a classical Electroencephalogram (EEG) device with multiple wires for signal transmission. The right panel demonstrates the contributions of this thesis. The top right features a wireless power transmission system efficiently delivering power to a typical stent. This system supports both monitoring and stimulation functionalities. The second top right displays a system integrating power transmission and data communication solutions for endovascular implantable devices. The second bottom right shows a high-speed optical data telemetry system developed for high-performance implantable BCI applications. The bottom right highlights novel hair-based electrodes designed for a fully wireless EEG device. This innovation provides an ambulatory EEG solution with enhanced comfort and suitability for long-term use.

wireless endovascular ECoG devices. This study addresses the challenges of space constraints, biocompatibility, and safety in Wireless Power Transfer (WPT) for stent-based devices in the brain. A novel WPT system is introduced, capable of delivering over 45 mW of power directly to a standard medical stent without modifying its structure or material. The system achieves a 7.26% DC-to-DC efficiency, the highest reported for stent-based brain implants without additional transceivers or specialized stent designs. Experimental results using real skin, bone, and vessel tissues align closely with finite element simulations, confirming accuracy and practicality. Safety assessments, including Specific Absorption Rate (SAR) analysis and temperature rise simulations, demonstrate compliance with regulatory standards and minimal risk to surrounding tissues. This work contributes to the scientific understanding of WPT in biomedical applications and opens new avenues for endovascular ECoG and neuromodulation devices.

Chapter 6 introduces a novel approach to EEG monitoring technology by addressing the limitations of conventional wet, dry, and implantable systems. This chapter details the design of electrically conductive, hair-like electrodes for long-term ambulatory monitoring of up to two weeks. These biocompatible, artificial hair strands, visually indistinguishable from natural hair, provide a non-invasive, socially acceptable, and comfortable alternative to traditional EEG systems. The electrodes eliminate the need for conductive gels, uncomfortable pressure, and bulky headgear, long-standing barriers to continuous brain monitoring. The design incorporates a conductive core surrounded by a biocompatible sheath, ensuring high-quality signal acquisition while maintaining low electrode impedance. Anchored by biodegradable, porous artificial follicles, the electrodes naturally integrate with scalp tissue and degrade over time, reducing the need for invasive removal procedures. Signal acquisition is facilitated by a lightweight, wireless "hair clip" device that securely attaches to the artificial hair, improving user comfort and aesthetic appeal. The design ensures signal redundancy and reliability by aligning electrode placement with the standard 10-20 EEG system, enabling continuous, long-duration monitoring for diagnostics, treatment, and neurological research.

This thesis represents a significant contribution to developing advanced wireless and battery-free systems, addressing critical challenges in healthcare and biomedical engineering while paving the way for innovative solutions in diagnostics and therapy.

1.4 Thesis structure

This thesis focuses on developing and exploring miniaturized wireless and battery-free systems for physiological monitoring and stimulation. It aims to address key challenges such as high data bandwidth requirements, wireless power delivery, size limitations, and user comfort in wearable and implantable biomedical devices.

Chapter 2 provides a comprehensive literature review, highlighting the current state of wireless and battery-free systems, their applications, and the technological challenges that remain unsolved. This chapter sets the stage for the subsequent research by identifying the gaps and opportunities in the field.

Chapter 3 explores wireless data communication technologies, presenting an optical telemetry system that addresses the high bandwidth requirements of physiological monitoring. This work, published in Xu et al. (2023), demonstrates how optical communication can overcome the limitations of conventional telemetry methods, providing a robust solution for high-fidelity data transmission in biomedical applications.

Chapter 4 extends the optical telemetry technology by integrating a feasible wireless power solution to support the system. This chapter includes more experimental results showing live data transmission through biological tissue and evaluates the bit error rate using random data. This chapter is published as Xu et al. (2024). The findings underscore the practicality of combining wireless power and data transmission in a single system for physiological monitoring.

Chapter 5 introduces a novel wireless power delivery system with high efficiency specifically designed for endovascular implantable devices. This chapter addresses critical challenges such as power budget constraints, size limitations, and implantation risks. The system is versatile, supporting monitoring and stimulation applications,

and represents a significant advancement in wireless power technology for biomedical devices.

Chapter 6 focuses on the development of novel hair electrodes that transform EEG devices into fully wireless systems with improved aesthetics. This work addresses the invasiveness and comfort issues associated with brain monitoring devices, enhancing user experience and usability. The innovative design makes EEG monitoring more practical for both clinical and everyday applications.

Chapter 7 concludes the thesis by summarizing the key contributions of the work and discussing potential future directions. It highlights the broader implications of miniaturized wireless and battery-free systems in healthcare and biomedical research, suggesting pathways for continued innovation in this rapidly evolving field.

Each chapter in this thesis is written to be as self-sufficient as possible. The **Bibliography** goes *after* the last chapter and *before* the first appendix.

Chapter 2

Literature Review

Firstly, this literature review explores the advancements and challenges in wireless and battery-free physiological monitoring and stimulation systems, emphasising their transformative potential in healthcare and biomedical research. These wireless power transfer and data communication systems eliminate the limitations of traditional tethered and battery-dependent designs, enabling long-term, minimally invasive applications for monitoring health conditions, diagnosing diseases, delivering therapies, restoring lost functions, and enhancing biological processes.

The review dives into key technologies underpinning these systems, including power casting, energy harvesting, bioelectronics, data communication and signal processing. It highlights recent innovations in wireless sensing platforms, stimulation modalities, and real-time closed-loop control systems. The review also addresses critical challenges such as miniaturisation, power efficiency, computational demands, data bandwidth limitations, and safety constraints like specific absorption rates. Emerging trends, such as energy-efficient designs, multi-source energy harvesting, and on-device machine learning, are identified as the future application trends for these technologies. This review underscores the potential of wireless and battery-free systems to revolutionise healthcare standards, enhance therapeutic precision, and facilitate groundbreaking research in biological and clinical sciences.

2.1 Introduction

Cells, tissues, and the human biological system are constantly in dynamic communication, exchanging and responding to electrical, chemical, and mechanical signals. These intricate interactions drive various biophysical and biological activities that underpin life itself Hong and Lieber (2019); Wellman et al. (2018); Won et al. (2020). This ongoing exchange is essential for maintaining homeostasis and supporting complex biological processes such as growth, repair, and adaptation to environmental changes. Understanding these mechanisms is crucial for advancing our knowledge of how biological systems operate, from cellular to entire organisms. This knowledge has profound implications for unlocking the mysteries of fundamental biological mechanisms, enabling the discovery of innovative diagnostic approaches, and paving the way for novel therapeutic interventions to treat a wide range of diseases Chen et al. (2017); Corrias et al. (2012); Grill et al. (2009)

Despite decades of research, our ability to record, interpret, and manipulate these bio-signals remains limited. The challenge lies in the complexity and diversity of the signals, which span a wide range of temporal and spatial scales. While significant, traditional bio-signal recording and stimulation technologies often fall short in capturing the full spectrum of these signals or delivering precise therapeutic interventions. However, recent advances in low-power, large-scale integrated circuits, cutting-edge electronics, and novel materials have revolutionised the field. These breakthroughs have enabled the collection and digitalisation of a collection of bio-signals with outstanding accuracy and efficiency Fattahi et al. (2014).

Simultaneously, modern devices are increasingly capable of interacting with physiological systems, offering new ways to deliver targeted stimulation or modulate biology-related environments. These capabilities have expanded the possibilities for both diagnostic and therapeutic applications. For example, precise electrical stimulation can help restore function in damaged neural circuits, while chemical delivery systems can modulate localised environments to promote tissue repair or counteract disease Jonsson et al. (2016).

The convergence of biology and electronics has given rise to a growing group of technologies that bridge these two domains. These technologies, often tailored to specific modalities, enable seamless integration between biological systems and devices. They range from wearable sensors and implantable devices to sophisticated tools for imaging and real-time data analysis. By building increasingly robust and versatile interfaces, researchers are expanding our understanding of biological processes and creating new opportunities for precision medicine, personalised healthcare, and improved quality of life for patients worldwide Kotov et al. (2009); Won et al. (2018).

This emerging synergy between biology and technology marks a transformative era where the boundaries between natural and artificial systems continue to blur, unlocking new possibilities for scientific exploration and human health advancements.

Physiological monitoring systems play a pivotal role in modern biomedical research and healthcare by continuously recording high-fidelity bio-signals and transmitting these data for advanced processing and analysis. These innovative sensing platforms have achieved remarkable milestones across various applications, revolutionising our ability to observe and understand complex biological processes. For instance, a high-density, long-term brain signal recording system enables researchers to capture detailed neural activity over extended periods, providing critical insights into brain functions and disorders Steinmetz et al. (2021). Similarly, advanced photometric systems can now precisely monitor cell-specific activities, allowing scientists to decode cellular behaviours and their roles in more extensive biological networks Burton et al. (2020a).

In cardiovascular health, monitoring chronic physiological changes has become a reality through sophisticated wearable and implantable sensors, which provide real-time data to assess conditions like hypertension and heart failure Reeder et al. (2019). Wireless oximetry probes, designed for continuous and localised oxygenation monitoring, have brought significant advancements in understanding tissue oxygen dynamics during chronic diseases or critical care scenarios Lazaro et al. (2019); Zhang et al. (2019a). Furthermore, implantable devices that integrate with smartphones are breaking new ground. For example, such a system can non-invasively read in vivo

blood flow information, offering patients and clinicians a portable and convenient diagnostic tool Vennemann et al. (2020a). Another groundbreaking development is using thermal conductivity changes in tissues to detect abnormal blood flow, aiding in managing conditions like hydrocephalus Krishnan et al. (2020). These technologies exemplify the transformative power of physiological monitoring systems in bridging the gap between data collection and actionable medical insights.

On the other hand, the delivery of targeted stimulation to biological systems has emerged as both a powerful treatment modality and a versatile tool for modulating biological properties. The repertoire of stimuli has expanded significantly beyond electrical energy to include optical, acoustic, magnetic, and thermal modalities, enhancing the versatility and precision of these interventions. Optogenetic stimulation, for example, has demonstrated the ability to alter social behaviours in mice by targeting specific neural circuits, showcasing its potential for psychiatric and behavioural research Yang et al. (2021). In neurology, optical stimulation of the brain has proven effective in alleviating epileptic seizures, offering a less invasive and more targeted approach compared to traditional therapies Paz et al. (2013).

In metabolic regulation, advanced stimulation techniques are being explored to control blood glucose levels, presenting a promising avenue for managing diabetes without pharmacological interventions. For patients with spinal cord injuries, stimulation technologies have enabled the restoration of walking ability by reactivating dormant neural pathways, bringing new hope for functional recovery. Drug delivery systems have also seen significant innovation, with targeted stimuli guiding therapeutic agents precisely to affected areas, minimising systemic side effects and enhancing treatment efficacy. Deep brain stimulation has become a cornerstone treatment for Parkinson's disease, significantly improving motor symptoms and quality of life for patients who do not respond to medications Krauss et al. (2021). Similarly, brain stimulation techniques are being employed to enhance working memory, opening new possibilities for addressing cognitive deficits associated with ageing and neurological disorders Khan et al. (2019).

Together, these physiological monitoring and stimulation advancements represent a

giant leap forward in biomedical science. Observing and modulating biological systems with such precision and versatility increases our understanding of complex physiological processes and enables the development of personalised and adaptive therapeutic strategies. This integration of monitoring and stimulation technologies is redefining the boundaries of what is possible in diagnostics, treatment, and research, indicating a new healthcare innovation era.

When sensing and stimulation platforms are combined with real-time data analysis capabilities, the intervention system can deliver targeted stimulation precisely when specific conditions are detected. These advanced systems, known as closed-loop control systems, represent a transformative approach to automated therapeutic interventions. By continuously monitoring physiological signals, analysing the data in real-time, and responding with immediate feedback, these systems eliminate the need for human intervention and ensure that stimulation is delivered only when required Mickle et al. (2019). Despite their promise, current closed-loop systems face significant challenges, primarily related to implantable devices' power constraints and size limitations. These constraints limit the computational capabilities of the implants, restricting them to performing only basic data analysis locally Hegde et al. (2021); Park et al. (2018); Ramot and Martin (2022).

The autonomous functionality of closed-loop systems offers numerous advantages, including adapting to dynamically changing physiological states. For example, one of the most demanding applications is seizure control. These systems can detect early warning signs of a potential seizure, such as abnormal neural activity patterns, and deliver preemptive stimuli to halt the seizure before it fully manifests Jonsson et al. (2016); Paz et al. (2013). This approach has shown immense potential for improving the quality of life for individuals with epilepsy, reducing the frequency and severity of seizures without the need for constant medication or manual intervention.

Two primary engineering solutions have emerged to address the challenges posed by implants' limited data analysis capabilities. The first solution involves designing the system as discrete parts, including a sensing implant, a stimulation unit, and an external data processing unit. These components are interconnected using wired or

wireless communication links to achieve closed-loop control. This modular approach allows each component to specialise in a specific function—sensing, data processing, or stimulation—leveraging the computational power of the external unit to perform complex analyses. However, this design introduces its own challenges, such as the need for reliable and efficient communication between the components. Wired systems may suffer from increased complexity due to long lead wires, which can cause discomfort or limit mobility for the patient. On the other hand, wireless communication systems must overcome issues like signal interference, latency, and power consumption.

The second solution to the problem of limited local computational capacity involves compressing data at the sensing implant and transmitting the compressed data to a cloud-based platform for processing. With its relatively unlimited computational resources, the cloud can perform sophisticated analyses of the incoming data and generate stimulation commands. These commands are then relayed back to the stimulation unit for execution. While this approach offers the advantage of advanced data analysis and scalability, it has drawbacks. One significant limitation is the dependence on an active Internet connection, which may not always be feasible in all settings. Furthermore, the time delay introduced by transmitting data to the cloud and receiving the stimulation command can be problematic in applications requiring ultra-fast response times, such as cardiac arrhythmia correction or acute pain management.

Despite these limitations, integrating real-time data analysis with sensing and stimulation platforms has already demonstrated groundbreaking potential across various applications. Future advancements in miniaturisation, power efficiency, and edge computing could further enhance the capabilities of these systems. For instance, developing ultra-low-power processors and advanced algorithms optimised for local processing could enable more complex analyses to be performed directly on the implant, reducing the reliance on external processing units or cloud platforms. Moreover, innovations in wireless communication protocols and energy harvesting technologies could address the challenges of power consumption and connectivity, paving the way for fully autonomous and self-sustaining closed-loop systems.

The ongoing and growing evolution of closed-loop control systems highlights a conjunction of disciplines, including bioengineering, electronics, and computational sciences, to create intelligent medical devices capable of revolutionising healthcare. By enabling precise, on-demand interventions tailored to an individual's unique physiological state, these systems promise to significantly improve treatment outcomes, enhance patient comfort, and reduce the burden on healthcare providers. As research continues, the potential applications for these systems will likely expand, offering new solutions for managing chronic conditions, enhancing rehabilitation, and even advancing human-machine interfaces.

2.2 Limitations of systems with battery and tethered

Electronic devices rely on power supplies to operate, and batteries are often considered a reliable and portable energy source. Tethered systems, on the other hand, offer a straightforward and highly efficient means of transferring energy, signal, data and other information using various modalities. These physical connections, such as conductive wires for electrical power and data, optical fibres for light-based communication, and tubes for liquid or air transfer are extensively utilised in research and medical devices due to their simplicity and effectiveness Boyden et al. (2005); Canales et al. (2015); Kim et al. (2016); Piatkevich et al. (2018); Pisanello et al. (2017). Despite widespread adoption, battery-powered and tethered systems face significant challenges when long-term use is required, particularly in applications demanding high mobility or minimal interference with the surrounding environment Minev et al. (2015); Sridharan et al. (2013).

The reliance on tethered systems introduces several issues that are particularly critical in scenarios requiring prolonged or dynamic operation. Fixation parts used to anchor the tethered system often add complexity and bulk, making them impractical for wearable or implantable devices. Furthermore, tethers can interfere with surrounding

tissues, causing irritation, inflammation, or even physical damage over time. This interference not only risks compromising the integrity of the tissue but also reduces the stability and reliability of the connection, which is crucial for consistent device performance in medical applications Fan et al. (2011); Lu et al. (2018).

Battery-powered systems, while eliminating the need for physical tethers for power present their own set of limitations. The energy density of current battery technologies is a primary constraint, limiting the duration for which these systems can operate without recharging or replacement. Additionally, the size and weight of batteries often impose restrictions on the design and functionality of devices, especially those intended for implantation. The need to recharge or replace batteries frequently increases the overall system complexity, requiring additional components such as charging circuits and external power supplies. In implantable systems, recharging can necessitate invasive procedures or bulky external equipment, which undermines the benefits of portability and convenience Burton et al. (2020b); Gutruf et al. (2018); Zhang et al. (2019c).

Another critical issue with batteries is the potential of failure, particularly in long-term applications. Battery failure can occur due to degradation of the chemical components over time, leading to reduced capacity or complete loss of functionality. This poses a significant risk in medical devices, as a failed battery could compromise the performance of life-critical systems. Additionally, the leakage of chemical materials from damaged or degraded batteries presents a serious hazard, with the potential to cause toxic contamination of surrounding tissues. This risk is especially problematic in implantable devices, where chemical contamination can lead to inflammation, infection, or other severe complications, making batteries unsuitable for many long-term applications Bhatia and El-Chami (2018); Goodman et al. (2006); Merchant et al. (2016).

Given these limitations, researchers and engineers are actively exploring alternative solutions to power and connect devices. Wireless energy transfer technologies, such as inductive coupling and resonant magnetic systems, are gaining traction to provide power without physical tethers. These systems offer the potential to reduce tissue

interference and improve device mobility while maintaining reliable energy delivery. Similarly, advancements in energy harvesting technologies, such as piezoelectric materials and thermoelectric generators, aim to harness energy from the environment or the human body to extend device operation time without needing batteries.

Innovations in battery technology are also being pursued to address the limitations of current systems. Solid-state batteries, for instance, promise higher energy densities and improved safety by eliminating the liquid electrolytes prone to leakage and failure. Miniaturised batteries and flexible energy storage devices are being developed to enable their integration into wearable and implantable devices without compromising design constraints.

Ultimately, overcoming the challenges associated with batteries and tethers will be critical to the next generation of electronic devices, particularly in fields like biomedical engineering, robotics, and the Internet of Things (IoT). By minimising physical constraints and maximising energy efficiency, these innovations could enable devices that are more compact, reliable, and capable of operating autonomously over extended periods. Such advancements can potentially revolutionise healthcare applications, scientific research, and beyond, paving the way for smarter, safer, and more versatile technologies.

2.3 Design considerations for wireless and battery-free systems

The physiological monitoring and stimulation system consists of four main parts; (I) an energy harvesting part, (II) a sensing part, (III) a stimulation part and (IV) a data processing part. Fig. 2.1 shows the logic of the system and the design consideration. For all power delivery, we listed the most popular modality and the design considerations related to the design challenge.

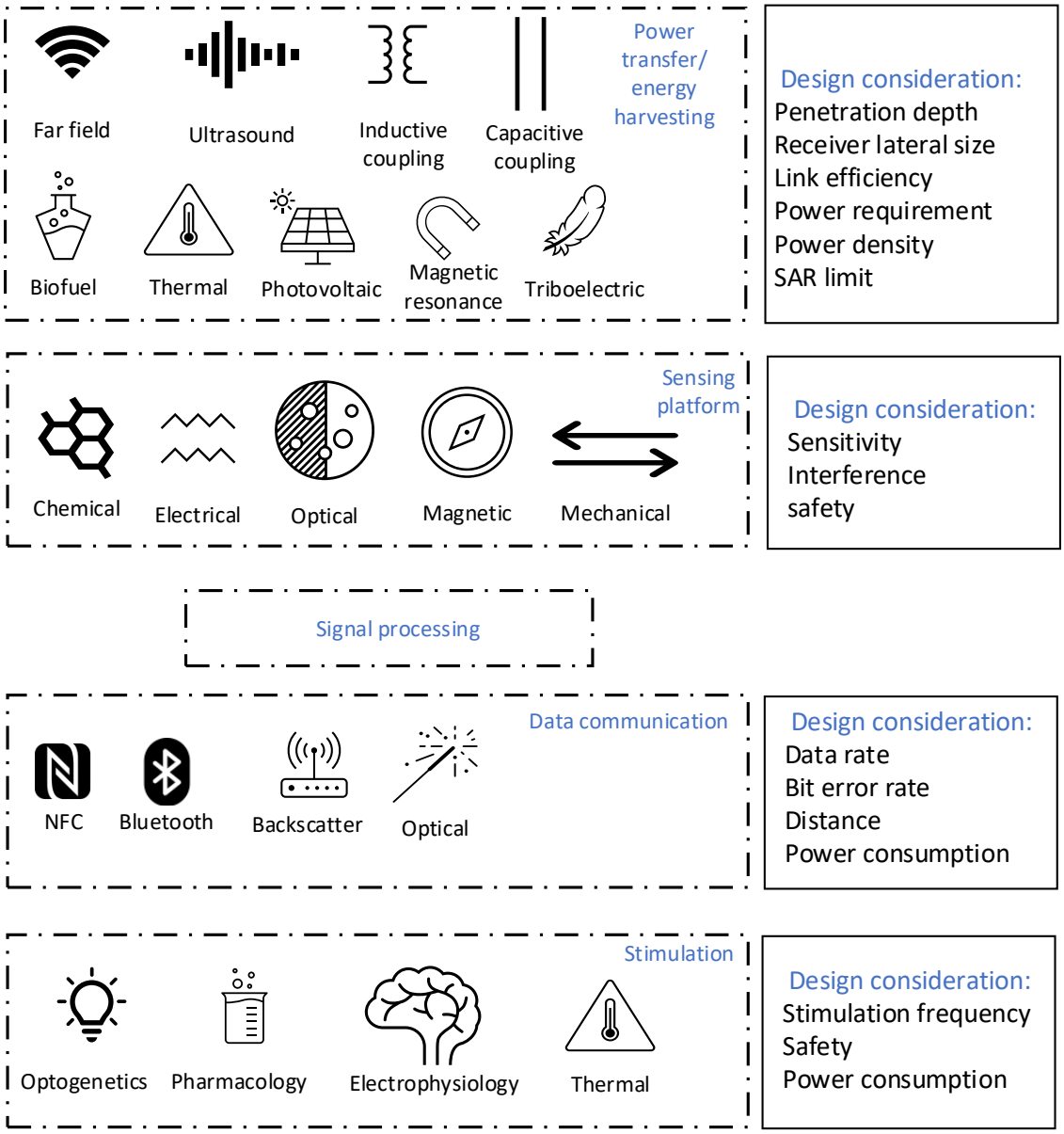

Figure 2.1 – Modalities for power transfer, energy harvesting, data telemetry, sensing and stimulation. This diagram indicates the considerations that, in our view, should be taken into account during the system design phase for each class.

2.4 Solutions for energy delivery and wireless data

Powering implantable devices and enabling reliable data transmission to and from these systems represent fundamental challenges in developing physiological monitoring and stimulation technologies. Achieving wireless energy transfer and data communication in implantable devices requires using specific channels and modalities, each with distinct advantages and limitations. Among the commonly explored methods are electromagnetic, ultrasound, optical, and mechanical modalities. Each modality offers unique benefits regarding energy delivery efficiency, tissue penetration, and data transmission capacity, but they also present specific technical hurdles that need to be addressed to optimise their performance.

The ultrasound channel, in particular, is notable for its ability to penetrate deeply into soft tissues, making it highly suitable for powering and communicating with devices implanted in deep or hard-to-reach locations. One of the key advantages of the ultrasound approach is its compatibility with miniaturised transducers. Reports in the literature describe submillimeter- and micrometre-scale piezoelectric transducers explicitly designed for neural implants, underscoring the potential for compact and efficient systems Ghanbari et al. (2019); Sonmezoglu et al. (2021). These piezoelectric materials convert acoustic waves into electrical energy, enabling wireless power delivery to the implantable device.

However, the power delivery efficiency of ultrasound channels is relatively low, typically reaching up to 0.23% under optimised conditions Chang et al. (2018b); Charthad et al. (2015); Ghanbari et al. (2019); Meng and Kiani (2016). While this efficiency level is sufficient for low-power applications, such as certain neural implants, it remains a limitation for devices requiring higher energy inputs. Data communication through ultrasound channels generally employs backscatter techniques to minimise power consumption in the device's internal components. Backscatter communication involves modulating the reflected ultrasound signal to encode data, significantly reducing the power the implant requires to transmit information.

The frequency of operation for piezoelectric transducers used in ultrasound systems

is typically less than 2 MHz Chang et al. (2018a); Charthad et al. (2015); Seo et al. (2015); Song et al. (2015), with optimal operating frequencies often falling below 5 MHz Barbruni et al. (2020). This relatively low-frequency range balances power delivery efficiency and tissue penetration depth while avoiding excessive attenuation. However, these frequency limitations impose constraints on the data transmission rate. For example, ultrasound-based data telemetry systems often achieve only a few hundred kilobits per second, which may be insufficient for high-bandwidth applications such as real-time video or large-scale data streaming.

Moreover, while backscatter-based data telemetry is energy-efficient, it introduces challenges in implementing advanced modulation schemes. Techniques such as Orthogonal Frequency-Division Multiplexing (OFDM), which can significantly increase data rates and improve spectral efficiency, are difficult to implement with backscatter communication due to their limited bandwidth and processing capabilities. Consequently, ultrasound channels are often restricted to simpler modulation schemes, limiting their data transmission capacity.

Despite these challenges, ultrasound remains a promising modality for powering and communicating with implantable devices. Its ability to penetrate deep tissues and support miniaturised transducers makes it an attractive option for applications in neural interfaces, cardiovascular monitoring, and other medical fields. Advances in material science, such as developing more efficient piezoelectric materials and transducer designs, could improve power delivery and data transmission efficiency. Similarly, innovations in signal processing and modulation techniques may enable higher data rates while maintaining low power consumption.

Researchers are also exploring hybrid approaches that combine multiple channels to maximise the potential of ultrasound and other modalities for implantable systems. For instance, integrating ultrasound with electromagnetic or optical systems could leverage the strengths of each modality, providing a more versatile and robust energy and data transfer solution. These hybrid systems could optimise tissue penetration, energy efficiency, and data bandwidth, addressing the limitations of individual channels.

Ultimately, overcoming the challenges of powering and communicating with implantable devices is critical for advancing biomedical engineering. By refining ultrasound-based systems and exploring complementary technologies, researchers can enable a new generation of implantable devices with enhanced functionality, reliability, and clinical impact. This progress holds the potential to transform healthcare by enabling more effective diagnostics, therapies, and long-term monitoring solutions.

2.5 Sensing platforms

The table 2.1 below provides a detailed summary of emerging and promising wireless sensing platforms specifically designed for a wide range of biomedical applications. These platforms represent the critical interface between biological systems and digital technologies, converting complex biological activities into quantifiable and processable signals that can be used for monitoring, diagnosis, and intervention Kawamura and Miyata (2016). Each sensing platform may consist of a single sensor for targeted detection or multiple sensors working together to monitor a comprehensive set of biomarkers. This flexibility enables customisation to suit specific clinical needs or research applications, offering significant potential for personalised and precision medicine Lee and Mutharasan (2005); Sawant (2017).

The modalities employed in these platforms are diverse and technologically sophisticated. They include amperometry, potentiometry, conductometry, and electrochemical approaches, which are well-suited for detecting chemical and ionic changes in biological systems. Optical sensing is frequently used for its high resolution and non-invasive capabilities, while piezoelectric sensing excels in detecting mechanical changes, such as pressure or vibration. Magnetic and thermal sensors extend the functionality of these platforms by enabling the detection of changes in magnetic fields or temperature, adding another layer of versatility and enabling applications in complex biological environments Ronkainen et al. (2010).

These sensing platforms have been developed to interact seamlessly with various physiological systems, including the nervous system, where they monitor electrical activ-

ity and neurotransmitter levels, and the cardiovascular system, where they provide real-time data on blood pressure, oxygenation, and flow dynamics. In the endocrine system, these platforms enable the detection of hormonal fluctuations critical for understanding metabolic and reproductive health. They also play a vital role in the urinary system by monitoring parameters such as hydration levels and kidney function. Furthermore, in the integumentary system, these sensors are utilised for skin monitoring, detecting changes in hydration, temperature, or biochemical markers associated with conditions like inflammation or wound healing.

The table categorises these platforms based on their technical capabilities, applications, and compatibility with biological systems. The table highlights not only the technological diversity of these platforms but also their significant potential to revolutionise healthcare by providing minimally invasive, continuous, and wireless monitoring solutions. As such, the table is a valuable resource for researchers, engineers, and clinicians seeking to develop or implement these advanced sensing technologies in various medical and research contexts.

Table 2.1 – Summary of wireless sensing platforms and their applications.

Interface	**Function**	**Modality**	**Technical highlights and main achievement**	**Year**
Neuro cells	Brain structures monitoring, neuronal activity	Photometric (Optical)	Wireless transceiver, 600 mW power consumptionfibre optic-cannula, lightweight and compact, battery powered Khiarak et al. (2018)	2018
Neuro cells	Recording cell-specific neuronal activity	Photometric (Optical)	Subdermal device for freely moving subjects, wireless, battery-free, 13.56MHz NFC for both data and powerBurton et al. (2020c)	2020

Continued on the next page

Interface	Function	Modality	Highlights and main achievement	Year
Neuro cells	Recording membrane potential from a group of neurons	Electric potential	Voltage imaging, simultaneously records multiple neurons, SNR 0.93 per 1mV bandwidth 1KHz, Adam et al. (2019)	2019
Neuro cells	Recording cellular signaling networks	Fluorescent (Optical)	Fluorescent to indicate the spatiotemporal dynamics of signal transduction pathways Greenwald et al. (2018)	2018
Neuro cells	Recording pH changes of living cells	Biochemistry (Optical)	Detect cellular processes by pH, pH imaging by fluorescent, genetically encoded pH Martynov et al. (2018)	2018
Brain signal	Recording brain signal, muscle signal	Bioelectrical	Far field energy harvesting, free moving insects, single-chip telemetry integrated Thomas et al. (2012)	2012
Brain signal	Recording neural spikes from the brain	Bioelectrical	Backscatter communication, 12.4 pJ/b Rosenthal et al. (2019)	2019

Continued on the next page

Interface	Function	Modality	Highlights and main achievement	Year
Brain signal	Recording pharmacological signal from optofluidic device	Optical	Optofluidic device, lightweight and injectable, NFC Zhang et al. (2019d)	2019
Brain signal	Recording posteromedial cortical rhythm	Optical (Imaging)	Camera imaging, fibre photometry, two-photon imaging, combined silicon probe Vesuna et al. (2020)	2020
Brain signal	Recording brain activities ECoG in a certain area at high electrode density	Bioelectrical	High-density electrodes (1000), wireless system, data compressing Musk (2019)	2019
Brain signal	Recording brain activities ECoG signals	Bioelectrical	Low-noise, low-power, high sampling rate Petkos et al. (2019)	2019
Cardiac signal	Recording and long-term monitoring cardiac abnormalities	Bioelectrical	Battery-free and wireless, electronic tattoo, epidermal interface, stretchable Alberto et al. (2020)	2020

Continued on the next page

Interface	Function	Modality	Highlights and main achievement	Year
Cardiac signal	Monitoring cardiac activities for baby	Bioelectrical	Analytics in the device, epidermal interface, stretchable, battery-free and wireless, infant care Chung et al. (2019)	2019
Cardiac signal	Monitoring respiration abnormalities from waist	Triboelectric	Triboelectric nanogenerator, wireless, sleep apnea detection Zhang et al. (2019b)	2019
Cardiac signal	Monitoring blood oxygenation	Optical	High-fidelity blood oxygenation reading, NFC, smartphones reading Lu et al. (2021)	2020
Cardiac signal	Monitoring blood oxygen saturation in heart	Optical	Real-time intravascular oxygen level, Bluetooth communication, catheter-type Chen et al. (2022a)	2021
Cardiac signal	Monitoring electrocardiogram for a long time	Bioelectrical	Patch format, small size, high signal quality, low power consumption, send data through smartphone Zulqarnain et al. (2020)	2022
Cardiac signal	Recording electrophysiological signals for cardiac or neural activities	Bioelectrical	Small- to large-scale, epidermal interfaces, magnetic resonance compatible, skin-like surface Tian et al. (2019)	2019

Continued on the next page

Interface	Function	Modality	Highlights and main achievement	Year
Cardiac signal	Monitoring blood flow information	Magnetic	Use magnetic flow meter to detect blood flow after a valve, NFC powered, smartphone on-demand reading Vennemann et al. (2020b)	2020
Biofluids	Monitoring fluid and detecting abnormalities	Biochemical	Long-term analysis of saliva, sweat, tears, and interstitial fluid, body interface, continuous reading Baker and Wolfe (2020)	2020
Endocrine	Continuously monitoring glucose level	Bioelectrical	Using passive inductor-capacitor tank as resonator to detect glucose level, wireless powered Hassan et al. (2020)	2022
Cortisol	Continuously detect stress level from sweat	Electro chemical	Epidermal, flexible, NFC power and data communication, differential pulse voltammetry reading Cheng et al. (2021)	2020
Cortisol	Monitoring cortisol level by implantable device	Electro physiological	Collect cellular activities from adrenal cortex, wireless, electrophysiological measurement Sunwoo et al. (2019)	2019

Continued on the next page

Interface	Function	Modality	Highlights and main achievement	Year
Mechanical	Monitoring bladder pressure	Electrical	Pressure measurement, Bluetooth Low Energy data communication, magnetic resonance power delivery Zhong et al. (2020)	2019

2.6 Stimulation platforms

The table2.2 provides an in-depth overview of advanced stimulation technologies, highlighting their diverse applications and the underlying mechanisms that enable interaction with biological tissues. Stimulation refers to the precise delivery of specific energy or stimuli to biological tissues, prompting a targeted physiological or therapeutic response. These technologies have become indispensable in modern medical treatments and research, offering controlled and minimally invasive solutions for managing various conditions. The ability to modulate biological processes through stimulation has opened new frontiers in healthcare, from restoring lost function to enhancing natural healing and controlling complex biological systems.

Several widely used stimulation modalities are included in the table, each tailored to distinct applications and biological mechanisms. Electrical stimulation, one of the most established approaches, uses controlled electrical currents to activate or inhibit neural or muscular activity. It is commonly applied in therapies for neurological disorders, such as deep brain stimulation for Parkinson's disease, and in devices like pacemakers and cochlear implants. Mechanical stimulation, which involves the application of physical forces such as pressure or vibration, is critical for promoting tissue repair, bone regeneration, and cellular differentiation. This modality leverages the body's natural mechanotransduction pathways, enabling responses essential for healing and adaptation.

Photonic stimulation uses light energy to influence biological systems and has been widely adopted in therapeutic and diagnostic contexts. Applications include photodynamic therapy for cancer treatment, laser therapies for dermatological conditions, and light-based modulation of neural activity. Optogenetic stimulation, an emerging and highly sophisticated technique, combines genetic engineering with photonic energy to achieve unprecedented precision. Optogenetics allows researchers and clinicians to control biological functions with millisecond accuracy by introducing light-sensitive proteins into specific cells. This modality is particularly transformative in neuroscience, where it is used to dissect neural circuits, study brain disorders, and explore innovative treatments.

Table2.2 categorises these wireless stimulation platforms based on their applications, providing a clear overview of their capabilities and potential. These platforms are grouped according to the systems they target and the therapeutic goals they achieve. For instance, neural stimulation platforms focus on applications such as controlling seizures, managing chronic pain, and restoring sensory or motor function. Cardiovascular platforms are designed to address arrhythmias, improve blood flow, or monitor and influence heart function in real time. Other platforms focus on endocrine and metabolic modulation, enabling therapies for diabetes and other hormonal disorders. At the same time, some are tailored for tissue repair, wound healing, or enhancing the body's regenerative capacity.

Wireless stimulation technologies are gaining significant attention due to their ability to operate without physical tethers, offering greater patient mobility and comfort while reducing the risk of infection or tissue damage. These platforms incorporate advanced energy transfer methods, such as inductive coupling, ultrasound, or optical systems, to power and control the stimulation units. This innovation eliminates the constraints of traditional wired systems, making them suitable for long-term applications and dynamic environments.

Table2.2 also highlights the ongoing advancements in these technologies, including miniaturisation, enhanced precision, and integration with other systems like wireless sensing or cloud-based data processing. These features underscore the potential of

wireless stimulation technologies to revolutionise medical treatments and research. By providing a comprehensive summary of their applications, capabilities, and limitations, the table is a valuable resource for researchers, engineers, and clinicians seeking to leverage these innovative platforms for improved therapeutic outcomes and a deeper understanding of biological systems.

Table 2.2 – Summary of wireless stimulation platforms and their applications.

Interface	**Function**	**Modality**	**Technical highlights and main achievement**	**Year**
Central nervous system	Deep brain stimulation to change the behaviour of mice	Magnetoelectric	Wireless, magnetoelectric nanoelectrodes to deliver stimulation, injectable, uses magnetic fields to control stimulation Kozielski et al. (2021)	2021
Central nervous system	Deep brain stimulation to treat neurological disorders	Thermal (magnetothermal)	Wireless, magnetothermal, nanoparticles as the medium to generate heat Chen et al. (2015)	2015
Peripheral nervous system	Deliver stimulation to nerve bundles by application	Electrical	Wireless, powered by ultrasonic, bidirectional communication, millimetre scale Kozielski et al. (2021)	2020

Continued on the next page

Interface	Function	Modality	Highlights and main achievement	Year
Central nervous system	Deliver stimulation to brain tissue	Electrical	Biofuel cell powered, fully small and light, wireless communication to control stimulation Lee et al. (2021)	2021
Spinal cord	Modulating spinal cord to control pain	Optogenetics	Minimally invasive, no optical fibre, stretchable, wireless power supply, and data communication Park et al. (2015)	2015
Spinal cord	Spinal cord stimulation to evoke hindlimb muscular activity	Optogenetics	Converts near-infrared (NIR) light to visible light for stimulation, heat pulling to process the material, nanoparticles as media Wang et al. (2020)	2019
Peripheral nervous system	Optogenetic therapy for retinitis pigmentosa	Optogenetics	Uses optogenetic tools as artificial photoreceptors to restore function Busskamp et al. (2012)	2012
Central nervous system	Deliver stimulation to control temporal-lobe epilepsy	Optogenetics	Real-time, closed-loop response, wireless, laser delivery Krook-Magnuson et al. (2013)	2013

Continued on the next page

Interface	Function	Modality	Highlights and main achievement	Year
Central nervous system	Combined electrical and optical stimulation	Electrical & Optical	Wireless inductive coupling powered, combined optical and electrical stimulation Jia et al. (2020)	2020
Peripheral nerve	Implantable nerve stimulator	Electrical	Commercial components to implement, wireless power and communication Sivaji et al. (2019)	2019
Bone tissue	Modulation of intramedullary fluid to change bone density	Mechanical	Wireless, battery-free, pressure modulation, on-demand control Chen et al. (2020)	2020
Peripheral nerve	Deliver stimulation to nerve bundle to restore function	Optical & Electrical	Uses optical energy to deliver stimulation, low volume, chronic stimulation, uses organic electrolytic photocapacitor Silverå Ejneby et al. (2021)	2021
Peripheral nerve	Deliver stimulation to the spinal cord for pain relief	Magnetoelectric & Electrical	Uses magnetoelectric effects to power the device and transfer data, small size, safety on high power Yu et al. (2020)	2020

2.7 Signal processing and data analysis

The signal processing unit plays a pivotal role in physiological monitoring and stimulation systems, bridging raw sensor data and actionable information. Its primary function is to improve and enhance the quality of the information collected from the sensor, making it suitable for real-time applications or further in-depth analysis. Within this framework, signal processing objectives in implantable devices can be broadly categorised into two main goals. The first is data compression, which reduces the bandwidth requirements for data communication and enables efficient transmission. The second is real-time processing, aimed at minimising the delay between sensing and response, a critical requirement for applications where immediate intervention is necessary.

One of the most significant challenges signal processing units address is the reduction of data rates through local, in-device processing. This is particularly important in implantable systems where wireless telemetry links often have limited bandwidth due to energy constraints and the physical limitations of transmitting signals through biological tissues Quiroga (2012a). Various techniques have been developed to achieve efficient data compression. Spike thresholding is a widely adopted method in which only spike counts exceeding a predetermined threshold are transmitted, drastically reducing the amount of data sent. Similarly, compressive sensing adaptively compresses data based on the monitored events, ensuring that only the most relevant information is preserved. Another advanced technique is spike sorting, which involves identifying and transmitting the features of neural spikes instead of the raw signal, significantly decreasing data volume Navajas et al. (2014b); Park et al. (2017a).

While these spike-based approaches effectively lower telemetry bandwidth requirements, their utility is often application-specific. For instance, transmitting spike data is highly suitable for targeted applications such as controlling prosthetics or neurostimulation devices. However, many other applications, such as brain disease monitoring, research on BCI algorithms, and neuro-electro-physiological studies, require the preservation of high-fidelity signals. These applications demand the transmission

of raw or minimally processed data to capture the full spectrum of neural activity, emphasising the need for adaptable and versatile signal-processing solutions.

In addition to compression, significant efforts in signal processing research focus on real-time in-device processing, which is crucial for minimising latency between sensing and action. Real-time processing requires low-power computing solutions to meet the strict energy constraints of implantable devices, which are limited by safety considerations and size restrictions. ASICs are commonly utilised in these systems to achieve efficient low-power operation. ASICs are custom-designed to handle specific processing tasks, ensuring they consume minimal power while maintaining high performance Kassanos et al. (2018); Pu et al. (2018).

Beyond traditional hardware, modern implantable devices increasingly leverage advanced algorithms for in-device processing, including machine learning and deep learning. These algorithms enable the device to recognise patterns, classify data, and make decisions autonomously, enhancing the system's responsiveness and adaptability Lai et al. (2018); Liu and Richardson (2021); Vellappally et al. (2019). However, implementing such computationally intensive algorithms within the constrained environment of an implant poses challenges, particularly in terms of power consumption and processing speed. To address this, researchers are exploring neuromorphic chips—hardware inspired by the structure and function of the human brain. Neuromorphic chips offer a promising solution by combining low power consumption with high performance and short latency, making them ideal for real-time applications in implantable devices Shaikh et al. (2019).

Integrating these advanced signal-processing techniques into physiological monitoring and stimulation systems has far-reaching implications. By reducing data rates, these systems can operate efficiently within the constraints of current wireless communication technologies, while real-time processing ensures timely interventions for critical applications. Moreover, the ongoing development of low-power computing solutions, machine learning, and neuromorphic hardware holds the potential to enhance the capabilities of these devices further. This progress will enable more sophisticated, autonomous, and versatile systems, paving the way for improved diagnostics, thera-

peutic interventions, and research into complex biological processes.

2.8 Conclusion

Wireless and battery-free physiological monitoring and stimulation systems represent a transformative leap in biomedical technology, offering a versatile and promising approach to addressing some of the most critical challenges in healthcare and biological research. These systems enable various applications, including fundamental biological studies, continuous health condition monitoring, disease diagnosis, therapeutic interventions, restoration of lost functions, and even the enhancement of natural body functions. Their ability to operate without batteries or physical tethers makes them uniquely suited for applications requiring long-term, minimally invasive operation and high mobility, providing unprecedented opportunities to improve patient outcomes and advance scientific understanding.

Developing wireless and battery-free systems involves a convergence of cutting-edge technologies spanning multiple disciplines. Key innovations include power casting and energy harvesting, which enable the wireless delivery and generation of power to support device operation. Advances in bioelectronics and biochemistry allow for precise sensing and stimulation at the molecular and cellular levels, while biomechanical and optoelectronic technologies expand the range of stimuli and data modalities these systems can leverage. Microfluidics further enhances the capability of these devices by enabling localised delivery of therapeutic agents or sampling of biomarkers. Additionally, data communication and signal processing technologies facilitate the efficient transfer and interpretation of large datasets. At the same time, on-device low-power data analysis and artificial intelligence algorithms enable real-time decision-making and adaptive control.

As the field advances, the vision of a fully integrated, wireless, and battery-free sensing platform equipped with an automatically triggered stimulation system appears increasingly achievable. Such systems promise to operate autonomously, providing

seamless feedback and intervention without human input. However, significant challenges remain in realising this vision. Miniaturisation of the system is a critical hurdle, as these devices must be small enough to be implanted or worn comfortably without compromising functionality. The trade-off between power consumption and computational capability is another key issue, as more complex tasks require more substantial energy resources, which are inherently limited in wireless and battery-free designs. High-bandwidth continuous data transmission remains a bottleneck for applications requiring real-time, high-fidelity signal monitoring. However, the constraints imposed by SAR limit the power levels that can be safely delivered to biological tissues.

Despite these challenges, the future of wireless and battery-free systems is bright, with several promising trends emerging from the reviewed literature. Efforts to improve power delivery efficiency are at the forefront, with researchers exploring novel energy transfer techniques and materials to maximise the energy available to the device. Simultaneously, innovations aimed at decreasing overall power consumption, such as energy-efficient circuit designs and neuromorphic computing, are helping to extend operational lifetimes. Harvesting energy from multiple sources, including body heat, motion, and environmental energy, offers a sustainable and versatile approach to powering these devices. Furthermore, integrating on-device Artificial Intelligence (AI) for data analysis transforms these systems into intelligent platforms capable of real-time decision-making and adaptive responses. Real-time closed-loop control systems, which link sensing and stimulation seamlessly, are also emerging as a critical feature, enabling devices to react instantly to changes in physiological conditions.

As these technologies continue to evolve, wireless and battery-free systems are poised to revolutionise research and clinical applications. In research, they enable unprecedented insights into biological processes by providing continuous, high-resolution data from living systems. In clinical practice, they offer minimally invasive, long-term solutions for managing chronic conditions, delivering precision therapies, and enhancing patient monitoring. These advancements are set to dramatically redefine healthcare and disease treatment standards, paving the way for a future where technology and biology are seamlessly integrated to improve human health and well-being.

Chapter 3

A Miniaturised Wireless Low-energy Data Telemetry Module

This chapter reproduces my published work, which addresses one of the core challenges in developing battery-free, wirelessly powered systems for physiological monitoring and stimulation: achieving reliable, high-speed data transmission in a miniaturised implantable device.

In the broader context of this thesis, the ability to transmit large volumes of physiological data at high bit rates while maintaining low power consumption and a small footprint is critical. As neural recording interfaces move toward higher channel counts, conventional wireless technologies struggle to meet increasing data bandwidth requirements without using bulky systems or high power demands. This chapter demonstrates how optical telemetry can be harnessed to overcome these limitations, offering a promising, compact, and energy-efficient alternative.

This work presents a proof-of-concept optical telemetry module that leverages a single LED to transmit data at a high bit rate while consuming low power and occupying minimal area. Our experiments demonstrated that we could achieve 108 Mbps and 54 Mbps back-telemetry data rates for tissue thicknesses of 3 mm and 8 mm, respectively.

The proposed module is designed to be powered by near-field coupling and achieves bidirectional communication through low-speed downlink from Near-Field Communication (NFC). It aims to minimise the size of the implant while providing reliable transmission that meets the requirements of high-speed wireless communication for a multi-electrode array neurotechnology implant external to the body.

The module's power consumption is 1.57 mW, including the power consumed by related circuits, resulting in an efficiency of 14.5 pJ/bit at a tissue thickness of 3 mm and a data rate of 108 Mbps. Using an optical lens, combined with the tissue scattering effect and optimised emission angle, makes the module robust to misalignments of up to ±5 mm and ±15°between the implantable and external units.

The LED in the implantable unit has dimensions of $0.98 \times 0.98 \times 0.6$ mm^3, and the testing module is composed of discrete components and laboratory instruments. This Chapter demonstrates the feasibility of balancing a small, reliable, and high-bit-rate data uplink between a neural implant and its proximal, wirelessly connected external unit.

This optical telemetry module has the potential to be integrated into a significantly miniaturised system through an ASIC. It can support up to 1,000 channels of neural recordings, each sampled at 9 kSps with a 12-bit readout resolution.

3.1 Introduction

Uncovering the neurophysiological mechanisms with electrophysiology approaches has driven the development of neural signal sensor implants with higher spatial and temporal resolution Chen et al. (2022b). With advancements in integrated circuits and materials, state-of-the-art neural signal sensor implants for animal research now feature 768 electrodes within a $750 \times 720\,\mu$m^2 area and can record from 10,240 sites using two probes Steinmetz et al. (2021). Sensors designed for human clinical studies include two 96-channel arrays occupying less than 36 mm^2 Colachis et al. (2021). Independent companies like Neuralink^{TM} are developing systems with more than 1,000

channels for human applications Pisarchik et al. (2019).

The demand for a better understanding of neural activities and improvements in decoding neural signals has pushed the Analog-to-Digital Converter (ADC) sampling rate beyond 30 kHz for each recording channel, with resolutions ranging from 10 to 16 bits Moore et al. (2021a). Leveraging these high-performance neural signal sensors, BCIs have achieved promising results, including precise control of robotic arms, movement of computer cursors, and typing at speeds approaching handwriting Bacher et al. (2015); Chaudhary et al. (2022); Hochberg et al. (2012); Pandarinath et al. (2017).

Brain-computer interface devices or neural signal recording systems comprise the signal collection, processing, and execution units. However, limitations in power and size have hindered the development of standalone devices capable of achieving the desired human functions. These systems are currently divided into internal and external units. The internal unit, an implant or set of implants near the sensing or stimulation site, must be miniaturised to minimise invasiveness. It typically contains only electrodes, lead wires, electronic hermetic housing, and signal acquisition circuits. In contrast, the external unit functions as a power source. It accommodates components that exceed the implant's volume or power constraints or acts as a relay to transmit neural activity data to another processing unit.

An interface between the internal and external units is necessary to deliver data and energy. In some advanced BCIs, particularly for research purposes, wired connections are commonly used for this interface Bacher et al. (2015); Donoghue et al. (2007). This is because high-performance, multichannel neural signal sensors require data streaming rates of tens of megabits per second to handle raw data. Wired solutions offer a straightforward means to meet design requirements for high data rates, compact size, adequate power supply, and safety. However, these wired systems significantly limit clinical applications and the diversity and duration of research experiments. They also increase the risk of device failure and tissue infection. Significant engineering efforts are currently focused on developing wireless transcutaneous systems to transfer high-rate data Liu et al. (2014c); Miranda and Meng (2010); Song et al. (2022). Me-

dia used for transcutaneous data and energy transfer include ultrasound, magnetic, electric, electromagnetic, and optical links.

Ultrasound channels offer one of the deepest penetrations into soft tissue, making them an attractive option for deep neural implants. The transducer for the acoustic link is typically small, with reported dimensions in the submillimeter range and less than half a cubic millimetre (mm^3) in recent literature Ghanbari et al. (2019); Sonmezoglu et al. (2021). The power delivery efficiency of the acoustic channel ranges from 1.93% to 0.23% Chang et al. (2018b); Charthad et al. (2015); Ghanbari et al. (2019); Meng and Kiani (2016). The data link for the acoustic channel typically employs a backscatter approach to maintain low power consumption in the internal unit. The resonant frequency of the piezoelectric material is usually less than 2 MHz Charthad et al. (2015); Seo et al. (2015); Song et al. (2015); Sonmezoglu et al. (2021), making the optimal frequency for acoustic channels often below 5 MHz Barbruni et al. (2020). However, implementing modulation schemes like OFDM is often challenging due to the backscatter approach used for data telemetry. As a result, ultrasound channels typically provide telemetry data links of only a few hundred Kbit/s.

Inductive links use alternating magnetic fields through coils to transmit energy and data. The inductive link offers high power transfer efficiency when the distance between the source and receiver is less than 30 mm Denisov and Yeatman (2010). A reported efficiency of 95% is achievable at a distance of 10 mm Haerinia and Shadid (2020). Inductive links typically operate at frequencies below 20 MHz to balance the transmitter's and transfer efficiency between the transmitter and receiver. These links can provide half-duplex bidirectional communication, with commercially available products reporting data rates of up to 800 Kbit/s.

The capacitive link utilises tissue as a dielectric medium to form a capacitor, creating a path for transferring data and power through tissue using a pair of capacitor plates Barbruni et al. (2020). The advantages of capacitive links for data and power telemetry include their high-frequency pass characteristics and the confined area of the energy field bin Mustapa et al. (2019). When transferring data and power through tissue, the electric field primarily impacts the tissue between the electrodes and does

not broadcast widely, as seen in electromagnetic fields Sharif and Sodagar (2022a). This characteristic enables multichannel capacitive links to be implemented on the same implant, extending the bandwidth. The plates for capacitive links range from $5 \times 5\,\text{mm}^2$ to $40 \times 40\,\text{mm}^2$, and the carrier frequency ranges from 0.2 MHz to 20 MHz Erfani et al. (2017b, 2018b); Jegadeesan et al. (2016); Narayanamoorthi (2019a); Sodagar and Amiri (2009a,b); Takhti et al. (2011).

The drawbacks of capacitive links include the potential for electric field-induced damage to living tissue in a localised area and limitations in miniaturization Erfani et al. (2018b). Another drawback is the requirement for close contact of the plates with the tissue surface, which presents challenges in applications where the tissue surface or contact area is not flat (e.g., areas with hair) Erfani et al. (2018b).

The most popular approach for data telemetry is the electromagnetic field, as it can quickly achieve both power delivery and bidirectional data communication simultaneously. However, two main challenges exist when using an electromagnetic field to transmit high-bandwidth data through tissue. First, living human tissue contains water, and skin tissue is conductive. This conductivity causes the absorption rate to increase exponentially with frequency. As a result, a significant amount of energy is absorbed by tissue when the radio frequency exceeds 2 GHz Christ et al. (2006); Drossos et al. (2000). Thus, using electromagnetic fields for high-bandwidth data transmission through human tissue presents challenges as the tissue becomes an inefficient communication channel. Second, as the electromagnetic frequency increases, the analog radio frequency front-end becomes a power-hungry component, consuming more energy than the neural signal recording sensor. In addition to the physical limitations, another issue with RF transmission is environmental interference, as many devices operate at the same frequency that implants propose to use.

In parallel with optimising the transmission channel to meet the requirements of uplink telemetry for recorded neural signals, there has been significant research into reducing the data rate by enabling more local data processing within the implant Quiroga (2012b). Popular solutions include spike thresholding, where only spike counts above a certain threshold are transmitted, and compressive sensing, which

adaptively compresses data based on events, converting raw signals into sets of featured spikes Navajas et al. (2014c); Park et al. (2017b). These spike-related approaches have significantly reduced the bandwidth requirements for telemetry data links. While spike signals are suitable for specific applications, transmitting high-fidelity signals is still essential for many applications, such as brain disease monitoring, BCI algorithm research, and neural electrophysiological studies.

The optical link is a promising solution for transmitting high-fidelity neural signals from high-channel-density sensors and has gained considerable attention from researchers in recent years Ackermann et al. (2008); Liu et al. (2012a); Nikita (2014). Advantages of optical links include their small transducer size (compared to inductive and capacitive links), high bandwidth, multiple modulation approaches, high energy efficiency, MRI compatibility, and robustness against environmental electromagnetic noise.

Optical transcutaneous links have already demonstrated promising results. For example, one implementation achieved a data rate of 300 Mbps using a Vertical Cavity Vertical-Cavity Surface-Emitting Laser (VCSEL) as the transducer and a super-fast photodiode as the receiver Marcellis et al. (2020). Other examples include in-vivo modules demonstrated in mice, where microscale inorganic light-emitting diodes (μ-ILEDs) served as the transducers and photodiode arrays acted as receivers. The transducer's small size enabled the chronic recording of neural dynamics in these studies, although the maximum data rate in the in-vivo experiments was limited to 27 kbit/s Burton et al. (2020d); Liu et al. (2014b).

Achieving an optimal balance between high data rate, low power consumption, small volume, and robustness to misalignment has not yet been fully demonstrated. LEDs show excellent potential as transducers for implementing optical transcutaneous uplinks due to their relatively small size and high wall-plug efficiency.

3.2 Methods

3.2.1 System design overview

This chapter presents a novel design for an optical telemetry module that employs a single LED and addresses the challenges of high-speed data transfer, low power consumption, and minimal volume. Our module is well-suited for data transmission in multi-electrode neural recording implants and is designed to operate subcutaneously to facilitate implant-to-surface data transfer. As this module is intended to be part of the neural recording implant, we designed the entire system, considering power supply, energy harvesting, and usability for both the telemetry module and the recording implant.

As shown in Fig. 3.1, the proposed system comprises an implant and an external unit. The external unit includes a behind-ear unit and an over-the-head unit. The behind-ear unit houses the rechargeable battery, power management circuits, and data storage or transmission components. The over-the-head unit, which is smaller and lighter, is positioned over the site where the internal implant is located beneath the skin. This unit includes an optical receiver that retrieves high-bandwidth data from the implant. we used a coil employing 13.56 MHz near-field coupling to demonstrate the concept of providing power and a minimally occupied forward control data link (downlink). This setup highlights the potential of our proposed design.

This design combines the high efficiency of inductive power delivery with the high data rate of the optical link. In addition to optimising power delivery efficiency, the forward data link can exchange control signals and send handshaking signals for the high-bandwidth optical communication channel. This approach enhances channel stability, simplifies the communication protocol and related hardware design, and lowers the power consumption of the internal unit. The overhead unit can also incorporate a local data processing unit to implement applications such as controlling a brain stimulation device to achieve closed-loop brain stimulation.

In Fig. 3.2, we present the critical components of our proposed system and demon-

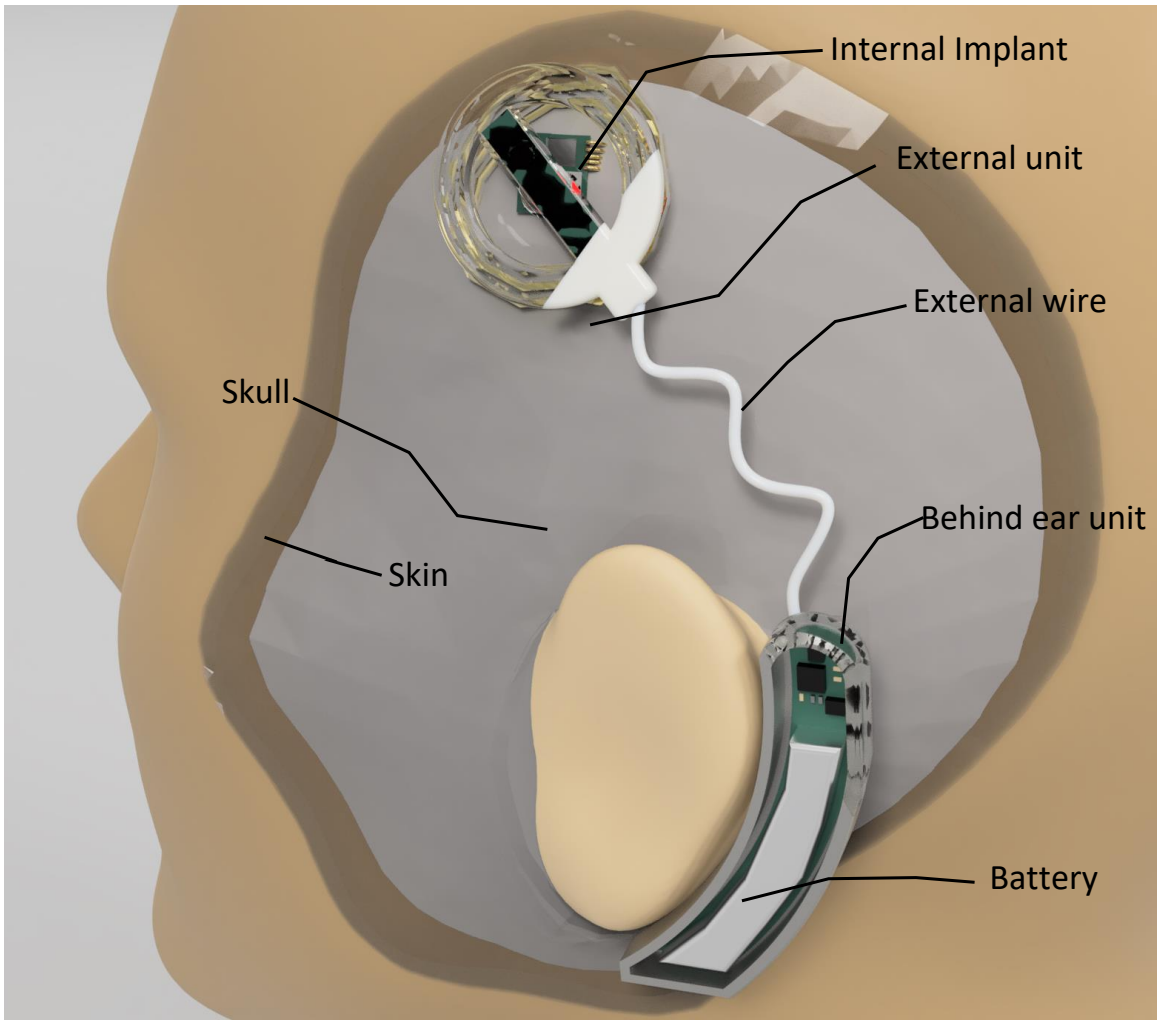

Figure 3.1 – The system design with its potential application. The system consists of an internal implant and an external unit, including a behind-ear unit. The proposed optical telemetry module resides in the internal implant and aims to send high-speed data from the sensor to the external unit. The external unit includes a receiver, a power delivery circuit, and a battery located in the behind-ear unit to reduce the weight of the overhead unit.

strate how the optical telemetry module integrates with the neural recording implant. In one possible implant configuration, high-density electrodes are positioned on the cortex to collect neural signals, while the analog front-end and analog-to-digital converter (ADC) are housed in a package replacing a small part of the skull. To minimise internal connections, the optical communication module is placed above the neural signal sensor, under the skin tissue. The transducer is a single 940 nm near-infrared

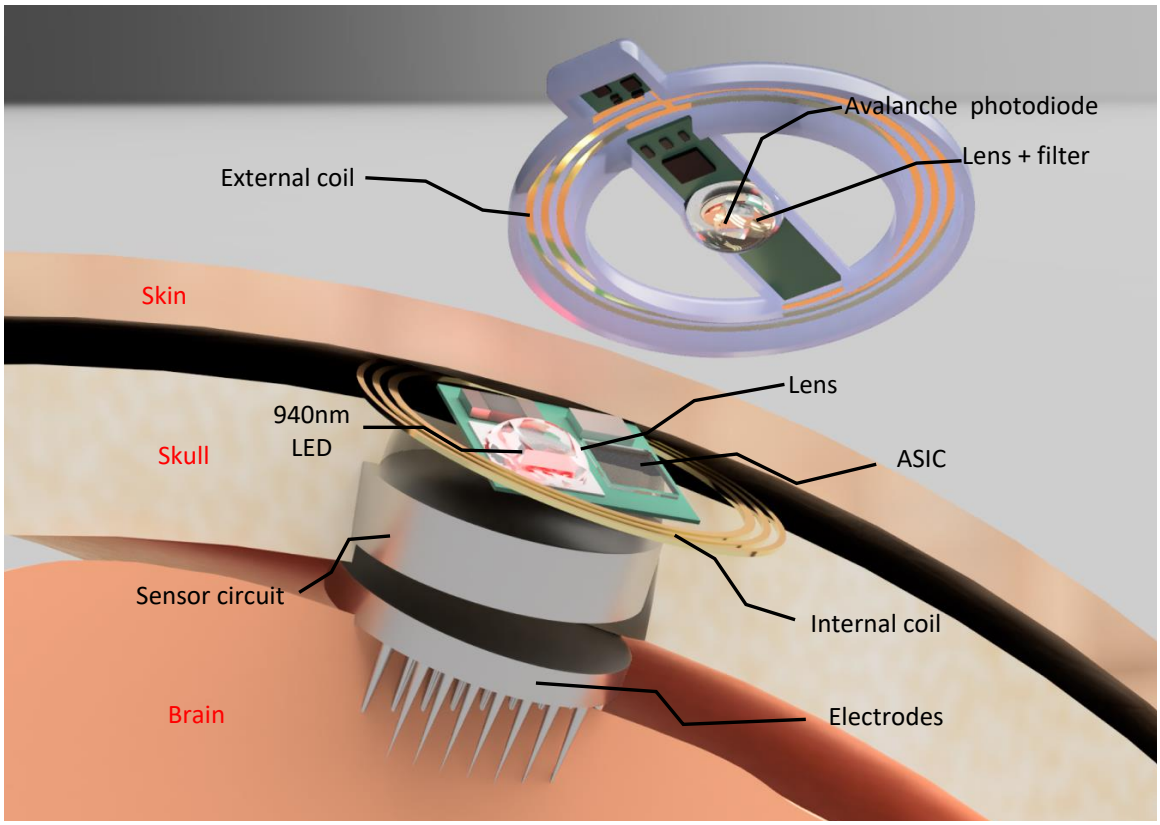

Figure 3.2 – The main components of the proposed system. Our experiments consider power harvesting via a conventional near-field antenna system. Power can also be delivered through optical energy harvesting, and the device has the potential to achieve bidirectional communication via an optical link.

InGaN LED, and an ASIC is utilised to encode data and modulate the LED. A lens is positioned on top of the LED to focus the beam with an optimal emitting angle that matches the tissue thickness. A thin, flexible printed circuit patch coil is wrapped around the communication module to receive energy from the external coil through an inductive link.

The low power consumption of the proposed communication module is achieved through the high wall-plug efficiency of the LED and the low interference of the optical channel. This setup allows using a highly sensitive Avalanche Photodiode (APD) with high gain to recover faint optical pulses from the internal unit, with minimal noise concerns. With the advantages of short-wavelength light, a high data rate can be achieved using a simple modulation approach, enabling circuit simplification and

eliminating power-hungry high-frequency analog components, thus further reducing power consumption.

3.2.2 Design and Implementation

Design requirement analysis

3.2.3 Data Rate Requirement

The communication module is designed to stream high-fidelity neural signals through skin tissue. Currently, clinically available neural signal sensors feature between 100 electrodes (e.g., Utah array Bhandari et al. (2010)) and 1024 electrodes (e.g., Neuralink Elon Musk (2019)). To identify a neural spike, both 0–1 mV magnitude Local Field Potential (LFP) and 0–10 μV Extracellular Action Potential (EAP) need to be recorded simultaneously Maslik et al. (2020). As a result, the minimal requirement for the Effective Number of Bits (ENOB) of the ADC is 8 bits Maslik et al. (2020), typically achieved with an ADC resolution exceeding 10 bits Navajas et al. (2014a); Zjajo (2016).

The data transmission requirement can be calculated using Equation 3.1:

$$D_s = \frac{n_{\text{Channels}} \times R_{\text{resolution}} \times f_{\text{sampling}}}{H_0} \tag{3.1}$$

Where H_0 is the encoding efficiency.

For example, consider a neural signal sensor with 100 channels, a sampling rate of 20 kSps, and an ADC resolution of 14 bits. Using Manchester encoding with an efficiency of 50%, the data rate requirement to send the raw neural signals is 56 Mbps.

3.2.4 Noise Analysis

For the proposed optical telemetry module, three main factors influence signal quality:

(I) Environmental Light Interference Compared to electromagnetic (EM) fields, fewer artificial signals operate in the open-air optical domain, and the directional nature of light transmission reduces the likelihood of interference between devices. Indoors, light sources primarily emit visible wavelengths (380–700 nm) with minimal energy in the near-infrared range. However, sunlight covers a broader spectrum, with significant power in the 900–1000 nm range. This presents a challenge for the proposed optical telemetry module. Therefore, the over-the-head unit must be designed to block sunlight from reaching the internal unit.

(II) Receiver Noise A high-speed, high-sensitivity photodiode is required to convert optical signals into electronic signals. The internal LED's emitted light is typically weak, and the photodiode must detect rapid light intensity changes, as the optical signals are designed as short-period pulses. Photodiodes inherently generate noise due to physical properties. The signal from the photodiode is small and needs amplification to restore information collected from the sensor. Typically, the photodiode's current signal is converted to a voltage signal using a Trans-Impedance Amplifier (TIA) and then passed through one or more cascaded amplifiers to further increase the voltage level for data recovery.

(III) Tissue Impact As light travels through the skin, it undergoes reflection, refraction, and absorption, leading to multipath effects and noise in the optical communication channel. Optical wavelengths from 350 nm to 2000 nm are commonly used in communication systems. For transcutaneous applications, the distance between the transmitter and receiver ranges from 0.5 mm (epidermal only) to over 10 mm (total skin thickness). Due to the short wavelength and relatively short transmission distance, the multipath effect can be considered negligible for transcutaneous optical channels.

The total noise introduced into the optical communication module can be calculated using Equation 3.2:

$$i^2{}_{\text{noise}} = i^2{}_{\text{env}} + i^2{}_{\text{Pd}} + i^2{}_{\text{TIA}} + i^2{}_{\text{AMP}} \tag{3.2}$$

Power Consumption Analysis

The power consumption of the uplink data module is the sum of the power consumed by the transducer and the power required for the circuit to control and modulate the transducer. A higher wall-plug efficiency of the transducer indicates less energy dissipation during energy conversion. Currently, LEDs exhibit the highest wall-plug efficiency for generating photons from electrical power. Additionally, integrated circuits consisting solely of digital components can operate at GHz frequencies with sub-microwatt power consumption. Removing high-frequency analog circuits from the design reduces the power consumption of the proposed communication modulation module.

3.2.5 Optical Channel Analysis

Human skin has three layers: epidermis, dermis, and subcutaneous fat. It acts as a complex, heterogeneous medium for light propagation Navajas et al. (2014c). The optical properties of human skin are characterised by its absorption and scattering coefficients Bashkatov et al. (2011). Haemoglobin in the blood and melanin in the epidermis are the primary substances responsible for absorption. Scattering, on the other hand, alters the direction and polarisation of light. Scattering can occur at the contact interface and within small regions where optical properties vary Bashkatov et al. (2005).

The main contributors to scattering are filamentous proteins and the fibrous structure of the tissue. Scattering occurs at individual fibrils and scattering centres formed by the interlacement of proteins and bundles Bashkatov et al. (2005). The distribution of blood, pigments, and protein bundles is inhomogeneous and varies over time, causing the absorption and scattering coefficients to fluctuate Bashkatov et al. (2005).

Both in vitro and in vivo studies indicate that light with wavelengths between 800 nm and 1200 nm has lower absorption and scattering coefficients in human skin tissue Graaff et al. (1993); Rajadhyaksha et al. (1995); Wan et al. (1981). This makes these

wavelengths suitable for optical power transfer through the skin and for building a power-efficient telemetry link.

To design the optical components of the communication module, we conducted simulations to assess the transmitted light power at the receiver side of the skin. Light propagation in tissue is described using the scalar stationary Radiation Transfer Theory (RTT), as shown in Equation 3.3 Bashkatov et al. (2011):

$$\frac{\partial I\left(\vec{r},\vec{s}\right)}{\partial s} = -\mu_t I\left(\vec{r},\vec{s}\right) + \frac{\mu_s}{4\pi}\int_{4\pi} I\left(\vec{r},\vec{s}'\right)\rho\left(\vec{s},\vec{s}'\right)d\Omega' \tag{3.3}$$

In Equation 3.3, $I\left(\vec{r},\vec{s}\right)$ represents the specific intensity at point $\vec{r}$ in the given direction $\vec{s}$. The term $\rho\left(\vec{s},\vec{s}'\right)$ is the scattering phase function, $d\Omega'$ is the unit solid angle about direction $\vec{s}'$, and μ_t is the total attenuation coefficient.

A least-squares Gaussian model can approximate the power intensity distribution at the receiver side under the assumption of an ideal smooth skin surface. This simplified simulation model allows for the analysis of light propagation through the skin of varying thicknesses. The Gaussian model is expressed in Equation 3.4 Ackermann et al. (2008):

$$J_{\mathrm{rx},\lambda}(r,\theta) = \frac{A}{\sigma\sqrt{2\pi}}e^{-\frac{r^2}{2\sigma^2}} \tag{3.4}$$

According to Ackermann et al. (2008), exponential and quadratic random coefficients are used to represent the Gaussian parameters A and σ, respectively.

In Fig. 3.3, D_r represents the size of the light source. For an LED, D_r corresponds to the emitting area of the diode. α is the emitting beam angle, which can be controlled through lens design. D_d is the diameter of the projected light spot, not accounting for the tissue scattering effect. D_s is the diameter of the light beam with the Full Width at Half Maximum (FWHM) energy of the Gaussian distribution on the skin surface. D_n is the lens diameter that focuses light onto the photodiode to increase the received optical power. T_n is the thickness of the skin tissue.

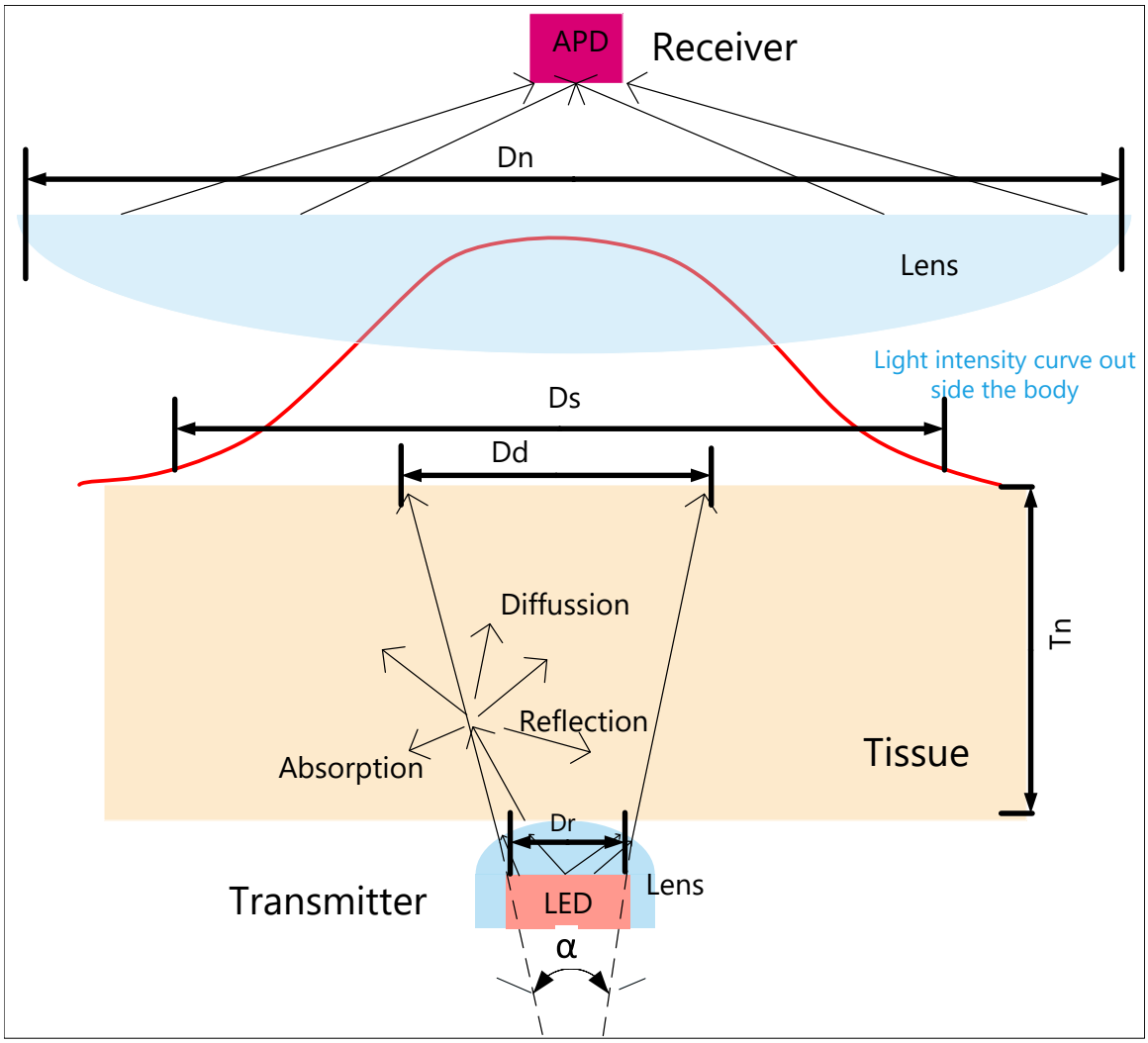

Figure 3.3 – The optical design of the subcutaneous telemetry module. The LED is the transmitter, and the APD is the receiver. The lens on the transmitter side controls the emitting beam angle α, while the lens on the receiver side collects light and focuses it onto the APD's surface.

Using Equation 3.4 and the quantitative optical properties of skin described in Ackermann et al. (2008), we implemented a Python script to simulate the effect of light passing through skin tissue.

From the simulation, we observed that for light with wavelengths between 800 nm and 980 nm, the optical channel in tissue is dominated by the scattering effect. When the tissue thickness is 3 mm, the shape of the light-emitting source remains observable. On the receiver side, the area affected by optical energy is approximately 90 times

larger than the light-emitting source size after passing through the tissue. Compared to a laser source, the optical power distribution on the skin surface has a plateau-like shape, making it more robust to the tissue's heterogeneous optical properties. For a laser source, the peak power on the receiver side is concentrated in a small hotspot and decreases rapidly from the central point, increasing the misalignment challenge. In laser-based systems, the receiving power drops significantly if the peak power falls on a pigmentation area.

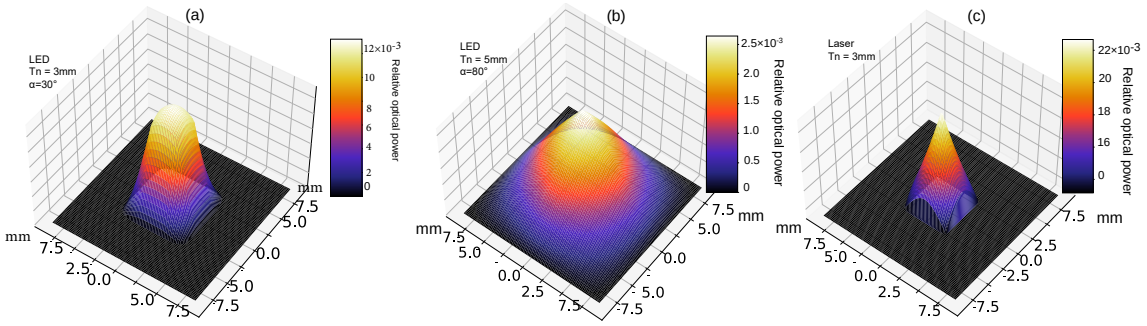

Figure 3.4 – Simulation results of the optical power distribution on the skin surface with different light sources and tissue thicknesses. (a) $T_n = 3\,\text{mm}$, $D_r = 0.98 \times 0.98\,\text{mm}$, $\alpha = 30°$. (b) $T_n = 5\,\text{mm}$, $D_r = 0.98 \times 0.98\,\text{mm}$, $\alpha = 80°$. (c) Laser source with a smaller spot size ($100\,\mu\text{m}$) and $T_n = 3\,\text{mm}$.

Fig. 3.5 illustrates the relationship between tissue thickness (T_n in Fig. 3.3), total optical power, affected tissue area, and light-emitting beam angles (α in Fig. 3.3). From the figure, we observe that smaller emitting angles result in less energy attenuation for thicker tissue. For thinner tissue and emitting angles less than 80°, the total received power remains constant while the collection area increases linearly. The simulation helps identify the optimal emitting angle for the light source to improve power efficiency.

For instance, with a skin thickness of 3 mm, we found that when the emitting angle is below 60°, the total received power and optical energy collection area achieve a good balance.

Fig. 3.6 shows the simulation results of the collected optical energy on the skin surface with varying skin thicknesses and lens diameters. The solid curve represents the received power on the photodiode, while the dashed line indicates the FWHM diameter

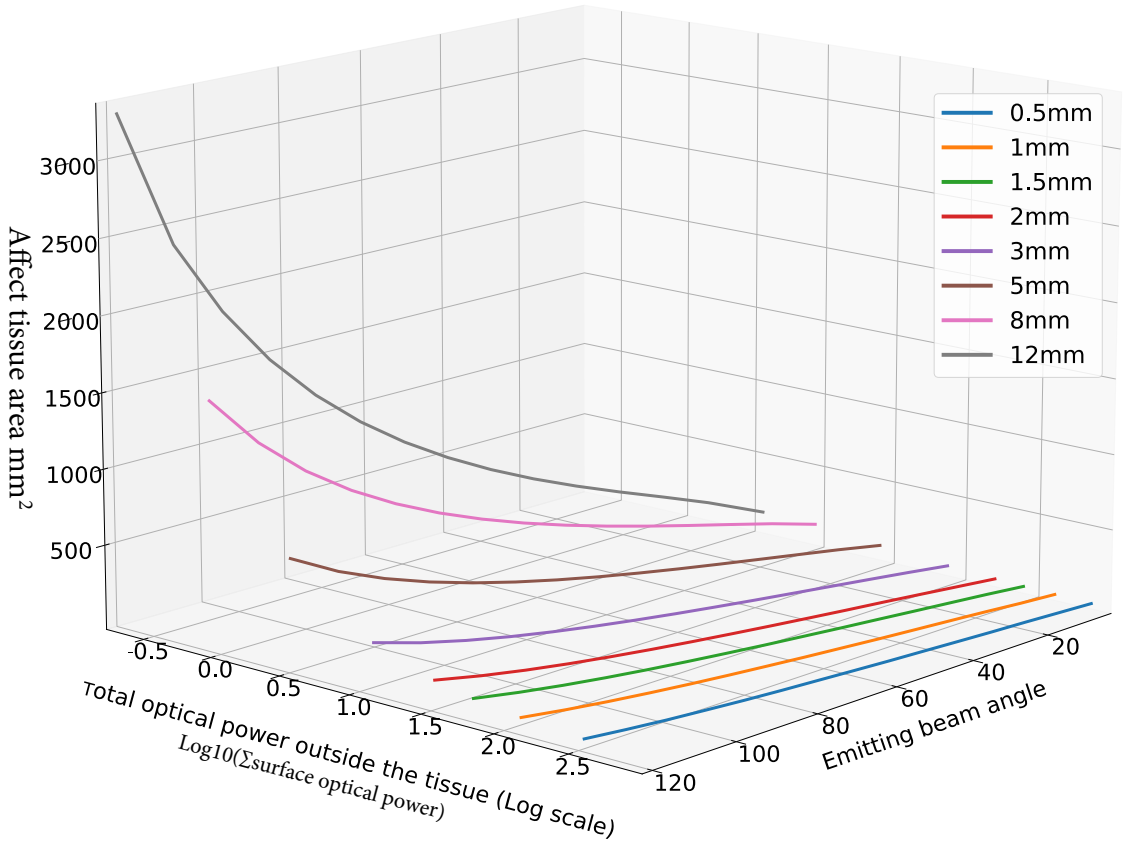

Figure 3.5 – Total optical energy on the skin surface with varying tissue thicknesses and light-emitting beam angles. The X-axis represents the emitting beam angle (α), the Y-axis represents the total optical power outside the tissue, and the Z-axis represents the area affected by optical power (mm^2).

of the light beam on the skin surface.

Fig. 3.6 reveals a sharp rise in collected energy when the lens diameter increases from 1 mm to a size approaching the FWHM spot diameter. However, as the lens diameter continues to increase, the attenuation caused by the optical material of the lens outweighs the benefits of the increased diameter, and the collected energy gradually decreases.

Notably, the figure shows that as skin thickness increases, the relative improved received energy due to the lens becomes more significant. The amount of collected optical energy stabilises for thicker tissue when the lens diameter reaches a certain threshold. This trend suggests that a lens with an optimal diameter matching the

tissue thickness can significantly enhance signal quality. Furthermore, a larger lens reduces alignment sensitivity when the optical source is located in thicker tissue.

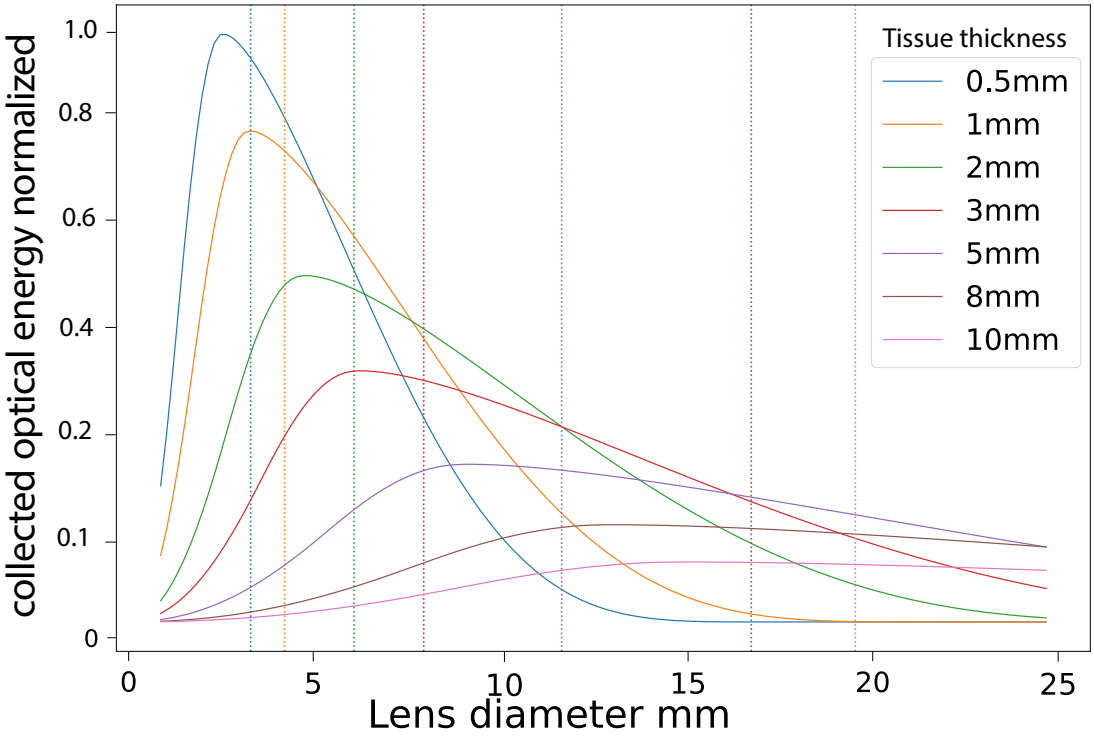

Figure 3.6 – Lens performance simulation results. The colour code represents different tissue thicknesses, and the dashed line indicates the FWHM diameter on the skin surface.

Module and Circuits Design

The system design of the proposed module is presented in Fig. 3.7, which displays the block diagram of the internal unit. The internal unit consists of several components, including an analog front end, an ADC, a microcontroller (MCU), an NFC power harvesting and communication module, an encoding unit, a power management unit, a pulse generator, and a dynamic voltage bias circuit. A crystal within the internal unit is a clock source, while a frequency multiplier provides a higher base clock for the pulse generator and encoding unit.

The bias tracking circuit, consisting of two instrumentation amplifiers and a low-power DAC, supplies a dynamic bias voltage to stabilise the LED's impedance. This

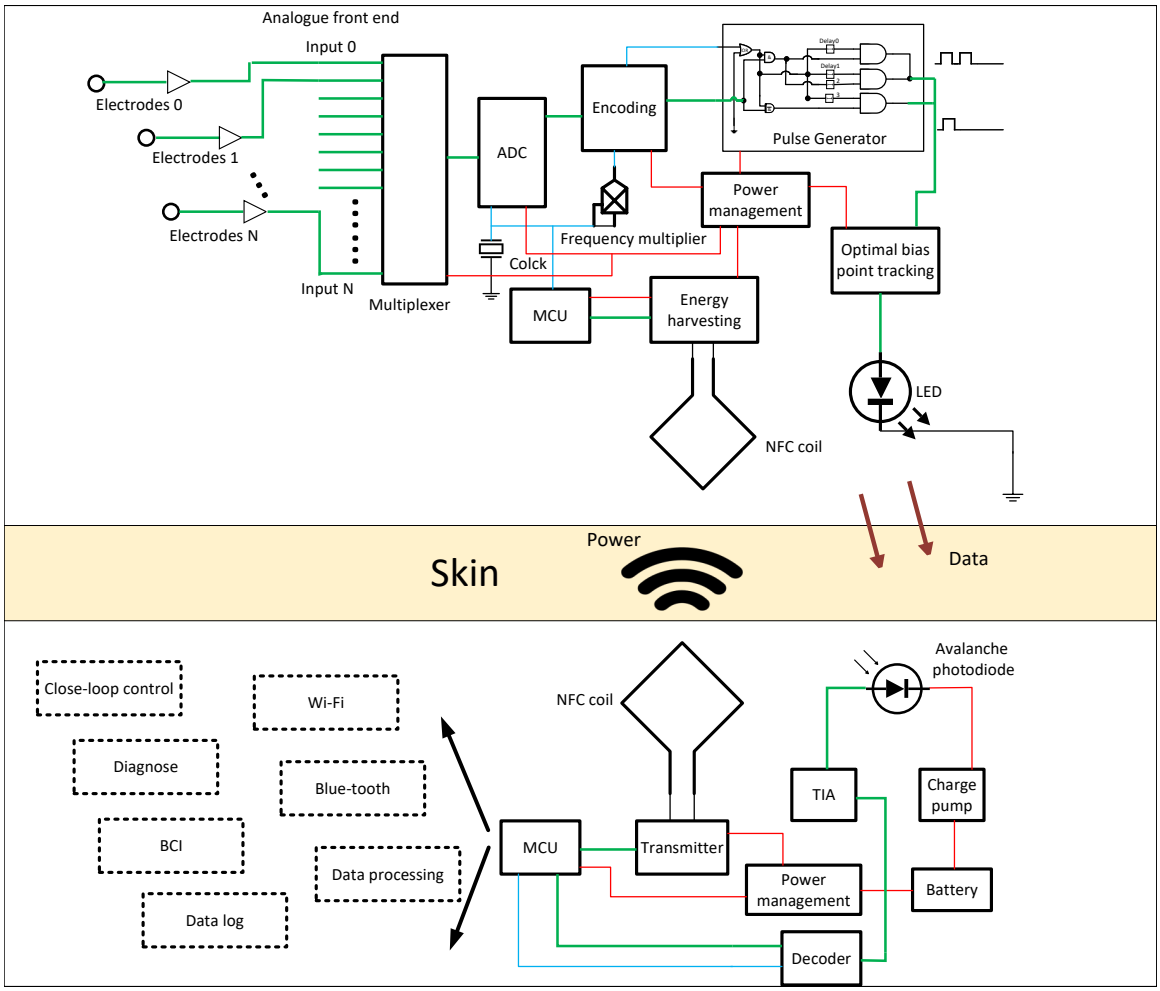

Figure 3.7 – The system block diagram. The upper part represents the internal implant. The yellow strip in the middle indicates the skin tissue. The lower part represents the external unit.

ensures the electrical pulse from the pulse generator successfully converts into an optical pulse, even under varying environmental light and temperature conditions.

Fig. 3.8 illustrates the circuit block diagram of the proposed pulse generator, which uses only digital components to ensure low power consumption. Instead of modulating pulse amplitude, pulse density encodes digital logic. This modified On Off Keying (OOK) modulation eliminates the need for a phase-locked loop, reducing complexity and power consumption.

The pulse generator comprises five delay units with two distinct delay times, Delay 1

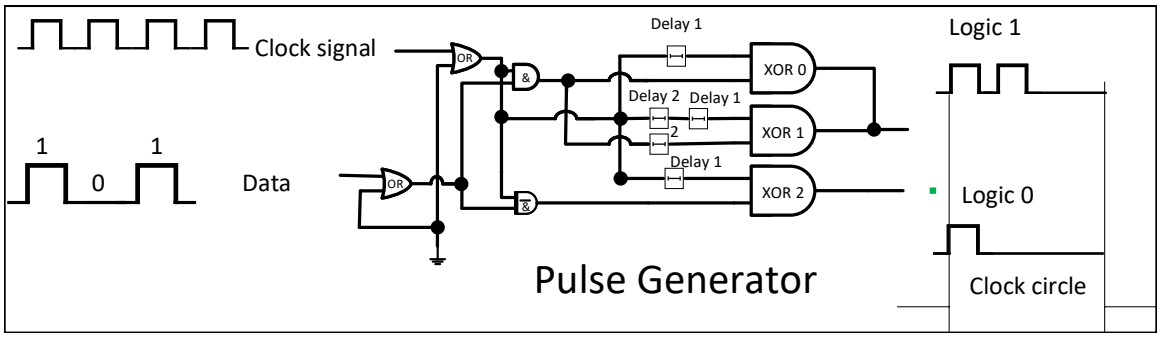

Figure 3.8 – The schematic diagram of the proposed pulse generator for the LED to generate optical spikes. The input is a digital signal from the sensor with a corresponding digital clock, and the output is a short pulse to drive the LED.

and Delay 2. Delay 1 defines the output pulse width, while Delay 2 is twice Delay 1. Logic gates compute the data and clock signals, producing pulses of varying densities in a single clock cycle. When the input data is logic-high, the output signal generates a double pulse (logic 1). The output produces a single pulse (logic 0) when the data is logic low. Delay 1 is set to be less than or equal to one-fifth of the clock cycle duration to ensure robust signal recovery on the receiver side.

The block diagram of the external unit circuit is shown in Fig. 3.9. A high-gain, low-noise APD collects optical signals. The TIA comprises two high-speed operational amplifiers (LTC 6268-10 and ADA4860) in a cascaded configuration. A low-side MOSFET switch (TPS55340) voltage booster elevates the APD voltage bias. The booster's internal switch connects to an inductor and a charge pump network to increase the output voltage further, enhancing the APD's gain.

After amplification, the APD's signal is sent to logic units for clock and data recovery. Clock recovery involves two steps. The first step generates a trigger signal for the cycle counter. This step detects optical pulses from the APD and produces a periodic trigger signal matching the optical pulse cycle. However, the trigger signal lacks stability and correct duty cycles, necessitating a second step. The second step refines the clock signal by excluding unstable edges and ensures a stable clock output with the correct duty cycle. The delay networks in the first step set the delay time to four times the interval between detected rising and falling edges. Data recovery is achieved through a cycle counter that counts pulses when the clock signal from the

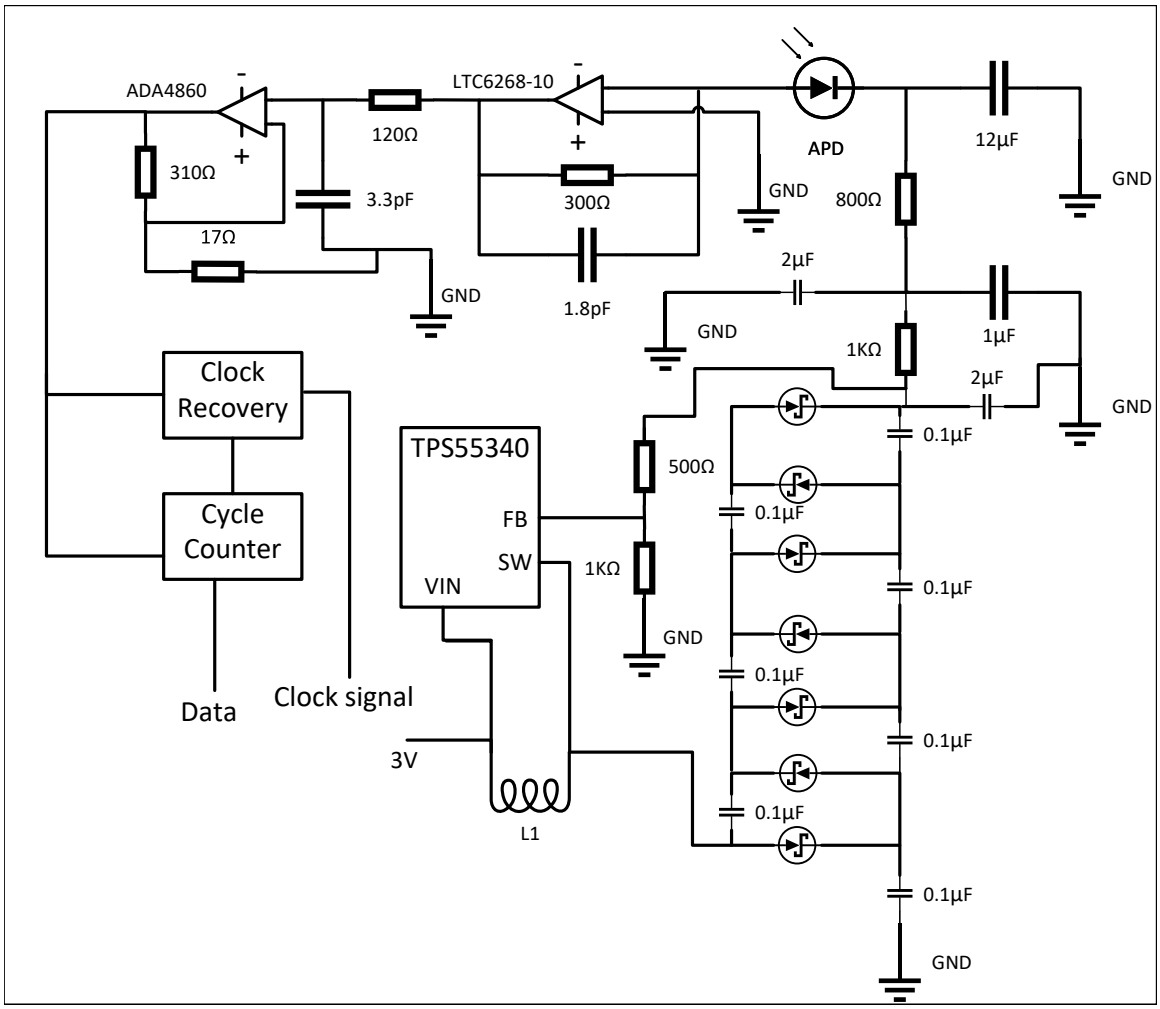

Figure 3.9 – The schematic diagram of the external unit, consisting of a TIA, APD bias voltage booster, and blocks for clock and data recovery from optical spikes.

first step is logic high. If the counter detects two pulses, the output is logic 1; if one pulse is detected, the output is logic 0. The output level remains stable until the next cycle begins. With the recovered clock signal, the digital logic can be processed further by a microcontroller and converted into standard digital bus signals, such as a serial peripheral interface (SPI).

LED Module and Impedance Analysis at High Frequency

LEDs exhibit high efficiency in generating optical signals within a small area, ranging from $25\,\mu m^2$ to approximately $1\,mm^2$ Hsiang et al. (2020). However, a significant

challenge in using LEDs for high-speed communication is their frequency response, which follows a first-order system with bandwidth typically up to hundreds of MHz Li et al. (2019). As the signal frequency increases, the parasitic capacitance reduces the LED efficiency and slows down the rise and fall times, significantly degrading signal quality. Research on high-speed visible light communication systems has tested and modelled LEDs to improve efficiency and signal quality Li et al. (2019, 2021).

These studies reveal that when the bias current passing through an LED is much smaller than the saturation current of the diode, the parasitic capacitance decreases exponentially. In contrast, the resistance decreases linearly Li et al. (2019, 2021). At the same time, the inductance of the LED remains relatively constant. This indicates that a high-power LED operating at a low current exhibits better efficiency at higher frequencies.

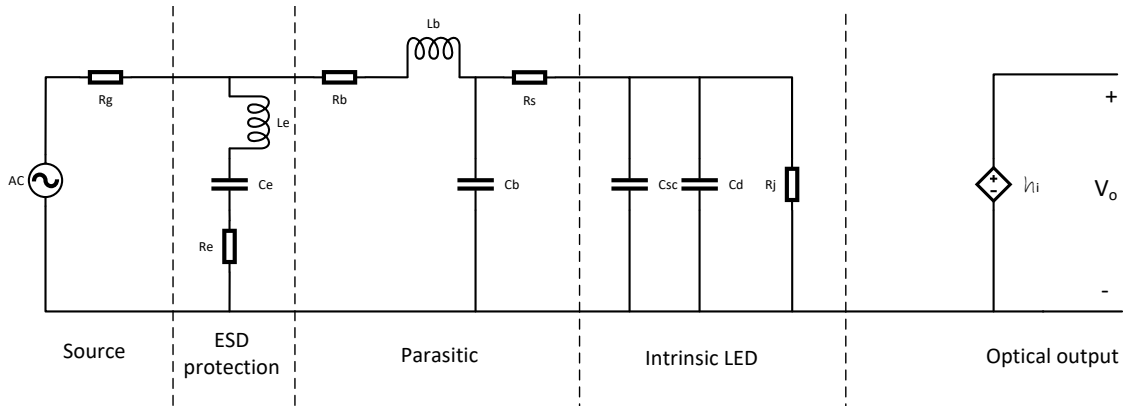

Figure 3.10 – Equivalent circuit of an LED. The LED model consists of three parts: the intrinsic properties of the diode junction, the parasitic components induced by manufacturing and packaging, and the Electrostatic Discharge (ESD) protection components typically integrated into commercial LEDs.

In Fig. 3.10, the equivalent circuit of the LED is depicted:

— R_g: Resistance of the signal source to the LED,

— R_b: Bonding wire resistance,

— L_b: Parallel bonding inductance,

— R_s: Series resistance,

— C_b: Bonding wire and pad capacitance,

— C_{sc}: Space-charge capacitance in the junction,

— C_d: Diffusion capacitance in the junction,

— R_j: Junction resistance, and

— L_e, C_e, R_e: The ESD diode's impedance, capacitance, and resistance.

The impedance of the LED can be calculated using Equation 3.5:

$$Z_{\text{LED}} = \left[\left(R_j \parallel \frac{1}{j\omega\left(C_d + C_{sc}\right)}\right) + R_s\right] \parallel \left[j\omega C_b + j\omega L_b + R_b\right] \parallel \left[j\omega L_e + \frac{1}{j\omega C_e} + R_e\right] \tag{3.5}$$

The frequency response of the LED communication system can be derived using the transfer function shown in Equation 3.6:

$$H\left(j\omega\right) = \frac{V_o}{V_s} = \frac{h_i}{iR_g + iZ_{\text{LED}}(j\omega)} \tag{3.6}$$

Here: - h_i: Gain of the photodiode at the receiver side. - V_o: Output voltage. - V_s: Input signal voltage.

I measured the impedance of the LED using an impedance spectroscopy device and developed Python code (available at the provided link) to estimate the model parameters. The code can also predict the LED's power consumption when delivering short-period pulses. To simplify the model, the intrinsic capacitance $C_d + C_{sc}$ is represented by a single parameter C_j. Table 3.1 shows the estimated parameters at different currents.

Using the estimated parameters, Fig. 3.11 illustrates the predicted LED impedance at high frequencies. During testing, we observed that when no bias voltage is applied to the LED or when the bias voltage does not generate a forward current above 50 nA, the LED's impedance fluctuates significantly across measurements. Under

Table 3.1 – The LED module parameter at different forward current.

Current	R_j (Ω)	C_j (nF)	R_s (Ω)	R_b (Ω)	C_b (pF)	L_b (nH)	R_e (Ω)	C_e (pF)	L_e (nH)
50 nA	5	0.05	4.3	0.2	2.3	0.24	17	48	98
500 nA	5.1	0.013	5.3	0.2	3.3	0.24	17	60.3	98
1 µA	5	0.04	5	0.2	3.1	0.24	17	273	98
10 µA	5	0.06	5	0.2	3.9	0.24	17	284	98
50 µA	1.75	0.06	1.85	0.2	4.2	0.24	17	324	98
100 µA	1.535	0.08	0.5	0.2	4.1	0.24	17	295	98
200 µA	1.355	0.44	0.5	0.2	3.71	0.25	17	345	98
5 mA	0.199	5.1	5.18	0.05	11.9	2.1	94	683	40.3
50 mA	0.048	7.4	0.48	0.19	8.12	1.72	3.78	113	2.75
100 mA	0.046	18	0.46	0.19	15.4	1.74	2.54	217	7.4

these conditions, sending short-period pulses with low current does not produce a stable optical pulse detectable by the APD.

A bias tracking circuit was incorporated into the design to ensure a minimal optimal forward current is maintained. With this small bias current, the LED's impedance at high frequencies becomes stable, enabling low-current electrical pulses to be converted into detectable optical pulses by the LED.

3.3 Results

3.3.1 Experiment setup

To evaluate the performance of our design, we conducted tests using a 940nm wavelength LED, a lens, and a high-frequency arbitrary waveform generator (Keysight P9336A) to implement the circuit of the internal unit. The front-end of the external unit was implemented using discrete components, including an ultra-low-noise and high-gain APD (MTAPD-07-010), a low-noise APD voltage bias circuit, and a high-speed TIA circuit. we 3D printed housing to hold an optical lens and a long-pass filter to implement the optical parts of the external unit. An oscilloscope equipped with a storage function was used to test the data recovery function and measure

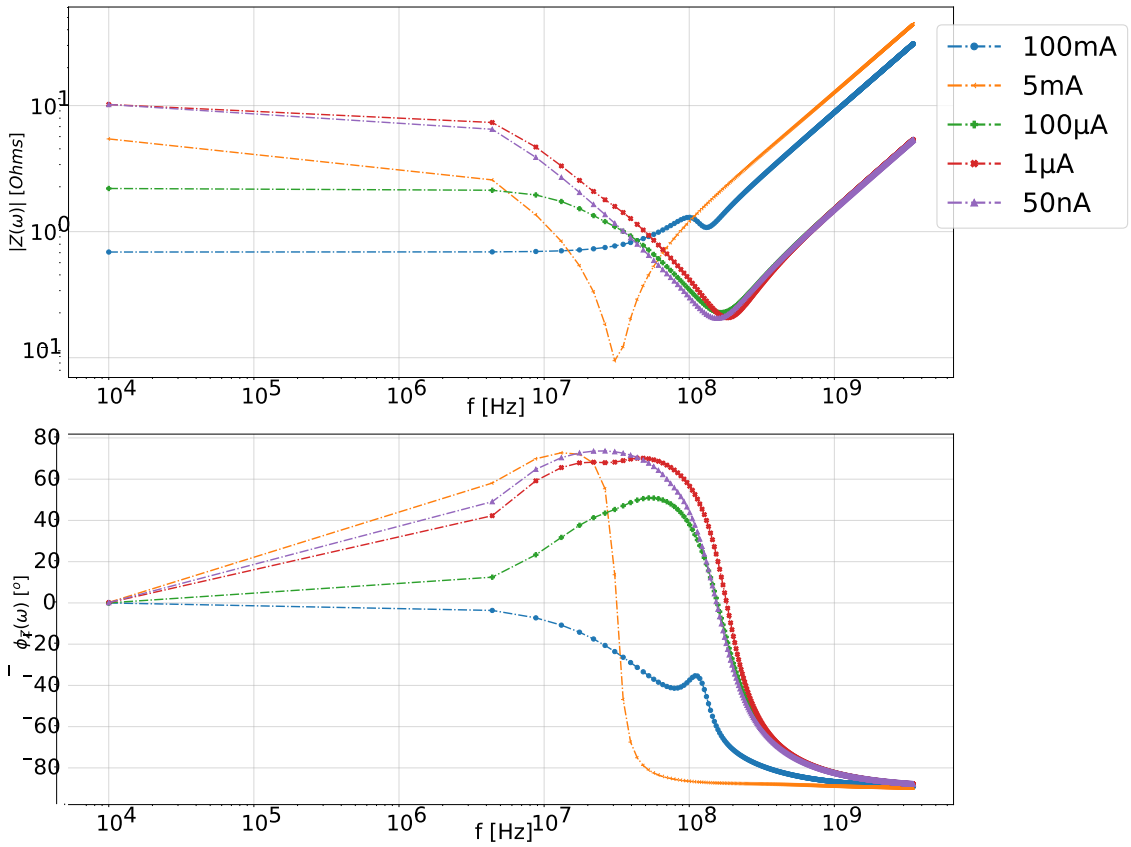

Figure 3.11 – LED impedance estimation using the estimated parameters at different currents with the LED model. The upper part shows the amplitude, and the lower part shows the phase.

data transfer performance. Fig. 3.12(a) depicts the experimental setup used to test the transmission distance and the impact of misalignment between the transmitter and receiver units, which were mounted on optical stages. To evaluate the performance of our design, we conducted tests using a 940 nm wavelength LED, a lens, and a high-frequency arbitrary waveform generator (Keysight P9336A) to implement the internal unit circuit. The front-end of the external unit was implemented using discrete components, including an ultra-low-noise, high-gain APD (MTAPD-07-010), a low-noise APD voltage bias circuit, and a high-speed TIA circuit. A 3D-printed housing was used to hold an optical lens and a long-pass filter, forming the optical parts of the external unit. An oscilloscope with storage functionality was used to test data recovery and measure data transfer performance.

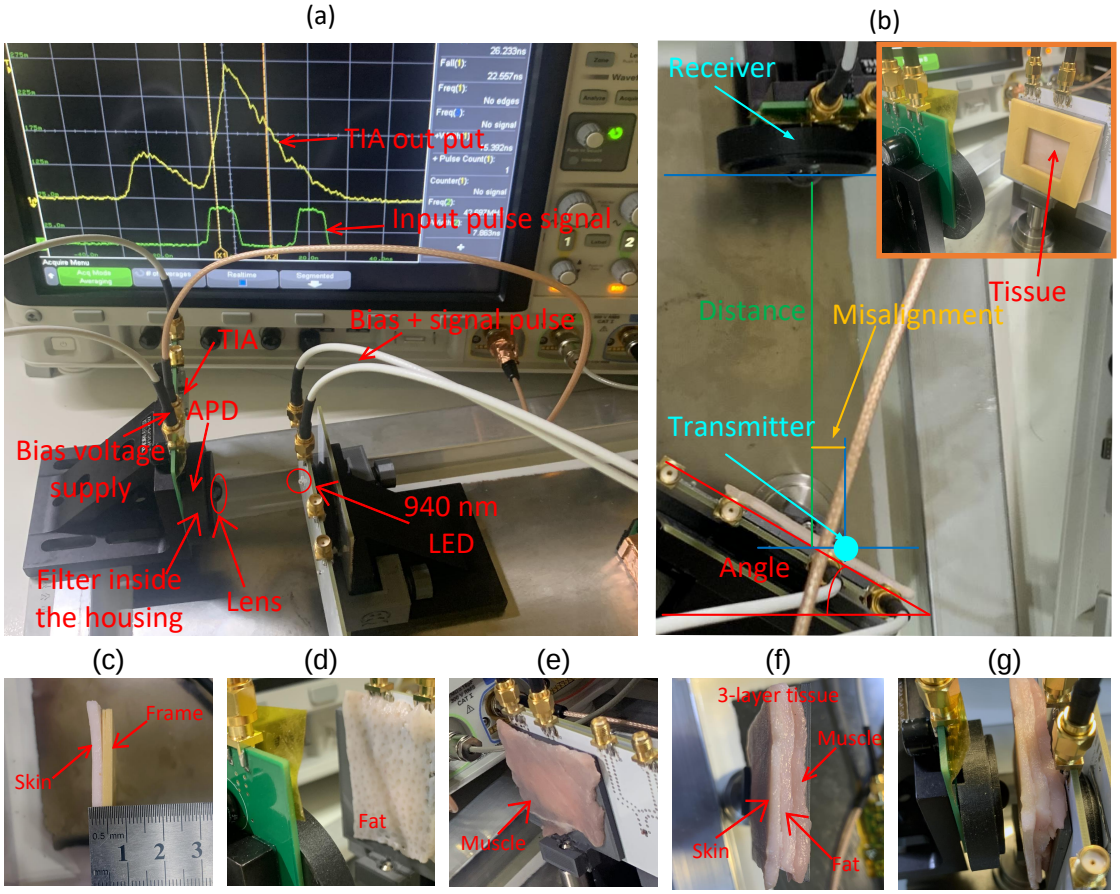

Figure 3.12 – The experiment setup. (a) The transmitter and the receiver are mounted on optical stages. The LED is mounted on the stage in the bottom right corner. The stage on the bottom left is the APD with optical lens. The oscilloscope shows the time domain signal from TIA and the waveform generator. (b) The setup and measurement of data transfer distance, misalignment angle and misalignment distance, and the frame to hold the tissue for testing. (c) The skin tissue from pork was used in the tests. The left is the skin tissue, and the yellow part on the right is a 3D-printed frame holding the skin. A ruler shows the thickness of the tissue. (d) The fat tissue from pork was used in the tests. The tissue is held by a 3D printed frame (the grey base behind the tissue) and mounted on the PCB with the LED transmitter to ensure no light leaks from the side. (e) The same setup was to test the performance with muscle tissue from pork. (f) Pork skin, fat, and muscle tissues were used in the tests and were held in place by a 3D-printed frame. The picture shows the three-layer tissue arranged with skin on the left, fat in the middle, and muscle on the right. During the experiment, the muscle side faced the LED to simulate subcutaneous transmission. (g) The test setup with tissue. The left part is the data receiver. The right part is the transmitter with tissue. The tissue is held by the grey frame and mounted on the PCB with the LED transmitter.

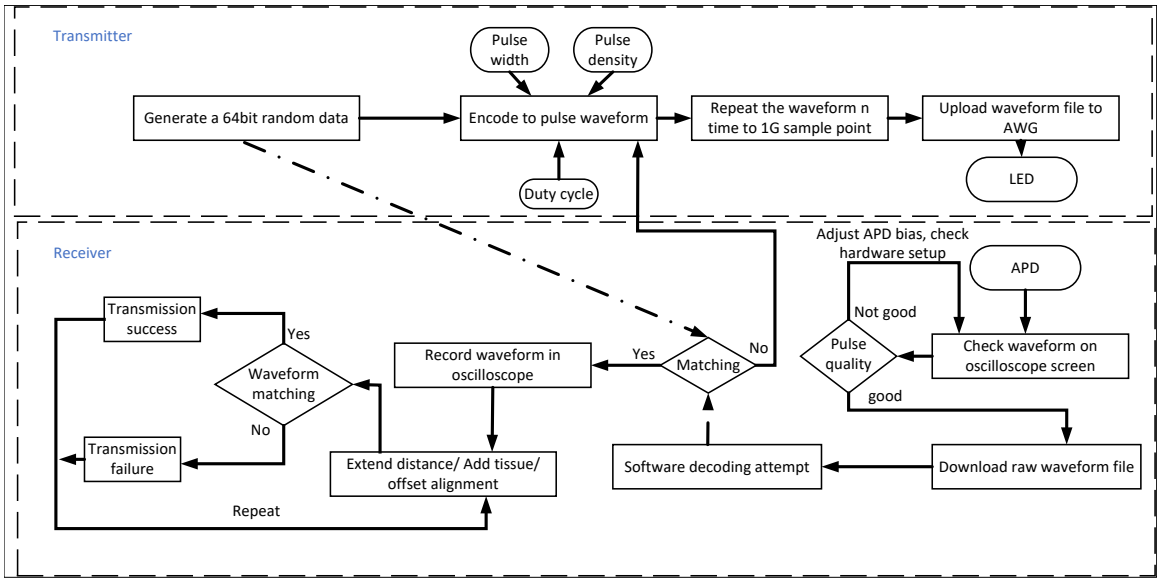

Figure 3.13 – The data transfer confirmation experiment protocol.

Fig. 3.12(a) shows the experimental setup used to test the transmission distance and the impact of misalignment between the transmitter and receiver units, which were both mounted on optical stages. In the figure, the time domain signal from both transmitter and receiver is captured by the oscilloscope. Fig. 3.12(b) illustrates the distance, misalignment, and angle measurement. The green line represents the distance, the yellow line indicates the misalignment, and the angle between the two red lines represents the misalignment angle. A 3D-printed frame was used to hold the tissue and test data transfer performance with tissue in between, as shown in the inset image in the top right corner of Fig. 3.12(b).

The transmission success was evaluated using the oscilloscope's waveform matching function. In the experiment, we tested data transfer in the air with and without the lens on the receiver side to verify the lens performance simulation results from the design stage. we used extracted skin, fat, and muscle tissue of varying thicknesses to test transmission performance with tissue between the transmitter and receiver.

To confirm successful data transfer, we generated a 64-bit random data segment, repeated it 256 times to create a 2 KB dataset, and encoded the data using the proposed modified OOK encoding described in the design section. This encoded

data was converted into a waveform file and uploaded to the arbitrary waveform generator, which periodically repeated pulses based on the data segment. When the waveform generator was active, we recorded the receiver-side waveform with no tissue in between. The recorded waveform was exported from the oscilloscope, and a Python script with an edge detection function was used to implement clock recovery and data decoding. The transmission was deemed successful if the decoded data matched the original data segment. Otherwise, the pulse width and density were adjusted, and the process was repeated until a positive result was obtained.

Once the initial data transfer was confirmed, misalignment, distance, and tissue were introduced to verify if the recorded waveform maintained the same pattern. The oscilloscope's built-in waveform pattern-matching function was used for this purpose. If the matching was successful, the transmission was confirmed; otherwise, it was not.

The oscilloscope's memory could store 4 Mpts(Million sample points), and the sampling rate was fixed at 5 GS/s. Under these settings, the receiving data could be recorded for a maximum of 0.4 ms for transmission confirmation. Due to the oscilloscope's limited storage, the length of the random data segment was fixed at 64 bits to simplify synchronisation between the waveform generator and the oscilloscope. Transmission confirmation was performed offline using Python code, which applied circular shifts to match the sent 64-bit data with the recovered data. The transmission was deemed successful if a match was found and sustained throughout the recording. Because of the small data segment and offline confirmation protocol, we could not measure the Bit Error Rate (BER) directly. Instead, the BER was estimated using the formula:

$$\text{BER} < \frac{1}{\text{data rate} \times 0.4 \times 10^{-3}}$$

For example, at a data rate of 108 Mbps, the estimated BER is below 2.31×10^{-5}.

3.3.2 Data rate testing result

Table 3.2 shows the successful data transfer testing result with different parameters and different thicknesses of tissue.

Table 3.2 – Testing result with misalignment and different tissue thickness

Tissue	Thickness (mm)	Distance (mm)	Receiver Lens	Maximum Misalignment*	Pulse Duration (ns)	Pulse Density (%)	Data Rate (Mbps)
None	N/A	3	Yes	±5 mm 45°	10	32	16
None	N/A	3	No	±2 mm 15°	10	32	8
None	N/A	15	No	±3 mm 15°	10	32	16
None	N/A	140	Yes	±20 mm 30°	1.5	0.125	108
Skin	2	3	Yes	±8 mm 45°	10	0.125	16
Skin	3	10	Yes	±5 mm 15°	1.5	0.125	108
Fat	2	3	Yes	±5 mm 30°	1.5	0.125	108
Fat	3	3	Yes	±3 mm 15°	1.5	0.125	108
Muscle	2	3	Yes	±8 mm 45°	1.5	0.125	108
Skin + Fat + Muscle	8	3	Yes	±5 mm 15°	3	0.125	54

Table note: The misalignment is measured as described in Fig. 3.12. The first value (in millimetres) represents the misalignment distance, and the second value (in degrees) represents the misalignment angle. * Pulse density (%) refers to the maximum pulse duty cycle in each clock cycle, calculated as: Pulse density $= \frac{\text{Pulse duration} \times \text{Max(number of pulses per bit)}}{\text{Clock cycle}} \times 100\%$.

3.3.3 Power consumption estimation

The power consumption of the proposed design's internal unit is estimated by combining the transducer power consumption with the circuit power consumption. Our LED modelling and impedance testing calculates the transducer power consumption. The circuit power consumption includes both the functional circuit consumption and the power management circuit consumption. The functional circuit comprises the pulse generator, encoder, and optimal bias tracking circuit.

As the bias voltage is intended to generate less than $1\,\mu$A current and the circuit

operates at a frequency below 500 Hz, the power consumption of the bias tracking circuit is essentially static. This circuit consumes 90 μW based on testing results.

The power consumption of the pulse generator and encoder circuits is dynamic, depending on the data transmission rate. The encoder is a digital data processing circuit, and its power consumption is calculated using the standard CMOS power consumption formula shown in Equation 3.7:

$$P_{\mathrm{C}} = P_{\mathrm{T}} + P_{\mathrm{L}} = \left(C_{\mathrm{PD}} \times V_{\mathrm{CC}}^2 \times f_{\mathrm{I}} \times N_{\mathrm{SW}}\right) + \left(C_{\mathrm{L}} \times V_{\mathrm{CC}}^2 \times f_O \times N_{\mathrm{SW}}\right) \tag{3.7}$$

In Equation 3.7:

— C_{PD} is the power-dissipation capacitance,

— V_{CC} is the supply voltage (set to 1.8 V for this calculation),

— f_{I} is the input signal frequency,

— N_{SW} is the number of bits switching,

— C_{L} is the load capacitance, and

— f_O is the output signal frequency.

The pulse generator designed for this module consists solely of digital logic gates and delay or buffer units. Using SPICE simulations in LTspice with TSMC's 350 nm model library, we estimated its power consumption under a 1.8 V power supply.

The efficiency of the DC-to-DC power management circuits in the internal unit is assumed to be 80%, which is reasonable for a low-power system. The total power consumption of the internal unit under different data transmission rates is listed in Table 3.3.

Table 3.3 – Power consumption estimation result at different data rates and power efficiency calculation result.

Data Rate (Mbps)	Pulse Width (ns)	Transducer Power Consumption (μW)	Circuit Power Consumption (mW)	Total Power (mW)	Power Efficiency (pJ/bit)
108	1.5	566	1.00	1.56	14.5
54	3	458	0.51	0.96	17.8
16	10	342	0.19	0.53	33.1

3.4 Discussion

I compared the system performance with state-of-the-art wireless communication approaches for bio-signal sensing implants. The results are shown in Fig. 3.14. The figure demonstrates that Impulse-Radio Ultra-Wideband (IR-UWB) achieves the highest data rate, reaching 1.66 Gbps for subcutaneous applications Song et al. (2022). The power consumption of the IR-UWB communication system ranges from 6 mW to several hundred milliwatts Ando et al. (2016); Even-Chen et al. (2020); Mirbozorgi et al. (2015). Despite its high data rate, IR-UWB technology maintains top-level power efficiency compared to other technologies. However, challenges remain, including the large antenna size (close to 100 mm^2) and stability issues caused by misalignment. For neural implants, individual curvature differences necessitate custom antenna designs for each recipient if the antenna is mounted on the skull.

Ultrasonic communication modules are advantageous due to their small size, low power consumption, and superior tissue penetration depth. However, ultrasonic communication faces challenges such as low data rates and limited modulation approaches, as it is typically based on backscatter communication Seo et al. (2016). Radio-Frequency (RF) backscatter communication modules also have sub-milliwatt power consumption for the internal unit and can achieve data rates up to 25 Mbps Moore et al. (2021b).

High-speed optical links reported in other studies use vertical-cavity surface-emitting

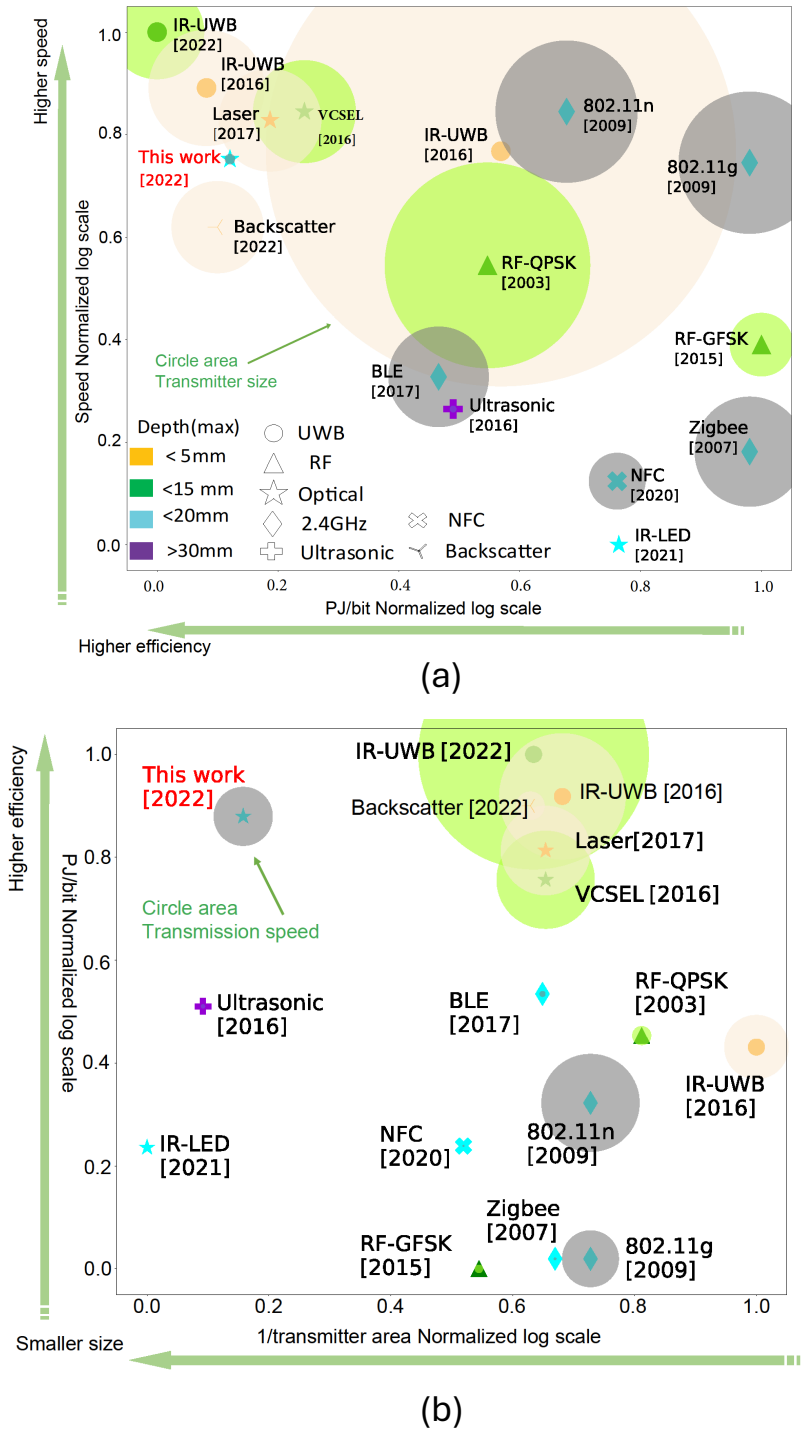

Figure 3.14 – Performance comparison chart of the state-of-the-art technologies. (a) compare the data transfer energy efficiency and speed. The x-axis indicates the power efficiency of the data transmission, the y-axis indicates the data rate, and the circle area represents the size of the data transfer transmitter. The color code represents the tissue penetration depth, and the marker shape represents the technology it used. (b) compare the data transmitter size and the transfer speed. The x-axis indicates the transmitter size, the y-axis indicates the data transfer energy efficiency, and the circle area represents the data transfer rate.

lasers (VCSELs) as transducers De Marcellis et al. (2017, 2020); Liu et al. (2012b) and conventional laser driver circuits to operate the laser diodes. Laser-based transducers offer higher modulation bandwidth than LEDs, achieving data rates of up to 300 Mbps De Marcellis et al. (2020). However, the drawbacks of lasers for implantable applications include their larger volume and more complex driver circuits.

The comparison graph shows that the LED-based high-speed optical link provides a well-balanced solution in terms of volume, speed, power consumption, and power efficiency, making it an optimal communication module for subcutaneous neural signal sensors.

3.4.1 Design Trade-offs

The proposed module balances volume, energy efficiency, data rate, and biosafety, with data transmission performance standing at the forefront of current state-of-the-art wireless communication systems for implantable devices. However, the current design and implementation have some drawbacks.

First, in the external unit, we use a high reverse voltage bias APD to detect short-period optical pulses with very low optical energy. In this design, the bias voltage is 160–200 V, posing a potential risk to living tissue if the high-voltage part is not properly insulated. We state this risk for complete transparency; otherwise, this high-voltage and extremely low current carrying wire is on a very small-length internal wiring system and, in practice, often covered by a high-grade insulating material.

Second, to transfer power efficiently into the internal unit, we used near-field coupling, which includes a coil in the internal unit. This approach limits the miniaturisation capability of the entire system, as coil efficiency decreases with smaller coil sizes.

Third, the LED-based transmitter has the potential to establish an optical downlink since it can detect light with shorter wavelengths than it emits. However, we did not implement bidirectional optical communication in this study. Our experiments revealed that the LED's impedance fluctuated when we introduced a modulated external light source, causing the optical pulses to become unstable.

3.5 Conclusion

This chapter presents the design of a subdermal optical telemetry module that balances a high data rate, high power efficiency, and low volume. By simulating the optical properties of tissue, we optimised the optical design to improve power efficiency and signal quality. By selecting a high-saturation-current near-infrared LED and driving it with low-amplitude voltage pulses with an optimal bias current, the LED generates 1.5 ns short pulses with reasonably high efficiency. The proposed design was implemented with discrete components and tested using animal tissue. The module achieves a data rate of 108 Mbps through 3 mm of tissue with a tolerance for misalignment of up to 5 mm and $\pm 15°$. The module's power consumption is below 1.57 mW, with a data transmission efficiency of 14.5 pJ per bit. The transducer's volume in the proposed module is less than 1 mm^3, making this solution highly promising for miniaturisation and various applications.

Chapter 4

A Leadless Power Transfer and Wireless Telemetry Solution for An Endovascular Electrocorticography

This chapter reproduces my published work and highlights another critical application area for miniaturised wireless and battery-free physiological monitoring. Specifically, it addresses the unique challenges of eBCIs, which aim to minimise invasiveness by integrating stent-based electrodes within the brain's vasculature.

In this thesis's broader context, removing long, in-body cables stands out as a pivotal advancement. Such cables introduce risks ranging from complications of vascular damage to increased infection likelihood and limited patient mobility. By demonstrating a wireless and leadless solution, this work directly aligns with the thesis goal of developing safer, more practical, and clinically translatable systems.

Within this chapter, the incorporation of FUS for wireless power transfer and optical telemetry for data communication illustrates how different modalities can be fused to overcome the inherent constraints of endovascular implants. Achieving multi-Mbps data rates and delivering sufficient power through tissue layers confirms the feasibility of an entirely leadless eBCI implant with minimal energy overhead and without the reliance on bulky or risky wiring.

This chapter introduces a wireless and leadless telemetry and power transfer solution for ECoG. The proposed solution includes an optical telemetry module and a FUS power transfer system. The proposed system can be miniaturised to fit in an endovascular stent, removing the need for long, intrusive cables. The optical telemetry achieves data transmission speeds of over 2 Mbps, capable of supporting 41 ECoG channels at a 2 kHz sampling rate with 24-bit resolution. The FUS power transfer system delivers up to 10 mW of power to the implant through the scalp(6 mm), skull(10 mm), and subdural space(5 mm), adhering to safety limits. Testing on bovine tissue (10 mm thick bone, 7 mm thick skin) confirmed the system's efficacy. This leadless and wireless solution eliminates the need for long cables and auxiliary implants, potentially reducing complications and enhancing the clinical applicability of eBCIs. The proposed system represents a step forward in enabling safer and more effective ECoG for a broader range of patients.

4.1 Introduction

Endovascular brain-computer interfaces have opened up new frontiers in human-machine interaction and have the potential to revolutionise the way we understand and treat neurological disorders Mahmood et al. (2022a); Oxley et al. (2016, 2021); Soldozy et al. (2020a). It offers several benefits for high-fidelity chronic recordings of cortical neural activities. Firstly, it provides a minimally invasive approach, as it can be implanted through a blood vessel, reducing the risk of infection and tissue damage compared to traditional invasive methods. Additionally, the stent-electrode array allows for stable, long-term recordings due to its integration with the vessel wall, which results in fewer movement-related artifacts and improved signal quality Brannigan et al. (2023); Majidi et al. (2023). This enables researchers and clinicians to gain deeper insights into brain function and develop more effective therapies for neurological disorders.

However, a significant limitation of the current stent-electrode array is the requirement of a long cable within the vessel to carry the signal to a recording device fixated

in the chest. This arrangement presents a risk to the recipient, possibly leading to complications such as thrombosis, vessel injury, or infection Opie et al. (2020); Oxley (2022). Furthermore, the cable can pose a significant challenge in pediatric applications, as children constantly grow and develop Fry et al. (2023); Mitchell et al. (2023); Sanjeev and Karpawich (2006). The fixed cable length may not accommodate changes in the distance from the vessel to the recording device as the child grows, potentially leading to complications and the need for repeated surgical adjustments Sun et al. (2021).

To address these issues, it is crucial to develop a wireless telemetry module that satisfies the volume and dimension limits of the stent and can power itself by harvesting energy from an outside source. This wireless solution would improve eBCIs' safety level and expand the potential applications of the stent-electrode array across different age groups and clinical scenarios. However, several challenges have prevented the invention of the telemetry module, including:

Area and volume limitation: The telemetry and power harvesting module needs to be small enough to fit within the confines of the blood vessel without causing discomfort or impeding blood flow Oxley et al. (2016). The diameter of the stent for eBCIs is 5 mm to 9 mm to fit in the superior sagittal sinus. Designing a compact module that incorporates transducers for receiving energy converting it into electrical power, and integrating components for modulation and encoding to transmit data presents a significant challenge. This is further compounded by the need to integrate control and power management circuits, all within the limited available space.

Power consumption limitation: The module must be highly energy-efficient, as excessive power consumption will exceed the power delivery and harvesting budget and could generate heat, potentially damaging surrounding tissues Nelson et al. (2020). Furthermore, for chronic recording, the power needs to be supplied and harvested continuously, which imposes constraints on the long-term safety concern and available energy format.

High data rate requirement: Capturing high-frequency neural activity and accommodating the data generated by many electrodes necessitate a high data rate. A

high sampling rate is required to accurately capture the high-frequency features of neural activity. At the same time, sufficient resolution of the ADC is crucial to cover the dynamic range of the neural signals Aggarwal and Chugh (2022). As the number of electrodes increases, the data rate multiplies accordingly, leading to a substantial amount of information that needs to be transmitted continuously.

Signal tissue penetration depth and absorption rate limitation: Wireless transmission of neural data through biological tissues can be challenging due to signal attenuation and absorption Karimi et al. (2021); Yoo et al. (2021b). The telemetry module must be able to transmit signals through various tissue layers while maintaining adequate signal strength and minimising interference or distortion.

The development of a miniaturised wireless power and data module for eBCIs presents a multitude of challenges that require innovative engineering solutions. Moreover, the module must be biocompatible, robust, and reliable, considering it will operate in a highly sensitive and dynamic environment within the human body Kanaan and Sabaawi (2021). Addressing these challenges necessitates interdisciplinary collaboration, combining expertise in microelectronics, materials science, biomedical engineering, and signal processing.

Currently, significant efforts are underway to develop power and data transmission solutions for in-body implantable devices, and some of them can be used for ECoG systems. Among these, inductive links can offer power budgets exceeding 50 mW and provide data telemetry with high data rates Iqbal et al. (2022a); Kim and Ho (2022); yu Hu et al. (2024); Zhang et al. (2022). However, inductive link-based technologies require specific structures or special materials to transform the stent into an efficient antenna. This presents challenges for clinical implementation because introducing a novel stent structure design requires long-term clinical trials to demonstrate its safety before it can be used in humans.

Other technologies, such as thermoelectric, triboelectric, and biofuel, can fit within a stent yu Hu et al. (2024). However, these technologies can only offer power levels in the microwatt (µW) range Roy et al. (2022); Yoo et al. (2021a), which is insufficient to power ECoG circuits that continuously sense and transmit data. Piezoelectric

devices can be sized to fit within a stent and can provide power levels in the milliwatt (mW) range Khan et al. (2024). Nevertheless, they typically rely on backscatter or passive methods for data telemetry, which do not offer sufficient data rates to transfer high-fidelity neural signals Khan et al. (2024).

This chapter introduces a novel solution that utilises optical telemetry for data transmission and piezoelectric energy harvesting for power delivery. By combining these two technologies, we address the challenges of size (cross-sectional area and volume), data rate, and power delivery and harvesting, leveraging the advantages of each.

4.2 Background

Optical telemetry, particularly in implantable medical devices for neural recording, presents a compelling advancement in ensuring efficient data transmission while adhering to the stringent size and power constraints inherent to such applications Xu et al. (2023). The core principle of optical data telemetry hinges on transmitting data through optical signals, utilising light, typically in the infrared or near-infrared spectrum, to encode and transmit information from the implantable device to an external receiver. This technology capitalises on the intrinsic advantages of light as a medium, enabling high data rates, minimised power consumption, and a substantial reduction in the size of the telemetry module, thereby aligning well with the imperatives of modern implantable neural recording devices.

The optical data solution represents a powerful combination of three essential qualities: compact size, low power consumption, and high data rate. Together, these attributes effectively tackle the ongoing challenge of achieving a balance between size, power efficiency, and data transmission speed in implantable wireless devices Drakopoulou et al. (2023). The compact size of the optical telemetry module is a crucial innovation that allows for its integration into tiny implantable devices, thereby enhancing the capabilities of neural interfacing and recording technologies. Additionally, the module's low power requirements significantly reduce the challenges as-

sociated with power harvesting circuits and the limitations of the implant's power source.

Furthermore, optical telemetry's high data transmission speed plays a crucial role in enabling the real-time transfer of neural data. This capability is essential for applications such as brain-computer interfaces, real-time monitoring of neurological disorders, and closed-loop neurostimulation systems Tanskanen et al. (2020). This high-speed data transmission feature allows for the reliable and almost instant transfer of extensive neural information, facilitating prompt interventions and precise evaluations in clinical and research environments. The wireless aspect of optical telemetry increases the flexibility and comfort of implantable neural recording devices, removing the requirement for external wires that might increase infection risks and limit patient movement. With these standout characteristics, optical data telemetry technology considerably advances the development of implantable medical devices, creating an environment that supports more advanced and patient-focused neural recording and interfacing solutions.

Piezoelectric energy harvesting is a burgeoning field within medical device technology, stemming from the unique ability of piezoelectric materials to convert mechanical energy into electrical energy when subjected to stress or strain Upendra et al. (2024). This principle underpins the development of self-sustaining power systems within medical devices, capitalising on the abundance of ambient mechanical energy sources such as body movements, blood flow, or external vibrations. A notable feature of piezoelectric energy harvesting technology is its compact form and high energy density, particularly advantageous for small-sized implantable or wearable medical devices Sezer and Koç (2021). These attributes alleviate the spatial constraints and power limitations traditionally associated with integrating batteries or other external power sources, thus significantly enhancing the feasibility and functionality of miniaturised medical devices.

Piezoelectric materials' compactness and high energy density are pivotal in advancing various medical devices' size, power budget, and reliability. For instance, self-powered pacemakers Jegadeesan et al. (2017), insulin pumps Tamura et al. (2018), and cochlear

implants Tamura et al. (2022) have been developed by harnessing the piezoelectric phenomena to convert biomechanical energy from heartbeats, muscle movements, or external vibrations into electrical energy that powers these devices or deliver the desired function directly. Moreover, piezoelectric energy harvesting technology facilitates the continuous operation of critical monitoring systems and sensors, integral in chronic disease management and remote patient monitoring, by providing a steady and sustainable power supply Narayanamoorthi (2019b).

However, despite these advantages, there are several drawbacks associated with piezoelectric energy harvesting technology. One of the primary challenges is the relatively low energy conversion efficiency compared to other energy harvesting technologies, which may necessitate additional power management systems to ensure a consistent energy supply. Furthermore, the biocompatibility and packaging method of piezoelectric materials within the human body remain areas of active investigation, as piezoelectric material will raise safety concerns when implanted in the human body, and packaging could potentially compromise power harvesting efficiency Aldaoud et al. (2018); Sedehi et al. (2021). Despite these challenges, piezoelectric materials' compact nature and high energy density leave them as one of the best candidates for powering eBCIs by harvesting energy within the stent.

Focused ultrasound waves offer new opportunities for piezoelectric energy harvesting for implantable devices. This technique uses ultrasonic waves, concentrated at a specific point inside the body, to transmit energy directly to the device through the skin and tissue. Unlike general ultrasound, which disperses energy over a wider area, FUS concentrates energy precisely at a specific target area. This targeted approach allows for more efficient energy transfer, minimising energy dissipation through non-targeted tissues and reducing the potential for unintended heating or damage. Still, the related ultrasound-piezoelectric issues need further investigations, such as pressure amplitude at deep tissue Erfani et al. (2017a), toxic material's connection with tissue Koruprolu et al. (2018)Erfani et al. (2018a), and relatively low power output Mustapa et al. (2019).

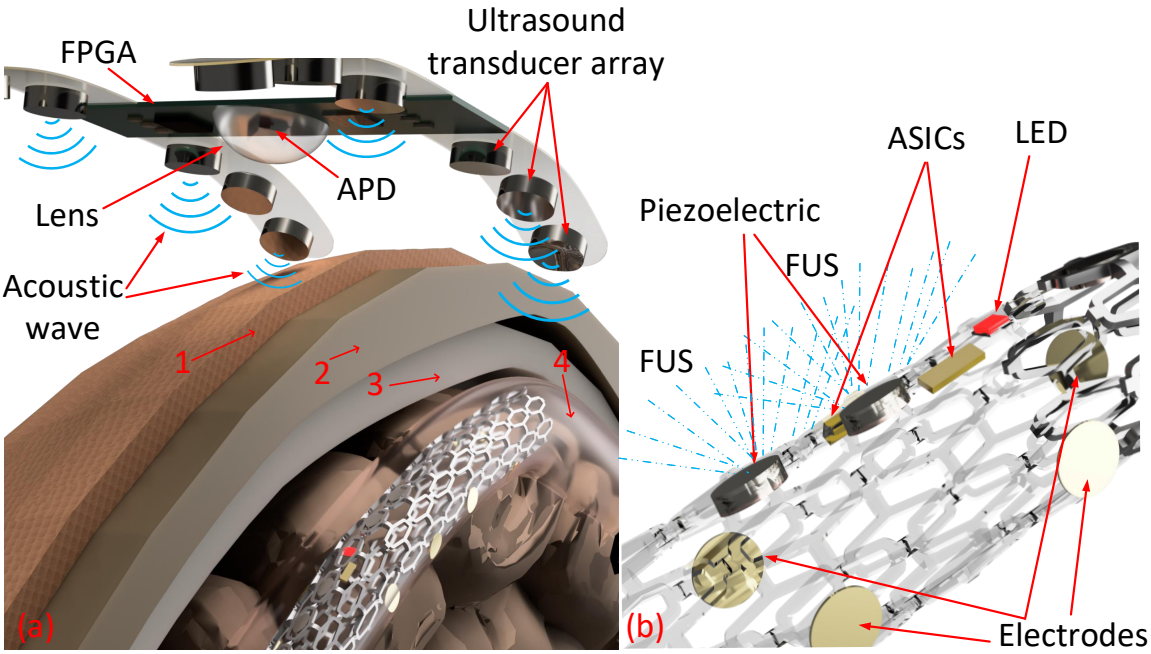

Figure 4.1 – Full system illustration with stent details. (a) Illustration of the system. The green arrow shows the tissues. (1) Skin tissue, (2) Bone tissue, (3) Dura mater, (4) Superior sagittal sinus. The system will have two parts. An implantable stent and an external device. All electrical components for the implantable part will sit in the stent in the superior sagittal sinus. The external device sits over the scalp and aligns with the implant. In the external device, an avalanche photodiode is used to collect optical signals from the implant, and a Field Programmable Gate Arrays (FPGA) is used to decode the optical data. The ultrasound transducer array in the external device will generate focused ultrasound that delivers energy to the stent. Sub-figure b shows the stent with functional components. The sensing electrodes are on the stent to sense electrical signals from the cortex. Three piezoelectrics sit in the stent to convert energy from FUS to power the circuit. The optical transmitter, an 810 nm wavelength LED (shown in red), sits in a space within the stent. Two ASICs with control and sensing circuits, energy harvesting and power management circuit and LED driver sit in other spaces within the stents.

4.3 Method

Here, we present a wireless solution for eBCIs that meets the requirements of low-volume, low-energy, high data rate and can be powered wirelessly. This solution includes an optical data telemetry module with a single LED transducer. With a simplified circuit design, the data telemetry module can transmit data at a high bit rate while consuming low power and occupying a minimal area. Our experiments

showed that we could achieve a 5 Mbps telemetry data rate and consume less than 4 mW of power with 7 mm bone and 10 mm soft tissues (fat, muscle and skin) between the transmitter and the receiver. The result indicates that the proposed module can transmit neural recording from a 32-channel electrode array, with each channel sampled at 9.7 kHz with 16-bit resolution.

The proposed solution includes a piezoelectric energy harvesting unit with multiple small piezoelectric power harvesters attached to the stent. Our simulation result showed we could harvest a maximum of 3 mW from one piezoelectric before the delivered acoustic pressure reaches the safety limit. With six or more piezoelectrics, we can easily have more than a 10 mW power budget to supply all the sensing, data telemetry, and potential stimulation circuits. Fig. 4.1 shows the conceptual design of the proposed module working with an eBCIs. In the implant part, three small piezoelectric harvesters are embedded in the stent to power the circuits. An 810 nm wavelength LED sits in the stent as the transducer for data telemetry. Two small ASICs embedded in the stent are the sensing, control, data communication, and power management circuits. In Fig. 4.1, above the head is the internal structure of the concept external device for the implant. It will be attached over the head using a headphone-like fixture. This fixture is designed to maintain the external device in a relatively fixed position on the head. During the implantation surgery, the position of the implant is precisely determined, and a Computed Tomography (CT) scan may be required to establish the optimal initial attachment point for the external device.

The headphone-like fixture uses the two ears as the reference point for the location, and the cross-bar of the headphone-like structure is used to decide the cross-section position of the external device. This fixture can help the external device sit in a relatively fixed position on the head. Once the external device is attached, an algorithm will be employed to adjust the phase of the ultrasound transducers within the array. This adjustment allows the system to scan and focus the ultrasound energy, ensuring maximum energy delivery to the implant site. This scan and re-focus algorithm will compensate for the rough alignment of the external device, as there is no precise fixed position for the external device.

Benefiting from the small size of the piezoelectric components and the LED, the proposed module has a transducer volume of less than 2 mm^3 (One LED and One piezoelectric). The module has significant potential for miniaturisation ability. The proof-of-concept testing board created in this work uses discrete components, and the total volume is less than 14 mm^3 (excluding Printed Circuit Board (PCB)), indicating that with future ASIC development, the volume of the module can be smaller than 4.5 mm^3. The entire module can be easily embedded into a stent with this volume.

To validate the proposed design, we did analysis, simulation, and proof-of-concept experiments according to the following parameters of success:

4.3.1 Optical channel analysis

Research has shown that wavelengths between 750 nm and 850 nm possess optimal optical properties for penetrating all tissue layers of the human head Firbank et al. (1993); Sawosz et al. (2016). Technologies such as Functional Near-Infrared Spectroscopy (fNIRS), which require light to pass through tissues from the outside to the brain, commonly use wavelengths around 800 nm Jeong et al. (2022). Based on this evidence, we chose 810 nm for our data telemetry to leverage this optimal transmission window. In the passage of 810 nm wavelength light through the human head's layers, distinct optical behaviours are observed (see Fig. 4.2).

The Superior sagittal sinus wall, characterised by a thin endothelial lining, shows low absorption and diffusion at this wavelength, with reflection influenced by refractive index differences between blood and adjacent tissues. The Dura Mater, a dense collagen and elastin membrane, exhibits moderate absorption and high diffusion, with reflection arising from refractive index disparities. The skull, comprising cortical and trabecular bone, has low absorption, moderate diffusion due to its porous structure, and reflection at tissue interfaces. Connective tissue, rich in collagen, elastin, and proteoglycans, demonstrates low absorption and moderate diffusion, with reflection at tissue boundaries. The skin, with its epidermal melanin and dermal blood vessels, shows moderate absorption and high diffusion, with reflection at the interfaces of its

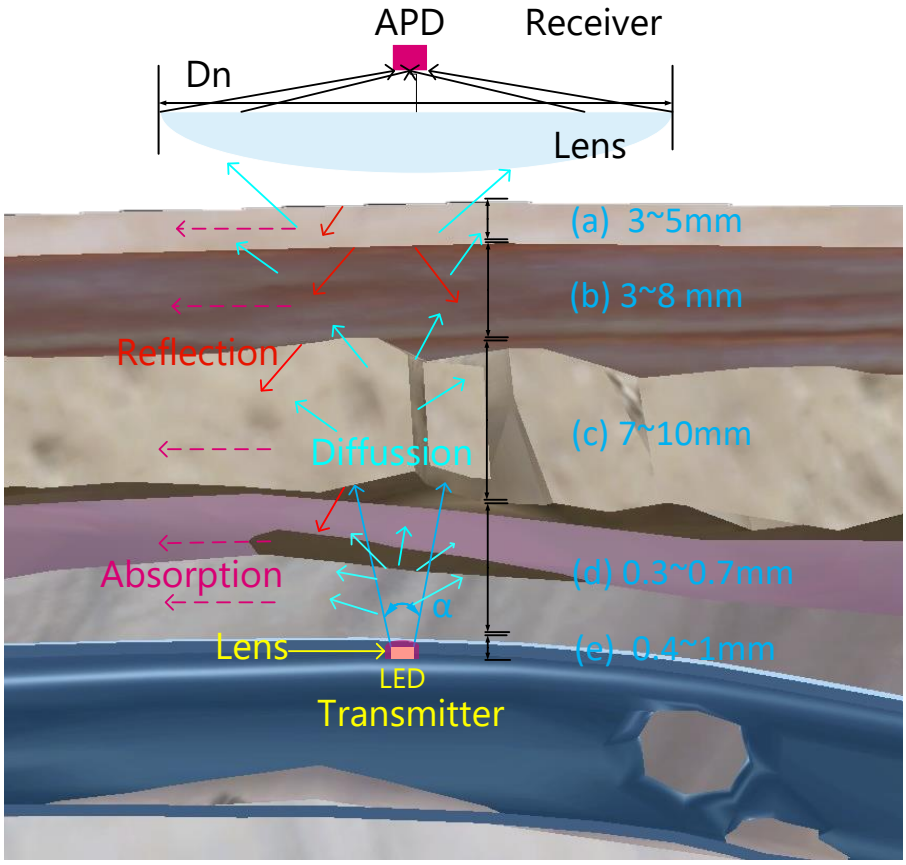

Figure 4.2 – Optical property of the data communication part. (a) Skin, (b) Connective tissue, Galea aponeurotica, Loose areolar connective tissue, Periosteum, (c) Skull, (d) Dura Mater, (e) Superior sagittal sinus Wall. Dn is the diameter of the lens. Alpha is the emitting angle of the LED, which the emitting lens can control. The arrows represent the diffusion (blue), reflection (red), and absorption effect (pink).

layers. Overall, the optical properties at 810 nm involve varying absorption, diffusion, and reflection, primarily influenced by blood, melanin, and water absorption, the fibrous nature of tissues, and structural complexities facilitating light scattering and reflection at tissue interfaces.

4.3.2 System design

Fig. 4.3 shows the system's block diagram and the device's conceptual design. To eliminate the need for a long cable connecting the brain to the chest, our plan inte-

grates energy harvesting, sensing, control, power management, and communication modules directly within the stent. An external device will be positioned over the implant site outside the body for seamless communication and power delivery. To accommodate the stent's dimensions, we propose utilising two ASICs to house the required circuitry. The first ASIC will encompass the global controller and sensing circuitry, including a multiplexer, amplifier, ADC, and temperature sensor. The second ASIC will contain the energy harvesting, power management, bias, and pulse generator circuits. By making the circuit into two smaller ASICs, the chips can be more easily adapted to fit the constrained dimensions of the stent and minimise the impair to the surrounding tissue or blood flow, which provides more flexibility in component placement and optimises the use of the stent's internal space. Separating power-intensive components (such as energy harvesting and power management circuits) from sensitive analog components (like amplifiers and ADCs) can reduce the risk of noise interference and improve signal integrity. This can result in higher accuracy and better overall performance of the implant.

The external device comprises three primary units: a data receiver unit, a wireless power delivery unit, and a power and battery management unit. We use an APD as the optical data receiver given its exceptional sensitivity and high-speed performance. A FPGA is used in our bench experiment for data recovery due to its flexibility and processing capabilities, which far exceed our needs. The power management unit will be responsible for battery management, supplying the bias voltage required for the APD, and providing power to the FPGA.

4.3.3 System powering plan

The proposed solution for powering the implant in the brain incorporates an external transducer array and an array of minute piezoelectric materials embedded within the stent itself. The transducer array, situated externally over the head, is meticulously engineered to generate focused ultrasound waves. These waves are directed explicitly toward the stent's location within the brain, ensuring precision in energy delivery.

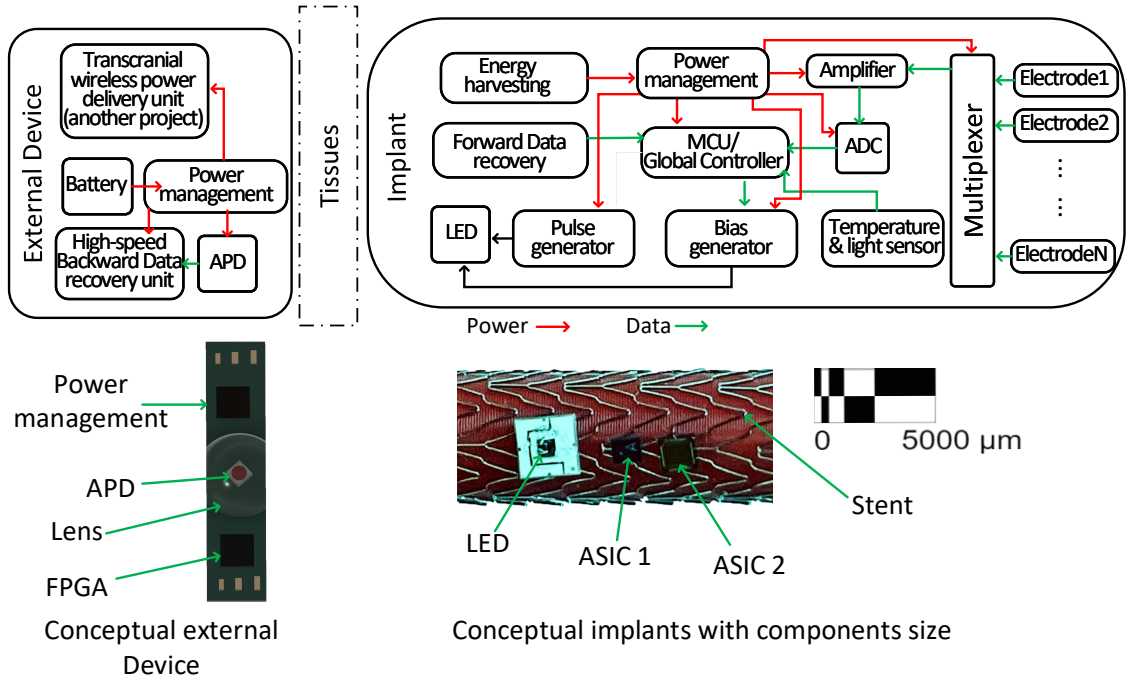

Figure 4.3 – System block diagram. The top left corner shows the blocks in the external device. The upper right part shows the blocks in the implant. The lower right part shows the potential components' size with an actual stent. The LED is commercially available and has a big substrate. We need a customised smaller substrate to meet our purpose.

The transducer array comprises numerous individual transducers, each of which can be controlled independently. This allows for fine-tuning the ultrasound beam in terms of intensity, focus, and direction, ensuring that the energy is delivered accurately to the stent while minimising exposure to the surrounding brain tissue.

The stent, positioned within a blood vessel in the brain, is designed to be minimally invasive while providing the necessary support to the vessel. Embedded within the stent are small piezoelectric materials, which can convert acoustic energy from ultrasound waves into electrical energy. A lead-free potassium-sodium niobate ($K_{0.5}Na_{0.5}NbO_3$ KNN) with high piezoelectric coefficient d_{33} is employed Iqbal et al. (2022b). These materials are selected for their high energy conversion efficiency and biocompatibility, ensuring they function effectively within the body without inducing adverse reactions. The piezoelectric materials are connected to the energy harvesting circuit, which con-

verts the harvested electrical energy into a stable power supply for the other circuits.

The FUS is generated by a group of ultrasound generators in the external unit. To ensure the safety of the ultrasound energy, we not only set intensity limits for each ultrasound generator but also carefully control the intensity of the FUS waves to prevent any potential damage to the surrounding brain tissue. Additionally, we plan to use the telemetry channel to include feedback mechanisms, letting the external unit adjust the output power dynamically and ensuring that the energy delivery and conversion processes operate efficiently and safely.

Overall, this solution provides a novel method of powering endovascular implants in the brain, utilising the synergy between FUS and piezoelectric materials to create a self-sufficient system that enhances patient monitoring and intervention capabilities while adhering to stringent safety standards.

Fig. 4.4 shows the structure of piezoelectric elements that we proposed in this chapter. The piezoelectric material surface is covered by a metallic conductive layer and an electrode connection with the stent. The existence of multiple piezoelectric elements ensures a constant and high-power generation.

Fig. 4.5 visually represents the modelling and simulation process of focused ultrasound propagation through the human brain. Fig. 4.5(a) displays real CT scan images from the Visible Human Project, processed using the iSEG tool Dionigi et al. (2017), providing a detailed cross-sectional view of the human head with various layers and anatomical details. This initial simulation uses ultrasound waves with an initial pressure of P_0 =30 kPa and a frequency of f =1 MHz.

Fig. 4.5(b) presents a modelled representation of the human head created with Sim4Life Sim4Life (2011), along with a single spherical focused ultrasound transducer, highlighting the positioning and biological interaction. This transducer generates the focused ultrasound waves used in the simulation.

Fig. 4.5(c) illustrates the dynamics of acoustic wave propagation through the head, showcasing the transient solution and demonstrating how these waves rapidly change over time. It also presents the transient acoustic pressure experienced at the scalp,

providing insight into the intensity of the waves as they initially interact with the head.

Finally, Fig. 4.5(d) depicts the steady-state solution, capturing the point where the acoustic waves stabilise and no longer change significantly over time. The acoustic pressure along the focal line is displayed, indicating the precise pressure within the targeted region of the brain where the ultrasound is most concentrated. The steady-state acoustic pressure along the Z-axis, shown in Fig. 4.5(d), clearly demonstrates the effect of the skull bone on the acoustic pressure concentration; therefore, it is expected that the critical temperature rise occurs at the skull.

Overall, Fig. 4.5 offers a holistic view of how focused ultrasound interacts with and propagates through the intricate structures of the human head and brain.

Acoustic-thermal analysis is carried out to meet the long-term thermal safety criteria. Transient ultrasound-thermal analysis for P_0 =30 kPa and f =1 MHz case is shown in Fig. 4.6(a) to Fig. 4.6(d). Due to the acoustic pressure concentration on the skull, the skull temperature rises to the critical temperature. Multiple ultrasound parameter variations are set with the limitation of temperature rise below 2°C. The temperature rise for all frequencies is always below 2°C for P_0 =30 kPa; thus, the acoustic pressure is used for the safe ultrasound.

4.3.4 Experiment setup

To evaluate the design and performance of the telemetry module and its associated system, we manufactured custom PCBs featuring discrete components for experimental purposes. Using 3D printing technology, we created holders to securely position the PCBs and the biological tissue samples during testing. These 3D-printed holders facilitated optimal optical alignment and precise control over distance and potential misalignment settings.

The tissue samples were freshly obtained bovine skin, complete with subcutaneous tissue and bone. All the tissue samples were purchased from the local Supermarket.

The 3D-printed frame maintained a firm grip on the tissue samples throughout the experiment. The prepared tissue samples are depicted in Fig. 4.7.

4.3.5 Testing protocol

To confirm the effectiveness of data transmission via the prototype device, we established a comprehensive testing protocol outlined as follows: Initially, we generate a sequence of random numbers using a random number generator. We add a 32-bit prefix to this sequence as a starting indicator for data transmission. This prefix consists of four repeats of an 8-bit fixed pattern, which helps align the signal for decoding at the receiver's end.

Following this, the combination of random numbers and the prefix is encoded using either pulse-density modulation or pulse-width modulation, depending on the test iteration and the data transmission speed being tested. We use an Analog Discovery 2 (AD2), a FPGA multi-function instrument device from DIGILENT and its Application Programming Interface (API) to create a signal with binary voltage levels, simulating the digital control and data transmission circuits of our proposed system. The output signal from the AD2 is then connected to a custom testing board designed to include our optical pulse generator circuits built from individual components. In response to the data sent, the board's LED emits optical pulses, marking the completion of the transmission test sequence.

At the receiving end, an avalanche photodiode captures the optical pulses and converts them into electrical signals. These signals are then amplified by a trans-impedance amplifier, followed by a cascaded operational amplifier, and fed into another AD2 unit. In this second AD2, the ADC converts the analog signals into digital format, making them ready for transfer to a Personal Computer (PC). This PC uses an adaptive peak-searching algorithm to identify the pulses. After finding the peaks, the algorithm decodes the signal into a binary sequence based on set pulse-density thresholds.

The software begins by searching for the start indicator. Due to the lack of synchro-

nisation between sending and receiving, a single 8-bit pattern is used as the search criterion. Once a matching pattern is found, the data following the last bit of the prefix is extracted and shortened to 1520 bits.

The software then compares this 1520-bit sequence with the transmitted initial data to calculate the BER. Subsequently, the receiving PC signals the transmitting PC to generate a new set of random numbers for the next test. A comprehensive testing setup was deployed to accurately evaluate the BER at specified transmission speeds. This testing verifies the time domain signal quality and ensures the data transmission is valid. This setup can create random images, encode them using the described method, and then decode them to conduct a thorough bit-level comparison between the sent and received image data, counting the total erroneous bits found. To establish a dependable BER metric, this testing protocol was performed continuously for 24 hours at each set transmission speed. The tests were conducted indoors with ambient lighting kept around 200 Lux, without direct sunlight exposure, and without using any environmental light shielding during the BER tests, to ensure the system's effectiveness under typical operating conditions without direct sunlight.

Fig. 4.8 shows the testing protocol and how we verify the successful data transmission. This testing protocol comprehensively evaluates the prototype device's data transfer capabilities, considering synchronisation, signal decoding, and error rate analysis. The power consumption is measured by connecting a voltage source to the power management part directly and measuring the input current, so the power consumption already includes the power consumption of the power management unit, LED driver and the driver for data.

To test the power harvesting plan, we combined COMSOL Multiphysics (1998) and Sim4Life simulation software Sim4Life (2011) to test the harvested energy under the safety limit. Fig. 4.9 (a) shows the model parameters and piezoelectric element characteristics. Fig. 4.9 (b) illustrates two primary results. The ultrasound frequency plays a vital role in piezoelectric energy generation as it affects the mechanical stress in the piezoelectric. The stent orientation is crucial as it affects the ultrasound-solid interactions. To address the effects of misalignment of the external device and the implant.

in our system design and evaluation, we implemented multiple piezoelectric elements (1 to 6) in the implantable energy harvester within the stent. This multi-element configuration meets the size limit and offers advantages against misalignment. Using an array of piezoelectric elements, the energy harvesting is distributed over a small area, not a single point. This means that even if some elements are not perfectly aligned due to misalignment, other elements can compensate, ensuring consistent power delivery. We conducted simulations to evaluate the impact of angular misalignments between the transmitter and receiver. we analysed misalignment angles shown in Fig. 4.9 ranging from 0°to 5°in both azimuthal and elevation planes.

4.4 Result

We did data transfer experiments using the protocol described in Fig. 4.8. The result is shown in Table 4.1.

Table 4.1 – Testing results for pulse width modulation (PWM) and pulse-density modulation (PDM).

Data rate (Mbps)	Tissue	Modulation	Power consumption (mW)	Efficiency (nJ/bit)
0.5	Bone (5 mm) + Skin (7 mm)	PWM	1.1	2.3
1	Bone (5 mm) + Skin (7 mm)	PWM	1.3	1.3
2	Bone (5 mm) + Skin (7 mm)	PWM	1.8	0.9
5	Bone (5 mm) + Skin (7 mm)	PWM	2.7	0.54
1	Bone (5 mm) + Skin (7 mm)	PDM	1.4	1.4
3	Bone (5 mm) + Skin (7 mm)	PDM	2.7	0.9
2	Bone (8 mm) + Skin (7 mm)	PWM	2.1	1.05
5	Bone (8 mm) + Skin (7 mm)	PWM	3.4	0.68
3	Bone (8 mm) + Skin (7 mm)	PDM	2.4	0.8
2	Bone (10 mm) + Skin (7 mm)	PWM	2.6	1.3
5	Bone (10 mm) + Skin (7 mm)	PWM	3.8	0.76
3	Bone (10 mm) + Skin (7 mm)	PDM	2.9	0.96

From the result, we can find that the data transfer efficiency is higher when using pulse width modulation. Still, Pulse Width Modulation (PWM) requires more precision timing to ensure the optical pulses can be decoded at the receiver side. When we use pulse-density modulation, we can relax more on timing and simplify the driver circuit for data.

Fig. 4.10 shows the power harvesting result of the proposed power harvesting plan. We can see that a single piezoelectric generates the maximum power of 3.0 mW, and with the six elements, the sum of power output is 10.0 mW. With rotated piezoelectric elements, a high power output can be generated by tuning the frequency of FUS waves. These results illustrate the tunding of the frequency and placement of the FUS transducer for each piezoelectric; we can get the sum of the maximum single piezoelectric and reach a high level of power generation.

Fig. 4.11 presents the results of the BER test conducted at transmission speeds of 5 Mbps and 3 Mbps, utilising 10 mm bone and 7 mm skin as mediums. The figure illustrates the setup used for the BER assessment, including the real-time generation of a random image for testing purposes. Analysis of the data reveals that, at a transmission speed of 5 Mbps with PWM, the BER was maintained below $1.09e^{-8}$. Conversely, employing a transmission speed of 3 Mbps with Pulse-Density Modulation (PDM) resulted in a BER below $1.62e^{-9}$. The duration of the BER assessment exceeded 24 hours, during which more than 400 Gb of data were transmitted. The use of fresh tissue in these experiments imposed a limitation on the duration of the BER test due to the continuous dehydration of the tissue, which affects its optical and electrical properties. Observations from the test indicate that the BER exhibited fluctuations that appeared to follow a discernible pattern, potentially linked to variations in environmental lighting. However, due to the constrained timeframe of the experiment, a definitive correlation between environmental lighting conditions and BER fluctuations could not be established.

4.5 Discussion

The wireless and leadless power and data system proposed in this chapter represents a transformative advancement for eBCIs, addressing critical power and data transmission challenges in current eBCIs designs. The most notable contribution is eliminating the long, cumbersome cable that traditionally runs from the brain to the chest. Removing this cable significantly reduces the risk of blood flow obstruction

and vessel damage, which is especially beneficial for vulnerable populations. Pediatric patients, in particular, benefit from this solution as it eliminates the need to accommodate body growth by adjusting cable length.

A key advantage of the proposed system lies in its enhanced data transfer capabilities within the extremely limited on-site space. While existing communication methods such as near-field, far-field, and ultra-wideband can offer higher data transmission speeds with lower power consumption, their transmitters and antennas are too large to fit within a stent. Other methods, like ultrasound backscatter and body area communication, have compact transmitters that can fit inside a stent but fail to meet the bandwidth requirements for high-fidelity ECoG data transmission. Our system, however, achieves a data transfer rate exceeding 2 Mbps, marking a significant improvement that enables real-time transmission of detailed ECoG data, crucial for effective monitoring and intervention.

Regarding power transfer, the system provides efficient and safe energy delivery to the implant site. However, ensuring consistent and reliable wireless power transfer in vivo remains a significant challenge due to attenuation caused by variable tissue, bone, and blood environments. This is a well-known issue in similar systems, and while our solution shows promise, extensive real-world testing will be necessary to confirm that it can perform in complex, variable biological environments as effectively as in controlled simulations.

Another concern regarding power transfer is its suitability for long-term applications. For FUS power delivery, an acoustic couplant is necessary for the external FUS device to effectively transmit energy to the proposed ECoG system. Traditional couplants, such as ultrasound gels, can dry out over time, require frequent reapplication, and may cause skin irritation or discomfort during extended use. These factors could limit the practicality and patient compliance for continuous or long-term applications. To address this challenge, future research should investigate the use of solid-state biocompatible couplants such as hydrogels, hydrophilic polymers, and 3D-printed rubber materials Chen et al. (2021); Gao et al. (2023) for the FUS device.

Another significant technical challenge is achieving hermetic packaging in the system's

design. The telemetry module needs an optical window within its packaging while seamlessly integrating into an endovascular stent. As medical devices become more compact, their designs and manufacturing processes become increasingly intricate, impacting reliability, durability, and overall system performance. This complexity underscores the importance of thorough testing and multiple design iterations to ensure optimal outcomes.

Biocompatibility is also a significant concern. While removing the long cable reduces certain risks, introducing new electronic components and materials directly into critical regions like the bloodstream or brain tissue presents new challenges. There is potential for tissue reactions, unforeseen long-term effects, and other adverse events arising from the body's interaction with foreign materials. Rigorous biocompatibility testing of newly introduced materials or design changes is essential to prevent potential complications and ensure patient safety.

Furthermore, although software simulations and modelling provide invaluable insights, they may only partially replicate real-world scenarios. Human physiology and tissue responses are complex, and the device's behaviour under actual human conditions might present unanticipated challenges that simulations need to account for. Consequently, extensive in-vivo testing and post-implantation monitoring are crucial to validate the system's performance and safety in real-world settings.

Finally, the leadless power and data solution for eBCIs offers a promising direction that addresses many drawbacks of current systems. However, it also introduces new challenges that require careful consideration, rigorous testing, and continuous monitoring to ensure its viability, safety, and efficacy in practical applications.

4.6 Conclusion

In conclusion, this chapter presents a novel optical wireless telemetry module designed for integration within a smart stent, aiming to overcome the limitations of current eBCIs such as the Stentrode™. The proposed module enhances the eBCIs' applicabil-

ity for patients with weak blood vessels or susceptible vasculature by eliminating the need for a long wire connecting the stent electrodes to the encapsulated electronics. It addresses the challenges associated with pediatric applications.

The telemetry module, which can transfer data at a maximum of 5 Mbps and operate with less than 3 mW power consumption, demonstrates its potential through proof-of-concept experiments using discrete components and fresh bovine bone, muscle, and skin tissue. Future developments of ASICs will further refine the optical telemetry module's performance and pave the way for more versatile, safer, and less invasive eBCIs, ultimately transforming the landscape of neuroscience, engineering, and medical devices.

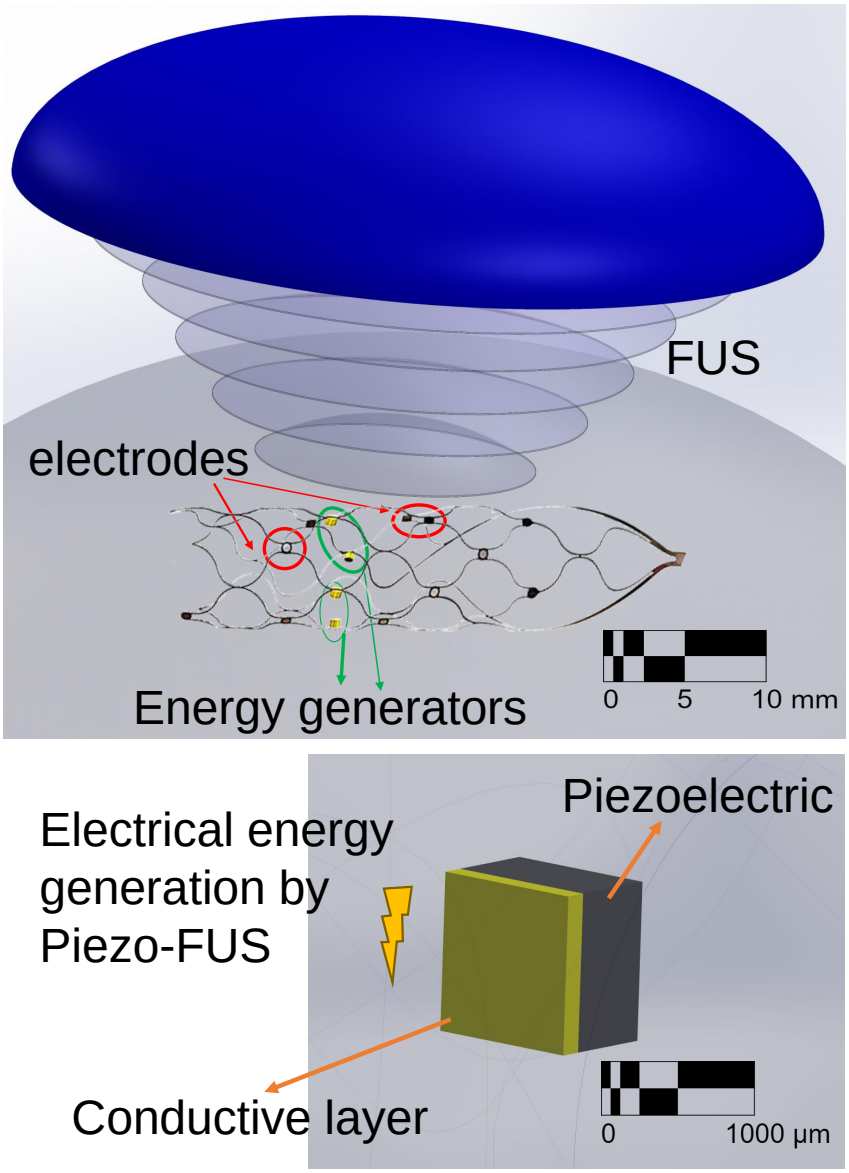

Figure 4.4 – The structure of the piezoelectric harvester Illustrating the process of electrical energy generation using piezo-FUS: A focused ultrasound beam (blue ellipse) targets a stent embedded with a thin layer of piezoelectric material (highlighted in orange). Upon interaction with the ultrasound, the piezoelectric layer converts the acoustic energy into electrical energy, represented by the lightning bolt symbol.

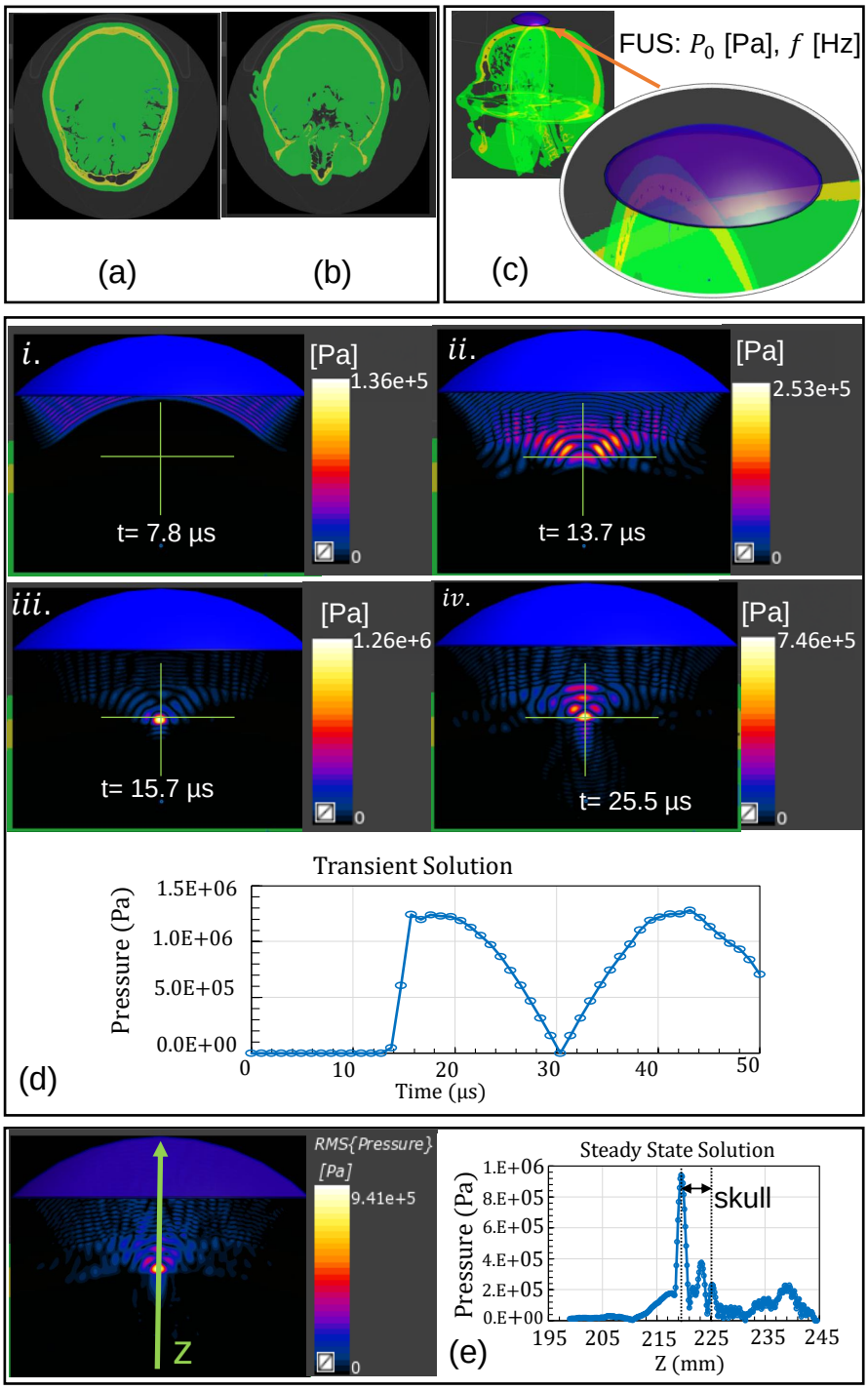

Figure 4.5 – Modelled focused ultrasound with the brain, (a) real CT scan images, (b) modelled human head and a single spherical focused ultrasound transducer, (c) P_0 acoustic wave propagation through the head by the transient solution and the transient acoustic pressure at the scalp, and (d) the steady state solution of acoustic pressure and the acoustic pressure at the focal line.

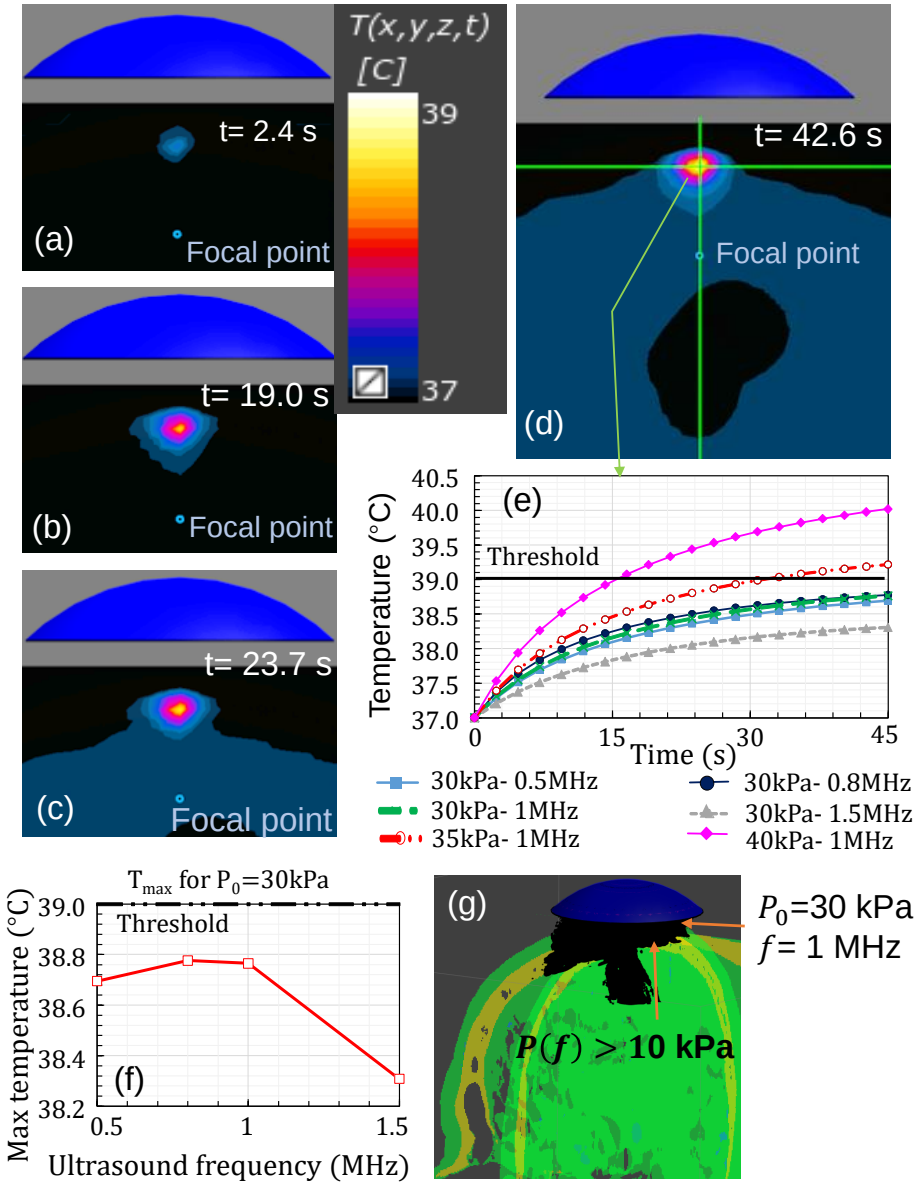

Figure 4.6 – Ultrasound-thermal analysis. (a)—(d) The transient temperature contours over time with P_0 =30 kPa and f =1 MHz, (e) temperature at the top of the skull over time for different acoustic settings, (f) maximum temperature versus ultrasound frequency, and (g) The steady-state iso-volume pressure > 10 kPa inside the brain.

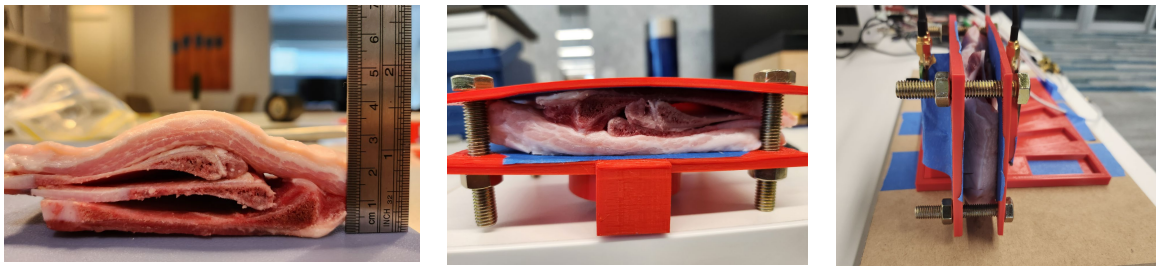

(a) (b) (c)

Figure 4.7 – This figure shows the tissue we used. (a) The tissues and their thickness. The top layer is skin tissue with subcutaneous fat. The lower three layers are bones. During the experiments, we stack different layers of bones to get different thicknesses of bone. (b) We use a 3D-printed frame to hold the tissues and use screws to put pressure to make the tissue firmly connected. (c) The experiment setup with tissues in between. The middle is the tissues. The left side is the receiver PCB, and the right side is the transmitter.

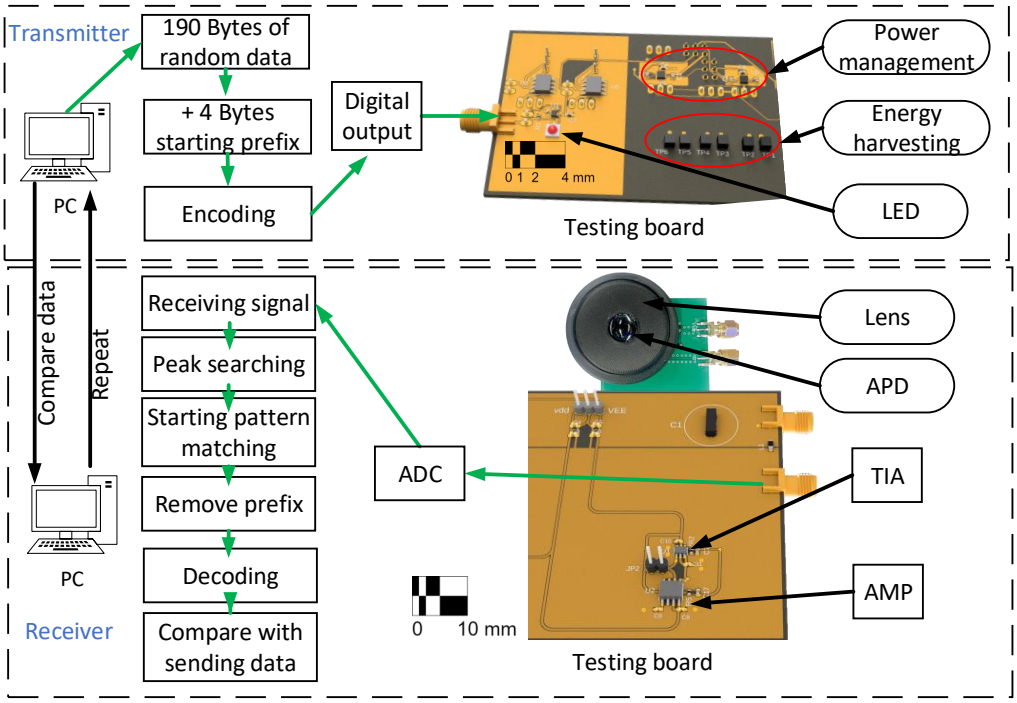

Figure 4.8 – The upper portion of the diagram represents the transmitter. A computer running a program generates 190 bytes of random data at a time, limited by the buffer size of the digital Input/Output (I/O) device. The program then adds a 4-byte prefix consisting of repeating fixed data to indicate the beginning of the transmission. The data is subsequently encoded into a pulse signal using either pulse width or pulse-density modulation. A digital I/O device generates the pulse and sends it to the testing board, producing optical pulses based on the input pulse signal. The lower portion of the diagram represents the receiver. Our testing board includes an analog front-end that converts the received optical pulses into electrical signals. An ADC digitises the signal and sends it to a computer. Depending on the modulation scheme used, the program on the computer performs different operations. For pulse-density modulation, it conducts peak searching and marks the pulses on the timeline. It uses a duty cycle searching and labelling algorithm to determine the pulse width for pulse width modulation. The program searches for the repeated prefix pattern once the signal is converted into binary format. When an entire segment of the prefix is matched, the program considers this as the starting point of the data and removes the prefix accordingly. After decoding, the program compares the recovered signal with the original transmitted data to verify the data transfer and calculate the error rate.

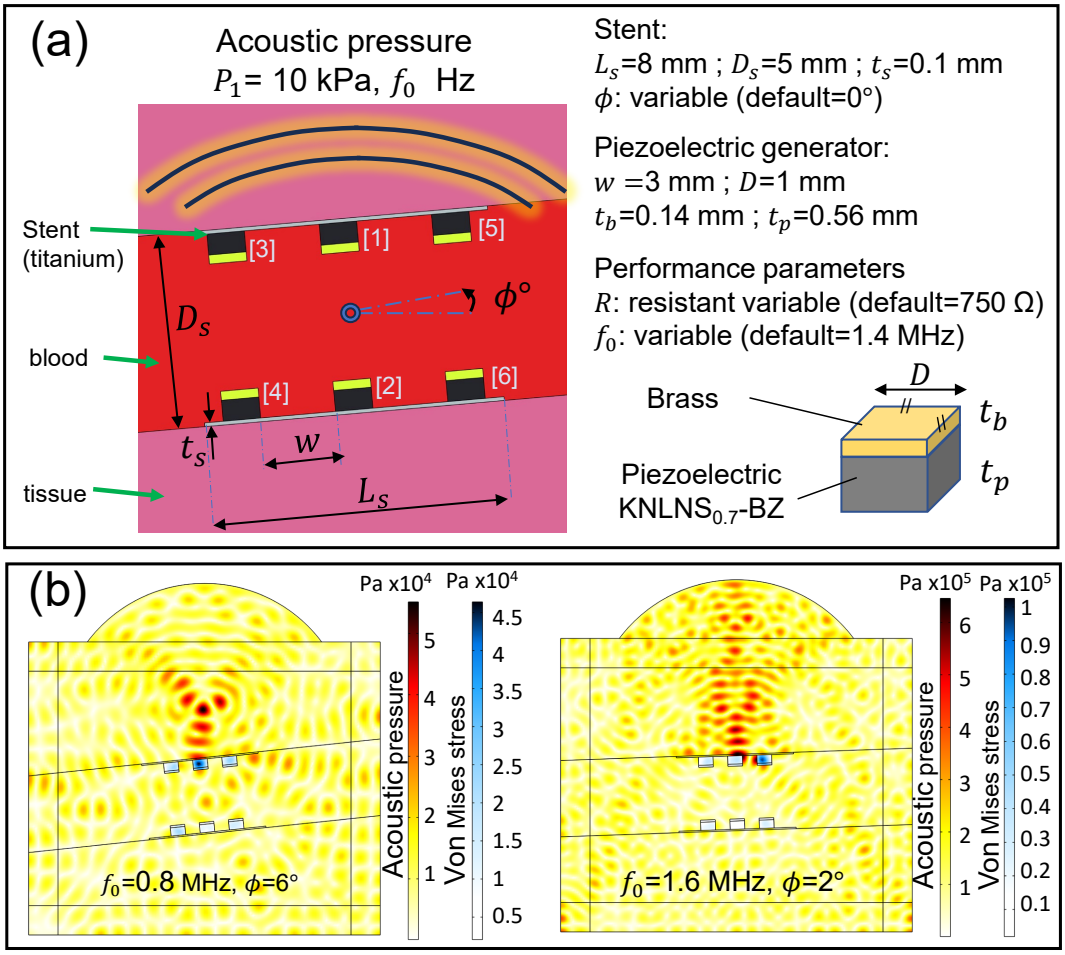

Figure 4.9 – The acoustic-electro-mechanical simulation of energy harvesting system, (a) model parameters of piezoelectric generators, biomedical tissues, and acoustic pressure, (b) acoustic pressure in the tissue surrounding the piezoelectric generators and von Mises stress on the piezoelectric generators for two settings.

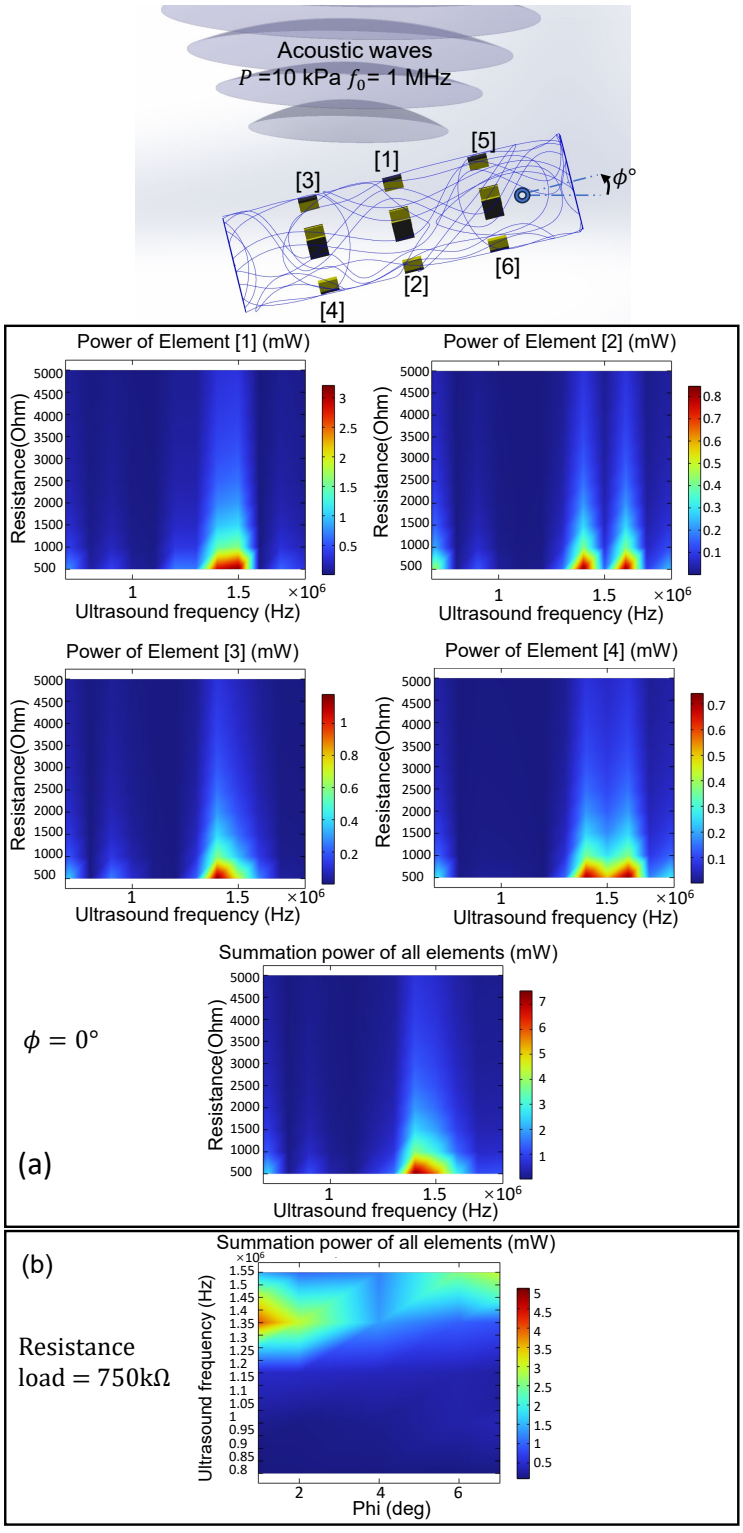

Figure 4.10 – Simulation of piezoelectric power generation with FUS acoustic pressure, (a) piezoelectric power output from element number [1] to [4], and power summation for all elements. Power comparison versus ultrasound frequency and resistance load connection, and (b) the effect of stent-system orientation on the power output.

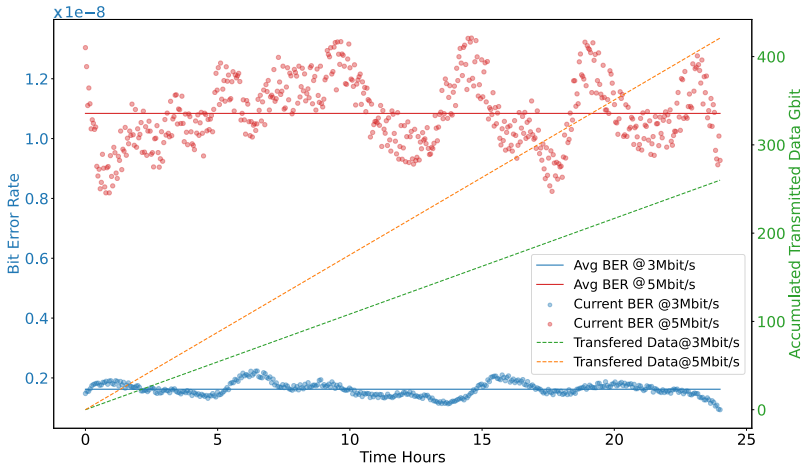

Figure 4.11 – The diagram delineates the setup and outcomes of the BER testing procedure. The horizontal axis (X-axis) indicates the duration of testing, with each evaluation extending over 24 hours. The representation includes red dots and a corresponding red line, which illustrates the real-time BER measurements and the overall BER outcome, respectively, for a 5 Mbps transfer rate. Similarly, blue dots and a solid blue line depict the real-time BER observations and cumulative results for a 3 Mbps transfer rate. Additionally, the orange and green lines signify the total volume of data transmitted during the BER assessment, amounting to 260 Gbit for the 3 Mbps rate and 421 Gbit for the 5 Mbps rate. We recorded a video(Link) showing the experimental arrangement, featuring the real-time decoded random image on the computer screen. Positioned at the left is the AD2 device serving as the receiver, while the right showcases the AD2 device functioning as the transmitter. Central to the setup is the tissue sample utilised for testing purposes.

Chapter 5

A High-efficiency Wireless Power Transfer System for Smart Endovascular Devices

This chapter reproduces my work prepared for publication, which addresses another critical component in realising fully wireless and battery-free devices. Specifically, it tackles the challenge of delivering sufficient power to stent-based implants in the brain without resorting to long lead wires—a key objective in the broader context of Miniaturised Wireless and Battery-Free Systems for Physiological Monitoring and Stimulation.

Building on the principle of leadless design introduced in previous chapters, this work demonstrates how a subcutaneous relay can convert inductive coupling to capacitive coupling to efficiently power devices inside the vasculature. This approach simplifies the device architecture and significantly reduces potential complications by eliminating the need for a lengthy wired connection to a subcutaneous chest implant. The system's successful experimental validation across real tissue layers, combined with supporting finite element simulations, underscores its feasibility for clinical translation.

WPT for stent-based medical devices in the brain, such as Endovascular Electro-

corticography (endoECoG) devices, faces challenges. Typical stent-based endoECoG consists of electrodes placed on a stent and connected with a set of long lead wires to a subcutaneous chest implant responsible for wireless energy harvesting and data telemetry. Eliminating the long lead wires is not trivial or straightforward, introducing a great set of challenges. This work demonstrates a feasible method to deliver power directly to a standard medical stent without modifying its structure, mechanically or electrically.

The proposed system employs a subcutaneous relay that converts inductive coupling to capacitive coupling, enhancing power transfer efficiency while maintaining minimal invasiveness. Experimental validation was performed using real skin, bone, and vessel tissues, and finite element simulations were conducted to confirm model accuracy.

Experiments demonstrated over 45 mW of power delivery without exceeding safety limits, sufficient for powering endoECoG devices and biosignal sensors. The system achieved 7.26% Direct Current (DC)-to-DC efficiency, the highest reported for stent-based implants without additional transceivers or specialised stent designs. Results closely matched simulations, confirming practical viability. Safety assessments, including SAR analysis and temperature rise simulations, showed compliance with regulatory standards and minimal risk to surrounding tissues.

This work demonstrates a reasonably efficient and safe power delivery to stent-based implants in the brain, considering the anatomical challenges regarding the surgical delivery, paving the way for fully wireless, minimally invasive neuroprosthetic devices. The external device does not require close skin contact, making it suitable for long-term applications and improving patient comfort. Future efforts will optimise system components and address manufacturing challenges to facilitate clinical translation.

5.1 Introduction

Significant advancements have been made in developing stent-based biomedical implants, an invasive device that offers relatively lower-risk surgical delivery procedures

Kobo et al. (2020). With progress in electronics, stents now provide mechanical support and are equipped with sensing and stimulation capabilities Vishnu and Manivasagam (2020); Zhang et al. (2023a). This evolution enables stents to function beyond passive interventions, expanding their applications to monitoring and potentially to active interventions Soldozy et al. (2020b); Zhang et al. (2023a).

These stent-based biomedical implants open new avenues for disease management and treatment. For example, endoECoG devices offer a relatively lower invasiveness method for long-term brain monitoring and high-performance brain-computer interfaces Oxley et al. (2016); Soldozy et al. (2020a). Currently, the endoECoG device includes a stent with electrodes in the Superior Sagittal Sinus (SSS), a companion unit in the chest area that provides power and houses the electronics, and a long cable connecting the stent in the brain to the companion unit. This device functions as a monitoring system and has the potential for brain stimulation to treat epilepsy and other neurological diseases Oxley et al. (2016); Oxley (2024). However, the lead cable is the most critical challenge for the current device. The cable traverses through the blood vessel and requires an opening in the vessel wall for exit. These factors introduce risks, especially for long-term use, which lowers recipients' acceptance and limits applications Mitchell et al. (2023).

While significant progress has been made in WPT systems, delivering power directly to a leadless stent remains a substantial and open problem, not to mention a great deal of effort around making data telemetry wireless. Challenges include limited space, the specialised mechanical structure of the stent and issues for electrical requirement adjustments, energy signal attenuation by biological tissues, and the need to meet biocompatibility and safety regulations Chen et al. (2014); Herbert et al. (2022). By addressing this challenge, endoECoG devices can become fully wireless, and after eliminating the lead-wire-related risks, these devices can reach their full potential and widespread application.

Researchers have explored various WPT techniques to address the challenge of powering stent-based biomedical implants. These techniques include near-field inductive coupling Mahmood et al. (2022b), magnetic resonance coupling Li et al. (2012), far-

field RF energy transfer Shah and Yoo (2020), optical power delivery Xu et al. (2024); Zhao et al. (2020), and acoustic power transfer Xu et al. (2024).

Near-field inductive coupling relies on a pair of coils nearby (less than one wavelength apart). Designing an efficient receiver coil within the limited space of a stent is extremely challenging Abdin et al. (2024). Some studies have attempted to use the entire stent as a receiving coil, showing promising results Herbert et al. (2022). However, this approach requires specially designed stents with coil-like structures, as standard stents lack effective inductive properties Islam et al. (2020). Using such specialised stents introduces challenges for clinical approval due to unproven long-term mechanical stability, safety and the use of non-standard materials.

Magnetic resonance coupling faces similar obstacles when applied to stent-based implants. The requirement for resonant structures and efficient coupling over small volumes makes it difficult to implement within the confined space of a stent Li et al. (2012); Xu et al. (2020). Achieving sufficient power transfer efficiency while meeting safety regulations remains problematic.

Far-field RF energy transfer allows smaller antennas to fit within a stent. However, at the high frequencies required for effective far-field transmission, tissue absorption increases significantly Liu et al. (2014a). This reduces power transfer efficiency and raises concerns about tissue heating and compliance with regulatory safety limits on electromagnetic exposure Bercich et al. (2013). Therefore, using far-field RF energy transfer to power a stent-based implant struggles to provide enough power without reaching the safety limit.

Optical links are promising for data transfer due to high bandwidth capabilities Xu et al. (2023) but are less suitable for energy transfer in implantable devices. The optical-to-electrical power conversion efficiency of photovoltaic cells at the implant site is too low to meet the energy demands, especially considering the light scattering by the biological tissues Dinis and Mendes (2021); Xu et al. (2023).

Acoustic Power Transfer emerges as a promising alternative due to its ability to penetrate deep tissues with a lower attenuation window with the skull. It allows for

small-sized receivers compatible with the dimensions of the stent and offers higher safety margins concerning tissue heating Kim et al. (2021). However, the primary challenges for acoustic power transfer in stent-based implants include the biocompatibility of piezoelectric materials used in acoustic transducers and the development of packaging technologies that can integrate these materials into stents without compromising mechanical properties or causing adverse biological reactions Xu et al. (2024).

Although various WPT techniques offer potential solutions, each presents a unique set of challenges when applied to stent-based implants. Overcoming these obstacles requires innovative approaches to accommodate the spatial constraints of stents and anatomical features for surgical implantation, maintain biocompatibility, and comply with required safety regulations.

Capacitive Coupling WPT is a technology that uses electric fields to transmit power between two conductive materials separated by a dielectric medium Sharif and Sodagar (2022b). In this system, the transmitter and receiver each consist of a pair of plates that form capacitors, with the intervening space or material acting as the dielectric. When an Alternating Current (AC) is applied to the transmitter's plate, it generates an oscillating electric field that induces a corresponding current in the receiver's plate, thereby transferring power Sharif and Sodagar (2022b).

capacitive coupling WPT has gained attention for implantable medical devices due to its potential for miniaturisation and reduced sensitivity to alignment compared to other WPT technologies Narayanamoorthi (2019b); Tamura et al. (2022). The thin and flat nature of capacitive plates makes them suitable for integration into small implants where space is at a premium. In recent years, capacitive coupling WPT has been utilised to power various wearable and implantable devices because of its simplicity and flexibility Sedehi et al. (2021). In addition, capacitive coupling can be advantageous in scenarios where magnetic fields need to be minimised, such as in patients undergoing Magnetic Resonance Imaging (MRI) Erfani et al. (2018a).

Although capacitive coupling WPT offers benefits for powering biomedical devices, it faces significant challenges when applied to implantable devices. The contact impedance between the capacitive plates and biological tissue is a major issue, which

can significantly affect power transfer efficiency Erfani et al. (2017a). Sudden changes in this contact impedance lead to power losses and generate high electric fields that may unintentionally stimulate nerves or muscles Erfani et al. (2018a). Additionally, capacitive plates placed directly against the skin for long-term applications can cause tissue irritation and damage Hossain et al. (2021). These factors limit the practical usability of capacitive coupling for implants that require consistent, long-term power delivery Mustapa et al. (2019).

This work presents a novel WPT system capable of transmitting power directly into a standard medical stent in the brain. The system provides a power budget exceeding 100 mW before reaching safety limits, sufficient for high-fidelity neural activity recording circuits, multiple biosignal recordings, and neuromodulation circuits. Designed for long-term applications, the external unit can maintain a naturally loose contact with the skin. Based on our research, this work offers the highest WPT efficiency for a stent-based biomedical implant without requiring additional space or modifications to the structure of a typical stent. By providing these benefits, the proposed system is an ideal power transfer solution for an endoECoG device. With this WPT system, the endoECoG device can be fully wireless without a lead wire or an extra implant unit for power and data. The proposed system utilises a high-efficiency inductive link and a more flexible capacitive link to deliver power into the brain area. By employing a subcutaneous relay, the system effectively addresses the challenge of plate-to-tissue contact impedance and offers a relatively minimally invasive solution for the endoECoG device.

Fig. 5.1 shows the structure of the proposed WPT system within the endoECoG application. The system comprises three main components: an external unit, a subcutaneous passive relay, and the receiver stent. The external device includes a power source, e.g., a battery, control circuits, and a coil for near-field inductive WPT to the subcutaneous relay. The external unit is worn over the head and uses a magnet for precise alignment with the subcutaneous relay coil beneath the scalp, ensuring efficient power transfer.

The subcutaneous passive relay is formed as a thin metal film with a silicone coating,

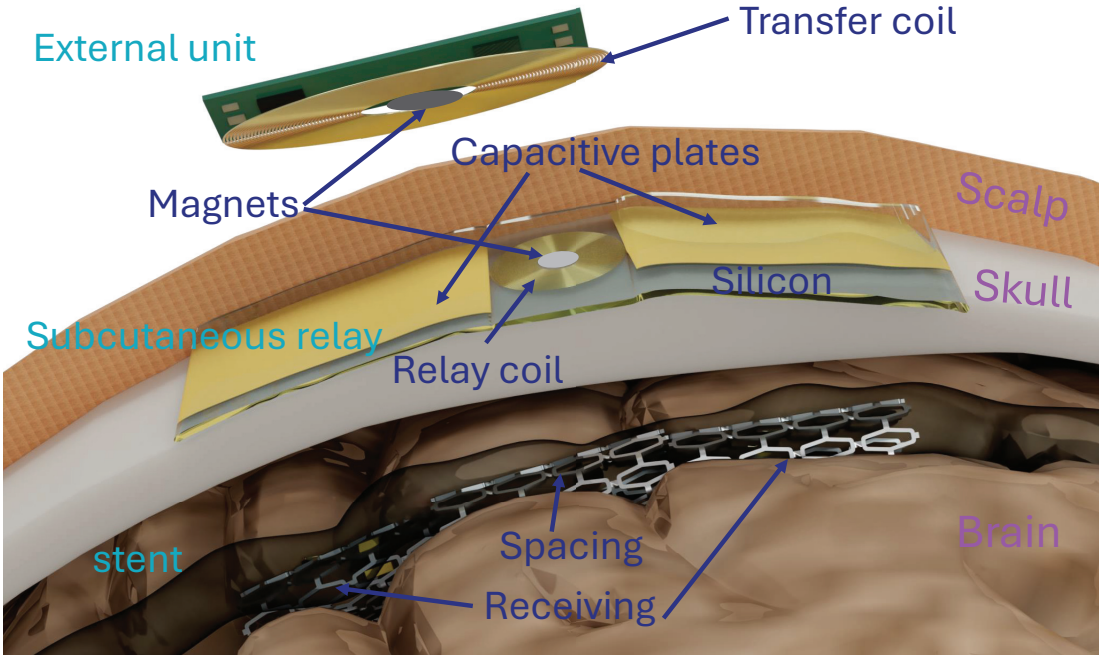

Figure 5.1 – Conceptual design of the proposed WPT system for endoECoG device. The relay is under the periosteum and above the skull. The relay is a passive device embedded in a thin silicone film. There is a magnet pair to align the external coil and the really. The external unit aligns with the relay using a magnet. The stent has three sections: the two ends are the power-receiving stent (marked as receiving), and the optional middle section (marked as spacing) provides extra space for electronics.

which can be inserted under the periosteum layer of the scalp. Its structure consists of two metal plates serving as capacitive pole pairs and a flat coil in the gap between the two plates. The flat coil receives power through inductive coupling from the external device's coil, then delivers energy using the plates to the stent beneath the relay through the skull via capacitive coupling. This design overcomes challenges related to contact impedance and skin-related issues that plague traditional capacitive coupling methods and brings the transmitter plates closer to the receiver in a minimally invasive manner. The thickness of the metal layer of the relay is less than 35 μm. Depending on manufacturing capabilities, the total thickness of this relay can be less than 0.2 mm, ensuring the recipient's comfort.

The receiver stent is a standard stent with three sections: two sections at the ends acting as the power receiving stents and a middle section between them to separate the

two receiving pairs and provide space to house the functional circuits. The middle section is unnecessary for obtaining power, as it only provides a gap between the receiving pairs. The two end sections of the stent act as capacitive poles corresponding to the two capacitive plate poles in the subcutaneous relay. The harvesting circuits can reside in the middle section or be embedded in one end of the stent section, using a short lead wire to connect to the other section. Depending on the stent's length requirements and the depth of its position, the passive relay plate pairs need to have matching lengths and sizes to maximise power transfer efficiency. This design does not require structural modifications to the stent, preserving its validated long-term safety, mechanical integrity, and medical functionality. The power-harvesting circuits for capacitive coupling contain only diodes and capacitors. These components have a very small volume and size, allowing them to be integrated with sensing or stimulation circuits and miniaturised to fit within the stent, enabling a fully functional smart stent without a lead wire.

The design aims to continuously deliver over 40 mW of power into the stent placed in the superior sagittal sinus to meet continuous signal monitoring requirements. When there is a requirement for stimulation, the system can deliver over 100 mW of power without reaching the safety limit. With this design, the subcutaneous relay addresses challenges related to contact impedance between the capacitive pole plates and the tissue. As the capacitive pole plates are under the scalp and embedded in a biocompatible material that has been proven for long-term safety, there is no concern about skin damage caused by the capacitive pole plates during extended use. The external device uses classical near-field inductive coupling, and a single pair of magnets helps align the external device with the relay. The size and weight of the external device can be easily managed with current manufacturing technology, allowing it to meet both functional and aesthetic requirements and ensuring high acceptance by recipients for daily wear.

5.2 Results

To test and verify this proposed WPT system's feasibility, performance and safety, we conducted four stages of experiments, including relay-to-stent capacitive WPT efficiency testing, whole system WPT power budget and efficiency testing, finite element simulation verification and safety simulation. The experiments setup and testing protocols are detailed in Section 5.3, and the main results are described here.

5.2.1 Relay to stent capacitive WPT efficiency

Fig. 5.2 shows the relay to stent capacitive WPT efficiency testing results. Fig. 5.2(a) shows the optimal parameters for a 10 mm stent section length at different depths (D_t). From the results, we observe that for capacitive coupling WPT through bone, two frequency windows can transmit power from the relay to the stent with higher efficiency: one window between 34 MHz and 47 MHz and another window around 190 MHz to 700 MHz. When the stent depth is $D_t = 1$ mm, we achieve a peak efficiency of 20.86% with a stent section gap of $L_{sgp} = 15$ mm, capacitive relay plate size of $L_{cp} \times W_{cp} = 10 \times 12$ mm^2, plate gap distance $L_{cgp} = 15$ mm, at a frequency of 46.56 MHz. For other stent implantation depths, the optimal plate size, plate gap, and stent gap are shown in Fig. 5.2.

The results show that when the stent depth is less than 10 mm, the plate gap should equal the stent gap, and the gap distance should be longer than the stent section length. When the stent implantation depth is greater, a larger capacitive plate is needed to achieve higher efficiency. For deeper implanted stents, we need a larger gap at the stent side and a smaller gap at the plate side. When the stent depth reaches 30 mm, the peak efficiency drops to 12.37% with a much larger plate (40×18 mm^2) and a stent gap distance of 20 mm. We believe that further increasing the plate size may help the system achieve higher efficiency at this stent implantation depth, but doing so would make the implantation of the relay more challenging. It may not be practical via minimally invasive methods in clinical settings. Therefore, our experiment limited the maximum plate size to 40×20 mm^2.

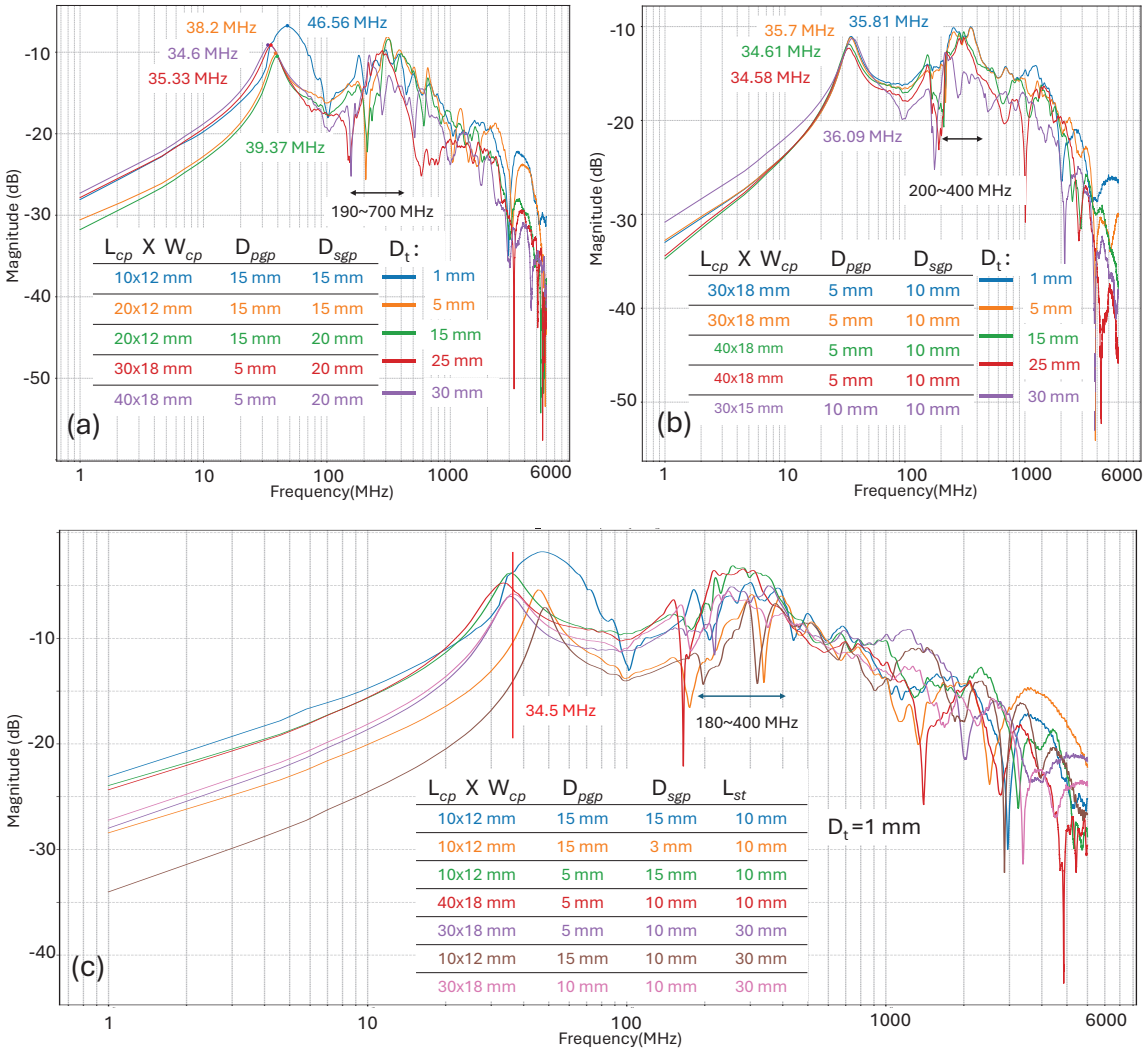

Figure 5.2 – (a) optimal parameters for 10 mm stent section length at a different implantation depth (D_t). (b) optimal parameters for 30 mm stent section length at different implantation depths. (c) Power transfer efficiency changes trend when implantation depth is 1 mm. In the figure table, L_{cp} is the length of the capacitive plate, W_{cp} is the width of the capacitive plate, D_{pgp} is the gap distance of the capacitive plates, D_{sgp} is the gap distance of the two receiving stents, L_{st} is the length of the receiving stent section. All the dimension symbols are illustrated in Fig. 5.8, and we use the same symbols for the paper.

Fig. 5.2(b) shows the testing results of the optimal parameters for a 30 mm stent section length at different depths (D_t). Compared to the 10 mm stent sections, the 30 mm stent sections exhibit lower efficiency. When the stent depth is 1 mm, the maximum efficiency is 7.9% with a plate size of 30×18 mm^2, plate gap of 5 mm, and stent gap of 10 mm. The peak efficiency is achieved at 35.81 MHz. We also observe two high-efficiency windows for these longer stent sections: the first window around 36 MHz and the second between approximately 220 MHz and 400 MHz. The average efficiency is much lower than the 10 mm stent sections, but the parameter variance is smaller. When the stent depth increases from 1 mm to 30 mm, the efficiency only drops to 7.47%. When the stent section length is 30 mm, the plate sizes are close to our set maximum size, and when the depth is 30 mm, a smaller plate can achieve high efficiency. For the 30 mm section length, the peak efficiency frequency is in the higher frequency window, but we prefer to use the lower frequency window for our proposed system. We chose the lower frequency window because for endoECoG, the stent is in the SSS, and the depth is usually less than 2 mm. When the depth is shallow, the peak in the higher frequency window is very close to the peak in the lower frequency window. Additionally, waveform-generating circuits and power amplifier circuits have higher efficiency for our proposed system when operating at frequencies below 100 MHz.

Fig. 5.2(c) shows the efficiency change when the stent depth is fixed at 1 mm, illustrating the change of stent length and the gap with varying capacitive plate size and gap. From the results, we observe that when the stent section length is 10 mm, the best efficiency is achieved when the stent gap equals the capacitive plate gap. When the stent gap becomes shorter, the maximum efficiency drops significantly, but the maximum efficiency frequency remains similar. Suppose the stent gap is kept unchanged and the capacitive plate gap is shortened. In that case, the maximum efficiency drops less than when changing the stent gap, but the maximum efficiency frequency decreases. If we keep the capacitive plate gap unchanged but increase the capacitive plate size, we find that the maximum efficiency is close to the maximum efficiency with a similar plate gap but significantly different plate sizes; moreover, a

larger plate size compared to the stent size results in lower efficiency.

For a 30 mm stent section length, similar to the 10 mm stent section length, the efficiency is high when the capacitive plate length equals the stent section length. Unlike the 10 mm stent, the efficiency for the 30 mm stent section drops less when the gap distance changes, but when the plate size becomes smaller, the efficiency drops sharply with the frequency shifting to higher frequencies. From the results, we can estimate that when using a 30 mm stent section, if we further increase the stent section gap and the plate gap, we may achieve higher efficiency, but this would exceed the dimensions of our testing platform and a larger plate may not be practical in clinical applications.

The relay-to-stent capacitive coupling power transfer results indicate that the capacitive plate in the relay should have a length equal to the length of the stent section and a width about 2—3 times the diameter of the stent. The gap distance of the stent section should be greater than 10 mm, and longer stent sections do not significantly increase power transfer efficiency.

5.2.2 Full system efficiency result

Table 5.1 presents the full system testing results using the optimal parameters obtained from the relay-to-stent capacitive WPT efficiency tests. The detailed experiment setup and how we measure the power input and output are described in Section 5.3. After fine-tuning the PWM duty cycle, the amplifier's LC tank, and the transmission coil, we achieved a 7.26% DC-to-DC transmission efficiency. This DC-to-DC efficiency is calculated using Equ. 5.1. The table also recorded the circuit power consumption for the gate driver and the Microcontroller (MCU), denoted as P_{sys}. The overall system efficiency is 5.25%; however, since the MCU and the gate driver circuits are not designed specifically for this purpose, they contain many components that consume power but do not contribute to our transmission. Therefore, we exclude these power consumptions from our transmission efficiency calculation. When applying this technology to a real-world application, designing a specific chip can reduce

the circuit power consumption below 30 mW and close the system efficiency to the DC-to-DC transmission efficiency.

$$\eta_{\text{trs}} = \frac{P_{\text{rec}}}{V_{\text{in}} \times I_{\text{in}}} \tag{5.1}$$

Table 5.1 – Full system testing result.

Parameter	**Description**	**Value**
f	PWM signal frequency	46.6 MHz
D	PWM duty cycle	48.79%
$L_{\text{CP}} \times W_{\text{CP}}$	Capacitive plate size	10×12 mm^2
D_{pgp}	Capacitive plate gap length	15 mm
L_{st}	Stent section length	10 mm
D_{sgp}	Stent section gap length	15 mm
L_{tr}	Transmission coil inductance	1.18 μH
L_{re}	Receiver coil inductance	1.04 μH
C_{d}	Gap distance between coils	8 mm
V_{in}	Amplifier input DC voltage	13.5 V
I_{in}	Amplifier input current (RMS)	45.5 mA
P_{t}	Transmission power	614 mW
P_{sys}	Circuits power consumption	235 mW
P_{rec}	Receiving power	44.6 mW
η_{sys}	System efficiency	5.25%
η_{trs}	Transmission efficiency	7.26%

5.2.3 Finite Element simulation result

To verify the whole system performance under a more controllable environment with real anatomical structure, we did a finite element simulation with our proposed system and compared it with the experiment results. Table 5.2 compares our finite element simulation results with our experimental results. Both the finite element simulation

and our experiment used the same setup, including plate sizes, gap distances, coil sizes, and distances. In our finite element analysis, the AC-to-AC efficiency of our proposed system is 9.1%. By estimation, our experiment achieved an AC-to-AC efficiency of 13.35%. We cannot directly compare the AC-to-AC efficiency or DC-to-DC efficiency because we can only obtain AC-to-AC efficiency in the finite element simulation due to the absence of amplifier circuits. In the experiment, measuring the AC input and output power requires an RF power meter, which we do not have.

The table shows that the experimental results demonstrate higher efficiency than the simulation. We believe the main reason is that the silicone layer in the simulation is much thicker than in our design and experimental setup. We aim to keep the insulating coating on the capacitive plates as thin as possible for our capacitive coupling relay. In the experiment, we used silicone adhesive as the coating and kept it as thin as possible, with a final thickness of around 4–8 μm.

In the simulation, since the curved surface covers over 800 mm^2, creating a fine grid smaller than 2 μm would result in more than 2.3 billion cells, requiring high-performance computing resources and significant time to obtain results. Therefore, instead of simulating with a thinner coating layer, we varied the coating layer thickness to verify how the film thickness affects efficiency. We performed two rounds of new simulations: the first with a 0.8 mm silicone layer and the second with the same 0.4 mm silicone layer, but we moved the relay metal part only 0.08 mm above the bottom of the silicone film. We adjusted the grid to 0.04 mm to ensure that the solver accurately captures the structure of the design.

From the results, we observed that with a thinner film, the simulation results are close to our experimental measurements. This indicates that a thinner layer of insulating material increases the transmission efficiency.

5.2.4 Safety verification results

To verify this proposed WPT system's safety, SAR and temperature rise analysis were conducted using finite element simulation results.

Table 5.2 – Simulation result compared with the experiment result.

	Input Power (DC)	**Input power (AC)**	**AC-AC efficiency**	**DC-DC efficiency**
Experiment	614 mW	491.2 mW†	13.35%	7.26%
Simulation (0.4 mm)∗	–	600 mW	9.1%	–
Simulation (0.8 mm)‡	–	600 mW	7.42%	–
Simulation (asymmetry)ᵀ	–	600 mW	10.71%	–

(†) AC power is estimated by the input power of the amplifier and 80% efficiency of the power amplifier.
(∗) The thickness of the silicone insulation layer is 0.4 mm, and the metal layer is in the middle.
(‡) The thickness of the silicone insulation layer is 0.8 mm, and the metal layer is in the middle.
(ᵀ) The thickness of the silicone insulation layer is 0.8 mm, and the metal layer is 0.04 mm above the bottom (close to the skull) of the silicone insulation.

Table 5.3 – SAR analysis result.

Tissue	**Peak Spatial SAR (W/kg)**	**Mass-Averaged SAR avg.10g (W/kg)**
Skin	1.6	0.161
Skull	0.58	0.068
CSF	0.024	0.023
Cerebellum	7.7×10^{-4}	1.4×10^{-4}
Grey matter	3.35×10^{-3}	2.7×10^{-3}
Total	1.6	0.13

Table 5.3 presents the WPT results obtained with an input power of 600 mW. The **Peak Spatial SAR** is computed over a specific mass using moving constant-mass cubes, as specified in IEEE/IEC 62704-1. The **Mass-Averaged SAR** calculates the 10-gram average of the electric field according to Annex P of ISO/TS 10974.

The results show that the WPT in skin tissue is the highest among all tissues in our system. With an input power of 600 mW, the WPT values for all tissues remain below the safety limit of 2 W/kg, ensuring compliance with regulatory standards. We also observed that the skin tissue's peak spatial WPT value is much higher. The reason is the skin on the scalp is very thin, and the electric magnetic (EM) fields are concentrated at the area between the transmission coil and the relay receiving coil, which makes some parts of the skin have a high peak spatial WPT, but with 10-gram averaged mass, the WPT level becomes lower.

Fig. 5.3(a), (b), and (c) illustrate the spatial distribution of the WPT within the head model. The peak spatial WPT is concentrated beneath the external coil and above the skull. The area below the subcutaneous relay exhibits low WPT values, indicating minimal exposure in deeper tissues.

Fig. 5.3(e) shows the results of the temperature rise simulation. Our simulation shows no significant temperature rise in any tissue after 1,800 seconds (30 minutes) of continuous operation. The graph displays the final temperature distribution at 14,400 seconds (4 hours). The bottom part of the head model includes a temperature projec-

tion map. The light and dark yellow volumetric areas over the head represent regions where the temperature rise exceeds 0.1°C and 0.2°C, respectively. The temperature increase occurs only at the relay and the space above the relay. On the implant side, no temperature rise is observed.

These results demonstrate that our system is safe to operate and will not cause any damage to the surrounding tissues due to excessive heating or electromagnetic exposure. The low WPT values and minimal temperature rise confirm the feasibility of the proposed wireless power transfer system for long-term biomedical implant applications.

5.3 method

5.3.1 System architecture

Fig. 5.4 illustrates the functional circuit blocks of the proposed system, which represent what circuits are included in the external unit, subcutaneous relay, and the implanted stent-based device.

The external unit sits outside the body. It consists of a rechargeable battery, a PMU, a MCU, a DC to DC booster, a Class-E amplifier, and gate driver circuits for the GaN transistor in the Class-E amplifier, and a transmission coil. The rechargeable battery serves as the system's energy source. Depending on the required battery life and weight considerations, the battery may be placed at another location to ensure that the external unit worn over the head remains lightweight. The PMU provides multiple DC rails for other components in the external unit and manages the charging and discharging of the battery.

The MCU acts as the system's control centre. It provides control signals to the DC-DC booster to dynamically adjust the transmission power. It generates a PWM signal for the driver circuits used in inductive power transmission. Instead of using high-frequency signal generation circuits, We also use this MCU to generate the PWM

signal, as it significantly reduces the complexity and offers an easy way to adjust the signal frequency and duty cycle. The distance between the transmission and receiving coils in near-field inductive coupling power transmission affects the resonant frequency. For a typical inductive coupling system, we can add a tuning capacitor to improve the efficiency, but for our proposed system, the receiving coil is in the passive relay and cannot be fine-tuned to match variations in coil distance. Therefore, we equipped the external unit with the ability to adjust the frequency on the fly to maximise power transfer efficiency. Utilising this MCU-based design, we can achieve high efficiency by dynamically fine-tuning the waveform and frequency and reducing the external unit's size and weight.

The DC-DC booster provides the power amplifier's boosted DC voltage, with the MCU's voltage level controlled. This design enables the system to dynamically adjust the output power to meet the requirements of the implant. The driver circuits receive the PWM signal from the MCU and match the impedance and voltage levels to drive the power amplifier. The power amplifier is a Class-E amplifier consisting of a GaN transistor to ensure high efficiency at the desired frequency. The subcutaneous relay contains no active components and can be manufactured using a single metal film layer. This relay serves as an energy conduit, converting inductive coupling to capacitive coupling to allow typical stents to receive power. On the implant side, the two sections of the stent serve as the capacitive poles. Simple rectifier circuits with ultra-low-capacitance Schottky diodes convert the AC to DC and supply it to a buck-boost converter that provides regulated DC power for the sensing or stimulation circuits.

This design achieves high-efficiency power transfer with simplified circuits, making the external unit small and lightweight. With the current manufacturing ability of integrated circuits, all components in this design for the implant part can be miniaturised to fit within the stent without affecting blood flow, enabling a fully functional endoECoG device without a lead wire.

5.3.2 System Modeling

Fig. 5.5 shows the comprehensive circuit model of this power transfer system. The system transmission efficiency depends on the inductive link to the relay and the capacitive coupling to the stent implant. Here, we define the inductor coupling factor between L_1 and L_2 as K, and the Laplace variable as s. Equ. 5.2 shows the system transfer function.

We derive the transfer function using Kirchhoff's Voltage Law (KVL). As the capacitance between the transmission coil and receiving coil is very small, we simplify the function by ignoring C_{T_S1} and C_{T_S2}. The transfer function is derived based on the current through three loops: the transmission coil loop, the middle network loop, and the load loop.

We define the current through L_1 as I_1 and the current through L_2 as I_2. The impedance of inductors is calculated as shown in Equ. 5.3, and the impedance of capacitors is calculated as shown in Equ. 5.4. The mutual inductance of L_1 and L_2 is given by Equ. 5.5. The equation for the transmission coil loop is shown in Equ. 5.6, the equation for the middle network loop is shown in Equ. 5.7, and the load loop equation is given in Equ. 5.8.

By solving Equs. 5.6, 5.7, and 5.8 with I_1, I_2, and V_{Load}, we obtain the transfer function. As the function is complex, we use Python's Symbolic Mathematics Solver (SymPy) to solve it. The fully solved transfer function is attached as code in the appendix. The output can be used for circuit simulation and parameter estimation to determine tissue capacitance and other parameters.

$$H(s) = \frac{V_{\text{Load}}(s)}{V_{\text{in}}(s)} \tag{5.2}$$

$$Z_L(n) = s \cdot L_n \tag{5.3}$$

$$Z_C(n) = \frac{1}{s \cdot C_n} \tag{5.4}$$

$$M = K \cdot \sqrt{L_1 \cdot L_2} \tag{5.5}$$

$$\mathrm{eq}_{t\_\mathrm{loop}} = \mathrm{Eq}\left(V_{\mathrm{in}} - I_1 \cdot R_{\mathrm{L1}} - I_1 \cdot Z_{\mathrm{L1}} - I_1 \cdot Z_{\mathrm{CL1}} - I_2 \cdot Z_{\mathrm{M}},\ 0\right) \tag{5.6}$$

$$\begin{aligned}
\mathrm{eq}_{n_\mathrm{loop}} = \mathrm{Eq}\Big(& - I_1 \cdot Z_{\mathrm{M}} - I_2 \cdot Z_{\mathrm{L2}} - I_2 \cdot Z_{\mathrm{CL2}} - I_2 \cdot R_{\mathrm{L2}} \\
& - I_2 \cdot R_2 - I_2 \cdot \Big(R_{\mathrm{T1}} + R_{\mathrm{T2_1}} \\
& + R_{\mathrm{T3_1}} + R_{\mathrm{T4_1}} + R_{\mathrm{T2_2}} + R_{\mathrm{T3_2}} \\
& + R_{\mathrm{T4_2}}\Big) - I_2 \cdot \Big(Z_{C_{T1_1}} \\
& + Z_{C_{T2_1}} + Z_{C_{T3_1}} + Z_{C_{T4_1}} \\
& + Z_{C_{T1_2}} + Z_{C_{T2_2}} + Z_{C_{T3_2}} + Z_{C_{T4_2}} \\
& \quad + Z_{C_{T1_3}} + Z_{C_{T2_3}} + Z_{C_{T3_3}} + Z_{C_{T4_3}} \\
& + Z_{C_{T1_4}} + Z_{C_{T2_4}} + Z_{C_{T3_4}} + Z_{C_{T4_4}}\Big) \\
& - V_{\mathrm{out}},\ 0\Big)
\end{aligned} \tag{5.7}$$

$$\mathrm{eq}_{L\_\mathrm{loop}} = \mathrm{Eq}\left(V_{\mathrm{out}}, I_2 \cdot (R_{12} + Z_{C_L})\right) \tag{5.8}$$

5.3.3 Experiment setup

To validate the design and test the performance of our WPT system, we built a testing platform using several sections of human coronary stents (SYNERGY™ XD from Boston Scientific), a section of bovine bone, and a section of bovine vessel. The bovine tissues were freshly purchased from a local butcher and replaced every 24 hours to maintain their water content and freshness. Fig. 5.6(a) shows the experimental

setup design, and Fig. 5.6(c), (d), (e), and (f) display the actual testing platform. From Fig. 5.6, we use the same symbol to indicate the dimension; the meaning of the symbol are:

— L_{cp}: capacitive plate length,

— W_{cp}: capacitive plate width,

— D_{pgp}: gap distance between the capacitive plate pair,

— B_{t}: Bone tissue thickness,

— D_{t}: Distance between the bottom of the bone to the top of the receiving stent,

— L_{st}: receiving stent length,

— D_{sgp}: gap distance between the receiving stent section pair, and

— C_{d} The distance between the transmitting coil and receiving coil and it equals to the thickness of the skin tissue.

We 3D-printed a container, see Fig. 5.6(c), equipped with fixtures to hold the bone tissue securely and control the stent's distance and position. The container was filled with saline solution to simulate the dura and CSF properties. The first step of the experiment involved determining the characteristics of the power transfer system from the relay to the stent. This step allowed us to identify the optimal frequency and the optimal width and length of the capacitive plates to match specific lengths of the stent at certain distances for efficient capacitive coupling power delivery. Based on the results from this initial step, the second step was to verify the performance of the entire power transfer system using the optimal parameters.

In **Experiment Step One**, we used 50 μm thick copper film as the capacitive plates. We cut the film to the designed dimensions (shown as length L_{cp} and width W_{cp} in Fig. 5.6) and soldered a 50 Ω coaxial cable to each pair of film plates. We then coated one side of the film with an electronics-grade silicone adhesive (Chip Quik

EGS10C) and attached the plates to the bone. The silicone adhesive ensured good and stable contact between the plates and the bone, provided electrical insulation, and maintained stable dielectric properties, simulating the silicone coating in our real-world application. We also tested the optimal gap distance (shown as D_{pgp} in Fig. 5.6) between the plates during the experiment. The coaxial cables were connected to impedance-matching networks to match the impedance to 50 Ω, then connected to port A of the VNA (Rohde & Schwarz ZNLE6).

We soldered coated gold wires separately to each section for the stent sections, with the other end of the short wire soldered to a 50 Ω coaxial cable. After soldering, we coated all the solder joints with epoxy to prevent shorting and strengthen the connections. The open ends of the coaxial cables were also sealed with epoxy to prevent saline from entering and altering their properties. These coaxial cables were connected to impedance-matching networks to match the impedance to 50 Ω, then connected to port B of the VNA.

After preparation, we inserted the stent into the bovine vessel and placed it into our 3D-printed container filled with saline. The container featured marker points and fixtures to ensure proper alignment and control of the stent's position. We recorded the VNA readings at different stent positions. We repeated these steps for each stent length to determine the optimal parameters for different stent lengths; the detailed testing procedure is described in the testing protocol section.

In **Experiment Step Two**, we selected the plate size and gap distance that demonstrated good performance based on the results from Step One. We then connected the coaxial cable attached to the copper film to a flat coil with an inductance close to the calculated optimal value. This configuration simulated the entire relay and implant part of the proposed system.

For the **external part**, we used an MCU development board (NXP KV5x) to generate the desired PWM signal. We manufactured a custom PCB featuring a gate driver (LMG1020) and a Class-E amplifier with a GaN transistor (EPC2019). The output of the amplifier was connected to a flat PCB coil serving as the transmission coil.

On the **implant side**, we connected the coaxial cable to a bridge rectifier formed by four low-capacitance Schottky diodes (NSR01F30). We used a current source(Stanford Research Systems CS580) to simulate the load and measure the receiving power. The system's input power was measured using the DC power supply (GIGOL DP832) that provided power to our Class-E power amplifier. We set the power supply to a fixed DC voltage and recorded the RMS current shown on the power supply. We use the current source as a variable load to get the maximum receiving power at each setup. We use a computer-controlled multi-function instrument (AD2 from Digilent) to generate a ramp-up control voltage so the current source draws a known current. Then, we read the output voltage from the monitoring port of the current source. The product of the control voltage, control ratio, and monitoring voltage yielded the received power. The maximum power was recorded for efficiency calculation, with the tested power efficiency calculated using Equ. 5.1.

In our testing platform, we used off-the-shelf products that met our requirements but included some features which did not accurately reflect real-world applications. So, we excluded the power consumption of the MCU and the gate driver circuits for the system power transmission efficiency calculation and listed the results separately.

5.3.4 Testing protocol

Fig. 5.7 illustrates our testing procedure, experimental steps, and the methods used for recording results. The testing procedure begins with the selection of stent dimensions. For the application of an endoECoG device, the ideal position for the stent is the SSS, the largest vessel in the brain area. When we position the stent close to the visual cortex and motor cortex regions, the stent length can range from 30 mm to 80 mm, and the diameter is approximately 5 to 8 mm. In our experiments, we used a coronary stent as the material, with a 5.75 mm diameter close to the vessel diameter of the intended application site. For stent length, we tested sections of 10 mm and 30 mm. We tested distances of 1 mm, 3 mm, 5 mm, 10 mm, 15 mm, and 20 mm for the gap length to determine the optimal performance distance. The total length of the stent

area is calculated as (stent section size $\times 2$) plus the gap distance, resulting in tested total lengths ranging from 21 mm to 80 mm, covering the intended application site.

As shown in Fig. 5.7, we have several variables in our experiment: two different stent lengths ($L_{\mathrm{st}} = 10$ mm and 30 mm), eight capacitive plate sizes (L_{cp} and W_{cp}), six gap distances between the two capacitive plates (D_{pgp}), eight distances from the stent to the bone (D_{t}), six gap distances between the two sections of the stent (D_{sgp}), and frequencies from 1 MHz to 6 GHz. We designed the procedure and protocol to find the optimal parameters for this proposed power transfer system based on the theoretical modelling shown in Fig. 5.5. To ensure the accuracy of the VNA measurements, impedance matching is performed for the specified frequency bands (shown in Fig. 5.7).

First, we separately perform a one-port VNA measurement for the stents and capacitive plate. From this step, we obtain rough readings to estimate the impedance and then adjust the matching network to bring it as close to 50 Ω as possible at each band's central frequency. For this step, we only consider the plate size and the gap distance between the two plates on the capacitive plate side. For the stent side, we consider the length of the stent and the gap between the stent sections. Other variables are ignored in this step to simplify the testing.

After this step, we fix the inductance and capacitance values in the matching network for each frequency band, stent, and capacitive plate size, preparing for the next two-port measurement step. During the two-port measurement, each frequency band and each combination of stent and plate size has a matching network configured to ensure the device under test's (Device Under Test (DUT)'s) impedance is close to 50 Ω.

We only tested with the optimal parameters determined from the previous tests for the whole system transmission test. No extra matching network is connected to either the transmitter or the receiving side in this test. For the transmission side, the impedance matching is done with the amplifier side, and for the output, we use the current source to simulate a variable load and get the peak power. For the input power range, We ramped up the input power from approximately 200 mW to 1 W

using 0.5 V voltage steps. We recorded all the peak received power for power transfer efficiency calculations.

Based on our research, this work is the first to use capacitive coupling to deliver power through bone to a stent-based receiver, including bone tissue in the testing. Previous works using capacitive coupling for power delivery to deep implants have used large plates as receivers or only performed modelling without progressing to bone tissue experiments. Testing different stent lengths and matching transmitter capacitive plate lengths and widths provides insight into capacitive coupling with bone tissue in between. The recorded data can be used for this capacitive power transfer system and aid in capacitive data communication or other transcranial power delivery or data communication systems. Following this experiment procedure can ensure the accuracy of the measurement and record correct data.

5.3.5 Finite Element Model and Analysis

To test the system's performance under a more controllable environment and using a realistic skull and scalp structure, we designed the proposed system model and performed finite element simulations and analyses to verify the bench-top testing results. Fig. 5.8 shows the setup of the finite element analysis. The human head model was purchased from the Population Head Model (PHM) Repository (DOI: 10.13099/ViP-PHM-V1.0), a collection of 50 de-identified head models including skin, skull, grey matter (GM), white matter (WM), CSF, cerebellum, and ventricles. We chose a head with average dimensions as the simulation model. We placed our relay model in the middle of the head above the skull. The relay model has the same dimensions as the one in our full-system efficiency bench-top experiments, allowing us to verify the experimental and simulation results.

The capacitive plate size in the simulation is 10×12 mm^2, and the gap between the two plates is 15 mm. The coil in the relay has an outer diameter of 11 mm, 5.5 turns, a pitch of 0.4 mm, and a line width of 0.3 mm. Considering a parasitic capacitance of 0.9 pF and a 9 pF capacitance associated with the connecting plates, this coil is

optimised for a 40 MHz to 50 MHz inductive link without an extra tuning capacitor. For the simulation, we chose gold as the material for the relay and embedded it in a 0.4 mm thick silicone film. We modelled two stent sections with a diameter of 5 mm and a section length of 10 mm, and the gap between the two sections is 15 mm. We set the stent's material to platinum-iridium, a typical material for an endovascular stent. We used a slightly larger outer diameter for the external power delivery coil to increase efficiency. The transmitter coil has an outer diameter of 14 mm, 6 turns, a pitch of 0.5 mm, and a line width of 0.4 mm. The material for the external coil is silver to minimise resistance.

As this simulation involves complex structures with small curved parts, we manually set up an adaptive grid to maintain the fine structure of our simulation object while balancing simulation time and result detail. We used a $3 \times 3\text{mm}^2$ grid as the global mesh grid and then set up a 100mm (length) $\times$80 mm (width) $\times$100mm (depth) region of interest (ROI) box with a 1×1 mm^2 grid for this region. We set a grid with 0.02 mm resolution for the relay to ensure all delicate structures are captured. For the silicone film, we intentionally increased the layer thickness from 0.05 mm to 0.4 mm to reduce the requirement of a fine grid for the curved surface. Then, we set a 0.04 mm grid for the stent film. For the external coil, we used a 0.05 mm grid. In total, we have 194 million cells for this simulation.

The receiving power is measured through an edge sensor across the two sections of the stent. We recorded frequency and time domain data for analysis for field and edge sensors.

5.3.6 Safety

To verify the safety of this power transfer system in practice, we conducted a WPT analysis using finite element simulation results. We performed a temperature rise simulation using Sim4Life software. We extracted the WPT values according to IEEE/IEC 62704-1 for each tissue type and obtained volumetric WPT values in the head area for the WPT analysis of Electrical and 62704-1 (2017). Both peak spatial

WPT and mass-averaged WPT (10 grams) were extracted for analysis. We set a unified 1×1 mm^2 grid for the temperature analysis and used the WPT analysis's electromagnetic (EM) field as the heating source. We set the initial thermal conditions for the skin, skull, and subcutaneous relay to 37°C and for the tissue below the skull to 38.5°C, the average internal temperature of a healthy person. The environmental temperature was set to 25°C. We configured the simulation to allow the tissue to reach a steady-state temperature equilibrium or run for a maximum of 14,400 seconds. We recorded the temperature changes in the grid at 30-second intervals.

5.4 discussion

This work presents a novel system that can transfer power directly to any metal-based, commercially available medical stent without the need for an extra receiving transceiver. The proposed system can deliver over 45 mW of power without reaching safety limits, sufficient to power an endoECoG device and multiple biosignal sensing devices. To our knowledge, this system achieves the highest WPT efficiency for delivering power into a standard stent in the brain area, providing the first proof that a fully wireless endoECoG is feasible in the near future. Incorporating a subcutaneous relay in the proposed system effectively addresses the challenge of low efficiency in WPT to stent-based bioelectronic devices. The subcutaneous relay enhances power transfer efficiency while maintaining a minimally invasive operation. Moreover, since the external device does not require close contact with the skin, the system is suitable for long-term applications, improving patient comfort and compliance.

Our experimental results, obtained using real skin, bone, and vessel tissues, closely match the detailed simulations, validating the accuracy of our models and demonstrating the practicality of further developing this technology. This high degree of correlation between experimental and simulation results underscores the reliability of our approach. In practical applications, the alignment between the relay and the stent can be achieved using medical imaging techniques before and during the surgical procedure, ensuring precise placement. A pair of magnets facilitate the alignment

between the external device and the relay. Notably, the proposed system would likely be MRI-compatible. The stent is a standard device already proven safe for MRI, and the relay is a passive device made of non-magnetised material. When the alignment magnets are temporarily removed, the device can undergo MRI scanning without issues, ensuring patients can still benefit from MRI diagnostics.

Table 5.4 summarises the state-of-the-art research efforts to deliver power into a stent. Our work achieves the highest transfer efficiency without requiring any extra transceiver or specially designed stent. The practicality score (PS) column evaluates the technology's readiness for real-world application, considering factors such as implantation size and invasiveness for brain implantation, power budget, system design for long-term usage, manufacturing challenges, and regulatory approval challenges. Each factor contributes one point to the total practicality score, with a maximum score of 5 indicating the highest practicality and closeness to clinical application. The table shows that our work offers a comprehensive advantage for WPT in fully wireless endoECoG devices.

Based on our research, no stent-based power transfer system is designed for use in the brain area that has been tested *in vivo*. One reason for this is the low practicality of previous works. For example, the study Tamura et al. (2021) achieves over 15% efficiency but requires a 20×60 mm^2 plate attached to the side of the implant, which is not feasible in the brain area without damaging surrounding tissue. The work Tamura et al. (2022) reports 35% AC-AC efficiency; however, the stent used in this study is essentially a metal tube without a stent structure. In practice, implanting such a long tube into the vessels in the brain area is impossible. The research Aldaoud et al. (2018) is designed to use a typical stent to receive power, but bone tissue was not considered in the design and experiments, and an efficiency of 2.6% is too low for real-world applications. Inductive links generally offer higher efficiency, but all the works listed here utilise specially designed stents to function as antennas.

Despite the promising advantages of the proposed system, there are still some unaddressed challenges. Firstly, manufacturing the relay may face difficulties. We aim to make the insulation layer as thin as possible on the bone side, with the total thickness

of the relay being less than 0.5 mm. However, the mechanical properties of such a thin device may make it difficult to manufacture or may render it prone to damage during the surgical procedure. Secondly, although our system shows the highest efficiency reported at over 10%, it is still relatively low compared to the wired system. This lower efficiency impacts the overall system, particularly regarding the external device's battery requirements. When considering long-term applications, balancing the battery life and the weight of the external device will be challenging. For example, assuming an endoECoG device consumes 15 mW continuously, operating it for over 24 hours would require a battery with a capacity exceeding 15 Wh on the external side, which may weigh around 100 g with current battery technology. This could significantly affect the recipient's long-term comfort and willingness to wear the device.

Future work should focus on addressing these challenges. Improving the manufacturing process of the relay, possibly through the development of new materials or fabrication techniques, could enhance mechanical robustness while maintaining the desired thinness. Additionally, further optimising the system's efficiency, perhaps through circuit design improvements or advanced materials, could reduce power requirements and consequently decrease battery size and weight. Exploring energy-efficient operational modes or duty cycling could also help mitigate battery constraints. Our work lays a solid foundation for developing fully wireless, minimally invasive endoECoG devices with significant potential to positively impact patient care.

5.5 Conclusion

This work presented a novel WPT system capable of delivering power directly to a standard medical stent in the brain area without modifying its structure. The proposed system utilises a subcutaneous relay to convert inductive coupling to capacitive coupling, effectively overcoming challenges associated with power transfer efficiency and biocompatibility in stent-based biomedical implants. Our system achieved over 45 mW of power delivery without reaching safety limits, sufficient to power an endoECoG

device and multiple biosignal sensing devices.

Experimental results obtained using real skin, bone, and vessel tissues closely matched our detailed simulations, validating our models' accuracy and demonstrating our approach's practicality. The system maintains minimal invasiveness and does not require close contact with the skin, making it suitable for long-term applications while improving patient comfort and compliance.

Compared to existing methods, our system offers the highest WPT efficiency for delivering power to a standard stent without requiring additional transceivers or specially designed stents. This advancement represents a significant step toward realising fully wireless, minimally invasive endoECoG devices, with the potential to significantly enhance patient care and expand the capabilities of implantable biomedical devices.

In conclusion, the proposed WPT system demonstrates the feasibility of efficiently and safely powering stent-based biomedical implants in the brain area. This technology paves the way for fully wireless, minimally invasive implantable devices, potentially transforming the landscape of neuroprosthetics and biosensing technologies. By enabling high-efficiency power delivery without compromising safety or patient comfort, our work significantly advances wireless biomedical implant systems and opens new avenues for research and clinical applications.

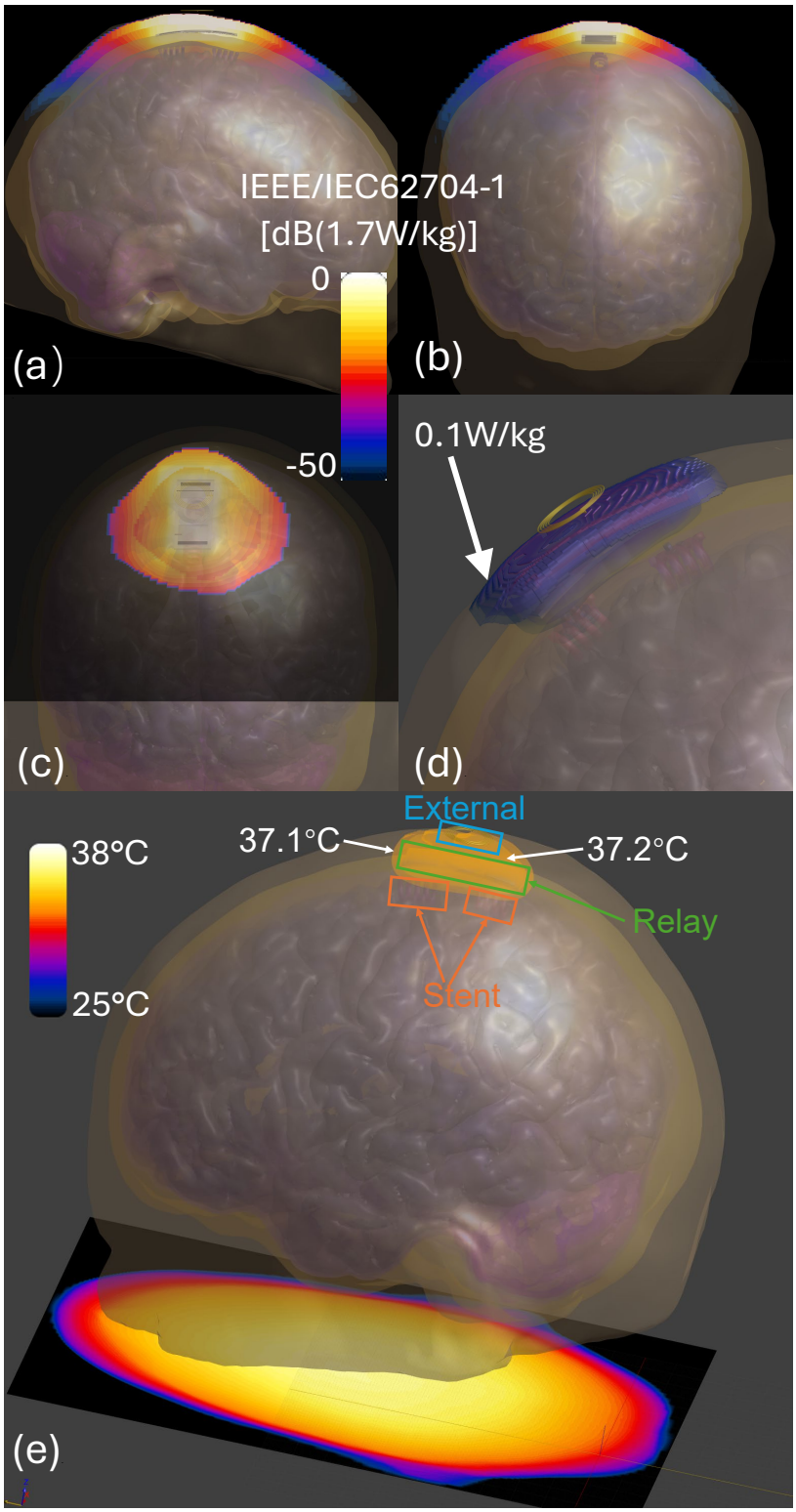

Figure 5.3 – Results of WPT analysis. (a) Right sagittal view of the WPT values. (b) The frontal view shows the WPT values and distribution. (c) Transverse view of the WPT analysis. (d) WPT volume exceeding 0.1 W/kg. (e) Left sagittal view of the temperature rise analysis. The colour map for the WPT analysis is on a decibel (dB) scale, with the maximum value of 1.7 W/kg mapped to the 0 dB reference. The colour map for the temperature analysis uses a linear scale, mapped from 25°C to 38°C.

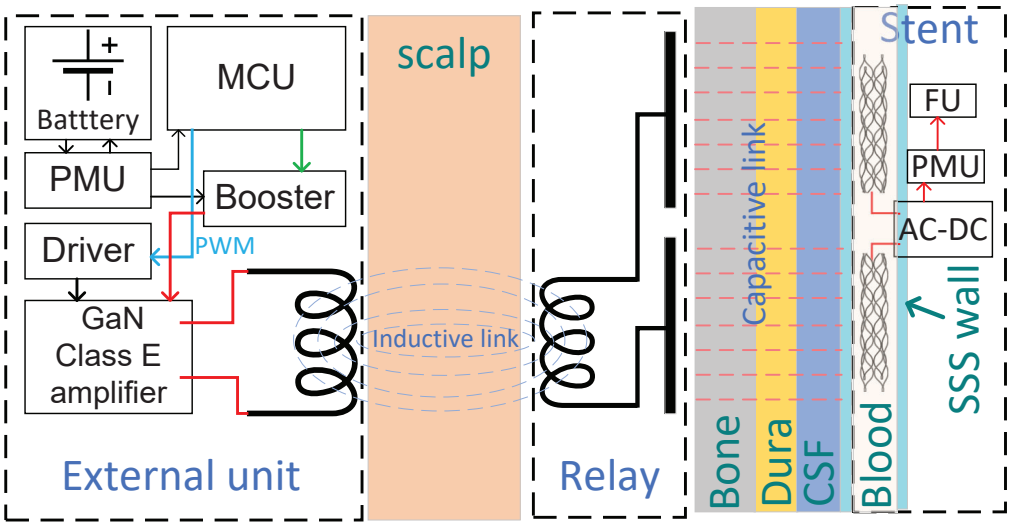

Figure 5.4 – System functional circuits block diagram. MCU: Microcontroller Unit, PMU: Power management unit, Booster: DC to DC voltage booster circuits, Driver: Gate driver circuits. AC-DC: Convert AC to DC to supply to the Power Management Unit (PMU). FU: is a functional circuit unit providing signal sensing, data transmission, and optional stimulation functions. CSF: cerebrospinal fluid. SSS:superior sagittal sinus

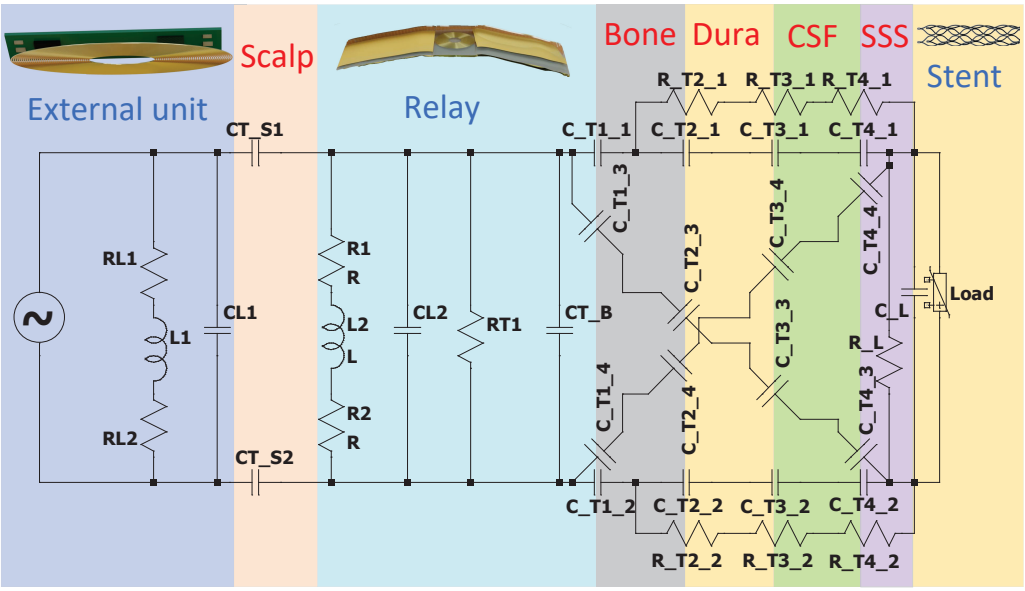

Figure 5.5 – Proposed system equivalent circuit model. L_1: Transmission coil inductance; R_{L1}, R_{L2}: Transmission coil resistance. C_{L1}: Transmission coil parasitic capacitance. C_{T_S1} and C_{T_S2}: Capacitance between the transmission coil and receiving coil. L_2: Receiving coil inductance. R_1 and R_2: Receiving coil resistance. C_{L2}: Receiving coil parasitic capacitance. R_{T1}: Resistance between the two capacitive plates in the relay. C_{T_B}: Capacitance between the two capacitive plates. C_{T1_1} and C_{T1_2}: Capacitance between the plate and bone tissue. R_{T2_1} and R_{T2_2}: Resistance between the bone and Dura tissue. C_{T2_1} and C_{T2_2}: Capacitance between the bone and Dura tissue. R_{T3_1} and R_{T3_2}: Resistance between the Dura and the Cerebrospinal Fluid (CSF). C_{T3_1} and C_{T3_2}: Capacitance between the Dura and CSF. R_{T4_1} and R_{T4_2}: Resistance between CSF and SSS. C_{T4_1} and C_{T4_2}: Capacitance between the CSF and SSS. C_{S_1} and C_{S_2}: Capacitance of the two receiving stents to the SSS. R_L: Resistance between the two receiving stents. C_L: Load capacitance. R_{Load}: Load resistance. C_{T1_3}, C_{T1_4}, C_{T2_3}, C_{T2_4}, C_{T3_3}, C_{T3_4}, C_{T4_3} and C_{T4_4}: Capacitances associated with each capacitive plate in the relay to the far-side receiving stent SSS across the Bone, Dura, CSF and SSS.

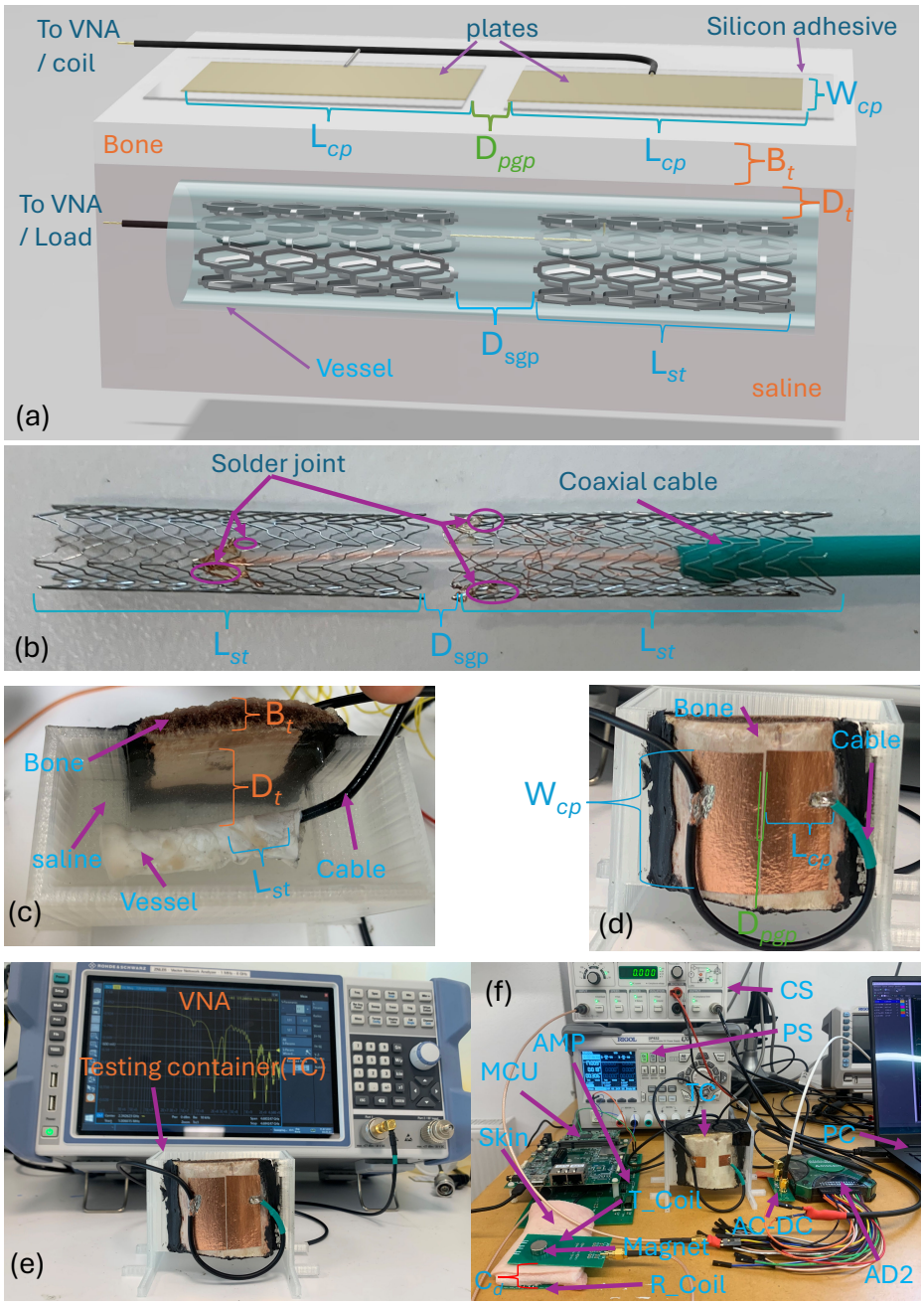

Figure 5.6 – Experiment setup illustration. (a) experiment setup 3D model. (b) Shows the stents we used in the experiment with the cable connection. (c) The actual setup will be with the vessel, bone, and saline. When running the experiment, we have a clamp cover to clamp the stent to a position with designed D_{t} and D_{sgp}. The cover has been removed in this figure to show the internal structure. (d) The actual capacitive plate with the connection cable is shown. (e) shows the overview of the 3D printed testing container with our testing Vector Network Analyser (VNA). (f) shows the full system efficiency testing setup with the MCU-based PWM generator, Gate driver and Power amplifier board(AMP), transmission coil (T_Coil), receiving coil (R_Coil), testing power supplier (PS), AC to DC circuits (AC-DC), and the voltage-controlled current source (CS) as the load to measure peak harvested power. The data collection and load control device, the AD2 device, and the PC used to program the MCU and connect the AD2 device are also shown in the photo.

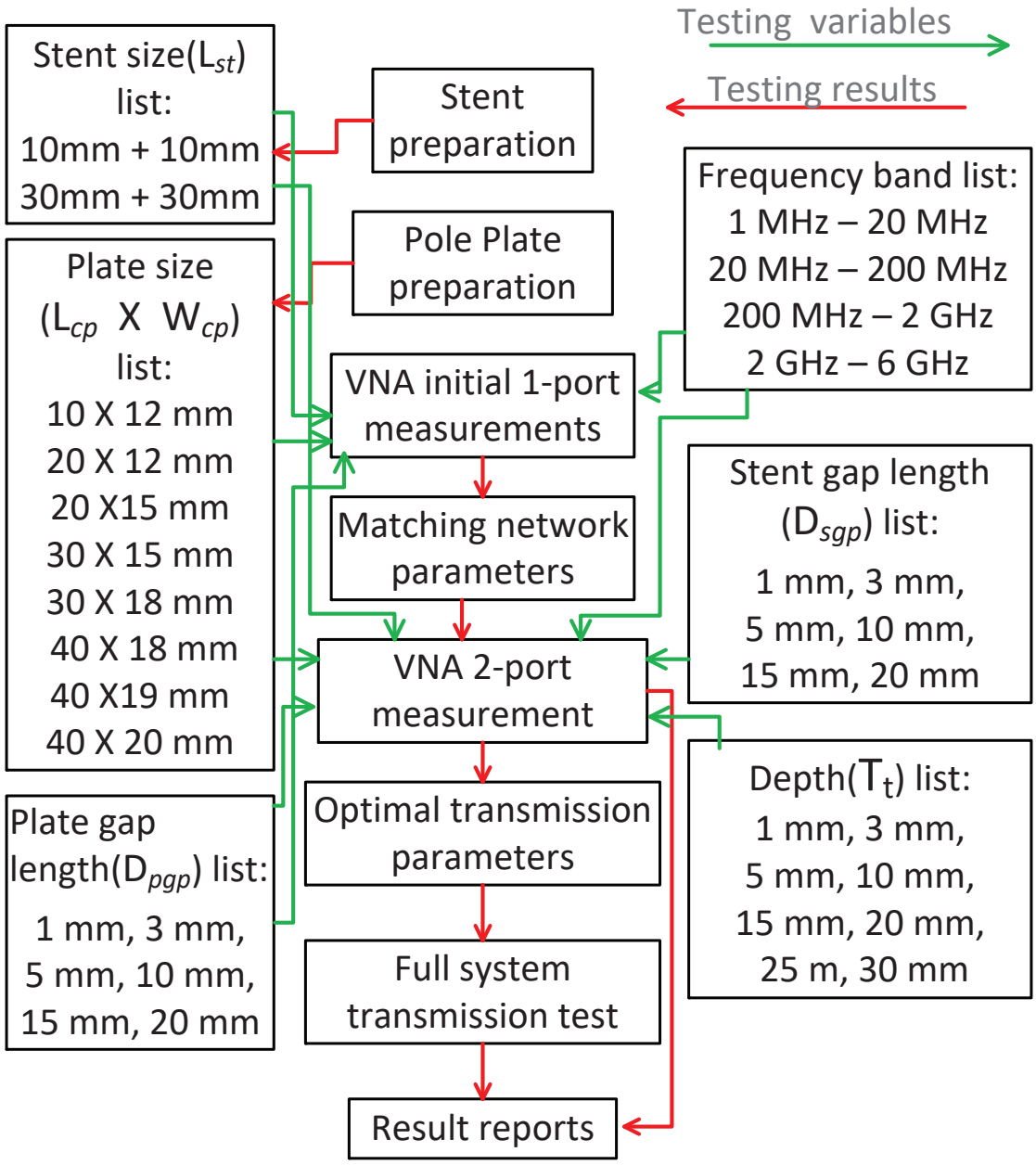

Figure 5.7 – Flow chart shows our testing procedure and parameters we tested during the experiment stage.

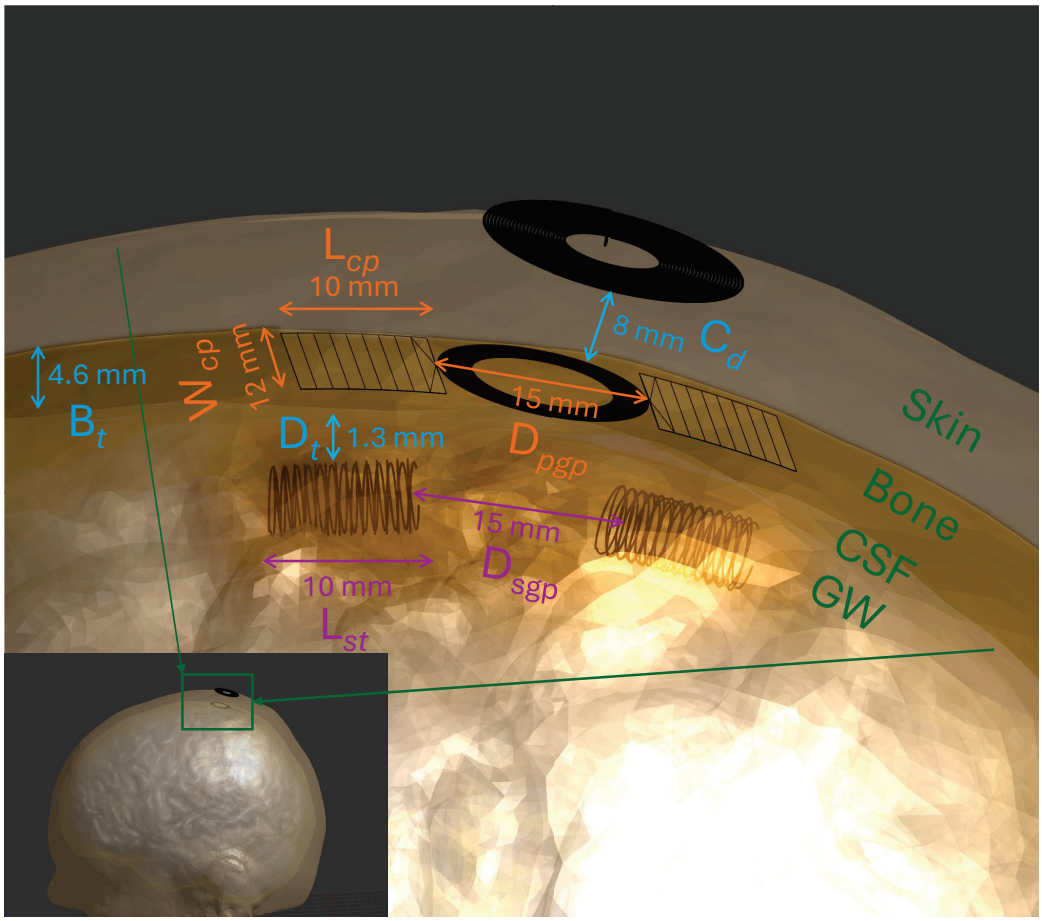

Figure 5.8 – Finite element analysis and safety verification setup. Transmission efficiency finite element analysis and safety verification setup. The bottom left corner shows the head model we used for the simulation and the position of our system. The main graph shows the dimensions of the external coil, relay, and stents.

Table 5.4 – Metrics against state-of-the-art.

Reference	Stent-based	Special Stent	Modality	Frequency (MHz)	Receiving Power (mW)	DC-DC Efficiency (%)	AC-AC Efficiency (%)	Testing Tissue	Transmission Depth (mm)	Practicality score	SAR
This work	Y	N	Capacitive relay	45.6	45*	7.26	13.35	Vessel, Bone, Skin	14	5	0.16
Aldaoud et al. (2018)	Y	N	Capacitive	260	1.37†	<1.04‡	2.6	Muscle	15	3	1.38
Aldaoud et al. (2018)	Y	N	Inductive	4	9.5†	<1.14‡	1.9	Muscle	30	2	0.06
Tamura et al. (2022)	Y	Y	Capacitive	434	100†	<14‡	35	Skin, Fat, Vessel	5	1⊤	2
Tamura et al. (2021)	N	–	Capacitive	308	16.1†	<18.4	46.2	Skin, Fat	5	1	–
Shah et al. (2022)	Y	Y	Inductive	915	34.4†	<0.24‡	1.2	Minced Pork	Far Field	3	2
Xu et al. (2024)	Y	Y	Acoustic	1.4	10†	<1	–	Simulation Only	15	3	–
Haeberlin et al. (2014)	N	–	Optical	–	2.5⋆	<0.2	–	Skin	3	1⊤	–

(∗) DC power.
(†) AC power.
(‡) Estimated value by calculation, not reported in origin paper.
(⊤) Not designed for head area.
Practicality score: higher number denotes the technology is close to the application.

Chapter 6

An Artificial Hair-electordes For Leadless Ambulatory Electroencephalogram

This chapter introduces a novel conductive hair-electrode system tailored for continuous, long-term ambulatory EEG monitoring. Each hair-electrode is an electrically conductive artificial hair strand anchored in a biodegradable follicle, enabling minimally invasive scalp integration and eliminating the need for gels or bulky headgear. A lightweight, wireless clip wearable further enhances user comfort and mobility. Benchtop experiments in a phantom environment using fresh pork tissue showed that our hair-electrodes capture high-quality EEG signals comparable to traditional wet electrodes while addressing significant drawbacks such as skin irritation, mechanical pressure, and conspicuousness. These findings highlight the potential for an unobtrusive and user-friendly EEG solution that could significantly improve long-term neurophysiological monitoring in clinical and research settings.

6.1 Introduction

Ambulatory electroencephalogram (EEG) monitoring is rapidly becoming an essential tool in both clinical and research contexts, especially for conditions such as epilepsy, sleep disorders, and a wide range of neurological dysfunctions that may only manifest sporadically or under specific conditions Seneviratne and D'Souza (2019). Capturing these transient events often requires extended, continuous recording of brain activity in naturalistic environments over several days or weeks. However, traditional EEG systems have long been hindered by the limitations of existing electrode technologies, which do not adequately meet the needs of long-term monitoring. Wet electrodes, for instance, have provided high-quality signals due to the application of conductive gels or saline solutions that facilitate low-impedance contact with the scalp. Despite this advantage, their reliance on messy and easily drying conductive media significantly complicates the recording preparation process. The gels or solutions used can dry out over time, causing signal degradation and necessitating repeated adjustments or reapplication, which is disruptive and uncomfortable for the wearer. Moreover, the gel-based setup is cumbersome and requires skilled personnel for proper placement, making long-term ambulatory monitoring impractical for most individuals Lawley et al. (2015).

Dry electrode technology, positioned as a more user-friendly alternative, eliminates the need for conductive gels but introduces a different set of complications. These electrodes typically rely on mechanical pressure to ensure adequate contact with the skin, which can lead to discomfort, irritation, and difficulty sleeping or performing daily activities Hinrichs et al. (2020). Extended use of dry electrodes can result in headaches, pressure sores, and motion artefacts if the contact is disturbed by normal movements, leading to big motion artefacts in the signal Hinrichs et al. (2020). Both wet and dry EEG solutions further require the use of electrode caps or headgear, which often appear bulky, alienating, and socially awkward. The inconvenience associated with wearing an apparent EEG cap outside of a clinical setting can negatively impact the user's mental well-being and willingness to adhere to the extended monitoring protocol. Comfort poses another significant challenge as the weight and

heat generated by the cap, combined with the pressure of multiple electrode contact points, can disrupt or disturb regular routines, notably sleep Hinrichs et al. (2020), which is a critical period for monitoring brain activity.

These collective drawbacks underscore the urgent need to develop more advanced, user-centric EEG technologies that can reliably capture continuous brain signals without causing discomfort or social anxiety. Innovations such as flexible, textile-based electrodes and minimally invasive sensor arrays are being explored to reduce setup time, mitigate skin irritation, and provide stable, high-fidelity readings over days or weeks. Wearable devices seamlessly blending into everyday clothing or accessories could also address the social acceptability hurdle, allowing individuals to maintain normal lifestyles while undergoing vital neurological assessments. Moreover, integrating wireless data transmission and efficient power management is paramount, ensuring that devices remain indistinct and reliable for extended recordings. In sum, while the demand for ambulatory EEG systems continues to rise, the limitations of wet and dry electrodes—related to comfort, maintenance, social acceptability, and data quality—highlight an acute need for next-generation electrode solutions that can finally unlock the true potential of long-term, real-world neurological monitoring.

6.1.1 Background

Wet electrode EEG systems trace their origins back nearly a century, to the earliest days of brain-wave recording, when researchers discovered that applying a conductive gel or paste between the electrode and the scalp greatly enhanced signal fidelity Müller-Putz (2020). Over time, these electrodes were often fabricated from metals such as silver, gold, and silver chloride. This metal-with-gel configuration became the gold standard in clinical and research environments because it maintains low-impedance contact and enables high-quality neural signal capture Li et al. (2020). Recent developments have focused on refining conductive materials and gels to improve recording stability, reduce setup time, and enhance user comfort Soufineyestani et al. (2020). However, wet electrodes come with notable drawbacks, including time-

consuming preparation, the messy nature of gel application, and the tendency for gels to dry out during extended monitoring sessions. Applying or reapplying conductive media can also be intrusive and uncomfortable for patients, particularly in long-term or ambulatory monitoring scenarios Soufineyestani et al. (2020). These limitations underscore the need for more user-friendly electrode innovations that meet the evolving demands of EEG diagnostics and research.

Dry electrode EEG systems emerged to address the cumbersome and time-intensive setup required by traditional wet electrodes, with late twentieth-century research aimed at eliminating the need for messy conductive gels Lopez-Gordo et al. (2014). Pioneers in this field experimented with new materials and electrode designs that could record brain signals directly from the scalp, removing the requirement for specialized interface gels Di Flumeri et al. (2019). Recent developments feature a range of specialized sensor geometries—from comb-like devices Duvinage et al. (2013) to spring-loaded designs Zhang et al. (2023b)—all intended to enhance comfort and maintain stable electrode-skin contact. These innovations have significantly increased the feasibility of mobile, user-friendly EEG systems, paving the way for their use in consumer brain-computer interfaces and rapid clinical screenings. However, dry electrodes also pose certain challenges. Maintaining consistent contact often depends on mechanical pressure, which can become uncomfortable over extended periods Di Flumeri et al. (2019), and this approach increases susceptibility to motion artefacts if the user frequently moves, thereby degrading signal quality. Consequently, dry electrode systems continue to evolve as researchers strive to balance comfort, stability, and signal fidelity, underscoring the need for further innovation in long-term, unobtrusive EEG monitoring solutions Li et al. (2020).

Implantable devices designed for long-term brain signal monitoring represent one of the most advanced solutions in neurotechnology, offering high-fidelity access to neural activity from directly within the skull Weisdorf et al. (2019). Unlike external electrode systems that depend on gel interfaces or mechanical contact, these devices place electrodes or electrode arrays in close proximity to cortical or subcutaneous structures Djurhuus et al. (2023). This close interface produces higher-quality record-

ings, making implantable systems invaluable for applications such as chronic seizure detection, neural prosthetics, and research on neural plasticity Djurhuus et al. (2023). However, this invasive approach carries inherent risks, including potential infection at the implantation site, tissue damage or scarring that can degrade signal quality over time, and the possibility of adverse immune reactions. Additionally, implantable devices must be robust enough to function reliably within a biological environment for extended periods, raising concerns about power management, heat generation, and materials biocompatibility Pal Attia et al. (2023). Despite these challenges, advancements in surgical techniques and biocompatible materials continue to push the boundaries of what implantable brain monitoring technology can achieve, promising transformative clinical and research implications if safety and longevity can be reliably ensured.

6.1.2 Design concept

While there are significant advancements in wet, dry, and implantable EEG technologies, none of these approaches fully address the growing demand for continuous, long-term brain monitoring over several days to weeks. Wet electrodes, while delivering quality signals, rely on messy conductive gels that dry out and disrupt recordings. Dry electrodes, on the other hand, often sacrifice comfort by applying pressure to the scalp. Both technologies typically require obtrusive headgear that is socially unpleasant and compromises user comfort, particularly during sleep. Implantable devices promise higher-quality data but have substantial risks and remain a level of invasive. These limitations underscore the urgent need for a next-generation EEG system that is minimal or non-invasive, offers sustained comfort throughout daily activities and overnight use, and meets aesthetic requirements for social acceptability. Such technological breakthroughs would unlock the full potential of long-term neural monitoring for diagnostics, treatment, and research without the current trade-offs in comfort, user compliance, and data reliability.

This work introduces a novel, hair-like EEG electrode design tailored for long-term

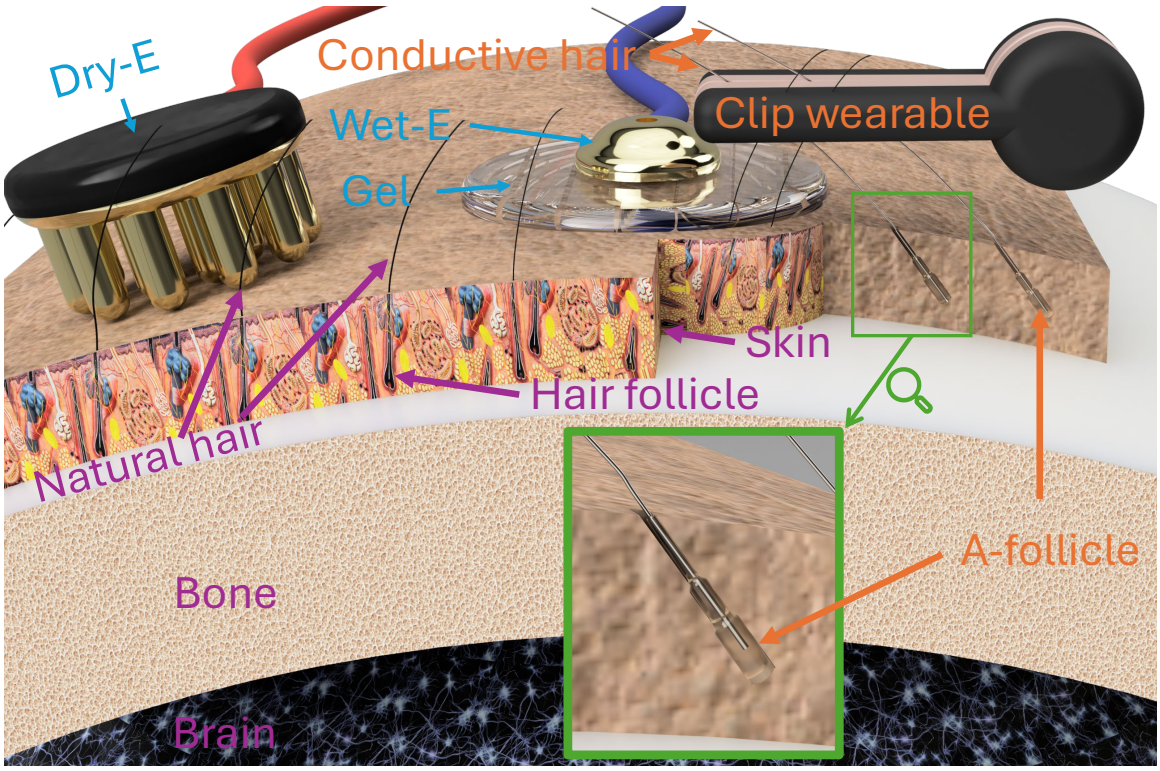

Figure 6.1 – hair-electrodes illustration and comparison. Dry–E: Conventional dry electrodes for EEG. These electrodes require mechanical pressure to maintain stable contact with the scalp. Active dry electrodes typically include a cable that supplies power to an onboard amplifier and transmits the recorded signals to downstream circuitry. Wet-E: Conventional wet electrodes for EEG. These rely on a conductive gel to facilitate electrical contact between the metal electrode and the skin surface. A-follicle: Artificial follicle. This bottom portion of the conductive hair-electrode provides firm anchoring within the tissue and helps minimise foreign-body sensations. Clip Wearable: A conceptual, lightweight, fully wireless device designed to attach to both natural and artificial hair-electrodes for continuous EEG signal acquisition.

ambulatory monitoring, which spans from three days up to two weeks without the drawbacks of conventional wet or dry electrode systems. The proposed electrodes take the form of electrically conductive, artificial hair strands that are implanted into the scalp, similar to natural hair. Their natural, hair-like appearance is intended to address social and aesthetic concerns and user comfort while still capturing high-quality EEG signals without the need for conductive gels or uncomfortable mechanical pressure.

Fig. 6.1 compares the conceptual device with traditional dry and wet electrodes. The left and middle sections of the figure depict existing dry and wet electrode systems, which typically rely on bulky caps, conductive gels, or sustained pressure. In contrast, our proposed system on the right features artificial hair strands with a conductive core surrounded by a biocompatible, hair-like sheath. This design minimizes discomfort once implanted and maintains stable, low-impedance contact with the scalp. Each artificial hair strand is anchored by a bottle-shaped "artificial follicle" that is both porous and hydrophilic, allowing it to bond securely with surrounding skin tissue. The porous nature of the follicle helps maintain low electrode impedance, while its shape ensures a firm attachment that prevents accidental detachment. Notably, this artificial follicle is fabricated from biodegradable materials such as silk, which degrade naturally over several weeks. As the follicle breaks down, the implanted artificial hair loosens and eventually falls out on its own, reducing the risk of long-term infection and eliminating the need for invasive removal procedures.

To collect EEG signals from these conductive hair strands, we propose a lightweight, wireless "hair clip" device that interfaces with the artificial hair via conductive contacts on its inner surface. Weighing less than 20 grams, the clip can be discreetly attached to a small bundle of artificial and natural hair, thus remaining both comfortable and visually unobtrusive. By eliminating the need for large electrode caps or cables, this design improves user comfort and reduces the social stigma associated with wearing conspicuous EEG headgear in daily life or during sleep. Furthermore, multiple artificial hair strands can be implanted at each scalp site following the 10-20 EEG placement system to ensure signal redundancy and maintain low overall

impedance.

This hair-electrode concept combines comfort, aesthetics, and reliable signal capture into a single solution for extended EEG monitoring. By addressing the limitations of conventional wet and dry electrodes—such as messy gels, pressure-based contact, and obtrusive headgear—this technology has the potential to significantly enhance user compliance, enabling long-duration EEG studies and more accurate monitoring of neurological conditions in real-world settings.

6.2 Method

6.2.1 experiment setup

To evaluate the performance of our proposed conductive hair-electrode design, we constructed a comparative experimental platform that simulates realistic scalp conditions. A custom 3D-printed container was filled with saline solution. We positioned a movable dipole inside this container whose depth, position, and orientation could be precisely adjusted. We systematically tested signal quality under different configurations by rotating the dipole perpendicular or parallel to the electrode plane.

Fresh pork tissue—consisting of skin, subcutaneous fat, and muscle layers—was used to approximate the electrical and mechanical properties of the human scalp. The pork skin was implanted with our conductive artificial hair strands and placed on a 3D-printed shelf within the saline container. This shelf ensured direct contact between the lower muscle layer and the saline solution while preventing the solution from leaking into or bypassing other tissue layers. As a result, we created a controlled phantom-like setup that allowed for objective comparisons of EEG signal quality between various electrode configurations.

For EEG signal acquisition, we allocated a 10×10 mm area of pork skin for implanting the conductive artificial hair at a density of 64 hairs per 100 mm^2. A typical cup-shaped wet electrode was placed adjacent to this region as a reference. Both

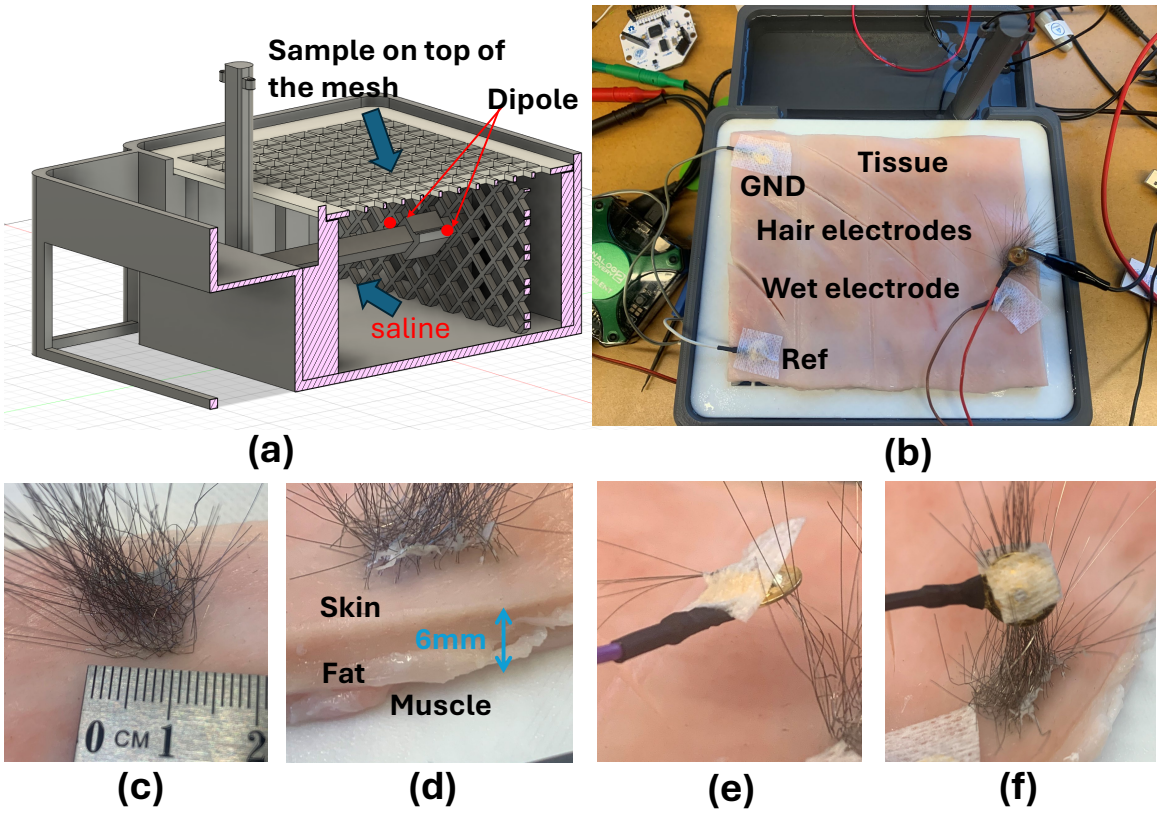

Figure 6.2 – hair-electrodes testing experiment setup. (a) Schematic of the testing container and dipole source placement. A mesh supports the tissue sample above the saline, positioning the dipole approximately 20 mm from the electrodes. (b) Photograph of the experiment in progress, illustrating the skin, fat, and muscle layers atop the mesh. The ground electrode is visible in the top left corner.

electrode types were connected to the same EEG biosensing board (OpenBCI Cyton, 8-channel), sharing the same ground and reference electrodes to ensure fair signal comparisons. The dipole source in the saline was driven by a voltage-controlled current source (Stanford Research CS580), which received its input from a programmable waveform generator (Analog Discovery 2, Digilent). The voltage-controlled current source was configured at a ratio of 1 V/μA, generating a known sinusoidal current at frequencies of 1, 3, 5, 9, 20, 28, 40, 70 and 110 Hz. We sampled the resulting signals at 250 Hz and applied a 50 Hz notch filter to suppress power-line interference.

Fig. 6.2 (c)–(f) shows our conductive artificial hair strands, which are made of 316L stainless steel wire with a diameter of approximately 60μm. Each strand was implanted at a 30°–45°angle, with 3–5 mm of wire beneath the skin. Careful inspection

ensured the wire remained entirely within the skin layer and did not pass through it. We used a clip to connect single-hair or multi-hair bundles to an EEG channel during testing. For the wet reference electrode, we applied the conductive gel and fixed it in place with an adhesive strip. The ground and reference electrodes were positioned on the far side of the tissue to minimize interference. This setup enabled direct, side-by-side signal amplitude and quality comparisons between our hair and traditional wet electrodes under controlled conditions.

6.3 Result

We calculated the Signal-to-Noise Ratio (SNR) to compare the wet electrode and our proposed hair-electrodes. Figure6.3 shows the SNR comparison with different signal frequencies and different numbers of hairs connected as one electrode.

We calculated the SNR to compare the performance of conventional wet electrodes with our proposed hair-electrodes. Fig. 6.3 illustrates the SNR comparison across different signal frequencies and varying numbers of hair-electrodes grouped as a single unit. The results are presented as relative comparisons, as measuring the absolute SNR of the EEG device in our experimental setup was not feasible due to uncontrollable background noise.

To ensure accurate SNR comparisons, signals from the wet and hair-electrodes were collected simultaneously. To minimize the influence of DC offset on the calculation, frequencies below 0.2 Hz were excluded from the analysis. Table 6.1 summarizes the average SNR improvement of the hair-electrodes relative to the wet electrode.

The results show that the optimal SNR performance was achieved when six hair-electrodes were combined, beyond which no significant improvement was observed. For comparisons between hair-electrodes and wet electrodes, configurations with three or more hair-electrodes consistently demonstrated an SNR improvement of over 2 dB across most frequency bands. Notably, at higher frequencies (>70 Hz), the SNR improvement exceeded 4 dB. Despite its small contact area, even a single hair-electrode

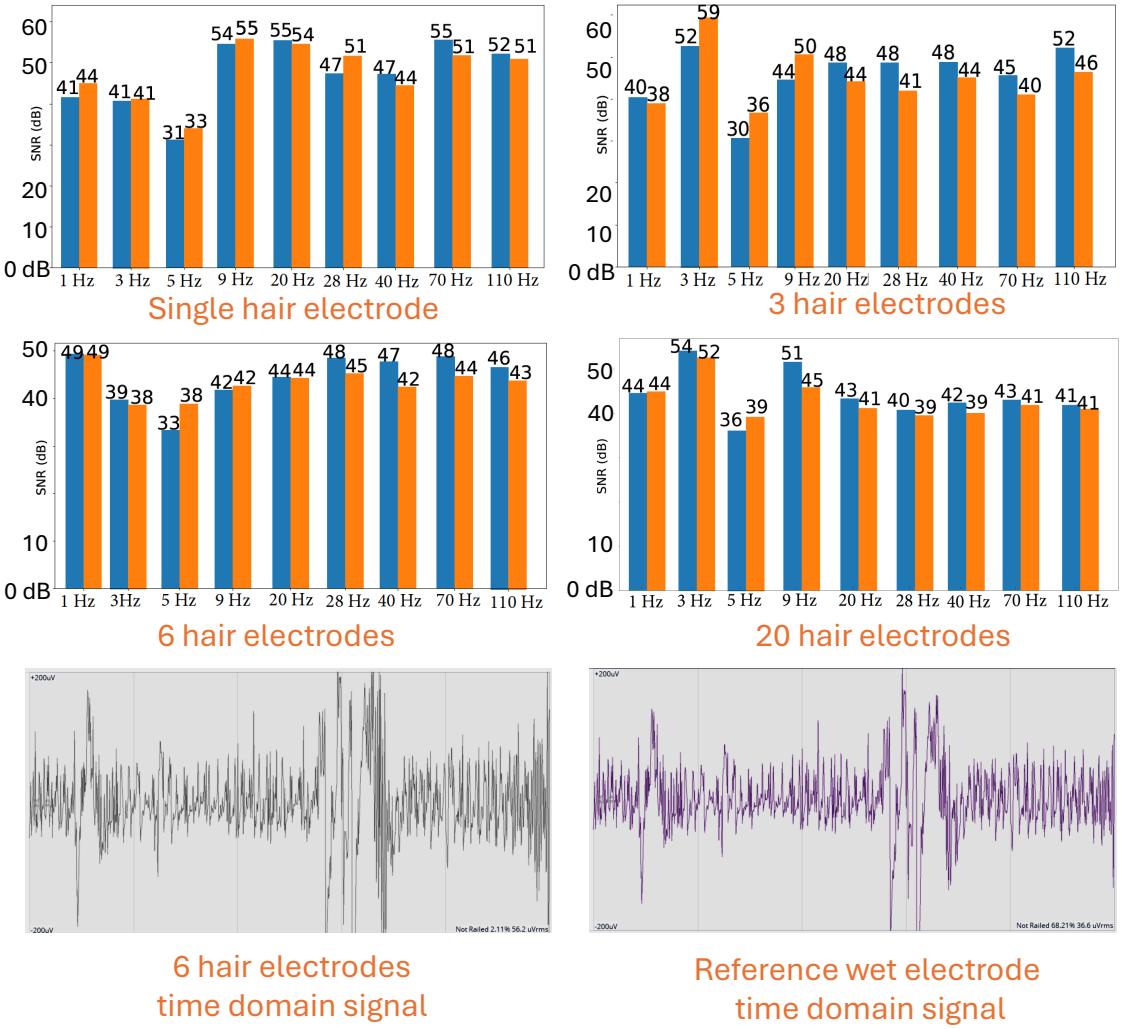

Figure 6.3 – Relative SNR Comparison Results. The Y-axis represents the signal frequency, while the X-axis indicates the SNR values. The top-left subplot compares the SNR of a single hair-electrode with that of a wet electrode. The top-right subplot shows the SNR comparison when three hair-electrodes are combined and treated as a single electrode against a wet electrode. The bottom-left subplot presents the results for six combined hair-electrodes compared to a wet electrode. Finally, the bottom-right subplot illustrates the SNR comparison when 20 hair-electrodes are combined and evaluated against a wet electrode. The time domain signal from 6 hair electrodes and a reference wet electrode is shown at the bottom. The signal pattern and amplitude are comparable from hair electrodes to the wet electrodes.

achieved an SNR comparable to the wet electrode.

However, the hair-electrode exhibited slightly lower SNR for signals at 5 Hz, likely due to interference from power line noise at 50 Hz. Overall, these findings indicate that a single hair-electrode can provide comparable SNR performance to a wet electrode, while configurations with three to six hair-electrodes offer a modest SNR improvement of approximately 1 dB.

Table 6.1 – Average SNR gain with hair-electrode.

Number of hair-electrodes	single	3	6	20
Average SNR gain(dB)	-0.1	1	1.2	0.9

6.4 Discussion

Despite the promising advantages of conductive hair-electrodes for long-term EEG monitoring, several significant obstacles must be resolved before such a system can be clinically or commercially adopted. One primary concern involves the potential for foreign-body sensation or skin irritation, particularly if the artificial follicles fail to integrate seamlessly with the scalp. Therefore, specialised surface treatments and biocompatible coatings are required to reduce inflammation risk and promote stable bonding between the artificial follicle and living tissue. Such treatments could also include anti-bacterial or anti-inflammatory agents, further reducing infection risk during implantation.

Fabricating conductive hair with a biocompatible artificial follicle poses another challenge, requiring an interdisciplinary effort involving materials science, biomedical engineering, and advanced manufacturing techniques such as micro-moulding or electrospinning. The chosen materials must combine mechanical strength to withstand physical movement in everyday living environments and, at the same time, maintain sufficient electrical conductivity for reliable signal capture. Meanwhile, the artificial follicle must be carefully engineered to degrade in a controlled manner depending on the intended replacement schedule.

Beyond the electrodes themselves, designing a wearable, wireless hair clip capable of efficiently collecting EEG signals adds another layer of complexity. Continuous data recording and streaming place stringent demands on battery life, which must be balanced against overall device weight. A practical, user-friendly system requires ultra-low-power electronics, reliable wireless communication, and an ergonomic form factor that does not interfere with daily activities or sleep.

For clinical diagnosis, EEG signals from multiple scalp locations are often needed, and electrode placements typically follow standardized configurations like the 10-20 system Soufineyestani et al. (2020). When multiple electrode sites are required, the design and engineering challenges for the clip-based wearable increase significantly. Each additional site calls for its own cluster of artificial hairs and corresponding contact points, all while remaining discreetly packaged and minimizing mechanical stress on the scalp. Balancing these competing priorities comfort, durability, data quality, and battery life is crucial. With careful design, the wearable hair clip can evolve into a practical and widely accepted solution for continuous, long-term EEG monitoring.

6.5 Conclusion

In conclusion, our novel conductive hair-electrode system represents a significant step toward truly wireless, long-term ambulatory EEG monitoring. By embedding a conductive core within artificial hair strands, anchoring them in specially engineered artificial follicles, and integrating them with a lightweight wireless clip, we have addressed many of the limitations of conventional wet and dry electrode solutions. In our tests, using fresh pork tissue, which closely mimics the mechanical and electrical properties of the human scalp. The hair-electrodes reliably captured EEG signals in this phantom environment, indicating the success of the design concept. Our comparative evaluations with traditional wet electrodes showed competitive signal quality, underscoring the potential for a more comfortable, discreet, and durable option.

Nevertheless, several challenges remain. Fine-tuning the material properties of the

artificial hair and follicle to ensure optimal biocompatibility, balancing battery life and weight in the wearable clip, and developing novel contact points for multi-site recordings all require further research. With continued refinements and interdisciplinary collaboration, the artificial hair-electrode approach could pave the way for extended EEG monitoring that is more user-friendly, socially acceptable, and clinically effective.

Chapter 7

Discussion and Conclusion

This thesis presents significant advancements in the field of miniaturized wireless and battery-free systems for physiological monitoring and stimulation, addressing critical challenges in power delivery, data communication, device miniaturization, and user comfort. Through a comprehensive and systematic approach, this work contributes to the development of innovative technologies that hold the potential to revolutionize biomedical diagnostics, therapy, and research.

A key achievement of this thesis is the development of a high-bandwidth optical telemetry system designed for brain signal sensing. This system establishes a robust foundation for wireless data communication, meeting the stringent requirements of physiological monitoring. The optical telemetry module demonstrates exceptional performance in terms of data rate, power efficiency, and miniaturization, making it a viable solution for next-generation neural implants. This work also introduces integration strategies that combine wireless data communication with power delivery solutions, addressing the dual needs for energy and information transfer in a single system.

To further overcome the limitations of existing eBCIs, this thesis introduces a novel optical telemetry module combined with FUS power transfer. This innovative system eliminates the need for long wires, enhancing its clinical applicability for patients with fragile blood vessels and pediatric populations. Proof-of-concept experiments

demonstrate the feasibility of high-speed data transmission and efficient power transfer within safety limits, paving the way for broader adoption of wireless eBCIs in medical and neuroscience applications.

Another major contribution is the design of a WPT system capable of delivering sufficient energy to standard stents without modifying their structure or material. This system achieves unprecedented efficiency while maintaining compliance with safety standards, making it suitable for powering endoECoG devices and other biosignal sensors. The experimental validation of this system using real biological tissues confirms its practical viability and highlights its potential for widespread clinical use.

In addition to advancements in power and data transfer, this thesis addresses the challenge of user comfort and social acceptability in brain monitoring systems. A novel hair-like electrode design is introduced for EEG monitoring, offering a non-invasive, aesthetically pleasing, and biocompatible alternative to conventional wet, dry, and implantable systems. This innovation combines comfort and reliability, enabling long-term ambulatory monitoring for durations of up to two weeks. By aligning electrode placement with the standard 10-20 EEG system, this work ensures both signal redundancy and high-quality data acquisition.

7.1 Future Works

The contributions of this thesis have broad implications for the future of healthcare and biomedical research. By addressing key technical and practical challenges, the proposed systems enable new possibilities for minimal-invasive or non-invasive diagnostics, personalized therapies, and long-term monitoring in real-world settings. These advancements have the potential to significantly enhance patient outcomes, reduce healthcare costs, and provide deeper insights into complex physiological processes.

Looking ahead, future research could focus on further miniaturizing and integrating these systems through advanced fabrication techniques such as ASICs and novel ma-

terials. Additionally, exploring more energy harvesting methods could enhance the sustainability and versatility of these technologies. Expanding the scope of these solutions to other physiological systems and conditions, such as cardiovascular monitoring or metabolic regulation, could further broaden their impact.

List of References

Zain Ul Abdin, Abdul Basir, Syed Ahson Ali Shah, Izaz Ali Shah, Youngdae Cho, and Hyoungsuk Yoo. Efficient and reliable wireless power transfer stent rectenna system for abdominal aortic aneurysm surveillance. *Advanced Materials Technologies*, n/a(n/a):2400342, 2024. ISSN 2365-709X.

D Michael Ackermann, Brian Smith, Xiao-Feng Wang, Kevin L Kilgore, and P Hunter Peckham. Designing the optical interface of a transcutaneous optical telemetry link. *IEEE Transactions on Biomedical Engineering*, 55(4):1365–1373, 2008. ISSN 0018-9294.

Yoav Adam, Jeong J. Kim, Shan Lou, Yongxin Zhao, Michael E. Xie, Daan Brinks, Hao Wu, Mohammed A. Mostajo-Radji, Simon Kheifets, Vicente Parot, Selmaan Chettih, Katherine J. Williams, Benjamin Gmeiner, Samouil L. Farhi, Linda Madisen, E. Kelly Buchanan, Ian Kinsella, Ding Zhou, Liam Paninski, Christopher D. Harvey, Hongkui Zeng, Paola Arlotta, Robert E. Campbell, and Adam E. Cohen. Voltage imaging and optogenetics reveal behaviour-dependent changes in hippocampal dynamics. *Nature*, 569(7756):413–417, 2019. ISSN 1476-4687.

Swati Aggarwal and Nupur Chugh. Review of machine learning techniques for EEG based brain computer interface. *Archives of Computational Methods in Engineering*, 29:1–20, 2022. ISSN 1134-3060.

José Alberto, Cristina Leal, Cláudio Fernandes, Pedro A Lopes, Hugo Paisana, Aníbal T de Almeida, and Mahmoud Tavakoli. Fully untethered battery-free biomonitoring electronic tattoo with wireless energy harvesting. *Scientific reports*, 10(1):1–11, 2020. ISSN 2045-2322.

A. Aldaoud, J. M. Redoute, K. Ganesan, G. S. Rind, S. E. John, S. M. Ronayne, N. L. Opie, D. J. Garrett, and S. Prawer. Near-field wireless power transfer to stent-based biomedical implants. *IEEE Journal of Electromagnetics, RF and Microwaves in Medicine and Biology*, 2(3):193–200, 2018. ISSN 2469-7257.

Hiroshi Ando, Kenichi Takizawa, Takeshi Yoshida, Kojiro Matsushita, Masayuki Hirata, and Takafumi Suzuki. Wireless multichannel neural recording with a

128-mbps uwb transmitter for an implantable brain-machine interfaces. *IEEE Transactions on Biomedical Circuits and Systems*, 10(6):1068–1078, 2016. ISSN 1932-4545.

Daniel Bacher, Beata Jarosiewicz, Nicolas Y Masse, Sergey D Stavisky, John D Simeral, Katherine Newell, Erin M Oakley, Sydney S Cash, Gerhard Friehs, and Leigh R Hochberg. Neural point-and-click communication by a person with incomplete locked-in syndrome. *Neurorehabilitation and neural repair*, 29(5): 462–471, 2015. ISSN 1545-9683.

Lindsay B. Baker and Anthony S. Wolfe. Physiological mechanisms determining eccrine sweat composition. *European Journal of Applied Physiology*, 120(4): 719–752, 2020. ISSN 1439-6327.

Gian Luca Barbruni, Paolo Motto Ros, Danilo Demarchi, Sandro Carrara, and Diego Ghezzi. Miniaturised wireless power transfer systems for neurostimulation: A review. *IEEE Transactions on Biomedical Circuits and Systems*, 14(6): 1160–1178, 2020. ISSN 1932-4545.

Alexey N Bashkatov, EA Genina, VI Kochubey, and VV Tuchin. Optical properties of human skin, subcutaneous and mucous tissues in the wavelength range from 400 to 2000 nm. *Journal of Physics D: Applied Physics*, 38(15):2543, 2005. ISSN 0022-3727.

Alexey N Bashkatov, Elina A Genina, and Valery V Tuchin. Optical properties of skin, subcutaneous, and muscle tissues: a review. *Journal of Innovative Optical Health Sciences*, 4(01):9–38, 2011. ISSN 1793-5458.

Rebecca A Bercich, Daniel R Duffy, and Pedro P Irazoqui. Far-field rf powering of implantable devices: Safety considerations. *IEEE Transactions on Biomedical Engineering*, 60(8):2107–2112, 2013. ISSN 0018-9294.

Rajmohan Bhandari, Sandeep Negi, and Florian Solzbacher. Wafer-scale fabrication of penetrating neural microelectrode arrays. *Biomedical microdevices*, 12(5): 797–807, 2010. ISSN 1572-8781.

Neal Bhatia and Mikhael El-Chami. Leadless pacemakers: a contemporary review. *Journal of geriatric cardiology: JGC*, 15(4):249, 2018.

Muhammad Zaki bin Mustapa, Shakir Saat, Yusmarnita Yusof, and Muslimah Meor Shaari. Capacitive power transfer in biomedical implantable device: a review. *Int J Pow Elec and Dri Syst*, 10(2):935–942, 2019.

Edward S Boyden, Feng Zhang, Ernst Bamberg, Georg Nagel, and Karl Deisseroth. Millisecond-timescale, genetically targeted optical control of neural activity. *Nature neuroscience*, 8(9):1263–1268, 2005. ISSN 1546-1726.

Jamie FM Brannigan, Adam Fry, Nicholas L Opie, Bruce CV Campbell, Peter J Mitchell, and Thomas J Oxley. Endovascular brain-computer interfaces in poststroke paralysis. *Stroke*, 2023. ISSN 0039-2499.

Alex Burton, Sofian N Obaid, Abraham Vázquez-Guardado, Matthew B Schmit, Tucker Stuart, Le Cai, Zhiyuan Chen, Irawati Kandela, Chad R Haney, and Emily A Waters. Wireless, battery-free subdermally implantable photometry systems for chronic recording of neural dynamics. *Proceedings of the National Academy of Sciences*, 117(6):2835–2845, 2020a. ISSN 0027-8424.

Alex Burton, Sofian N Obaid, Abraham Vázquez-Guardado, Matthew B Schmit, Tucker Stuart, Le Cai, Zhiyuan Chen, Irawati Kandela, Chad R Haney, and Emily A Waters. Wireless, battery-free subdermally implantable photometry systems for chronic recording of neural dynamics. *Proceedings of the National Academy of Sciences*, 117(6):2835–2845, 2020b. ISSN 0027-8424.

Alex Burton, Sofian N Obaid, Abraham Vázquez-Guardado, Matthew B Schmit, Tucker Stuart, Le Cai, Zhiyuan Chen, Irawati Kandela, Chad R Haney, and Emily A Waters. Wireless, battery-free subdermally implantable photometry systems for chronic recording of neural dynamics. *Proceedings of the National Academy of Sciences*, 117(6):2835–2845, 2020c. ISSN 0027-8424.

Alex Burton, Sofian N Obaid, Abraham Vázquez-Guardado, Matthew B Schmit, Tucker Stuart, Le Cai, Zhiyuan Chen, Irawati Kandela, Chad R Haney, and Emily A Waters. Wireless, battery-free subdermally implantable photometry systems for chronic recording of neural dynamics. *Proceedings of the National Academy of Sciences*, 117(6):2835–2845, 2020d. ISSN 0027-8424.

Volker Busskamp, Serge Picaud, José-Alain Sahel, and Botond Roska. Optogenetic therapy for retinitis pigmentosa. *Gene therapy*, 19(2):169–175, 2012. ISSN 1476-5462.

Andres Canales, Xiaoting Jia, Ulrich P Froriep, Ryan A Koppes, Christina M Tringides, Jennifer Selvidge, Chi Lu, Chong Hou, Lei Wei, and Yoel Fink. Multifunctional fibers for simultaneous optical, electrical and chemical interrogation of neural circuits in vivo. *Nature biotechnology*, 33(3):277–284, 2015. ISSN 1546-1696.

Ting Chia Chang, Marcus J Weber, Jayant Charthad, Spyridon Baltsavias, and Amin Arbabian. End-to-end design of efficient ultrasonic power links for scaling towards submillimeter implantable receivers. *IEEE Transactions on Biomedical Circuits and Systems*, 12(5):1100–1111, 2018a. ISSN 1932-4545.

Ting Chia Chang, Marcus J Weber, Jayant Charthad, Spyridon Baltsavias, and Amin Arbabian. End-to-end design of efficient ultrasonic power links for scaling

towards submillimeter implantable receivers. *IEEE Transactions on Biomedical Circuits and Systems*, 12(5):1100–1111, 2018b. ISSN 1932-4545.

Jayant Charthad, Marcus J Weber, Ting Chia Chang, and Amin Arbabian. A mm-sized implantable medical device (imd) with ultrasonic power transfer and a hybrid bi-directional data link. *IEEE Journal of solid-state circuits*, 50(8): 1741–1753, 2015. ISSN 0018-9200.

Ujwal Chaudhary, Ioannis Vlachos, Jonas B Zimmermann, Arnau Espinosa, Alessandro Tonin, Andres Jaramillo-Gonzalez, Majid Khalili-Ardali, Helge Topka, Jens Lehmberg, and Gerhard M Friehs. Spelling interface using intracortical signals in a completely locked-in patient enabled via auditory neurofeedback training. *Nature Communications*, 13(1):1–9, 2022. ISSN 2041-1723.

Joshua C Chen, Peter Kan, Zhanghao Yu, Fatima Alrashdan, Roberto Garcia, Amanda Singer, CS Lai, Ben Avants, Scott Crosby, and Zhongxi Li. A wireless millimetric magnetoelectric implant for the endovascular stimulation of peripheral nerves. *Nature Biomedical Engineering*, pages 1–11, 2022a. ISSN 2157-846X.

Luzeng Chen, Guangzhi Zeng, Dengke Guo, Jinghua Liu, Xiang Zhang, Shaoting Lin, and Kai Zhang. Soft elastic hydrogel couplants for ultrasonography. *Materials Science and Engineering: C*, 119:111609, 2021. ISSN 0928-4931.

Ritchie Chen, Gabriela Romero, Michael G. Christiansen, Alan Mohr, and Polina Anikeeva. Wireless magnetothermal deep brain stimulation. *Science*, 347(6229): 1477–1480, 2015.

Ritchie Chen, Andres Canales, and Polina Anikeeva. Neural recording and modulation technologies. *Nature Reviews Materials*, 2(2):1–16, 2017. ISSN 2058-8437.

Xing Chen, Daniel Brox, Babak Assadsangabi, York Hsiang, and Kenichi Takahata. Intelligent telemetric stent for wireless monitoring of intravascular pressure and its in vivo testing. *Biomedical Microdevices*, 16(5):745–759, 2014. ISSN 1572-8781.

Xing Chen, Aitor Morales-Gregorio, Julia Sprenger, Alexander Kleinjohann, Shashwat Sridhar, Sacha J Van Albada, Sonja Grün, and Pieter R Roelfsema. 1024-channel electrophysiological recordings in macaque v1 and v4 during resting state. *Scientific data*, 9(1):1–16, 2022b. ISSN 2052-4463.

Z. Chen, S. Noh, R. D. Prisby, and J. B. Lee. Implanted wireless intramedullary fluid modulator for bone density augmentation. In *2020 IEEE 33rd International Conference on Micro Electro Mechanical Systems (MEMS)*, pages 384–387, 2020. ISBN 2160-1968.

Chen Cheng, Xin Li, Gang Xu, Yanli Lu, Sze Shin Low, Guang Liu, Long Zhu, Caidong Li, and Qingjun Liu. Battery-free, wireless, and flexible electrochemical patch for in situ analysis of sweat cortisol via near field communication. *Biosensors and Bioelectronics*, 172:112782, 2021. ISSN 0956-5663.

Andreas Christ, Theodoros Samaras, Anja Klingenböck, and Niels Kuster. Characterization of the electromagnetic near-field absorption in layered biological tissue in the frequency range from 30 mhz to 6000 mhz. *Physics in Medicine and Biology*, 51(19):4951, 2006. ISSN 0031-9155.

Ha Uk Chung, Bong Hoon Kim, Jong Yoon Lee, Jungyup Lee, Zhaoqian Xie, Erin M. Ibler, KunHyuck Lee, Anthony Banks, Ji Yoon Jeong, Jongwon Kim, Christopher Ogle, Dominic Grande, Yongjoon Yu, Hokyung Jang, Pourya Assem, Dennis Ryu, Jean Won Kwak, Myeong Namkoong, Jun Bin Park, Yechan Lee, Do Hoon Kim, Arin Ryu, Jaeseok Jeong, Kevin You, Bowen Ji, Zhuangjian Liu, Qingze Huo, Xue Feng, Yujun Deng, Yeshou Xu, Kyung-In Jang, Jeonghyun Kim, Yihui Zhang, Roozbeh Ghaffari, Casey M. Rand, Molly Schau, Aaron Hamvas, Debra E. Weese-Mayer, Yonggang Huang, Seung Min Lee, Chi Hwan Lee, Naresh R. Shanbhag, Amy S. Paller, Shuai Xu, and John A. Rogers. Binodal, wireless epidermal electronic systems with in-sensor analytics for neonatal intensive care. *Science*, 363(6430):eaau0780, 2019.

Samuel C. Colachis, Collin F. Dunlap, Nicholas V. Annetta, Sanjay M. Tamrakar, Marcia A. Bockbrader, and David A. Friedenberg. Long-term intracortical microelectrode array performance in a human: a 5 year retrospective analysis. *Journal of Neural Engineering*, 18(4):0460d7, 2021. ISSN 1741-2560 1741-2552.

Alberto Corrias, Pras Pathmanathan, David J. Gavaghan, and Martin L. Buist. Modelling tissue electrophysiology with multiple cell types: applications of the extended bidomain framework. *Integrative Biology*, 4(2):192–201, 2012. ISSN 1757-9708.

Andrea De Marcellis, Elia Palange, Marco Faccio, Guido Di Patrizio Stanchieri, and Timothy G Constandinou. A 250mbps 24pj/bit uwb-inspired optical communication system for bioimplants. In *2017 IEEE Biomedical Circuits and Systems Conference (BioCAS)*, pages 1–4, 2017. ISBN 1509058036.

Andrea De Marcellis, Guido Di Patrizio Stanchieri, Marco Faccio, Elia Palange, and Timothy G Constandinou. A 300 mbps 37 pj/bit pulsed optical biotelemetry. *IEEE Transactions on Biomedical Circuits and Systems*, 14(3):441–451, 2020. ISSN 1932-4545.

Alexey Denisov and Eric Yeatman. Ultrasonic vs. inductive power delivery for miniature biomedical implants. In *2010 International Conference on Body Sensor Networks*, pages 84–89, 2010. ISBN 142445817X.

Gianluca Di Flumeri, Pietro Aricò, Gianluca Borghini, Nicolina Sciaraffa, Antonello Di Florio, and Fabio Babiloni. The dry revolution: Evaluation of three different EEG dry electrode types in terms of signal spectral features, mental states classification and usability. *Sensors*, 19(6):1365, 2019. ISSN 1424-8220.

H Dinis and PM Mendes. A comprehensive review of powering methods used in state-of-the-art miniaturized implantable electronic devices. *Biosensors and Bioelectronics*, 172:112781, 2021. ISSN 0956-5663.

Marco Dionigi, Mauro Mongiardo, Giuseppina Monti, and Renzo Perfetti. Modelling of wireless power transfer links based on capacitive coupling. *International Journal of Numerical Modelling: Electronic Networks, Devices and Fields*, 30(3-4):e2187, 2017. ISSN 0894-3370.

Bjarki D Djurhuus, Pedro F Viana, Esben Ahrens, Sofie S Nielsen, Harishchandra L Srinivasan, Mark P Richardson, Preben Homøe, Harutomo Hasegawa, Ali A Zarei, and Pia LK Gauger. Minimally invasive surgery for placement of a subcutaneous EEG implant. *Frontiers in Surgery*, 10:1304343, 2023. ISSN 2296-875X.

John P Donoghue, Arto Nurmikko, Michael Black, and Leigh R Hochberg. Assistive technology and robotic control using motor cortex ensemble-based neural interface systems in humans with tetraplegia. *The Journal of physiology*, 579(3): 603–611, 2007. ISSN 0022-3751.

Sofia Drakopoulou, Francesc Varkevisser, Linta Sohail, Masoumeh Aqamolaei, Tiago L Costa, and George D Spyropoulos. Hybrid neuroelectronics: towards a solution-centric way of thinking about complex problems in neurostimulation tools. *frontiers in electronics*, 4, 2023.

Antonios Drossos, Veli Santomaa, and Niels Kuster. The dependence of electromagnetic energy absorption upon human head tissue composition in the frequency range of 300-3000 mhz. *IEEE Transactions on Microwave Theory and Techniques*, 48(11):1988–1995, 2000. ISSN 0018-9480.

Matthieu Duvinage, Thierry Castermans, Mathieu Petieau, Thomas Hoellinger, Guy Cheron, and Thierry Dutoit. Performance of the emotiv epoc headset for p300-based applications. *Biomedical engineering online*, 12:1–15, 2013.

Neuralink Elon Musk. An integrated brain-machine interface platform with thousands of channels. *Journal of Medical Internet Research*, 21(10), 2019.

R. Erfani, F. Marefat, A. M. Sodagar, and P. Mohseni. Transcutaneous capacitive wireless power transfer (c-wpt) for biomedical implants. In *IEEE International Symposium on Circuits and Systems (ISCAS)*, pages 1–4, 2017a. ISBN 2379-447X.

R. Erfani, F. Marefat, and P. Mohseni. Biosafety considerations of a capacitive link for wireless power transfer to biomedical implants. In *2018 IEEE Biomedical Circuits and Systems Conference (BioCAS)*, pages 1–4, 2018a. ISBN 2163-4025.

Reza Erfani, Fatemeh Marefat, Amir M Sodagar, and Pedram Mohseni. Transcutaneous capacitive wireless power transfer (c-wpt) for biomedical implants. In *2017 IEEE International Symposium on Circuits and Systems (ISCAS)*, pages 1–4, 2017b. ISBN 1467368539.

Reza Erfani, Fatemeh Marefat, and Pedram Mohseni. Biosafety considerations of a capacitive link for wireless power transfer to biomedical implants. In *2018 IEEE Biomedical Circuits and Systems Conference (BioCAS)*, pages 1–4, 2018b. ISBN 1538636034.

Nir Even-Chen, Dante G. Muratore, Sergey D. Stavisky, Leigh R. Hochberg, Jaimie M. Henderson, Boris Murmann, and Krishna V. Shenoy. Power-saving design opportunities for wireless intracortical brain–computer interfaces. *Nature Biomedical Engineering*, 4(10):984–996, 2020. ISSN 2157-846X.

David Fan, Dylan Rich, Tahl Holtzman, Patrick Ruther, Jeffrey W Dalley, Alberto Lopez, Mark A Rossi, Joseph W Barter, Daniel Salas-Meza, and Stanislav Herwik. A wireless multi-channel recording system for freely behaving mice and rats. *PloS one*, 6(7):e22033, 2011. ISSN 1932-6203.

Pouria Fattahi, Guang Yang, Gloria Kim, and Mohammad Reza Abidian. A review of organic and inorganic biomaterials for neural interfaces. *Advanced materials*, 26 (12):1846–1885, 2014. ISSN 0935-9648.

M Firbank, M Hiraoka, M Essenpreis, and D T Delpy. Measurement of the optical properties of the skull in the wavelength range 650-950 nm. *Physics in Medicine and Biology*, 38(4):503, apr 1993.

Adam Fry, Erica Breyman, Edward LaGrassa, Thomas Oxley, and David Putrino. *Ethical Considerations of Endovascular Brain–Computer Interfaces*, pages 43–63. Springer, 2023.

Wanjia Gao, Yi Chen, and Wenyi Liu. Research and optimum selection of coupling agent materials in ultrasonic measurement. *Journal of Materials Research and Technology*, 26:1006–1015, 2023. ISSN 2238-7854.

Mohammad Meraj Ghanbari, David K Piech, Konlin Shen, Sina Faraji Alamouti, Cem Yalcin, Benjamin C Johnson, Jose M Carmena, Michel M Maharbiz, and Rikky Muller. A sub-mm 3 ultrasonic free-floating implant for multi-mote neural recording. *IEEE Journal of Solid-State Circuits*, 54(11):3017–3030, 2019. ISSN 0018-9200.

RR Goodman, B Kim, SIII McClelland, PB Senatus, LM Winfield, SL Pullman, Q Yu, B Ford, and GM McKhann. Operative techniques and morbidity with subthalamic nucleus deep brain stimulation in 100 consecutive patients with advanced parkinson's disease. *Journal of Neurology, Neurosurgery and Psychiatry*, 77(1):12–17, 2006. ISSN 0022-3050.

R Graaff, ACM Dassel, MH Koelink, FFM De Mul, JG Aarnoudse, and WG Zijlstra. Optical properties of human dermis in vitro and in vivo. *Applied optics*, 32(4):435–447, 1993. ISSN 2155-3165.

Eric C. Greenwald, Sohum Mehta, and Jin Zhang. Genetically encoded fluorescent biosensors illuminate the spatiotemporal regulation of signaling networks. *Chemical Reviews*, 118(24):11707–11794, 2018. ISSN 0009-2665. doi: 10.1021/acs.chemrev.8b00333.

Warren M Grill, Sharon E Norman, and Ravi V Bellamkonda. Implanted neural interfaces: biochallenges and engineered solutions. *Annual review of biomedical engineering*, 11(1):1–24, 2009.

Philipp Gutruf, Vaishnavi Krishnamurthi, Abraham Vázquez-Guardado, Zhaoqian Xie, Anthony Banks, Chun-Ju Su, Yeshou Xu, Chad R Haney, Emily A Waters, and Irawati Kandela. Fully implantable optoelectronic systems for battery-free, multimodal operation in neuroscience research. *Nature Electronics*, 1(12):652–660, 2018. ISSN 2520-1131.

Andreas Haeberlin, Adrian Zurbuchen, Jakob Schaerer, Joerg Wagner, Sébastien Walpen, Christoph Huber, Heinrich Haeberlin, Juerg Fuhrer, and Rolf Vogel. Successful pacing using a batteryless sunlight-powered pacemaker. *EP Europace*, 16(10):1534–1539, 2014. ISSN 1099-5129.

Mohammad Haerinia and Reem Shadid. Wireless power transfer approaches for medical implants: A review. *Signals*, 1(2):209–229, 2020. ISSN 2624-6120.

R. S. Hassan, J. Lee, and S. Kim. A minimally invasive implantable sensor for continuous wireless glucose monitoring based on a passive resonator. *IEEE Antennas and Wireless Propagation Letters*, 19(1):124–128, 2020. ISSN 1548-5757.

Manu Hegde, Winston Chiong, and Vikram R. Rao. New ethical and clinical challenges in "closed-loop" neuromodulation. *Neurology*, 96(17):799–804, 2021.

Robert Herbert, Hyo-Ryoung Lim, Bruno Rigo, and Woon-Hong Yeo. Fully implantable wireless batteryless vascular electronics with printed soft sensors for multiplex sensing of hemodynamics. *Science advances*, 8(19):eabm1175, 2022. ISSN 2375-2548.

Hermann Hinrichs, Michael Scholz, Anne Katrin Baum, Julia W. Y. Kam, Robert T. Knight, and Hans-Jochen Heinze. Comparison between a wireless dry electrode EEG system with a conventional wired wet electrode EEG system for clinical applications. *Scientific Reports*, 10(1):5218, 2020. ISSN 2045-2322.

Leigh R. Hochberg, Daniel Bacher, Beata Jarosiewicz, Nicolas Y. Masse, John D. Simeral, Joern Vogel, Sami Haddadin, Jie Liu, Sydney S. Cash, Patrick van der Smagt, and John P. Donoghue. Reach and grasp by people with tetraplegia using a neurally controlled robotic arm. *Nature*, 485(7398):372–375, 2012. ISSN 1476-4687.

Guosong Hong and Charles M Lieber. Novel electrode technologies for neural recordings. *Nature Reviews Neuroscience*, 20(6):330–345, 2019. ISSN 1471-0048.

A. N. M. S. Hossain, R. Erfani, P. Mohseni, and H. M. Lavasani. On the non-idealities of a capacitive link for wireless power transfer to biomedical implants. *IEEE Transactions on Biomedical Circuits and Systems*, 15(2):314–325, 2021. ISSN 1940-9990.

En-Lin Hsiang, Ziqian He, Yuge Huang, Fangwang Gou, Yi-Fen Lan, and Shin-Tson Wu. Improving the power efficiency of micro-led displays with optimized led chip sizes. *Crystals*, 10(6):494, 2020. ISSN 2073-4352.

Amjad Iqbal, Muath Al-Hasan, Ismail Ben Mabrouk, and Tayeb A. Denidni. Wireless powering and telemetry of deep-body ingestible bioelectronic capsule. *IEEE Transactions on Antennas and Propagation*, 70(10):9819–9830, 2022a.

Amjad Iqbal, Penchala Reddy Sura, Muath Al-Hasan, Ismail Ben Mabrouk, and Tayeb A. Denidni. Wireless power transfer system for deep-implanted biomedical devices. *Scientific Reports*, 12(1):13689, 2022b. ISSN 2045-2322.

S. Islam, X. Song, E. T. Choi, J. Kim, H. Liu, and A. Kim. In vitro study on smart stent for autonomous post-endovascular aneurysm repair surveillance. *IEEE Access*, 8:96340–96346, 2020. ISSN 2169-3536.

R. Jegadeesan, K. Agarwal, Y. X. Guo, S. C. Yen, and N. V. Thakor. Wireless power delivery to flexible subcutaneous implants using capacitive coupling. *IEEE Transactions on Microwave Theory and Techniques*, 65(1):280–292, 2017. ISSN 1557-9670.

Rangarajan Jegadeesan, Kush Agarwal, Yong-Xin Guo, Shih-Cheng Yen, and Nitish V Thakor. Wireless power delivery to flexible subcutaneous implants using capacitive coupling. *IEEE Transactions on Microwave Theory and Techniques*, 65 (1):280–292, 2016. ISSN 0018-9480.

Eugene Jeong, Minseok Seo, and Kyung-Soo Kim. Guide for wavelength selection of leds for fnirs systems. In *2022 22nd International Conference on Control, Automation and Systems (ICCAS)*, pages 1819–1822, 2022.

Y. Jia, U. Guler, Y. P. Lai, Y. Gong, A. Weber, W. Li, and M. Ghovanloo. A trimodal wireless implantable neural interface system-on-chip. *IEEE Transactions on Biomedical Circuits and Systems*, 14(6):1207–1217, 2020. ISSN 1940-9990.

Amanda Jonsson, Sahika Inal, Ilke Uguz, Adam J Williamson, Loïg Kergoat, Jonathan Rivnay, Dion Khodagholy, Magnus Berggren, Christophe Bernard, and George G Malliaras. Bioelectronic neural pixel: Chemical stimulation and electrical sensing at the same site. *Proceedings of the National Academy of Sciences*, 113(34):9440–9445, 2016. ISSN 0027-8424.

Amenah I Kanaan and Ahmed MA Sabaawi. Implantable wireless systems: A review of potentials and challenges. *Antenna Systems*, 2021. ISSN 1839688297.

Mohammad Javad Karimi, Alexandre Schmid, and Catherine Dehollain. Wireless power and data transmission for implanted devices via inductive links: A systematic review. *IEEE Sensors Journal*, 21(6):7145–7161, 2021. ISSN 1530-437X.

Panagiotis Kassanos, H Ip, and Guang-Zhong Yang. *Ultra-low power application-specific integrated circuits for sensing*, pages 281–437. Springer, 2018.

Akifumi Kawamura and Takashi Miyata. *4.2 - Biosensors*, pages 157–176. William Andrew Publishing, 2016. ISBN 978-0-323-37127-8.

Arshad Khan, Ravindra Joshi, Manish Kumar Sharma, Anindita Ganguly, Parag Parashar, Ting-Wei Wang, Sangmin Lee, Fu-Cheng Kao, and Zong-Hong Lin. Piezoelectric and triboelectric nanogenerators: Promising technologies for self-powered implantable biomedical devices. *Nano Energy*, 119:109051, 2024. ISSN 2211-2855.

Imad S Khan, Erin N D'Agostino, Daniel R Calnan, James E Lee, and Joshua P Aronson. Deep brain stimulation for memory modulation: a new frontier. *World neurosurgery*, 126:638–646, 2019. ISSN 1878-8750.

M Noormohammadi Khiarak, S Martel, Y De Koninck, and B Gosselin. Wireless optoelectronic fiber photometry headstage for deep brain structures monitoring. In *2018 IEEE Life Sciences Conference (LSC)*, pages 9–12, 2018. ISBN 1538667096.

Christina K Kim, Samuel J Yang, Nandini Pichamoorthy, Noah P Young, Isaac Kauvar, Joshua H Jennings, Talia N Lerner, Andre Berndt, Soo Yeun Lee, and Charu Ramakrishnan. Simultaneous fast measurement of circuit dynamics at

multiple sites across the mammalian brain. *Nature methods*, 13(4):325–328, 2016. ISSN 1548-7105.

Han-Joon Kim and John S. Ho. Wireless interfaces for brain neurotechnologies. *Philosophical Transactions of the Royal Society A: Mathematical, Physical and Engineering Sciences*, 380(2228):20210020, 2022.

Hyeonseok Kim, Bruno Rigo, Gabriella Wong, Yoon Jae Lee, and Woon-Hong Yeo. Advances in wireless, batteryless, implantable electronics for real-time, continuous physiological monitoring. *Nano-Micro Letters*, 16(1):52, 2024. ISSN 2311-6706.

Kyungmin Kim, Seok Geun Jang, Hae Gyun Lim, Hyung Ham Kim, and Sung-Min Park. Acoustic power transfer using self-focused transducers for miniaturized implantable neurostimulators. *IEEE access*, 9:153850–153862, 2021. ISSN 2169-3536.

Ofer Kobo, Majdi Saada, Simcha R Meisel, Elias Hellou, Aaron Frimerman, Rami Abu Fanne, Jameel Mohsen, Asaf Danon, and Ariel Roguin. Modern stents: where are we going? *Rambam Maimonides Medical Journal*, 11(2), 2020.

A. Koruprolu, S. Nag, R. Erfani, and P. Mohseni. Capacitive wireless power and data transfer for implantable medical devices. In *2018 IEEE Biomedical Circuits and Systems Conference (BioCAS)*, pages 1–4, 2018. ISBN 2163-4025.

Nicholas A Kotov, Jessica O Winter, Isaac P Clements, Edward Jan, Brian P Timko, Stéphane Campidelli, Smita Pathak, Andrea Mazzatenta, Charles M Lieber, and Maurizio Prato. Nanomaterials for neural interfaces. *Advanced Materials*, 21(40):3970–4004, 2009. ISSN 0935-9648.

K. L. Kozielski, A. Jahanshahi, H. B. Gilbert, Y. Yu, Ö. Erin, D. Francisco, F. Alosaimi, Y. Temel, and M. Sitti. Nonresonant powering of injectable nanoelectrodes enables wireless deep brain stimulation in freely moving mice. *Science Advances*, 7(3):eabc4189, 2021.

Joachim K Krauss, Nir Lipsman, Tipu Aziz, Alexandre Boutet, Peter Brown, Jin Woo Chang, Benjamin Davidson, Warren M Grill, Marwan I Hariz, and Andreas Horn. Technology of deep brain stimulation: current status and future directions. *Nature Reviews Neurology*, 17(2):75–87, 2021. ISSN 1759-4766.

Siddharth R Krishnan, Hany M Arafa, Kyeongha Kwon, Yujun Deng, Chun-Ju Su, Jonathan T Reeder, Juliet Freudman, Izabela Stankiewicz, Hsuan-Ming Chen, and Robert Loza. Continuous, noninvasive wireless monitoring of flow of cerebrospinal fluid through shunts in patients with hydrocephalus. *NPJ digital medicine*, 3(1):1–11, 2020. ISSN 2398-6352.

Esther Krook-Magnuson, Caren Armstrong, Mikko Oijala, and Ivan Soltesz. On-demand optogenetic control of spontaneous seizures in temporal lobe epilepsy. *Nature communications*, 4(1):1–8, 2013. ISSN 2041-1723.

Ying-Hui Lai, Yu Tsao, Xugang Lu, Fei Chen, Yu-Ting Su, Kuang-Chao Chen, Yu-Hsuan Chen, Li-Ching Chen, Lieber Po-Hung Li, and Chin-Hui Lee. Deep learning–based noise reduction approach to improve speech intelligibility for cochlear implant recipients. *Ear and Hearing*, 39(4):795–809, 2018. ISSN 1538-4667.

Andrew Lawley, Shaun Evans, Francesco Manfredonia, and Andrea E Cavanna. The role of outpatient ambulatory electroencephalography in the diagnosis and management of adults with epilepsy or nonepileptic attack disorder: a systematic literature review. *Epilepsy and Behavior*, 53:26–30, 2015. ISSN 1525-5050.

Antonio Lazaro, Marti Boada, Ramon Villarino, and David Girbau. Study on the reading of energy-harvested implanted nfc tags using mobile phones. *IEEE Access*, 8:2200–2221, 2019. ISSN 2169-3536.

Dahye Lee, Sung Hee Jeong, Seunghyeon Yun, Sunhyo Kim, Jaehoon Sung, Jungmin Seo, Suyeon Son, Ji Tae Kim, Lina Susanti, Youngseok Jeong, Sanghyun Park, Kangmoon Seo, Sung June Kim, and Taek Dong Chung. Totally implantable enzymatic biofuel cell and brain stimulator operating in bird through wireless communication. *Biosensors and Bioelectronics*, 171:112746, 2021. ISSN 0956-5663.

Young H. Lee and Raj Mutharasan. *CHAPTER 6 - Biosensors*, pages 161–180. Newnes, Burlington, 2005. ISBN 978-0-7506-7729-5.

Guang-Li Li, Jing-Tao Wu, Yong-Hui Xia, Quan-Guo He, and Hong-Guang Jin. Review of semi-dry electrodes for EEG recording. *Journal of Neural Engineering*, 17(5):051004, 2020. ISSN 1741-2552.

Xicong Li, Zabih Ghassemlooy, Stanislav Zvanovec, Min Zhang, and Andrew Burton. Equivalent circuit model of high power leds for vlc systems. In *2019 2nd West Asian Colloquium on Optical Wireless Communications (WACOWC)*, pages 90–95, 2019. ISBN 1728137675.

Xicong Li, Zabih Ghassemlooy, Stanislav Zvanovec, and Luis Nero Alves. An equivalent circuit model of a commercial led with an esd protection component for vlc. *IEEE Photonics Technology Letters*, 33(15):777–779, 2021. ISSN 1041-1135.

Xiuhan Li, Hanru Zhang, Fei Peng, Yang Li, Tianyang Yang, Bo Wang, and Dongming Fang. A wireless magnetic resonance energy transfer system for micro implantable medical sensors. *Sensors*, 12(8):10292–10308, 2012. ISSN 1424-8220.

Changrong Liu, Yong-Xin Guo, Hucheng Sun, and Shaoqiu Xiao. Design and safety considerations of an implantable rectenna for far-field wireless power transfer. *IEEE Transactions on Antennas and Propagation*, 62(11):5798–5806, 2014a. ISSN 0018-926X.

T. Liu, U. Bihr, S. M. Anis, and M. Ortmanns. Optical transcutaneous link for low power, high data rate telemetry. In *2012 Annual International Conference of the IEEE Engineering in Medicine and Biology Society*, pages 3535–3538, 2012a. ISBN 1558-4615.

T. Liu, U. Bihr, J. Becker, J. Anders, and M. Ortmanns. Live demonstration: In vivo verification of a 100 mbps transcutaneous optical telemetric link. In *2014 IEEE Biomedical Circuits and Systems Conference (BioCAS) Proceedings*, pages 186–186, 2014b. ISBN 2163-4025.

Tianyi Liu, Ulrich Bihr, Syed M Anis, and Maurits Ortmanns. Optical transcutaneous link for low power, high data rate telemetry. In *2012 Annual International Conference of the IEEE Engineering in Medicine and Biology Society*, pages 3535–3538, 2012b. ISBN 1457717875.

Tianyi Liu, Ulrich Bihr, Joachim Becker, Jens Anders, and Maurits Ortmanns. In vivo verification of a 100 mbps transcutaneous optical telemetric link. In *2014 IEEE Biomedical Circuits and Systems Conference (BioCAS) Proceedings*, pages 580–583, 2014c. ISBN 147992346X.

Xilin Liu and Andrew G Richardson. Edge deep learning for neural implants: a case study of seizure detection and prediction. *Journal of Neural Engineering*, 18(4): 046034, 2021. ISSN 1741-2552.

Miguel Angel Lopez-Gordo, Daniel Sanchez-Morillo, and F Pelayo Valle. Dry EEG electrodes. *Sensors*, 14(7):12847–12870, 2014. ISSN 1424-8220.

Luyao Lu, Philipp Gutruf, Li Xia, Dionnet L Bhatti, Xinying Wang, Abraham Vazquez-Guardado, Xin Ning, Xinru Shen, Tian Sang, and Rongxue Ma. Wireless optoelectronic photometers for monitoring neuronal dynamics in the deep brain. *Proceedings of the National Academy of Sciences*, 115(7):E1374–E1383, 2018. ISSN 0027-8424.

Wei Lu, Wubin Bai, Hao Zhang, Chenkai Xu, Antonio M. Chiarelli, Abraham Vázquez-Guardado, Zhaoqian Xie, Haixu Shen, Khizar Nandoliya, Hangbo Zhao, KunHyuck Lee, Yixin Wu, Daniel Franklin, Raudel Avila, Shuai Xu, Alina Rwei, Mengdi Han, Kyeongha Kwon, Yujun Deng, Xinge Yu, Edward B. Thorp, Xue Feng, Yonggang Huang, Joseph Forbess, Zhi-Dong Ge, and John A. Rogers. Wireless, implantable catheter-type oximeter designed for cardiac oxygen saturation. *Science Advances*, 7(7):eabe0579, 2021.

Amal Ibrahim Mahmood, Sadik Kamel Gharghan, Mohamed A Eldosoky, and Ahmed M Soliman. Near-field wireless power transfer used in biomedical implants: A comprehensive review. *IET Power Electronics*, 15(16):1936–1955, 2022a. ISSN 1755-4535.

Amal Ibrahim Mahmood, Sadik Kamel Gharghan, Mohamed A. Eldosoky, and Ahmed M. Soliman. Near-field wireless power transfer used in biomedical implants: A comprehensive review. *IET Power Electronics*, 15(16):1936–1955, 2022b. ISSN 1755-4535.

Shahram Majidi, Noam Harel, Miguel Escalon, Abbey Sawyer, Marta Lapinska, Aidan Rogers, Raul Nogueira, Douglas Weber, and David Putrino. Endovascular brain-computer interface to restore motor control for the command of digital devices in patients with severe quadriparesis (S38. 001). 2023.

A. De Marcellis, G. D. P. Stanchieri, M. Faccio, E. Palange, and T. G. Constandinou. A 300 Mbps 37 pJ/bit pulsed optical biotelemetry. *IEEE Transactions on Biomedical Circuits and Systems*, 14(3):441–451, 2020. ISSN 1940-9990.

Vladimir I. Martynov, Alexey A. Pakhomov, Igor E. Deyev, and Alexander G. Petrenko. Genetically encoded fluorescent indicators for live cell ph imaging. *Biochimica et Biophysica Acta (BBA) - General Subjects*, 1862(12):2924–2939, 2018. ISSN 0304-4165.

Michal Maslik, Lieuwe B Leene, and Timothy G Constandinou. Analogue front-end design for neural recording. *Handbook of Neuroengineering*, pages 1–26, 2020. ISSN 9811528489.

Miao Meng and Mehdi Kiani. A hybrid inductive-ultrasonic link for wireless power transmission to millimeter-sized biomedical implants. *IEEE Transactions on Circuits and Systems II: Express Briefs*, 64(10):1137–1141, 2016. ISSN 1549-7747.

Faisal M Merchant, Tammie Quest, Angel R Leon, and Mikhael F El-Chami. Implantable cardioverter-defibrillators at end of battery life: opportunities for risk (re)-stratification in icd recipients. *Journal of the American College of Cardiology*, 67(4):435–444, 2016. ISSN 0735-1097.

Aaron D Mickle, Sang Min Won, Kyung Nim Noh, Jangyeol Yoon, Kathleen W Meacham, Yeguang Xue, Lisa A McIlvried, Bryan A Copits, Vijay K Samineni, and Kaitlyn E Crawford. A wireless closed-loop system for optogenetic peripheral neuromodulation. *Nature*, 565(7739):361–365, 2019. ISSN 1476-4687.

Ivan R Minev, Pavel Musienko, Arthur Hirsch, Quentin Barraud, Nikolaus Wenger, Eduardo Martin Moraud, Jérôme Gandar, Marco Capogrosso, Tomislav Milekovic, and Léonie Asboth. Electronic dura mater for long-term multimodal neural interfaces. *Science*, 347(6218):159–163, 2015. ISSN 0036-8075.

Henrique Miranda and Teresa H Meng. A programmable pulse uwb transmitter with 34In *IEEE Custom Integrated Circuits Conference 2010*, pages 1–4, 2010. ISBN 1424457602.

S Abdollah Mirbozorgi, Hadi Bahrami, Mohamad Sawan, Leslie A Rusch, and Benoit Gosselin. A single-chip full-duplex high speed transceiver for multi-site stimulating and recording neural implants. *IEEE Transactions on Biomedical Circuits and Systems*, 10(3):643–653, 2015. ISSN 1932-4545.

Peter Mitchell, Sarah C. M. Lee, Peter E. Yoo, Andrew Morokoff, Rahul P. Sharma, Daryl L. Williams, Christopher MacIsaac, Mark E. Howard, Lou Irving, Ivan Vrljic, Cameron Williams, Steven Bush, Anna H. Balabanski, Katharine J. Drummond, Patricia Desmond, Douglas Weber, Timothy Denison, Susan Mathers, Terence J. O'Brien, J. Mocco, David B. Grayden, David S. Liebeskind, Nicholas L. Opie, Thomas J. Oxley, and Bruce C. V. Campbell. Assessment of safety of a fully implanted endovascular brain-computer interface for severe paralysis in 4 patients: The stentrode with thought-controlled digital switch (switch) study. *JAMA Neurology*, 80(3):270–278, 2023. ISSN 2168-6149.

Gregory E Moore, James D Rosenthal, Joshua R Smith, and Matthew S Reynolds. Adaptive wireless power transfer and backscatter communication for perpetual operation of wireless brain–computer interfaces. *Proceedings of the IEEE*, 110(1): 89–106, 2021a. ISSN 0018-9219.

Gregory E Moore, James D Rosenthal, Joshua R Smith, and Matthew S Reynolds. Adaptive wireless power transfer and backscatter communication for perpetual operation of wireless brain–computer interfaces. *Proceedings of the IEEE*, 110(1): 89–106, 2021b. ISSN 0018-9219.

COMSOL Multiphysics. Introduction to comsol multiphysics®. *COMSOL Multiphysics, Burlington, MA, accessed Feb*, 9(2018):32, 1998.

Elon Musk. An integrated brain-machine interface platform with thousands of channels. *Journal of medical Internet research*, 21(10):e16194, 2019.

Muhammad Zaki bin Mustapa, Shakir Saat, Yusmarnita Yusof, and Muslimah Meor Shaari. Capacitive power transfer in biomedical implantable device: a review. *International Journal of Power Electronics and Drive Systems (IJPEDS)*, 2019.

Gernot R Müller-Putz. Electroencephalography. *Handbook of Clinical Neurology*, 168:249–262, 2020. ISSN 0072-9752.

Vishnu Nair, Ashley N. Dalrymple, Zhanghao Yu, Gaurav Balakrishnan, Christopher J. Bettinger, Douglas J. Weber, Kaiyuan Yang, and Jacob T. Robinson. Miniature battery-free bioelectronics. *Science*, 382(6671):eabn4732, 2023.

R Narayanamoorthi. Modeling of capacitive resonant wireless power and data transfer to deep biomedical implants. *IEEE Transactions on Components, Packaging and Manufacturing Technology*, 9(7):1253–1263, 2019a. ISSN 2156-3950.

R. Narayanamoorthi. Modeling of capacitive resonant wireless power and data transfer to deep biomedical implants. *IEEE Transactions on Components, Packaging and Manufacturing Technology*, 9(7):1253–1263, 2019b. ISSN 2156-3985.

Joaquin Navajas, Deren Y. Barsakcioglu, Amir Eftekhar, Andrew Jackson, Timothy G. Constandinou, and Rodrigo Quian Quiroga. Minimum requirements for accurate and efficient real-time on-chip spike sorting. *Journal of Neuroscience Methods*, 230:51–64, 2014a. ISSN 0165-0270.

Joaquin Navajas, Deren Y Barsakcioglu, Amir Eftekhar, Andrew Jackson, Timothy G Constandinou, and Rodrigo Quian Quiroga. Minimum requirements for accurate and efficient real-time on-chip spike sorting. *Journal of neuroscience methods*, 230:51–64, 2014b. ISSN 0165-0270.

Joaquin Navajas, Deren Y Barsakcioglu, Amir Eftekhar, Andrew Jackson, Timothy G Constandinou, and Rodrigo Quian Quiroga. Minimum requirements for accurate and efficient real-time on-chip spike sorting. *Journal of neuroscience methods*, 230:51–64, 2014c. ISSN 0165-0270.

Bradley D Nelson, Salil Sidharthan Karipott, Yvonne Wang, and Keat Ghee Ong. Wireless technologies for implantable devices. *Sensors*, 20(16):4604, 2020. ISSN 1424-8220.

Konstantina S Nikita. *Handbook of biomedical telemetry*. John Wiley and Sons, 2014. ISBN 1118388615.

International Electrotechnical Commission (IEC)/Institute of Electrical and Electronics Engineers (IEEE) 62704-1. Determining the peak spatial-average specific ab-sorption rate (SAR) in the human body from wireless communications devices, 30 MHz to 6 GHz–Part 1: General requirements for using the finite-difference time-domain (FDTD) method for SAR calculations. 2017.

Nicholas L Opie, Stephen M Ronayne, Gil S Rind, Peter E Yoo, and Thomas J Oxley. Mechanical suitability of an endovascular braincomputer interface. In *8th International Winter Conference on Brain-Computer Interface (BCI)*, pages 1–6, 2020. ISBN 1728147077.

Thomas Oxley. Long-term safety of a fully implanted endovascular brain-computer interface for severe paralysis. *Archives of Physical Medicine and Rehabilitation*, 103(12):e53, 2022. ISSN 0003-9993.

Thomas J Oxley, Nicholas L Opie, Sam E John, Gil S Rind, Stephen M Ronayne, Tracey L Wheeler, Jack W Judy, Alan J McDonald, Anthony Dornom, and Timothy JH Lovell. Minimally invasive endovascular stent-electrode array for high-fidelity, chronic recordings of cortical neural activity. *Nature Biotechnology*, 34(3):320–327, 2016. ISSN 1087-0156.

Thomas J Oxley, Peter E Yoo, Gil S Rind, Stephen M Ronayne, CM Sarah Lee, Christin Bird, Victoria Hampshire, Rahul P Sharma, Andrew Morokoff, and Daryl L Williams. Motor neuroprosthesis implanted with neurointerventional surgery improves capacity for activities of daily living tasks in severe paralysis: first in-human experience. *Journal of Neurointerventional Surgery*, 13(2):102–108, 2021. ISSN 1759-8478.

Tom Oxley. A 10-year journey towards clinical translation of an implantable endovascular BCI a keynote lecture given at the BCI society meeting in brussels. *Journal of Neural Engineering*, 2024. ISSN 1741-2560.

Tal Pal Attia, Pedro F Viana, Mona Nasseri, Jonas Duun-Henriksen, Andrea Biondi, Joel S Winston, Isabel P. Martins, Ewan S Nurse, Matthias Dümpelmann, and Gregory A Worrell. Seizure forecasting using minimally invasive, ultra-long-term subcutaneous EEG: generalizable cross-patient models. *Epilepsia*, 64:S114–S123, 2023. ISSN 0013-9580.

Chethan Pandarinath, Paul Nuyujukian, Christine H Blabe, Brittany L Sorice, Jad Saab, Francis R Willett, Leigh R Hochberg, Krishna V Shenoy, and Jaimie M Henderson. High performance communication by people with paralysis using an intracortical brain-computer interface. *Elife*, 6:e18554, 2017. ISSN 2050-084X.

Eunkyoung Park, Jae-Woong Lee, Minhee Kang, Kyeongwon Cho, Baek Hwan Cho, and Kyu-Sung Lee. Detecting bladder biomarkers for closed-loop neuromodulation: A technological review. *International Neurourology journal*, 22 (4):228–236, 2018. ISSN 2093-4777 2093-6931. 30599493[pmid] PMC6312967[pmcid] inj.1836246.123[PII].

Jongkil Park, Gookhwa Kim, and Sang-Don Jung. A 128-channel FPGA-based real-time spike-sorting bidirectional closed-loop neural interface system. *IEEE Transactions on Neural Systems and Rehabilitation Engineering*, 25(12): 2227–2238, 2017a. ISSN 1534-4320.

Jongkil Park, Gookhwa Kim, and Sang-Don Jung. A 128-channel FPGA-based real-time spike-sorting bidirectional closed-loop neural interface system. *IEEE Transactions on Neural Systems and Rehabilitation Engineering*, 25(12): 2227–2238, 2017b. ISSN 1534-4320.

Sung Il Park, Daniel S. Brenner, Gunchul Shin, Clinton D. Morgan, Bryan A. Copits, Ha Uk Chung, Melanie Y. Pullen, Kyung Nim Noh, Steve Davidson,

Soong Ju Oh, Jangyeol Yoon, Kyung-In Jang, Vijay K. Samineni, Megan Norman, Jose G. Grajales-Reyes, Sherri K. Vogt, Saranya S. Sundaram, Kellie M. Wilson, Jeong Sook Ha, Renxiao Xu, Taisong Pan, Tae-il Kim, Yonggang Huang, Michael C. Montana, Judith P. Golden, Michael R. Bruchas, Robert W. Gereau, and John A. Rogers. Soft, stretchable, fully implantable miniaturized optoelectronic systems for wireless optogenetics. *Nature Biotechnology*, 33(12): 1280–1286, 2015. ISSN 1546-1696.

Jeanne T Paz, Thomas J Davidson, Eric S Frechette, Bruno Delord, Isabel Parada, Kathy Peng, Karl Deisseroth, and John R Huguenard. Closed-loop optogenetic control of thalamus as a tool for interrupting seizures after cortical injury. *Nature neuroscience*, 16(1):64–70, 2013. ISSN 1546-1726.

Konstantinos Petkos, Simos Koutsoftidis, Thomas Guiho, Patrick Degenaar, Andrew Jackson, Stephen E. Greenwald, Peter Brown, Timothy Denison, and Emmanuel M. Drakakis. A high-performance 8 nV/($\sqrt{\text{Hz}}$)Hz 8-channel wearable and wireless system for real-time monitoring of bioelectrical signals. *Journal of NeuroEngineering and Rehabilitation*, 16(1):156, 2019. ISSN 1743-0003.

Kiryl D Piatkevich, Erica E Jung, Christoph Straub, Changyang Linghu, Demian Park, Ho-Jun Suk, Daniel R Hochbaum, Daniel Goodwin, Eftychios Pnevmatikakis, and Nikita Pak. A robotic multidimensional directed evolution approach applied to fluorescent voltage reporters. *Nature chemical biology*, 14(4): 352–360, 2018. ISSN 1552-4469.

Ferruccio Pisanello, Gil Mandelbaum, Marco Pisanello, Ian A Oldenburg, Leonardo Sileo, Jeffrey E Markowitz, Ralph E Peterson, Andrea Della Patria, Trevor M Haynes, and Mohamed S Emara. Dynamic illumination of spatially restricted or large brain volumes via a single tapered optical fiber. *Nature Neuroscience*, 20(8): 1180–1188, 2017. ISSN 1546-1726.

Alexander N Pisarchik, Vladimir A Maksimenko, and Alexander E Hramov. From novel technology to novel applications: Comment on "an integrated brain-machine interface platform with thousands of channels" by elon musk from neuralink. *Journal of Medical Internet Research*, 21(10):e16356, 2019.

Yu Pu, Danny Butterfield, Jorge Garcia, Jing Xie, Mark Lin, Rohit Sauhta, Rick Farley, Steve Shellhammer, Moses Derkalousdian, and Adam Newham. An ultra-low-power 28nm cmos dual-die asic platform for smart hearables. In *IEEE Biomedical circuits and systems conference (bioCAS)*, pages 1–4, 2018. ISBN 1538636034.

Rodrigo Quian Quiroga. Spike sorting. *Current Biology*, 22(2):R45–R46, 2012a. ISSN 0960-9822.

Rodrigo Quian Quiroga. Spike sorting. *Current Biology*, 22(2):R45–R46, 2012b. ISSN 0960-9822.

Milind Rajadhyaksha, Melanie Grossman, Dina Esterowitz, Robert H Webb, and R Rox Anderson. In vivo confocal scanning laser microscopy of human skin: melanin provides strong contrast. *Journal of investigative dermatology*, 104(6): 946–952, 1995. ISSN 0022-202X.

Michal Ramot and Alex Martin. Closed-loop neuromodulation for studying spontaneous activity and causality. *Trends in Cognitive Sciences*, 26(4):290–299, 2022. ISSN 1364-6613.

Jonathan T Reeder, Jungil Choi, Yeguang Xue, Philipp Gutruf, Justin Hanson, Mark Liu, Tyler Ray, Amay J Bandodkar, Raudel Avila, and Wei Xia. Waterproof, electronics-enabled, epidermal microfluidic devices for sweat collection, biomarker analysis, and thermography in aquatic settings. *Science Advances*, 5(1):eaau6356, 2019. ISSN 2375-2548.

Niina J Ronkainen, H Brian Halsall, and William R Heineman. Electrochemical biosensors. *Chemical Society Reviews*, 39(5):1747–1763, 2010.

J. Rosenthal, A. Sharma, E. Kampianakis, and M. S. Reynolds. A 25 mbps, 12.4 pj/b dqpsk backscatter data uplink for the neurodisc brain–computer interface. *IEEE Transactions on Biomedical Circuits and Systems*, 13(5):858–867, 2019. ISSN 1940-9990.

Sourov Roy, A. N. M. Wasekul Azad, Somen Baidya, Mohammed Khorshed Alam, and Faisal Khan. Powering solutions for biomedical sensors and implants inside the human body: A comprehensive review on energy harvesting units, energy storage, and wireless power transfer techniques. *IEEE Transactions on Power Electronics*, 37(10):12237–12263, 2022.

Sanjeev Sanjeev and Peter P Karpawich. Superior vena cava and innominate vein dimensions in growing children: an aid for interventional devices and transvenous leads. *Pediatric cardiology*, 27:414–419, 2006. ISSN 0172-0643.

S. N. Sawant. *13 - Development of Biosensors From Biopolymer Composites*, pages 353–383. Elsevier, 2017. ISBN 978-0-12-809261-3.

P. Sawosz, S. Wojtkiewicz, M. Kacprzak, W. Weigl, A. Borowska-Solonynko, P. Krajewski, K. Bejm, D. Milej, B. Ciszek, R. Maniewski, and A. Liebert. Human skull translucency: post mortem studies. *Biomed. Opt. Express*, 7(12): 5010–5020, Dec 2016.

R. Sedehi, D. Budgett, J. Jiang, X. Ziyi, X. Dai, A. P. Hu, and D. McCormick. A wireless power method for deeply implanted biomedical devices via capacitively

coupled conductive power transfer. *IEEE Transactions on Power Electronics*, 36 (2):1870–1882, 2021. ISSN 1941-0107.

Udaya Seneviratne and Wendyl Jude D'Souza. *Chapter 10 - Ambulatory EEG*, volume 160, pages 161–170. Elsevier, 2019. ISBN 0072-9752.

Dongjin Seo, Jose M Carmena, Jan M Rabaey, Michel M Maharbiz, and Elad Alon. Model validation of untethered, ultrasonic neural dust motes for cortical recording. *Journal of Neuroscience Methods*, 244:114–122, 2015. ISSN 0165-0270.

Dongjin Seo, Ryan M Neely, Konlin Shen, Utkarsh Singhal, Elad Alon, Jan M Rabaey, Jose M Carmena, and Michel M Maharbiz. Wireless recording in the peripheral nervous system with ultrasonic neural dust. *Neuron*, 91(3):529–539, 2016. ISSN 0896-6273.

Nurettin Sezer and Muammer Koç. A comprehensive review on the state-of-the-art of piezoelectric energy harvesting. *Nano Energy*, 80:105567, 2021. ISSN 2211-2855.

S. A. A. Shah, Y. H. Lim, and H. Yoo. A novel development of endovascular aortic stent system featuring promising antenna characteristics. *IEEE Transactions on Antennas and Propagation*, 70(3):2214–2222, 2022. ISSN 1558-2221.

Syed Ahson Ali Shah and Hyoungsuk Yoo. Radiative near-field wireless power transfer to scalp-implantable biotelemetric device. *IEEE Transactions on Microwave Theory and Techniques*, 68(7):2944–2953, 2020. ISSN 0018-9480.

Shoeb Shaikh, Rosa So, Tafadzwa Sibindi, Camilo Libedinsky, and Arindam Basu. Real-time closed loop neural decoding on a neuromorphic chip. In *9th International IEEE/EMBS Conference on Neural Engineering (NER)*, pages 670–673, 2019. ISBN 1538679213.

Mohammad A Sharif and Amir M Sodagar. *Capacitive links for power and data telemetry to implantable biomedical microsystems*, pages 763–784. Springer, 2022a.

Mohammad A Sharif and Amir M Sodagar. *Capacitive links for power and data telemetry to implantable biomedical microsystems*, pages 763–784. Springer, 2022b.

Malin Silverå Ejneby, Marie Jakešová, Jose J. Ferrero, Ludovico Migliaccio, Ihor Sahalianov, Zifang Zhao, Magnus Berggren, Dion Khodagholy, Vedran Đerek, Jennifer N. Gelinas, and Eric Daniel Głowacki. Chronic electrical stimulation of peripheral nerves via deep-red light transduced by an implanted organic photocapacitor. *Nature Biomedical Engineering*, 2021. ISSN 2157-846X.

Sim4Life. Computable human phantoms. 2011.

Vishnoukumaar Sivaji, Dane W. Grasse, Seth A. Hays, Jesse E. Bucksot, Rahul Saini, Michael P. Kilgard, and Robert L. Rennaker. ReStore: A wireless peripheral nerve stimulation system. *Journal of Neuroscience Methods*, 320:26–36, 2019. ISSN 0165-0270.

A. M. Sodagar and P. Amiri. Capacitive coupling for power and data telemetry to implantable biomedical microsystems. In *4th International IEEE/EMBS Conference on Neural Engineering*, pages 411–414, 2009a. ISBN 1948-3554.

Amir M Sodagar and Parviz Amiri. Capacitive coupling for power and data telemetry to implantable biomedical microsystems. In *4th International IEEE/EMBS Conference on Neural Engineering*, pages 411–414, 2009b. ISBN 1424420725.

Sauson Soldozy, Steven Young, Jeyan S Kumar, Stepan Capek, Daniel R Felbaum, Walter C Jean, Min S Park, and Hasan R Syed. A systematic review of endovascular stent-electrode arrays, a minimally invasive approach to brain-machine interfaces. *Neurosurgical Focus*, 49(1):E3, 2020a. ISSN 1092-0684.

Sauson Soldozy, Steven Young, Jeyan S Kumar, Stepan Capek, Daniel R Felbaum, Walter C Jean, Min S Park, and Hasan R Syed. A systematic review of endovascular stent-electrode arrays, a minimally invasive approach to brain-machine interfaces. *Neurosurgical Focus*, 49(1):E3, 2020b. ISSN 1092-0684.

Minyoung Song, Yu Huang, Yiyu Shen, Chengyao Shi, Arjan Breeschoten, Mario Konijnenburg, Huib Visser, Jac Romme, Barundeb Dutta, and Morteza S Alavi. A 1.66 Gb/s and 5.8 pJ/b transcutaneous IR-UWB telemetry system with hybrid impulse modulation for intracortical brain-computer interfaces. In *IEEE International Solid-State Circuits Conference (ISSCC)*, volume 65, pages 394–396, 2022. ISBN 1665428007.

Seung Hyun Song, Albert Kim, and Babak Ziaie. Omnidirectional ultrasonic powering for millimeter-scale implantable devices. *IEEE Transactions on Biomedical Engineering*, 62(11):2717–2723, 2015. ISSN 0018-9294.

Soner Sonmezoglu, Jeffrey R. Fineman, Emin Maltepe, and Michel M. Maharbiz. Monitoring deep-tissue oxygenation with a millimeter-scale ultrasonic implant. *Nature Biotechnology*, 39(7):855–864, 2021. ISSN 1546-1696.

Mahsa Soufineyestani, Dale Dowling, and Arshia Khan. Electroencephalography (eeg) technology applications and available devices. *Applied Sciences*, 10(21):7453, 2020. ISSN 2076-3417.

Arati Sridharan, Subramaniam D Rajan, and Jit Muthuswamy. Long-term changes in the material properties of brain tissue at the implant–tissue interface. *Journal of Neural Engineering*, 10(6):066001, 2013. ISSN 1741-2552.

Nicholas A. Steinmetz, Cagatay Aydin, Anna Lebedeva, Michael Okun, Marius Pachitariu, Marius Bauza, Maxime Beau, Jai Bhagat, Claudia Böhm, Martijn Broux, Susu Chen, Jennifer Colonell, Richard J. Gardner, Bill Karsh, Fabian Kloosterman, Dimitar Kostadinov, Carolina Mora-Lopez, John O'Callaghan, Junchol Park, Jan Putzeys, Britton Sauerbrei, Rik J. J. van Daal, Abraham Z. Vollan, Shiwei Wang, Marleen Welkenhuysen, Zhiwen Ye, Joshua T. Dudman, Barundeb Dutta, Adam W. Hantman, Kenneth D. Harris, Albert K. Lee, Edvard I. Moser, John O'Keefe, Alfonso Renart, Karel Svoboda, Michael Häusser, Sebastian Haesler, Matteo Carandini, and Timothy D. Harris. Neuropixels 2.0: A miniaturized high-density probe for stable, long-term brain recordings. *Science*, 372(6539):eabf4588, 2021.

Tucker Stuart, Le Cai, Alex Burton, and Philipp Gutruf. Wireless and battery-free platforms for collection of biosignals. *Biosensors and Bioelectronics*, 178:113007, 2021. ISSN 0956-5663.

Lisa R Sun, Dana Harrar, Gerald Drocton, Carlos Castillo-Pinto, Philippe Gailloud, and Monica S Pearl. Endovascular therapy for acute stroke in children: age and size technical limitations. *Journal of Neurointerventional Surgery*, 2021. ISSN 1759-8478.

Sung Hyuk Sunwoo, Ju Seung Lee, SungJun Bae, Yiel Jae Shin, Chang Seong Kim, Soo Yeon Joo, Hong Sang Choi, Minah Suh, Soo Wan Kim, Young Jin Choi, and Tae-il Kim. Chronic and acute stress monitoring by electrophysiological signals from adrenal gland. *Proceedings of the National Academy of Sciences*, 116(4): 1146–1151, 2019.

Mohammad Takhti, Farzad Asgarian, and Amir M Sodagar. Modeling of a capacitive link for data telemetry to biomedical implants. In *IEEE Biomedical Circuits and Systems Conference (BioCAS)*, pages 181–184, 2011. ISBN 1457714701.

M. Tamura, Y. Naka, K. Murai, and T. Nakata. Design of a capacitive wireless power transfer system for operation in fresh water. *IEEE Transactions on Microwave Theory and Techniques*, 66(12):5873–5884, 2018. ISSN 1557-9670.

M. Tamura, K. Murai, and M. Matsumoto. Design of disposable film-type capacitive wireless charging for implantable medical devices. In *IEEE MTT-S International Microwave Symposium (IMS)*, pages 58–61, 2021. ISBN 2576-7216.

M. Tamura, T. Segawa, and M. Matsumoto. Capacitive coupler for wireless power transfer to intravascular implant devices. *IEEE Microwave and Wireless Components Letters*, 32(6):672–675, 2022. ISSN 1558-1764.

Jarno MA Tanskanen, Annika Ahtiainen, and Jari AK Hyttinen. Toward closed-loop electrical stimulation of neuronal systems: a review. *Bioelectricity*, 2 (4):328–347, 2020. ISSN 2576-3105.

Stewart J Thomas, Reid R Harrison, Anthony Leonardo, and Matthew S Reynolds. A battery-free multichannel digital neural/EMG telemetry system for flying insects. *IEEE Transactions on Biomedical Circuits and Systems*, 6(5):424–436, 2012. ISSN 1932-4545.

Limei Tian, Benjamin Zimmerman, Aadeel Akhtar, Ki Jun Yu, Matthew Moore, Jian Wu, Ryan J Larsen, Jung Woo Lee, Jinghua Li, and Yuhao Liu. Large-area MRI-compatible epidermal electronic interfaces for prosthetic control and cognitive monitoring. *Nature biomedical engineering*, 3(3):194–205, 2019. ISSN 2157-846X.

B Upendra, B Panigrahi, K Singh, and GR Sabareesh. Recent advancements in piezoelectric energy harvesting for implantable medical devices. *Journal of Intelligent Material Systems and Structures*, 35(2):129–155, 2024. ISSN 1045-389X.

Sajith Vellappally, Abdulaziz A Al Kheraif, Darshan Devang Divakar, Santhosh Basavarajappa, Sukumaran Anil, and Hassan Fouad. Tooth implant prosthesis using ultra low power and low cost crystalline carbon bio-tooth sensor with hybridized data acquisition algorithm. *Computer Communications*, 148:176–184, 2019. ISSN 0140-3664.

Bernhard Vennemann, Dominik Obrist, and Thomas Rösgen. A smartphone-enabled wireless and batteryless implantable blood flow sensor for remote monitoring of prosthetic heart valve function. *PLoS One*, 15(1):e0227372, 2020a. ISSN 1932-6203.

Bernhard Vennemann, Dominik Obrist, and Thomas Rösgen. A smartphone-enabled wireless and batteryless implantable blood flow sensor for remote monitoring of prosthetic heart valve function. *PLoS One*, 15(1):e0227372, 2020b. ISSN 1932-6203.

Sam Vesuna, Isaac V. Kauvar, Ethan Richman, Felicity Gore, Tomiko Oskotsky, Clara Sava-Segal, Liqun Luo, Robert C. Malenka, Jaimie M. Henderson, Paul Nuyujukian, Josef Parvizi, and Karl Deisseroth. Deep posteromedial cortical rhythm in dissociation. *Nature*, 586(7827):87–94, 2020. ISSN 1476-4687.

Jithin Vishnu and Geetha Manivasagam. Perspectives on smart stents with sensors: From conventional permanent to novel bioabsorbable smart stent technologies. *Medical Devices and Sensors*, 3(6):e10116, 2020. ISSN 2573-802X.

San Wan, R Rox Anderson, and John A Parrish. Analytical modeling for the optical properties of the skin with in vitro and in vivo applications. *Photochemistry and Photobiology*, 34(4):493–499, 1981. ISSN 0031-8655.

Ying Wang, Kai Xie, Haibing Yue, Xian Chen, Xuan Luo, Qinghai Liao, Ming Liu, Feng Wang, and Peng Shi. Flexible and fully implantable upconversion device for wireless optogenetic stimulation of the spinal cord in behaving animals. *Nanoscale*, 12(4):2406–2414, 2020. ISSN 2040-3364.

Sigge Weisdorf, Jonas Duun-Henriksen, Marianne J Kjeldsen, Frantz R Poulsen, Sirin W Gangstad, and Troels W Kjær. Ultra-long-term subcutaneous home monitoring of epilepsy—490 days of EEG from nine patients. *Epilepsia*, 60(11): 2204–2214, 2019. ISSN 0013-9580.

Steven M Wellman, James R Eles, Kip A Ludwig, John P Seymour, Nicholas J Michelson, William E McFadden, Alberto L Vazquez, and Takashi DY Kozai. A materials roadmap to functional neural interface design. *Advanced functional materials*, 28(12):1701269, 2018. ISSN 1616-301X.

Sang Min Won, Enming Song, Jianing Zhao, Jinghua Li, Jonathan Rivnay, and John A Rogers. Recent advances in materials, devices, and systems for neural interfaces. *Advanced Materials*, 30(30):1800534, 2018. ISSN 0935-9648.

Sang Min Won, Enming Song, Jonathan T Reeder, and John A Rogers. Emerging modalities and implantable technologies for neuromodulation. *Cell*, 181(1): 115–135, 2020. ISSN 0092-8674.

Dongdong Xu, Qian Zhang, and Xiuhan Li. Implantable magnetic resonance wireless power transfer system based on 3d flexible coils. *Sustainability*, 12(10): 4149, 2020. ISSN 2071-1050.

Zhangyu Xu, Nhan Duy Truong, Armin Nikpour, and Omid Kavehei. A miniaturized and low-energy subcutaneous optical telemetry module for neurotechnology. *Journal of Neural Engineering*, 20(3):036017, 2023. ISSN 1741-2552.

Zhangyu Xu, Majid Khazaee, Nhan Duy Truong, Deniel Havenga, Armin Nikpour, Arman Ahnood, and Omid Kavehei. A leadless power transfer and wireless telemetry solutions for an endovascular electrocorticography. *Journal of Neural Engineering*, 2024. ISSN 1741-2560.

Yiyuan Yang, Mingzheng Wu, Abraham Vázquez-Guardado, Amy J. Wegener, Jose G. Grajales-Reyes, Yujun Deng, Taoyi Wang, Raudel Avila, Justin A. Moreno, Samuel Minkowicz, Vasin Dumrongprechachan, Jungyup Lee, Shuangyang Zhang, Alex A. Legaria, Yuhang Ma, Sunita Mehta, Daniel Franklin, Layne Hartman, Wubin Bai, Mengdi Han, Hangbo Zhao, Wei Lu, Yongjoon Yu,

Xing Sheng, Anthony Banks, Xinge Yu, Zoe R. Donaldson, Robert W. Gereau, Cameron H. Good, Zhaoqian Xie, Yonggang Huang, Yevgenia Kozorovitskiy, and John A. Rogers. Wireless multilateral devices for optogenetic studies of individual and social behaviors. *Nature Neuroscience*, 24(7):1035–1045, 2021. ISSN 1546-1726.

Seungwon Yoo, Jonghun Lee, Hyunwoo Joo, Sung-Hyuk Sunwoo, Sanghoek Kim, and Dae-Hyeong Kim. Wireless power transfer and telemetry for implantable bioelectronics. *Advanced Healthcare Materials*, 10(17):2100614, 2021a.

Seungwon Yoo, Jonghun Lee, Hyunwoo Joo, Sung-Hyuk Sunwoo, Sanghoek Kim, and Dae-Hyeong Kim. Wireless power transfer and telemetry for implantable bioelectronics. *Advanced healthcare materials*, 10(17):2100614, 2021b. ISSN 2192-2640.

Z. Yu, J. C. Chen, F. T. Alrashdan, B. W. Avants, Y. He, A. Singer, J. T. Robinson, and K. Yang. Magni: A magnetoelectrically powered and controlled wireless neurostimulating implant. *IEEE Transactions on Biomedical Circuits and Systems*, 14(6):1241–1252, 2020. ISSN 1940-9990.

Xin yu Hu, Wen lu Yin, Fen Du, Chao Zhang, Pei Xiao, and Gaosheng Li. Biomedical applications and challenges of in-body implantable antenna for implantable medical devices: A review. *AEU - International Journal of Electronics and Communications*, 174:155053, 2024. ISSN 1434-8411.

Chong Zhang, Chengfeng Pan, Kai Fung Chan, Jinyang Gao, Zhengxin Yang, Kevin Kai Chung Leung, Dongdong Jin, Yuqiong Wang, Neng Xia, Zhipeng Ning, Xin Wang, Shuai Jiang, Zifeng Zhang, Qinglong Wang, Bo Hao, Philip Wai Yan Chiu, and Li Zhang. Wirelessly powered deformable electronic stent for noninvasive electrical stimulation of lower esophageal sphincter. *Science Advances*, 9(10): eade8622, 2023a.

Hao Zhang, Philipp Gutruf, Kathleen Meacham, Michael C Montana, Xingyue Zhao, Antonio M Chiarelli, Abraham Vázquez-Guardado, Aaron Norris, Luyao Lu, and Qinglei Guo. Wireless, battery-free optoelectronic systems as subdermal implants for local tissue oximetry. *Science advances*, 5(3):eaaw0873, 2019a. ISSN 2375-2548.

He Zhang, Jiwei Zhang, Zhiwei Hu, Liwei Quan, Lin Shi, Jinkai Chen, Weipeng Xuan, Zhicheng Zhang, Shurong Dong, and Jikui Luo. Waist-wearable wireless respiration sensor based on triboelectric effect. *Nano Energy*, 59:75–83, 2019b. ISSN 2211-2855.

Jiayan Zhang, Junshi Li, Zhe Huang, Dong Huang, Huaiqiang Yu, and Zhihong Li. Recent progress in wearable brain–computer interface (bci) devices based on

electroencephalogram (eeg) for medical applications: a review. *Health Data Science*, 3:0096, 2023b. ISSN 2765-8783.

Jungang Zhang, Rupam Das, Jinwei Zhao, Nosrat Mirzai, John Mercer, and Hadi Heidari. Battery-free and wireless technologies for cardiovascular implantable medical devices. *Advanced Materials Technologies*, 7(6):2101086, 2022.

Yi Zhang, Daniel C Castro, Yuan Han, Yixin Wu, Hexia Guo, Zhengyan Weng, Yeguang Xue, Jokubas Ausra, Xueju Wang, and Rui Li. Battery-free, lightweight, injectable microsystem for in vivo wireless pharmacology and optogenetics. *Proceedings of the National Academy of Sciences*, 116(43):21427–21437, 2019c. ISSN 0027-8424.

Yi Zhang, Daniel C. Castro, Yuan Han, Yixin Wu, Hexia Guo, Zhengyan Weng, Yeguang Xue, Jokubas Ausra, Xueju Wang, Rui Li, Guangfu Wu, Abraham Vázquez-Guardado, Yiwen Xie, Zhaoqian Xie, Diana Ostojich, Dongsheng Peng, Rujie Sun, Binbin Wang, Yongjoon Yu, John P. Leshock, Subing Qu, Chun-Ju Su, Wen Shen, Tao Hang, Anthony Banks, Yonggang Huang, Jelena Radulovic, Philipp Gutruf, Michael R. Bruchas, and John A. Rogers. Battery-free, lightweight, injectable microsystem for in vivo wireless pharmacology and optogenetics. *Proceedings of the National Academy of Sciences*, 116(43): 21427–21437, 2019d.

Jinwei Zhao, Rami Ghannam, Kaung Oo Htet, Yuchi Liu, Man-kay Law, Vellaisamy AL Roy, Bruno Michel, Muhammad Ali Imran, and Hadi Heidari. Self-powered implantable medical devices: photovoltaic energy harvesting review. *Advanced healthcare materials*, 9(17):2000779, 2020. ISSN 2192-2640.

Y. Zhong, B. Qian, Y. Zhu, Z. Ren, J. Deng, J. Liu, Q. Bai, and X. Zhang. Development of an implantable wireless and batteryless bladder pressure monitor system for lower urinary tract dysfunction. *IEEE Journal of Translational Engineering in Health and Medicine*, 8:1–7, 2020. ISSN 2168-2372.

Amir Zjajo. *Neural Signal Classification Circuits*, pages 77–93. Springer International Publishing, Cham, 2016. ISBN 978-3-319-31541-6.

Mohammad Zulqarnain, Stefano Stanzione, Ganesh Rathinavel, Steve Smout, Myriam Willegems, Kris Myny, and Eugenio Cantatore. A flexible ecg patch compatible with nfc rf communication. *npj Flexible Electronics*, 4(1):1–8, 2020. ISSN 2397-4621.

Appendix A

Appendix

As an appendix, this should contain some content that's not really required for the argument in the main body of the thesis, but is clearly relevant and supports the work.

A.1 Including published Paper

This section is attached to the paper I have published and included in Chapter3 and chapter4.

IOP Publishing J. Neural Eng. 20 (2023) 036017 https://doi.org/10.1088/1741-2552/acd147

Journal of Neural Engineering

PAPER

A miniaturized and low-energy subcutaneous optical telemetry module for neurotechnology

Zhangyu Xu[1], Nhan Duy Truong[1,2], Armin Nikpour[3,4] and Omid Kavehei[1,2,*]

[1] University of Sydney, School of Biomed Engineering, Sydney, NSW 2006, Australia
[2] BrainConnect Pty Ltd, Sydney, NSW 2006, Australia
[3] Univ Sydney, Fac Med & Hlth, Cent Clin Sch, Sydney, NSW 2006, Australia
[4] Royal Prince Alfred Hosp, Dept Neurol, Camperdown, NSW 2050, Australia
[*] Author to whom any correspondence should be addressed.

E-mail: omid.kavehei@sydney.edu.au

Keywords: low-energy, optical-telemetry, neurotechnology

OPEN ACCESS

RECEIVED
27 February 2023

ACCEPTED FOR PUBLICATION
28 April 2023

PUBLISHED
22 May 2023

Abstract

Objective. This study presents a proof-of-concept optical telemetry module that leverages a single light-emitting diode (LED) to transmit data at a high bit rate while consuming low power and occupying a small area. Our experiments showed that we could achieve 108 Mbit s^{-1} and 54 Mbit s^{-1} back telemetry data rates for tissue thicknesses of 3 mm and 8 mm, respectively. *Approach.* The proposed module is designed to be powered by near-field coupling and achieve bidirectional communication by low-speed downlink from near-field communication. It aims to minimize the size of the implant while providing reliable transmission that meets the requirements of high-speed wireless communication from a multi-electrode array neurotechnology implant outside the body. *Results.* The power consumption of the module is 1.57 mW, including the power consumption of related circuits, resulting in an efficiency of 14.5 pJ bit^{-1}, at a tissue thickness of 3 mm and a data rate of 108 Mbit. The use of an optical lens, combined with tissue scattering effect and optimized emission angle, makes the module robust to misalignments of up to $\pm$5 mm and $\pm 15^{\circ}$ between the implantable and external units. The LED in the implantable unit is only $0.98 \times 0.98 \times 0.6$ mm^3, and the testing module is composed of discrete components and laboratory instruments. *Significance.* This work aims to show how it is possible to strike a balance between a small, reliable, and high-bit-rate data uplink between a neural implant and its proximal, wirelessly connected external unit. This optical telemetry module has the potential to be integrated into a significantly miniaturized system through an application-specific integrated circuit and can support up to 1000 channels of neural recordings, each sampled at 9 kSps with a 12-bit readout resolution.

1. Introduction

Uncovering the neurophysiology mechanism with the electrophysiology approaches has pushed the development of neuro signal sensor implants with higher spatial and temporal resolution [1]. With the advancement of integrated circuits and materials, the state-of-the-art neuro signal sensor implants for animal research have 768 electrodes in a 750×720 μm^2 area and can record 10 240 sites from two probes [2]. The sensors for human clinical studies now include two 96-channels in less than 36 mm^2 [3]. Some independent company, such as Neuralink, is developing systems has more than 1000 channels for human [4]. The demand for a better understanding of neural activities and improving the performance of decoding neural signals have pushed the analog-to-digital converter (ADC) sampling rate to over 30 kHz for each recording channel with 10–16-bit resolution [5]. With those high-performance neural signal sensors, more and more brain-computer interfaces (BCIs) have achieved promising results, such as accurately controlling a robotic arm, moving a computer cursor, and typing at a speed close to handwriting [6–9].

BCI devices or neural signal recording systems comprise signal collecting, processing, and executing units. However, limitations in power and size have

IOP Publishing J. Neural Eng. 20 (2023) 036017 Z Xu et al

prevented the development of stand-alone devices with the desired human functions. These systems are currently divided into internal and external units. The internal unit, which is an implant or a set of implants located near the sensing or stimulation site, should be miniaturized to minimize invasiveness. It contains only electrodes, lead wires, electronic hermetic housing, and signal acquisition circuits. On the other hand, the external unit functions as a power source, accommodating components that exceed the volume or power constraints of the implant or serving as a relay to transmit neural activities to another processing unit. An interface between the internal and external units is required to deliver data and energy. In some advanced BCIs, the standard setup (mainly research-driven) uses wire as the internal and external interface [9, 10]. The reason is that the high-performance multichannel neural signal sensors have pushed the data streaming requirement to tens of megabits per second for raw data. The wired solutions provide the simplest way to meet the design requirements of high data rate, small size, adequate power supply, and safety concerns. Still, the wired system significantly limited the clinical applications and the diversity and duration of research experiments. The wired systems also increase the risk of device failure and tissue infection.

Currently, we can see a high degree of engineering efforts to achieve wireless transcutaneous systems to transfer high-rate data [11–13]. The medium that can establish the transcutaneous data and energy transfer includes ultrasound, magnetic field, electric field, electromagnetic field, and optical links.

Ultrasound channels offer one of the deepest penetrations into soft tissue, making them an attractive option for deep neural implants. The transducer for the acoustic link is typically small, with reported dimensions of submillimeter and less than half a millimeter cube (mm^3) in recent literature [14, 15]. The power delivery of the acoustic channel has an efficiency of 1.93%–0.23% [14, 16–18], and the data link for the acoustic link typically uses a backscatter approach to maintain the low power consumption in the internal part. The resonate frequency of the piezoelectric material is usually <2 MHz [16, 17, 19, 20], so the optimal frequency for the acoustic channels is often below 5 MHz [21]. However, due to the backscatter approach used for data telemetry links, implementing modulation schemes like orthogonal frequency-division multiplexing (OFDM) is often challenging. As a result, ultrasound channels can only typically provide a few hundred kbit s^{-1} telemetry data links.

Inductive links use alternating magnetic fields through coils to transmit energy and data. The inductive link offers high power transfer efficiency when the distance between the source and receiver is less than 30 mm [22]. A reported efficiency of 95% is achievable when the distance is 10 mm [23]. Inductive links typically operate at a frequency below 20 MHz to maintain a balance between the transmitter's efficiency and the efficiency between the transmitter and receiver. These links can provide half-duplex bidirectional communication, and commercially available products report an 800 kbit s^{-1} data rate.

The capacitive link utilizes the tissue as a dielectric medium to form a capacitor. It builds the path to transfer data and power between tissues using a pair of capacitor plates between tissues [21]. The advantage of capacitive link for data and power telemetry includes the high-frequency pass character and the confined area of the energy field [24]. When using a capacitive link to transfer data and power through tissue, the electric field only impacts the tissue between the electrodes and does not broadcast widely like an electromagnetic field [25]. This character also enables the multichannel capacitive link to be built on the same implant to extend the bandwidth. The plates for capacitive link range from 5×5 mm^2 to 40×40 mm^2 and the carrier frequency ranges from 0.2 to 20 MHz [26–31]. The drawback of the capacitive link includes the potential damage to the living tissue caused by the electric field in a small area and the limitation of the miniaturization ability [30]. Another drawback of the capacitive link is the need for close contact of the plates on the tissue surface, which adds a challenge to applying a capacitive link at a site where the tissue surface, or contact in general, is not flat (e.g. hairs) [30].

From above, the most popular approach is the electromagnetic field, as it can easily achieve power delivery and have bi-directional data at the same time. There are two challenges when using an electromagnetic field to send high bandwidth data through tissue. One is that the living human tissue consists of a large among of water. A large amount of skin tissue is conductive, meaning the absorption rate increases exponentially with frequency. A large amount of energy will be absorbed by tissue when the radio frequency is over 2 GHz [32, 33]. So, when carrying on high bandwidth data through tissue using electromagnetic, the human tissue becomes a questionable choice of the communication channel. Another challenge is that when the electromagnetic frequency increases, the analog radio frequency frontend becomes a power-hungry component and consumes more power than the neural signal recording sensor. Apart from the limitation originating from the physical property, another issue with RF transmission is the environment's interference, as many devices may operate at the same frequency that the implants are proposed to use.

Apart from optimizing the transmission channel to meet the requirement of uplink data telemetry of recorded neural signal, we can see a significant degree of efforts published each year to reduce the data rate by enabling more local data processing in the implant [34]. The popular solution includes spike thresholding, which only sends spike count over a certain

IOP Publishing J. Neural Eng. 20 (2023) 036017 Z Xu et al

threshold; another example is compressive sensing which adaptively compresses data by event, which turns the raw signal into a set of featured spikes [35, 36]. The spike-related approaches have significantly lowered the high bandwidth requirement of the telemetry data link. The spike signal meets some targeted applications very well. However, transmitting a high-fidelity signal is still needed for many applications such as brain disease monitoring, research on BCIs algorithms, and neural electrophysiological research.

The optical link is a promising solution for transmitting high-fidelity neural signal from high channel density sensors and has been explored by researchers in recent years [37–39]. The advantage of optical links includes small transducer size (relative to inductive and capacitive links), high bandwidth, multiple modulation approaches, high energy efficiency, magnetic resonance imaging (MRI) compatibility, and robustness against environmental EM noise.

Optical transcutaneous links have already achieved some promising results. One example has achieved a data rate of 300 Mbit s^{-1}, in which a vertical cavity surface emitting laser (VCSEL) is used as the transducer, and a super-fast photodiode is the receiver [40]. Other examples include modules that are demonstrated *in-vivo* in mice, where they used microscale inorganic light-emitting diode (LED) as the transducer and a group of photodiodes as the receiver. Benefit from the small size of the transducer, chronic recording of neural dynamics has been achieved in that work, but the maximum data rate in the *in-vivo* experiment only reached 27 kbit s^{-1} [41, 42]. Hence, a better balance of high data rate, low power consumption, small volume, and robust to misalignment has not yet been demonstrated. Therefore, there is an excellent potential for using LEDs as the transducer to implement optical transcutaneous uplinks as it has a relatively small size and a high wall-plug efficiency.

2. Methods

2.1. System design overview

In this work, we present a novel design for an optical telemetry module that employs a single LED and addresses the challenges of high-speed data transfer, low power consumption, and minimal volume. Our module is well-suited for data transmission in multi-electrode neural recording implants and is designed to operate subcutaneously to facilitate implant-to-surface data transfer. As this module is intended to be a part of the neural recording implant, we designed the entire system, taking into account power supply, energy harvesting, and usability for both the telemetry module and the recording implant.

The proposed system, as shown in figure 1, comprises an implant and an external unit. The external unit comprises a behind-ear unit and an over-the-head unit. The behind-ear unit houses the rechargeable battery, power management circuits, and data storage or transmission components. The over-the-head unit, which is smaller and lighter, is positioned over the site where the internal implant is located beneath the skin. This unit includes an optical receiver that retrieves high-bandwidth data from the implant. To demonstrate the concept, we used a coil that employed 13.56 MHz near-field coupling to provide power and less occupied forward control data link (downlink). This setup helped us showcase the potential of our proposed design.

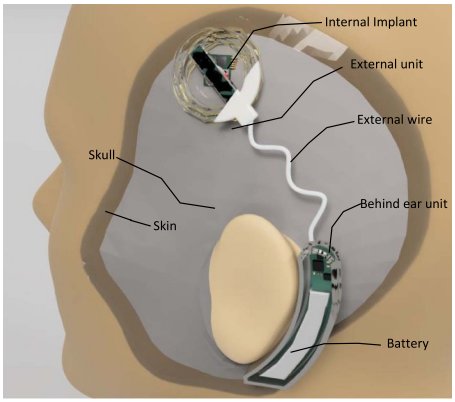

Figure 1. The system design with the potential application. The system consists of internal implant, external unit with a behind ear unit. The proposed optical telemetry module is in the internal implant and aims to send high-speed data from the sensor to the external unit. The external unit include receiver and power delivery circuit, and the battery is in the behind ear unit to reduce the weight of the overhead unit.

This design utilizes the high efficiency of inductive power delivery and the high data rate of the optical link. Apart from optimizing power delivery efficiency, the extra forward data can be used to exchange control signals and send handshaking signals for the high bandwidth optical communication channel. This link will further enhance the channel stability, simplify the communication protocol and related hardware design, and lower the internal unit's power consumption. The overhead unit can also have a local data processing unit to implement applications, like controlling a brain stimulation device to achieve closed-loop brain stimulation.

In figure 2, we present the critical component of our proposed system and demonstrate how the optical telemetry module works with the neural recording implant. In one possible implant configuration, high-density electrodes are positioned on the cortex to collect neural signals, while the analog front-end and ADC are located in a package that replaces a small part of the skull. The optical communication module is placed above the neural signal sensor under the skin tissue, minimizing internal connections. The transducer is a single 940 nm near-infrared InGaN LED, and an application-specific integrated circuit

IOP Publishing J. Neural Eng. 20 (2023) 036017 Z Xu et al

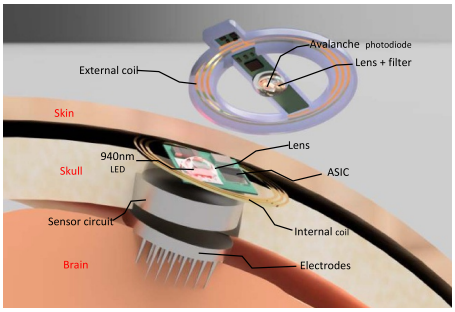

Figure 2. The main parts of the proposed system. Note that in our experiments we considered power harvesting via a conventional near-field antenna system. The power can be delivered also through optical energy harvesting and the device has a potential to achieve bidirectional communication via optical link.

(ASIC) is utilized to encode data and modulate the LED. A lens is positioned on top of the LED to focus the beam with an optimal emitting angle that matches the tissue thickness. A patch coil on a thin, flexible printed circuit is wrapped around the communication module to receive energy from the external coil through inductive link. The low power consumption of the proposed communication module is achieved through the high wall-plug efficiency of the LED and the low interference of the optical channel, which permits us to use a highly sensitive avalanche photodiode (APD) with high gain to recover the faint optical pulses from the internal unit with less concern about noise. With the advantage of the short wavelength of light, a high data rate can be achieved with a simple modulation approach that enables us to simplify the circuit and remove the power-hungry high-frequency analog part, thus further reducing power consumption.

2.2. Design and implementation

2.2.1. Design requirement analysis

2.2.1.1. Data rate requirement

The communication module is designed to stream high-fidelity neural signals throughout the skin tissue. Currently, the clinically available neural signal sensor has 100 (Utah array) [43] to 1024 (Neuralink) electrodes [44]. In order to identify a neural spike, both 0–1 mV magnitude local field potential and 0–10 μV extracellular action potential need to be recorded at the same time [45]. As a result, the minimal requirement of the effective number of bits of the ADC is eight-bits [45], which is usually achieved by an ADC with over ten-bits resolution [35, 46]. As described above, the data transmission requirement can be calculated as follow:

$$Ds = \frac{n_{\text{Channels}} \times R_{\text{resolution}} \times f_{\text{sampling}}}{H_0} \quad (1)$$

where H_0 is the encoding efficiency.

Take a neural-signal sensor with 100 channels as an example. When the sampling rate is 20 kSps, and the resolution of the ADC is 14 bits. When we use Manchester encoding with an efficiency of 50%, the data rate requirement will be 56 Mbit s^{-1} to send the raw neural signal out.

2.2.1.2. Noise analysis

For this proposed optical telemetry module, three main reasons will influence the signal quality. First is the environmental light interference. Compared to the electromagnetic (EM) field, fewer artificial signals work in the open-air optical domain, and the transmission of light has a specific direction that further reduces the chance of interference between different devices. Indoors, the light source is mainly visible (380 nm–700 nm wavelengths) and only have very limited energy in the near-inferred wavelength. However, sunlight covers a vast range of wavelengths, and the power in wavelengths from 900 nm to 1000 nm is much stronger than indoor light, which is the main challenge to this proposed optical telemetry module. As a result, the over-the-head unit also needs to be designed to block the sunlight shining into the internal unit.

The second source of the noise is from the receiver side. To convert the optical signal to an electronic signal that can be processed further, we need a photodiode with high speed and high sensitivity. The light from the internal LED can be feeble, and it needs to detect fast light intensity changes as the optical signal we designed is short period pluses. The photodiode will generate noise as the physic intrinsic. The signal from the photodiode is typically a small signal and needs to be further amplified to restore the information collected from the sensor. In most cases, the signal from the photodiode is a current signal requiring a trans-impedance amplifier (TIA) to turn it into a voltage signal and then send it to one or a few cascades amplifiers to increase voltage level further to help restore the data.

The third source of noise is the tissue impact. When the light travels through the skin, there is reflecting, refraction, and absorption of the light. The reflecting and refraction caused multipath effects generating noise and impacting the optical communication channel. The light wavelength ranging from 350 nm to 2000 nm are widely used in optical communication systems. For transcutaneous application, the distance between transmitter and receiver ranges from 0.5 mm (epidermal only) to over 10 mm (total skin thickness). With the short wavelength of light and the relatively short transmission distance, the multipath can be ignored for transcutaneous optical channels.

The total noise introduced to the optical communication module can be calculated as equation (2),

$$i^2_{\text{noise}} = i^2_{\text{env}} + i^2_{\text{Pd}} + i^2_{\text{TIA}} + i^2_{\text{AMP}}. \quad (2)$$

IOP Publishing J. Neural Eng. 20 (2023) 036017 Z Xu et al

2.2.1.3. Power consumption analysis

The power consumption of the uplink data module is the sum of the power consumption of the transducer and the power consumption of the circuit to control and modulate the transducer. The higher the wall-plug efficiency of the transducer indicates the less energy dissipates during the transformation. Currently, LEDs have the highest wall-plug efficiency in generating photons from electrical power, and the integrated circuits that only consist of digital components can operate at GHz with sub-microwatt power consumption. Removing the high-frequency analog circuits in the design will lower the power consumption of the proposed communication modulation module.

2.2.1.4. Optical channel analysis

The human skin has three layers: epidermis, dermis, and subcutaneous fat. The skin tissue presents as a complex heterogeneous medium to lights [47]. The optical properties of human skin can be characterized by absorption and scattering coefficient [48]. The hemoglobin in the blood and the melanin in the epidermis are the substances that dominate the absorption. The scattering effect changes the direction and polarization of the light. Scattering can happen both on the contacting interface and within a small region where the optical property varies [49]. The main factors that contribute to scattering are filamentous proteins and the fibrous structure of the tissue. The scattering can happen at both a single fibril and a scattering centers as the interlacement of the proteins and bundles [49]. The distribution of the blood, pigments and protein bundles are inhomogeneous and random in the skin and varies over time, which makes the absorption and scattering coefficient change over time [47].

Both *in vitro* and *in vivo* studies showed that the lights with a wavelength between 800 nm and 1200 nm have lower absorption and scattering coefficient for the human skin tissue [50–52], which is suitable for optical power transfer through the skin and building a power-efficient telemetry link.

To design the optical components for the optical communication module, we did a skin simulation to check the transmitted light power on the skin surface at the receiver side. The light propagation in a tissue can be described using the scalar stationary radiation transfer theory, which is described in equation (3) [47],

$$\frac{\partial I(\vec{r},\vec{s})}{\partial_s} = -\mu_t I(\vec{r},\vec{s}) + \frac{\mu_s}{4\pi}\int_{4\pi} I(\vec{r},\vec{s})\rho(\vec{s},\vec{s}')\,\mathrm{d}\Omega'. \tag{3}$$

In equation (3), $(\vec{r},\vec{s})$ is the specific intensity at the point $\vec{r}$ in the given direction $\vec{s}$. $\rho(\vec{s},\vec{s}')$ is the scattering phase function. $\mathrm{d}\Omega'$ is the unit solid angle about the direction $\vec{s}$, and μ_t is the total attenuation coefficient. A least-squares Gaussian model can fit the distribution and approximate the shape of the power intensity at the receiver side when we assume the skin has an ideal smooth surface, which simplifies the simulation model and helps us analyze the light pass-through skin with different thicknesses. The Gaussian model in the form of equation (4) [37],

$$Jrx\lambda(r,\theta) = \frac{A}{\sigma\sqrt{2\pi}}\mathrm{e}^{-\frac{r^2}{2\sigma^2}}. \tag{4}$$

According to [37], we use an exponential and quadratic random coefficient to represent the Gaussian parameters A and σ, respectively.

In figure 3, *Dr* is the light source size. For LED, *Dr* equals the emitting area in the diode.

α is the emitting beam angle that can be controlled by lens design.

Dd is the diameter of the projection light spot, which does not consider the tissue scatter effect.

Ds is the diameter of the light beam with the full width at half of the maximum (FWHM) energy of the Gaussian distribution on the skin surface.

Dn is the diameter of the lens to focalize the light to the photodiode to increase the receiving optical power on the receiver side.

Tn is the thickness of the skin tissue.

With equation (3) and the quantitative measure of skin's optical property in [37], we write a Python code (available on the link) to simulate the effect of light passing through skin tissue. Figure 4 shows the simulation result with optical energy distribution on skin surface.

From the simulation, we can find for lights in 800–980 nm wavelength, the optical channel of tissue is dominated by the scattering effect. When tissue thickness is 3 mm, we can still observe the shape of the light emitting source. On the receiver side, the

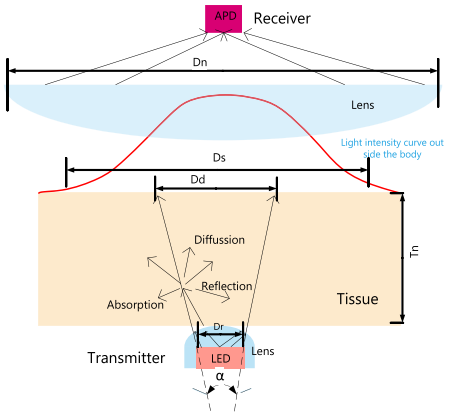

Figure 3. The optical design of the subcutaneous telemetry module. LED is the transmitter and the APD is the receiver. The lens at the transmitter side controls the emitting beam angle α, and the lens at the receiver side collecting light and focus on the APD's surface.

IOP Publishing J. Neural Eng. 20 (2023) 036017 Z Xu et al

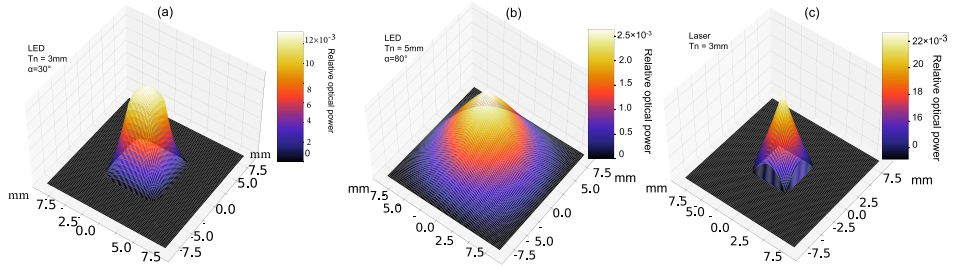

Figure 4. The simulation result of the optical power distribution on the skin surface with different light source with different tissue thickness. (a) $Tn = 3$ mm, $Dr = 0.98 \times 0.98$ mm and $\alpha = 30°$ (b) $Tn = 5$ mm, $Dr = 0.98 \times 0.98$ mm and $\alpha = 80°$ (c) use laser as the light source which has a relatively smaller spot size (100 μm) and $Tn = 3$ mm.

area that has the optical energy is around 90 times larger than the light emitting source size when the light passes the tissue. Compared with the laser source, the optical power distribution on the skin surface is a plateau shape, making it robust to the heterogeneous optical property of the tissue. For laser, the peak power on the receiver side is only in a small hot spot and decreases rapidly from the central point, increasing the misalignment challenges. For laser transmitters, the receiving power will significantly drop when the peak power point is a pigmentation area.

Figure 5 shows the relationship of tissue thickness (*Tn* in figure 3), total optical power, affecting tissue area and light-emitting beam angles (α in figure 3). From the figure, we can find that with thicker tissue, a small emitting angle will have less energy attenuation, and with thin tissue, emitting angle less than 80°, the total receiving power remains the same, but the collecting area increases linearly. The simulation can help us find the optimal emitting angle for the light emitting source to improve the power efficiency. Here we take 3 mm skin as an example. We can find that when the emitting angle is below 60°, the total receiving power and optical energy collecting area will be balanced well.

Figure 6 is the simulation result of the collected optical energy on the skin surface with different skin thicknesses and diameters of the lens. The solid curve is the receiving power on the photodiode. The dashed line is the FWHM diameter of the light beam on the skin surface. Figure 6 reveals that there has been a sharp rise when the lens diameter increases from 1 mm to a size that close to the spot diameter of the FWHM. With the increasing lens diameter, the attenuation caused by lens optical material overweight the benefit from the increasing diameter, and the collected energy gradually decreases. What can be clearly seen in this figure is when the skin thickness increases, the relative improvement of receiving energy from the help of a lens increases, and with thicker tissue, the amount of collected optical energy is projected to remain steady when the diameter of the lens reaches to a certain point. This trend indicates that a lens with an optimal diameter that matches the tissue thickness will significantly improve the signal quality, and a bigger lens will have less alignment requirement when the optical source is in a thicker tissue.

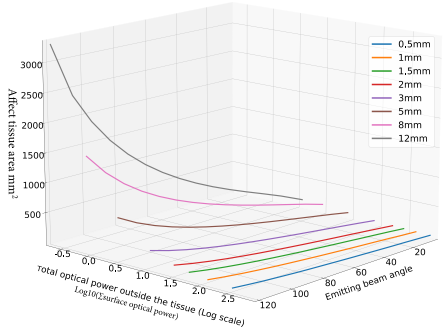

Figure 5. The total optical energy on the skin surface with different tissue thickness and light emitting beam angles. The X-axis is the emitting beam angle, the Y-axis is the total optical power outside the tissue, and the z-axis is the area affected by the optical power in mm^2.

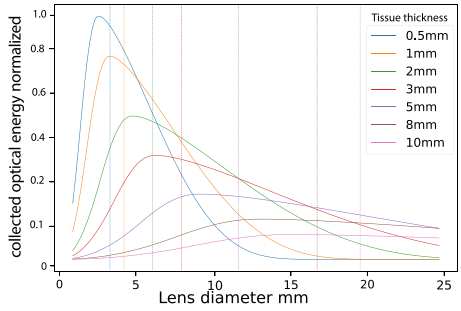

Figure 6. Lens performance simulation result. Color code indicates different tissue thickness, the dash line is the diameter of the FWHM diameter on skin surface.

2.2.2. Module and circuits design

The system design of the proposed system is presented in figure 7, which displays the block diagram of

IOP Publishing J. Neural Eng. 20 (2023) 036017 Z Xu et al

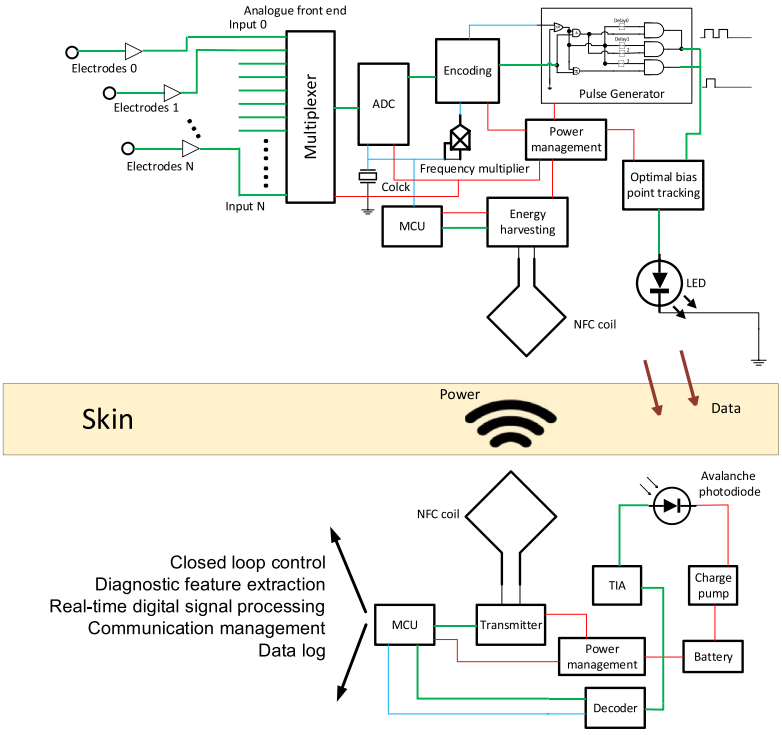

Figure 7. The system block diagram. The upper part is the internal implant. The yellow strip in the middle indicates the skin tissue. The lower part is the external unit.

the internal unit. The internal unit consists of several components, including an analog front end, an ADC, a microcontroller unit (MCU), an Near field communication (NFC) power harvesting and communication module, an encoding unit, a power management unit, a pulse generator, and a dynamic voltage bias circuit. The crystal within the internal unit serves as a clock source, while a frequency multiplier multiplies the base clock for the pulse generator and encoding unit. The bias tracking unit provides a bias current to the LED, ensuring it can generate short period optical pulses with low current digital signals from the pulse generator while maintaining low power consumption. The optimal bias tracking circuit, consisting of two instrumental amplifiers and a low-power digital-to-analog converter (DAC), is designed to provide a dynamic bias voltage that stabilizes the LED's impedance, allowing the electrical pulse from the pulse generator to turn to an optical pulse successfully. This circuit provides a dynamic bias voltage, which keeps the LED's impedance at a constant level, regardless of changes in environmental light and temperature.

Figure 8 is the proposed pulse generator's circuit block diagram that only uses digital components to ensure low power consumption. Instead of using plus amplitude, we use pulse density to encode digital logic. With this modified on-off-key modulation, the phase shift will not impact the signal's recovery and allows the phase locker removal.

The proposed pulse generator has five delay units with two different delay times, delay 1 and delay 2. The logic gates compute the data signal and clock signal, then output pluses with varying densities in a single clock circle. Here delay 1 is the output pulse width, and delay 2 equals two times of delay 1. From figure 8, we can find that when the data is logic high, then after the digital computing, the output signal is a double pulse shown as logic 1. When the data is logic low, the output is a single pulse shown as logic 0. When delay 1 $\leqslant$1/4 of the clock signal circle, the signal and clock can be recovered on the receiver side. Here we set the delay 1 $\leqslant$1/5 of the clock circle, so any phase shift of the delay unit will not influence the recovery of the data.

The block diagram of the circuit in the external unit showed in figure 9. A high gain low noise APD is chosen to collect optical signals. The TIA consists of two high-speed operational amplifiers (LTC 6268-10 and ADA4860) in a cascade connection. A booster with a low-side metal-oxide-semiconductor field-effect transistor (MOSFET) switch (TPS55340) is chosen to boost the voltage to provide voltage bias for the APD. The internal switch in the booster is directly connected to an inductor and a set of charge

IOP Publishing J. Neural Eng. 20 (2023) 036017 Z Xu et al

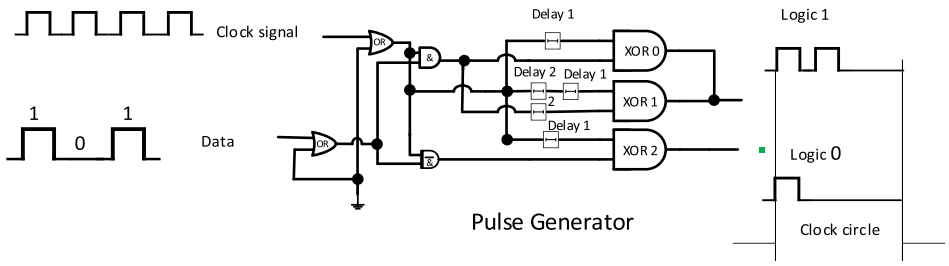

Figure 8. The schematic diagram of the proposed pulse generator for the LED to generate optical spikes. The input of the pulse generator is digital signal from the sensor with corresponding digital clock, and the output is short pulse to drive the LED to generate optical spikes.

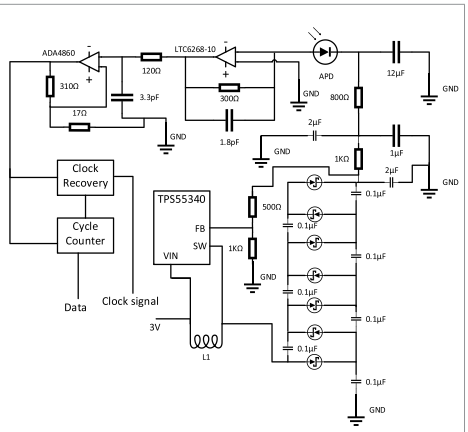

Figure 9. The schematic diagram of the external unit, consisting with TIA, APD bias voltage booster and blocks to recovery clock and data from optical spikes.

pump networks to further elevate the output voltage to increase the gain of the APD. After the amplifier, the signal from the APD is sent to two logic units to recover the clock and data signal.

The clock recovery is achieved in two steps. The first step is to recover a trigger signal for the cycle counter. The output of the first step is a periodically triggered signal which matches the optical pulse detected by the APD and works like a clock signal. As there is no phase locker for the pulse generator in the internal unit, the output of the first step only matches the optical pulse cycle but is not a stable clock signal. The duty cycle of the first step output is also not correct for clock synchronize that why a second step circuit is needed to recover the clock. The first step can be implemented with raising and falling edge detection and delay network circuits. The delay time is set to four times of the interval between every first rise and fall edge, which has been detected from the output of the TIA. When the edge detector detects the first rise edge, the output of the first step is set to logic high, and it reminded high until it reaches the delay time. The second step is designed to output a stable clock signal with the recovered data. The clock cycle of the second step output is the interval between every first rise edge that excluded all edges during the delay period, and the pulse width of the second step output is half of the delay time.

The data recovery is achieved by a cycle counter that continues count pulses when the output of first step clock recovery is logic high. When the pulse counter counts two pluses, the output of the data recovery is logic 1, and when the pulse counter result is one, the output is logic 0. The output level remained the same until a new counter cycle started. With the recovered clock signal, the digital logic can be processed further by a microcontroller and converted to a standard digital bus signal, for example, a serial peripheral interface.

2.2.3. LED module and impedance analysis at high frequency

The LEDs has high efficiency in generating optical signal within a small area from 25 μm^2 to around 1 mm^2 [53]. The challenge of LEDs for high-speed communication is the frequency response of LEDs follows the first order system with corresponding bandwidth up to hundreds of MHz [54]. When the frequency of the signal passing to the LED goes high, the parasitic capacitance lowers the LED efficiency and slows down the rising and falling time, significantly lowering the signal quality. Research on high-speed visible light communication systems has tested and modeled the LEDs for efficiency and signal quality improvement [54, 55]. From the result, we can find when the bias current passing through a LED is much smaller than the saturation current of the diode, the parasitic capacitance decreases exponentially with the resistance decreasing linearly [54, 55]. At the same time, the inductance of the LED remained at the same level, which means a high-power LED working at a low current will have a better efficiency performance at a higher frequency.

In figure 10, R_g is the resistance of the signal source to the LED. R_b is the bonding wire resistance. L_b is the parallel bonding inductance. R_s is the serial resistance. C_b is the bonding wire and

IOP Publishing J. Neural Eng. 20 (2023) 036017 Z Xu et al

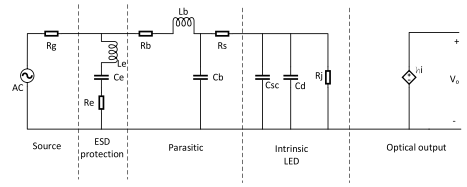

Figure 10. The equivalent circuit of LED. The LED model consists of three parts: the intrinsic property of the diode junction, the parasitic components induced by manufacturing and packaging, and the ESD protection components that are usually integrated into the commercial LEDs.

pad capacitance. C_{sc} is the space-charge capacitance in the junction. C_d is the diffusion capacitance in the junction. R_j is the junction resistance. L_e, C_e, R_e is the inductance, capacitance and resistance components in the Electrostatic discharge (ESD) diode. The impedance of the LED can be calculated as equation (5),

$$Z_{\mathrm{LED}} = \left[\left(R_j // \frac{1}{j\omega\left(C_d + C_{sc}\right)}\right) + R_s\right] // \left[\frac{1}{j\omega C_b} + j\omega L_b + j\omega L_b + R_b\right] // \left[j\omega L_e + \frac{1}{j\omega C_e} + R_e\right]. \tag{5}$$

The frequency response of the LED communication can be calculated by the following transfer function equation (6):

$$H(jw) = \frac{V_o}{Vs} = \frac{hi}{iR_g + iZ_{LED}\left(j\omega\right)} \tag{6}$$

hi is the gain of the photodiode at the receiver side.

We measured the impedance of the LED using an impedance spectroscopy device and wrote Python code (available on the link) to estimate the model's parameters and then predict the LED's power consumption when delivering short-period pulses. To simplify the model, the intrinsic capacitance $C_d + C_{sc}$ is represented with one parameter C_j.

Table 1 shows the estimated parameters at different currents.

Figure 11 shows the prediction of the LED on high frequency using the estimated parameter. During the testing, we discovered that when there is no bias voltage applied to the LED or when the bias voltage does not generate a forward current over 50 nA, the LED's impedance fluctuates from each measurement. When we send short-period pulses with a low current under this situation, the LED will not generate a stable optical pulse that the APD can detect. As a result, we added a bias tracking circuit in the design to provide a minimal optimal forward current. With the small current bias, the impedance of the LED at high frequency is stable, and low current voltage electrical pulses can be converted to a detectable optical pulse by the LED.

3. Results

3.1. Experiment setup

To evaluate the performance of our design, we conducted tests using a 940 nm wavelength LED, a lens, and a high-frequency arbitrary waveform generator (Keysight P9336A) to implement the circuit of the internal unit. The frontend of the external unit was implemented using discrete components, including an ultra-low-noise and high-gain APD (MTAPD-07-010), a low-noise APD voltage bias circuit, and a high-speed TIA circuit. We 3D printed a housing to hold an optical lens and a long-pass filter to implement the optical parts of the external unit. An oscilloscope equipped with a storage function was used to test the data recovery function and measure data transfer performance.

Figure 12(a) depicts the experimental setup used to test the transmission distance and the impact of misalignment between the transmitter and receiver units, which were both mounted on optical stages.

Figure 12(b) illustrates how the distance, misalignment, and angle were measured, with the green line representing the distance, the yellow line indicating the misalignment, and the angle between the two red lines representing the misalignment angle. A 3D printed frame was used to hold the tissue and test the data transfer performance with tissue in between, as shown in the sub-photo on the top right corner of figure 12(b). The transmission success judgment was achieved by the waveform matching function in the oscilloscope. In the experiment, we tested the data transfer in the air with and without the lens on the receiver side to verify the lens performance simulation results obtained in the design stage. We used extracted skin, fat, and muscle tissue with varying thickness to test the transmission performance with tissue between the transmitter and receiver. Data transfer experiment protocol is described in figure 13. To confirm the success of the data transfer, we generated a 64-bit random data segment, which we repeated 256 times to extend the data to 2 kB. We encoded the data using the proposed modified on-off-key encoding described in the design section and translated the data to a waveform file. We then uploaded the waveform file to the arbitrary waveform generator to generate periodically repeated pulses according to the data segment. When the arbitrary waveform generator started working, we recorded the waveform from the receiver side with no tissue in between. We exported the waveform data from the oscilloscope and used an edge detection function written in Python to implement the clock recovery and data decoding function described in the design section. If the decoding result matched the input data segment, we confirmed the

IOP Publishing J. Neural Eng. 20 (2023) 036017 Z Xu et al

Table 1. The LED module parameter at different forward current.

Current	R_j (Ω)	C_j (nF)	R_s(Ω)	R_b(Ω)	C_b(pF)	L_b(nH)	R_e(Ω)	C_e (pF)	L_e (nH)
50 nA	5	0.05	4.3	0.2	2.3	0.24	17	48	98
500 nA	5.1	0.013	5.3	0.2	3.3	0.24	17	60.3	98
1 μA	5	0.04	5	0.2	3.1	0.24	17	273	98
10 μA	5	0.06	5	0.2	3.9	0.24	17	284	98
50 μA	1.75	0.06	1.85	0.2	4.2	0.24	17	324	98
100 μA	1.535	0.08	0.5	0.2	4.1	0.24	17	295	98
200 μA	1.355	0.44	0.5	0.2	3.71	0.25	17	345	98
5 mA	0.199	5.1	5.18	0.05	11.9	2.1	94	683	40.3
50 mA	0.048	7.4	0.48	0.19	8.12	1.72	3.78	113	2.75
100 mA	0.046	18	0.46	0.19	15.4	1.74	2.54	217	7.4

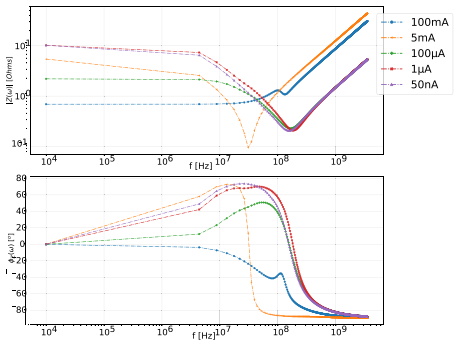

Figure 11. LED impedance estimation using the estimated parameter at different current with the LED model. Upper part shows the amplitude, and the lower part shows the phase.

data transfer was successful; otherwise, we adjusted the pulse width and density and repeated the process until we obtained a positive outcome. Once the initial data transfer was confirmed, we added misalignment, distance, and tissue to verify if the waveform remained the same pattern with the recorded signal using the built-in waveform pattern matching function of the oscilloscope. If the matching was successful, we confirmed the transmission was successful, and vice versa. As the oscilloscope had limited storage to hold the receiving signal, we fixed the length of the random data segment at 64 bits to minimize the experiment challenge of synchronizing the waveform generator and oscilloscope waveform catch. The data transmission confirmation was done by the Python code that performed circular shift and tried to match the sending 64-bit data and the recovered data. Once the first 64 bits found a match, and the matching could last until the end of the recording, we regarded this as a successful transmission. As a result of the small data segment and the offline data transmission confirmation protocol used in the experiment, we were not able to measure the bit error rate (BER). The oscilloscope's memory could hold 4 Mpts, and the sampling rate was fixed at 5 G samples per second. Under this setting, we could only record the receiving data in 0.4 ms for transmission confirmation. We can estimate the BER by calculation. If the transmission passed confirmation checking, the BER must be lower than $\frac{1}{\text{data rate}\times 0.4\times 10^{-3}}$. For example, when the data rate is 108 Mbit s^{-1}, we can confirm the BER is lower than 2.31×10^{-5}.

3.2. Data rate testing result

Table 2 shows the successful data transfer testing result with different parameters and different thickness of tissue.

3.3. Power consumption estimation

The power consumption of the proposed design's internal unit is estimated by combining the transducer power consumption with the circuit power consumption. The transducer power consumption is calculated from our LED modeling and impedance testing. The circuit power consumption includes both the functional circuit power consumption and the power management circuit power consumption. The functional circuit comprises the pulse generator, encoder, and optimal bias tracking circuit. As the bias voltage is intended to generate <1 μA current and the circuit is operating at a frequency <500 Hz, the power consumption of the bias tracking circuit is a

IOP Publishing J. Neural Eng. 20 (2023) 036017 Z Xu et al

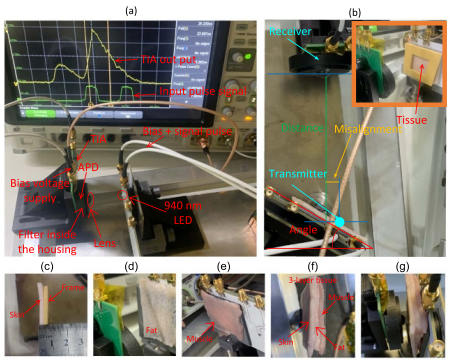

Figure 12. The experiment setup. (a) The transmitter and the receiver are mounted on optical stages. The LED is mounted on the stage shown in the bottom right corner. The stage on the bottom left is the APD with optical lens. Oscilloscope shows the signal from TIA and the waveform generator. (b) The setup and measurement of data transfer distance, misalignment angle and misalignment distance, and the frame to hold the tissue for testing. (c) The skin tissue from pork was used in the tests. The left part is the skin tissue, and the yellow part on the right side is a 3D-printed frame that holds the skin. A ruler shows the thickness of the tissue. (d) The fat tissue from pork was used in the tests. The tissue is held by a 3D printed frame (the grey base behind the tissue) and mounted on the PCB with the LED transmitter to ensure no light leaks from the side. (e) Same setup to test the performance with muscle tissue from pork. (f) Pork skin, fat, and muscle tissues were used in the tests, and were held in place by a 3D-printed frame. The picture shows the three-layer tissue arranged with skin on the left, fat in the middle, and muscle on the right. The muscle side was facing the LED during the experiment to simulate subcutaneous transmission. (g) The test setup with tissue. The left part is the data receiver. The right part is the transmitter with tissue. The tissue is held by the grey frame and mounted on the PCB with the LED transmitter.

static value, with the testing result, this circuit consumes 90 μW.

The power consumption of the plus generator circuit and the encoder circuit is a dynamic number related to the transferring data rate. The encoder is a digital data processing circuit, and the power consumption is calculated with standard complementary metal-oxide-semiconductor (CMOS) power consumption as equation (7).

In equation (7) C_{PD} is the power-dissipation capacitance, V_{CC} is the supply voltage. Here we use 1.8 V for the calculation. f_I is the input signal frequency, N_{SW} is the number of bits switching, C_L is the load capacitance and f_O is the output signal frequency,

$$P_C = P_T + P_L = \left(C_{PD} \times {V_{cc}}^2 \times f_I \times N_{SW}\right) + \left(C_L \times {V_{cc}}^2 \times f_O \times N_{SW}\right). \quad (7)$$

The pulse generator we designed for this module only consist digital logic gate and delay or buffer unit. We estimate the power consumption by SPIC simulation in LTSPICE with TSMC's 350 nm model library under 1.8 V power supply.

We assume the efficiency of the DC-to-DC power management circuits in the internal unit is 80%, which is a reasonable number for a low-power system. The calculation result of the total power consumption of the internal unit under different data transmitting rates is listed in table 3.

4. Discussion

We compared the system performance with some state-of-the-art wireless communication approaches for bio-signal sensing implants. The result is shown in figure 14. The figure shows that the impulse radio-ultra wide band (IR-UWB) has the highest data rate, reaching 1.66 Gb s^{-1} for subcutaneous application [11]. The IR-UWB communication system's power consumption ranges from 6 mW to a few hundred milliwatts [56–58]. With the advantage of a high data rate, the power efficiency of IR-UWB technology is still at the top level among other technologies. The challenges remained in IR-UWB technology, including the big antenna size of close to 100 mm^2, and the misalignment caused stability problems. For neural implants, if the antenna is on the skull, the individual curvature differences will require a custom antenna design for each recipient. Ultrasonic communication modules have the smallest size, lowest power consumption, and the best tissue penetration depth. The challenge with ultrasonic is the low data rate and limited modulation approach as it is a backscatter-based communication [59]. Radio frequency (RF) backscatter communication module also has sub-milliwatt power consumption for the internal unit, and a data rate can achieve 25 Mb s^{-1} [5]. High-speed optical links reported in other works use VCSEL as the transducer [38, 40, 60] and conventional laser driver circuits to drive the laser diodes. The laser-based transducer has higher modulation bandwidth compared to LEDs and has reached a 300 Mbit s^{-1} data rate [40]. The drawbacks of lasers for implantable applications are the big volume and more complex driver circuits. From the comparison graph, we can find that this LED-based high-speed optical link has balanced both volume, speed, power consumption, and power efficiency very well, which is the optimal communication module for subcutaneous neural signal sensors.

4.1. Design trade-offs

The proposed module has balanced both volume, energy efficiency, data rate, and biosafety well, and the data transmission performance stands at the top of current state-of-the-art wireless communication systems for implantable devices. However, the current design and implementation still have some drawbacks. First, in the external unit, we use a high reverse voltage bias APD to detect short-period optical pulse with a very low optical energy. In this design, the bias voltage is 160–200 V, which is a risk to living tissue if

IOP Publishing J. Neural Eng. 20 (2023) 036017 Z Xu et al

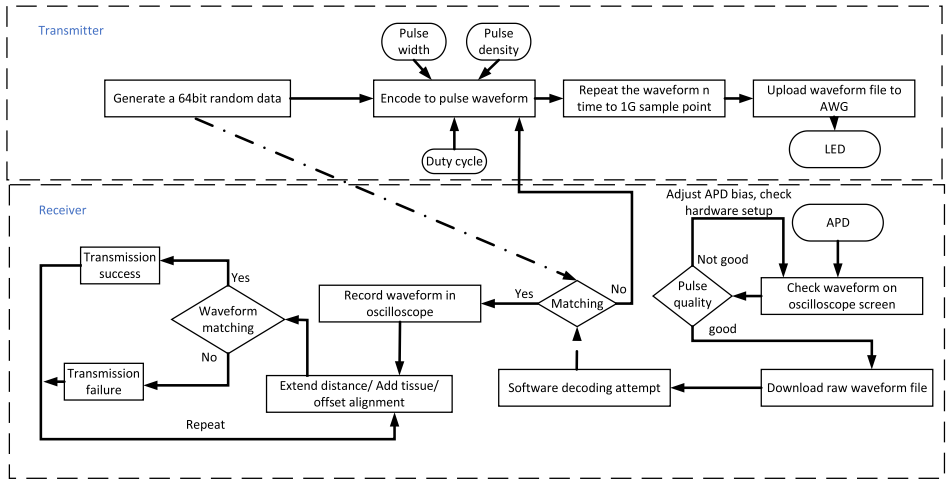

Figure 13. The data transfer confirmation experiment protocol.

Table 2. Data transfer testing result.

Tissue	Thickness (mm)	Distance (mm)	Receiver lens	Maximum misalignment[a]	Pulse duration (ns)	Pulse density (%)[b]	Data rate (Mbps)
None	N/A	3	Yes	±5 mm 45°	10	32	16
None	N/A	3	No	±2 mm 15°	10	32	8
None	N/A	15	No	±3 mm 15°	10	32	16
None	N/A	140	Yes	±20 mm 30°	1.5	0.125	108
Skin	2	3	Yes	±8 mm 45°	10	0.125	16
Skin	3	10	Yes	±5 mm 15°	1.5	0.125	108
Fat	2	3	Yes	±5 mm 30°	1.5	0.125	108
Fat	3	3	Yes	±3 mm 15°	1.5	0.125	108
Muscle	2	3	Yes	±8 mm 45°	1.5	0.125	108
Skin + fat + muscle	8	3	Yes	±5 mm 15°	3	0.125	54

[a] The misalignment is measured as described in figure 12(b), the first number in millimeter is the misalignment distance and the second number in degree is the misalignment angle.

[b] Pulse density % refers to the maximum pulse duty cycle in each clock cycle, which calculated as following equation

$$\text{Pulse density} = \frac{\text{Pulse duration} \times \text{Max(numberofper bit)}}{\text{Clock cycle}} \times 100\%.$$

Table 3. Power consumption estimation result at different data rate and power efficiency calculation result.

Data rate (Mbps)	Pulse width (ns)	Transducer power consumption (μW)	Circuit power consumption (mW)	Total power (mW)	Power efficiency (pJ/bit)
108	1.5	566	1	1.56	14.5
54	3	458	0.51	0.96	17.8
16	10	342	0.19	0.53	33.1

the high voltage part is not insulated well. Second, to transfer power into the internal part at high efficiency, we planned to use near field coupling, which includes a coil in the internal unit and will limit the miniaturization capability of the whole system as the coil efficiency drops with decreasing coil size. Thirdly, the LED-based transmitter has the potential to establish an optical downlink since it can detect light with a shorter wavelength than it emits. However, we did not implement bidirectional optical communication in this study because our experiment revealed that the LED's impedance fluctuated when we introduced a modulated external light source, causing the optical pulse to become unstable.

4.2. Future work

The optical telemetry module proposed in this work has a great potential to solve the challenge of bandwidth-hungry high-density neural recording implants. Thus, this work only presents a proof-of-concept validation. There are still some engineering challenges that have not been solved in this

IOP Publishing J. Neural Eng. 20 (2023) 036017 Z Xu et al

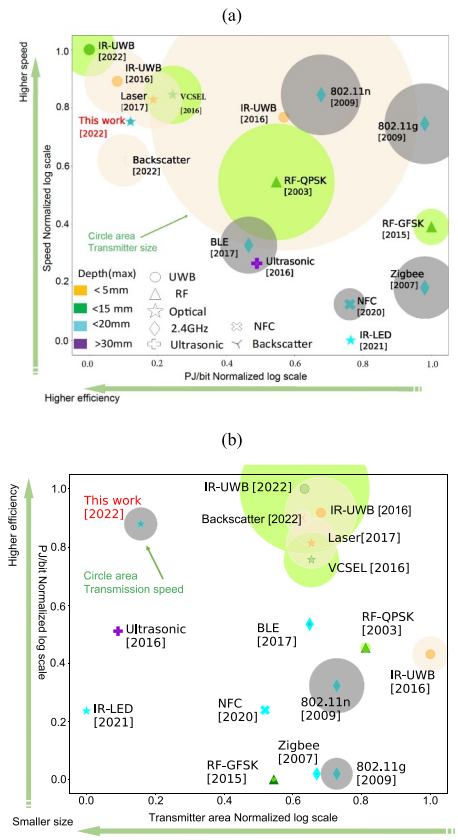

Figure 14. Performance comparison chart of the state-of-the-art technologies. (a) Compare the data transfer energy efficiency and speed. The *x*-axis indicates the power efficiency of the data transmission, the *y*-axis indicates the data rate, and the circle area represent the size of the data transfer transmitter. The color code represents the tissue penetration depth and the marker shape represent the technology it used. (b) Compare the data transmitter size and the transfer speed. The *x*-axis indicates the transmitter size, the *y*-axis indicates the data transfer energy efficiency, and the circle area represent the data transfer rate.

work like the hardware level implementation of the low-power consumption pulse generator, the hardware level implementation of the data and clock signal recovery circuits, and the miniaturization of the whole system.

5. Conclusion

This paper presents a design of a subdermal optical telemetry module that balances high data rate, high power efficiency, and low volume. By simulating the optical property of the tissue, we optimized the optical design to improve power efficiency and signal quality. By choosing a high-saturation-current near inferred LED and driving it with a low amplitude voltage pulse with an optimal bias current, the LED can generate 1.5 ns short pulses with reasonable high efficiency. The proposed design is implemented with discrete components and tested with animal tissue. The proposed module can achieve a 108 Mbit s^{-1} data rate with 3 mm tissue and tolerance with misalignment up to 5 mm and ±15°. The module's power consumption is below 1.57 mw, and the data transmission efficiency is 14.5 pJ per bit. The volume of the transducer in the proposed module is less than 1 mm^3, which gives the proposed solution an excellent potential for miniaturization and a wide variety of applications. Modeling codes and data for this paper are available via https://dx.doi.org/10.6084/m9.figshare.22699279.

Data availability statement

The data that support the findings of this study are openly available at the following URL/DOI: https://figshare.com/articles/journal_contribution/Data_telemetry/22699279.

Acknowledgments

The authors would like to express their gratitude to School of Biomedical Engineering for their assistance in providing access to 3D printing devices and manage the shipment of devices during COVID-19 lock down period.

Funding

The author acknowledges the financial support from the Australian Research Council under the Project DP230100019.

ORCID iD

Omid Kavehei https://orcid.org/0000-0002-2753-5553

References

[1] Chen X *et al* 2022 1024-channel electrophysiological recordings in macaque V1 and V4 during resting state *Sci. Data* **9** 1–16
[2] Steinmetz N A *et al* 2021 Neuropixels 2.0: a miniaturized high-density probe for stable, long-term brain recordings *Science* **372** eabf4588
[3] Colachis S C, Dunlap C F, Annetta N V, Tamrakar S M, Bockbrader M A and Friedenberg D A 2021 Long-term intracortical microelectrode array performance in a human: a 5 year retrospective analysis *J. Neural Eng.* **18** 0460d7
[4] Pisarchik A N, Maksimenko V A and Hramov A E 2019 From novel technology to novel applications: comment on "An integrated brain-machine interface platform with thousands of channels" by Elon Musk and Neuralink *J. Med. Internet Res.* **21** e16356
[5] Moore G E, Rosenthal J D, Smith J R and Reynolds M S 2021 Adaptive wireless power transfer and backscatter communication for perpetual operation of wireless brain–computer interfaces *Proc. IEEE* **110** 89–106

[6] Hochberg L R *et al* 2012 Reach and grasp by people with tetraplegia using a neurally controlled robotic arm *Nature* **485** 372–5

[7] Chaudhary U *et al* 2022 Spelling interface using intracortical signals in a completely locked-in patient enabled via auditory neurofeedback training *Nat. Commun.* **13** 1–9

[8] Pandarinath C, Nuyujukian P, Blabe C H, Sorice B L, Saab J, Willett F R, Hochberg L R, Shenoy K V and Henderson J M 2017 High performance communication by people with paralysis using an intracortical brain-computer interface *Elife* **6** e18554

[9] Bacher D, Jarosiewicz B, Masse N Y, Stavisky S D, Simeral J D, Newell K, Oakley E M, Cash S S, Friehs G and Hochberg L R 2015 Neural point-and-click communication by a person with incomplete locked-in syndrome *Neurorehabil. Neural Repair* **29** 462–71

[10] Donoghue J P, Nurmikko A, Black M and Hochberg L R 2007 Assistive technology and robotic control using motor cortex ensemble-based neural interface systems in humans with tetraplegia *J. Physiol.* **579** 603–11

[11] Song M *et al* 2022 A 1.66 Gb/s and 5.8 pJ/b transcutaneous IR-UWB telemetry system with hybrid impulse modulation for intracortical brain-computer interfaces *2022 IEEE Int. Solid-State Circuits Conf. (ISSCC)* vol 65 (IEEE) pp 394–6

[12] Miranda H and Meng T H 2010 A programmable pulse UWB transmitter with 34% energy efficiency for multichannel neuro-recording systems *2010 IEEE Custom Integrated Circuits Conf.* (IEEE) pp 1–4

[13] Liu T, Bihr U, Becker J, Anders J and Ortmanns M 2014 *In vivo* verification of a 100 Mbps transcutaneous optical telemetric link *IEEE Biomedical Circuits and Systems Conf. (BioCAS) Proc.* (*Lausanne, Switzerland*) (IEEE) pp 580–3

[14] Ghanbari M M, Piech D K, Shen K, Faraji Alamouti S, Yalcin C, Johnson B C, Carmena J M, Maharbiz M M and Muller R 2019 A sub-mm 3 ultrasonic free-floating implant for multi-mote neural recording *IEEE J. Solid-State Circuits* **54** 3017–30

[15] Sonmezoglu S, Fineman J R, Maltepe E and Maharbiz M M 2021 Monitoring deep-tissue oxygenation with a millimeter-scale ultrasonic implant *Nat. Biotechnol.* **39** 855–64

[16] Chang T C, Weber M J, Charthad J, Baltsavias S and Arbabian A 2018 End-to-end design of efficient ultrasonic power links for scaling towards submillimeter implantable receivers *IEEE Trans. Biomed. Circuits Syst.* **12** 1100–11

[17] Charthad J, Weber M J, Chang T C and Arbabian A 2015 A mm-sized implantable medical device (IMD) with ultrasonic power transfer and a hybrid bi-directional data link *IEEE J. Solid-State Circuits* **50** 1741–53

[18] Meng M and Kiani M 2016 A hybrid inductive-ultrasonic link for wireless power transmission to millimeter-sized biomedical implants *IEEE Trans. Circuits Syst.* II **64** 1137–41

[19] Song S H, Kim A and Ziaie B 2015 Omnidirectional ultrasonic powering for millimeter-scale implantable devices *IEEE Trans. Biomed. Eng.* **62** 2717–23

[20] Seo D, Carmena J M, Rabaey J M, Maharbiz M M and Alon E 2015 Model validation of untethered, ultrasonic neural dust motes for cortical recording *J. Neurosci. Methods* **244** 114–22

[21] Barbruni G L, Ros P M, Demarchi D, Carrara S and Ghezzi D 2020 Miniaturised wireless power transfer systems for neurostimulation: a review *IEEE Trans. Biomed. Circuits Syst.* **14** 1160–78

[22] Denisov A and Yeatman E 2010 Ultrasonic vs. inductive power delivery for miniature biomedical implants *2010 Int. Conf. on Body Sensor Networks* (IEEE) pp 84–89

[23] Haerinia M and Shadid R 2020 Wireless power transfer approaches for medical implants: a review *Signals* **1** 209–29

[24] Bin Mustapa M Z, Saat S, Yusof Y and Shaari M M 2019 Capacitive power transfer in biomedical implantable device: a review *Int. J. Power Electron. Drive Syst.* **10** 935–42

[25] Sharif M A and Sodagar A M 2022 Capacitive links for power and data telemetry to implantable biomedical microsystems *Handbook of Biochips* (Berlin: Springer) pp 763–84

[26] Sodagar A M and Amiri P 2009 Capacitive coupling for power and data telemetry to implantable biomedical microsystems *2009 4th Int. IEEE/EMBS Conf. on Neural Engineering* (IEEE) pp 411–4

[27] Takhti M, Asgarian F and Sodagar A M 2011 Modeling of a capacitive link for data telemetry to biomedical implants *2011 IEEE Biomedical Circuits and Systems Conf. (BioCAS)* (IEEE) pp 181–4

[28] Erfani R, Marefat F, Sodagar A M and Mohseni P 2017 Transcutaneous capacitive wireless power transfer (C-WPT) for biomedical implants *2017 IEEE Int. Symp. on Circuits and Systems (ISCAS)* (IEEE) pp 1–4

[29] Jegadeesan R, Agarwal K, Guo Y-X, Yen S-C and Thakor N V 2016 Wireless power delivery to flexible subcutaneous implants using capacitive coupling *IEEE Trans. Microw. Theory Tech.* **65** 280–92

[30] Erfani R, Marefat F and Mohseni P 2018 Biosafety considerations of a capacitive link for wireless power transfer to biomedical implants *2018 IEEE Biomedical Circuits and Systems Conf. (BioCAS)* (IEEE) pp 1–4

[31] Narayanamoorthi R 2019 Modeling of capacitive resonant wireless power and data transfer to deep biomedical implants *IEEE Trans. Compon. Packaging Manuf. Technol.* **9** 1253–63

[32] Christ A, Samaras T, Klingenböck A and Kuster N 2006 Characterization of the electromagnetic near-field absorption in layered biological tissue in the frequency range from 30 MHz to 6000 MHz *Phys. Med. Biol.* **51** 4951

[33] Drossos A, Santomaa V and Kuster N 2000 The dependence of electromagnetic energy absorption upon human head tissue composition in the frequency range of 300–3000 MHz *IEEE Trans. Microw. Theory Tech.* **48** 1988–95

[34] Quiroga R Q 2012 Spike sorting *Curr. Biol.* **22** R45–R46

[35] Navajas J, Barsakcioglu D Y, Eftekhar A, Jackson A, Constandinou T G and Quiroga R Q 2014 Minimum requirements for accurate and efficient real-time on-chip spike sorting *J. Neurosci. Methods* **230** 51–64

[36] Park J, Kim G and Jung S-D 2017 A 128-channel FPGA-based real-time spike-sorting bidirectional closed-loop neural interface system *IEEE Trans. Neural. Syst. Rehabil. Eng.* **25** 2227–38

[37] Ackermann D M, Smith B, Wang X-F, Kilgore K L and Peckham P H 2008 Designing the optical interface of a transcutaneous optical telemetry link *IEEE Trans. Biomed. Eng.* **55** 1365–73

[38] Liu T, Bihr U, Anis S M and Ortmanns M 2012 Optical transcutaneous link for low power, high data rate telemetry *Annual Int. Conf. IEEE Engineering in Medicine and Biology Society* (*28 August–1 September 2012*) pp 3535–8

[39] Nikita K S 2014 *Handbook of Biomedical Telemetry* (New York: Wiley) (https://doi.org/10.1002/9781118893715)

[40] Marcellis A D, Stanchieri G D P, Faccio M, Palange E and Constandinou T G 2020 A 300 Mbps 37 pJ/bit pulsed optical biotelemetry *IEEE Trans. Biomed. Circuits Syst.* **14** 441–51

[41] Burton A *et al* 2020 Wireless, battery-free subdermally implantable photometry systems for chronic recording of neural dynamics *Proc. Natl Acad. Sci.* **117** 2835–45

[42] Liu T, Bihr U, Becker J, Anders J and Ortmanns M 2014 Live demonstration: *in vivo* verification of a 100 Mbps transcutaneous optical telemetric link *IEEE Biomedical Circuits and Systems Conf. (BioCAS) Proc.* (*22–24 October 2014*) p 186

[43] Bhandari R, Negi S and Solzbacher F 2010 Wafer-scale fabrication of penetrating neural microelectrode arrays *Biomed. Microdevices* **12** 797–807

[44] Elon Musk N 2019 An integrated brain-machine interface platform with thousands of channels *J. Med. Internet Res.* **21** e1619

[45] Maslik M, Leene L B and Constandinou T G 2020 Analogue front-end design for neural recording *Handbook of Neuroengineering* ed T Nitish (Singapore: Springer) pp 1–26

[46] Zjajo A 2016 Neural signal classification circuits *Brain-Machine Interface: Circuits and Systems* (Cham: Springer International Publishing) pp 77–93

[47] Bashkatov A N, Genina E A and Tuchin V V 2011 Optical properties of skin, subcutaneous, and muscle tissues: a review *J. Innov. Opt. Health Sci.* **4** 9–38
[48] Lister T, Wright P A and Chappell P H 2012 Optical properties of human skin *J. Biomed. Opt.* **17** 090901
[49] Bashkatov A N, Genina E, Kochubey V and Tuchin V 2005 Optical properties of human skin, subcutaneous and mucous tissues in the wavelength range from 400 to 2000 nm *J. Phys. D: Appl. Phys.* **38** 2543
[50] Graaff R, Dassel A, Koelink M, De Mul F, Aarnoudse J and Zijlstra W 1993 Optical properties of human dermis *in vitro* and *in vivo Appl. Opt.* **32** 435–47
[51] Rajadhyaksha M, Grossman M, Esterowitz D, Webb R H and Anderson R R 1995 *In vivo* confocal scanning laser microscopy of human skin: melanin provides strong contrast *J. Invest. Dermatol.* **104** 946–52
[52] Wan S, Anderson R R and Parrish J A 1981 Analytical modeling for the optical properties of the skin with *in vitro* and *in vivo* applications *Photochem. Photobiol.* **34** 493–9
[53] Hsiang E-L, He Z, Huang Y, Gou F, Lan Y-F and Wu S-T 2020 Improving the power efficiency of micro-LED displays with optimized LED chip sizes *Crystals* **10** 494
[54] Li X, Ghassemlooy Z, Zvanovec S, Zhang M and Burton A 2019 Equivalent circuit model of high power LEDs for VLC systems *2019 2nd West Asian Coll. on Optical Wireless Communications (WACOWC)* (IEEE) pp 90–95
[55] Li X, Ghassemlooy Z, Zvanovec S and Alves L N 2021 An equivalent circuit model of a commercial LED with an ESD protection component for VLC *IEEE Photonics Technol. Lett.* **33** 777–9
[56] Even-Chen N, Muratore D G, Stavisky S D, Hochberg L R, Henderson J M, Murmann B and Shenoy K V 2020 Power-saving design opportunities for wireless intracortical brain–computer interfaces *Nat. Biomed. Eng.* **4** 984–96
[57] Ando H, Takizawa K, Yoshida T, Matsushita K, Hirata M and Suzuki T 2016 Wireless multichannel neural recording with a 128-Mbps UWB transmitter for an implantable brain-machine interfaces *IEEE Trans. Biomed. Circuits Syst.* **10** 1068–78
[58] Mirbozorgi S A, Bahrami H, Sawan M, Rusch L A and Gosselin B 2015 A single-chip full-duplex high speed transceiver for multi-site stimulating and recording neural implants *IEEE Trans. Biomed. Circuits Syst.* **10** 643–53
[59] Seo D, Neely R M, Shen K, Singhal U, Alon E, Rabaey J M, Carmena J M and Maharbiz M M 2016 Wireless recording in the peripheral nervous system with ultrasonic neural dust *Neuron* **91** 529–39
[60] De Marcellis A, Palange E, Faccio M, Stanchieri G D P and Constandinou T G 2017 A 250Mbps 24pJ/bit UWB-inspired optical communication system for bioimplants *2017 IEEE Biomedical Circuits and Systems Conf. (BioCAS)* (IEEE) pp 1–4

IOP Publishing J. Neural Eng. 21 (2024) 066009 https://doi.org/10.1088/1741-2552/ad8dfe

Journal of Neural Engineering

PAPER

A leadless power transfer and wireless telemetry solutions for an endovascular electrocorticography

Zhangyu Xu[1], **Majid Khazaee**[2], **Nhan Duy Truong**[1,5], **Deniel Havenga**[1], **Armin Nikpour**[3], **Arman Ahnood**[3] **and Omid Kavehei**[1,5,*]

[1] School of Biomedical Engineering, The University of Sydney, Camperdown, NSW 2050, Australia
[2] Department of AAU Energy, Aalborg University, Aalborg, Denmark
[3] School of Engineering RMIT University, Melbourne, VIC 3000, Australia
[4] Royal Prince Alfred Hospital, Camperdown, NSW 2050, Australia
[5] BrainConnect Pty Ltd, Darlington, NSW 2008, Australia
[*] Author to whom any correspondence should be addressed.

E-mail: omid.kavehei@sydney.edu.au

Keywords: endovascular electrocorticography, low power optical telemetry, piezoelectric, wireless telemetry, wireless power transfer.

Supplementary material for this article is available online

OPEN ACCESS

RECEIVED
1 July 2024

REVISED
15 October 2024

ACCEPTED FOR PUBLICATION
1 November 2024

PUBLISHED
12 November 2024

Abstract

Objective. Endovascular brain-computer interfaces (eBCIs) offer a minimally invasive way to connect the brain to external devices, merging neuroscience, engineering, and medical technology. Currently, solutions for endovascular electrocorticography (ECoG) include a stent in the brain with sensing electrodes, a chest implant to accommodate electronic components to provide power and data telemetry, and a long (tens of centimeters) cable travel through vessels with a set of wires in between. Removing this long cable is the key to the clinical viability of eBCIS as it carries risks and limitations, especially for patients with fragile vasculature. *Approach*. This work introduces a wireless and leadless telemetry and power transfer solution for ECoG. The proposed solution includes an optical telemetry module and a focused ultrasound (FUS) power transfer system. The proposed system can be miniaturised to fit in an endovascular stent, removing the need for long, intrusive cables. *Main results*. The optical telemetry achieves data transmission speeds of over 2 Mbit/s, capable of supporting 41 ECoG channels at a 2 kHz sampling rate with 24-bit resolution. The FUS power transfer system delivers up to 10 mW of power to the implant through the scalp(6 mm), skull(10 mm), and subdural space(5 mm), adhering to safety limits. Testing on bovine tissue (10 mm thick bone, 7 mm thick skin) confirmed the system's efficacy. *Significance*. This leadless and wireless solution eliminates the need for long cables and auxiliary implants, potentially reducing complications and enhancing the clinical applicability of eBCIs. The proposed system represents a step forward in enabling safer and more effective ECoG for a broader range of patients.

1. Introduction

Endovascular brain-computer interfaces (eBCIs) systems have opened up new frontiers in human-machine interaction and have the potential to revolutionize the way we understand and treat neurological disorders [1–4]. It offers several benefits for high-fidelity chronic recordings of cortical neural activities. Firstly, it provides a minimally invasive approach, as it can be implanted through a blood vessel, reducing the risk of infection and tissue damage compared to traditional invasive methods. Additionally, the stent-electrode array allows for stable, long-term recordings due to its integration with the vessel wall, which results in fewer movement-related artifacts and improved signal quality [5, 6]. This enables researchers and clinicians to gain deeper insights into brain function and develop more effective therapies for neurological disorders.

However, a significant limitation of the current stent-electrode array is the requirement of a long cable within the vessel to carry the signal to a

IOP Publishing J. Neural Eng. 21 (2024) 066009 Z Xu et al

recording device fixated in the chest. This arrangement presents a risk to the recipient, possibly leading to complications such as thrombosis, vessel injury, or infection [7, 8]. Furthermore, the cable can pose a significant challenge in pediatric applications, as children constantly grow and develop [9–11]. The fixed cable length may not accommodate changes in the distance from the vessel to the recording device as the child grows, potentially leading to complications and the need for repeated surgical adjustments [12].

To address these issues, it is crucial to develop a wireless telemetry module that satisfies the volume and dimension limits of the stent and can power itself by harvesting energy from an outside source. This wireless solution would improve eBCIs' safety level and expand the potential applications of the stent-electrode array across different age groups and clinical scenarios. However, several challenges have prevented the invention of the telemetry module, including:

Area and volume limitation: The telemetry and power harvesting module needs to be small enough to fit within the confines of the blood vessel without causing discomfort or impeding blood flow [1]. The diameter of the stent for eBCIs is 5 mm to 9 mm to fit in the superior sagittal sinus. Designing a compact module that incorporates transducers for receiving energy and converting it into electrical power, as well as integrating components for modulation and encoding to transmit data, presents a significant challenge. This is further compounded by the need to integrate control and power management circuits, all within the limited available space.

Power consumption limitation: The module must be highly energy-efficient, as excessive power consumption will exceed the power delivery and harvesting budget and could generate heat, potentially damaging surrounding tissues [13]. Furthermore, for chronic recording, the power needs to be supplied and harvested continuously, which imposes constraints on the long-term safety concern and available energy format.

High data rate requirement: Capturing high-frequency neural activity and accommodating the data generated by a large number of electrodes necessitate a high data rate. A high sampling rate is required to accurately capture the high-frequency features of neural activity, while sufficient resolution of the analog-to-digital converter (ADC) is crucial to cover the dynamic range of the neural signals [14]. As the number of electrodes increases, the data rate multiplies accordingly, leading to a substantial amount of information that needs to be transmitted continuously.

Signal tissue penetration depth and absorption rate limitation: Wireless transmission of neural data through biological tissues can be challenging due to signal attenuation and absorption [15, 16]. The telemetry module must be able to transmit signals through various tissue layers while maintaining adequate signal strength and minimizing interference or distortion.

The development of a miniaturized wireless power and data module for eBCIs presents a multitude of challenges that require innovative engineering solutions. Moreover, the module must be biocompatible, robust, and reliable, considering it will operate in a highly sensitive and dynamic environment within the human body [17]. Addressing these challenges necessitates interdisciplinary collaboration, combining expertise in microelectronics, materials science, biomedical engineering, and signal processing.

Currently, significant efforts are underway to develop power and data transmission solutions for in-body implantable devices and some of them can be used for ECoG systems. Among these, inductive links can offer power budgets exceeding 50 mW and provide data telemetry with high data rates [18–21]. However, inductive link-based technologies require specific structures or special materials to transform the stent into an efficient antenna. This presents challenges for clinical implementation because introducing a novel stent structure design requires long-term clinical trials to demonstrate its safety before it can be used in humans.

Other technologies, such as thermoelectric, triboelectric, and biofuel, have the potential to fit within a stent [18]. However, these technologies can only offer power levels in the microwatt (μW) range [16, 22], which is insufficient to power ECoG circuits that continuously sense and transmit data. Piezoelectric devices can be sized to fit within a stent and can provide power levels in the milliwatt (mW) range [23]. Nevertheless, they typically rely on backscatter or passive methods for data telemetry, which do not offer sufficient data rates to transfer high-fidelity neural signals [23].

Our work introduces a novel solution that utilizes optical telemetry for data transmission and piezoelectric energy harvesting for power delivery. By combining these two technologies, we address the challenges of size (cross-sectional area and volume), data rate, and power delivery and harvesting, leveraging the advantages of each.

2. Background

Optical telemetry, particularly in implantable medical devices for neural recording, presents a compelling advancement in ensuring efficient data transmission while adhering to the stringent size and power constraints inherent to such applications [24]. The core principle of optical data telemetry hinges on transmitting data through optical signals, utilizing

IOP Publishing J. Neural Eng. 21 (2024) 066009 Z Xu et al

light, typically in the infrared or near-infrared spectrum, to encode and transmit information from the implantable device to an external receiver. This technology capitalizes on the intrinsic advantages of light as a medium, enabling high data rates, minimized power consumption, and a substantial reduction in the size of the telemetry module, thereby aligning well with the imperatives of modern implantable neural recording devices.

The optical data solution represents a powerful combination of three essential qualities: compact size, low power consumption, and high data rate. Together, these attributes effectively tackle the ongoing challenge of achieving a balance between size, power efficiency, and data transmission speed in implantable wireless devices [25]. The compact size of the optical telemetry module is a crucial innovation that allows for its integration into tiny implantable devices, thereby enhancing the capabilities of neural interfacing and recording technologies. Additionally, the module's low power requirements significantly reduce the challenges associated with power harvesting circuits and the limitations of the implant's power source.

Furthermore, the high data transmission speed provided by optical telemetry plays a crucial role in enabling the real-time transfer of neural data. This capability is essential for applications such as brain-computer interfaces, real-time monitoring of neurological disorders, and closed-loop neurostimulation systems [26]. This high-speed data transmission feature allows for the reliable and almost instant transfer of extensive neural information, facilitating prompt interventions and precise evaluations in both clinical and research environments. The wireless aspect of optical telemetry increases the flexibility and comfort of implantable neural recording devices, removing the requirement for external wires that might increase infection risks and limit patient movement. With these standout characteristics, optical data telemetry technology considerably advances the development of implantable medical devices, creating an environment that supports more advanced and patient-focused neural recording and interfacing solutions.

Piezoelectric energy harvesting is a burgeoning field within medical device technology, stemming from the unique ability of piezoelectric materials to convert mechanical energy into electrical energy when subjected to stress or strain [27]. This principle underpins the development of self-sustaining power systems within medical devices, capitalizing on the abundance of ambient mechanical energy sources such as body movements, blood flow, or external vibrations. A notable feature of piezoelectric energy harvesting technology is its compact form and high energy density, particularly advantageous for small-sized implantable or wearable medical devices [28]. These attributes alleviate the spatial constraints and power limitations traditionally associated with integrating batteries or other external power sources, thus significantly enhancing the feasibility and functionality of miniaturized medical devices.

Piezoelectric materials' compactness and high energy density are pivotal in advancing the size, power budget, and reliability of various medical devices. For instance, self-powered pacemakers [29], insulin pumps [30], and cochlear implants [31] have been developed by harnessing the piezoelectric phenomena to convert biomechanical energy from heartbeats, muscle movements, or external vibrations into electrical energy that powers these devices or deliver the desired function directly. Moreover, piezoelectric energy harvesting technology facilitates the continuous operation of critical monitoring systems and sensors, integral in chronic disease management and remote patient monitoring, by providing a steady and sustainable power supply [32].

However, despite these advantages, there are several drawbacks associated with piezoelectric energy harvesting technology. One of the primary challenges is the relatively low energy conversion efficiency compared to other energy harvesting technologies, which may necessitate the incorporation of additional power management systems to ensure a consistent energy supply. Furthermore, the biocompatibility and packaging method of piezoelectric materials within the human body remain areas of active investigation, as piezoelectric material will raise safety concerns when implanted in the human body, and packaging could potentially compromise power harvesting efficiency [33, 34]. Despite these challenges, piezoelectric materials' compact nature and high energy density leave them as one of the best candidates for powering eBCIs by harvesting energy within the stent.

Focused ultrasound (FUS) waves offer new opportunities for piezoelectric energy harvesting for implantable device. This technique uses ultrasonic waves, concentrated at a specific point inside the body, to transmit energy through the skin and tissue directly to the device. Unlike general ultrasound, which disperses energy over a wider area, FUS concentrates energy precisely at a specific target area. This targeted approach allows for more efficient energy transfer, minimizing the dissipation of energy through non-targeted tissues and reducing the potential for unintended heating or damage. Still, the related ultrasound-piezoelectric issues need further investigations, such as pressure amplitude at deep tissue [35], toxic material's connection with tissue [36, 37], and relatively low power output [38].

3. Method

Here, we present a wireless solution for eBCIs that meet the requirements of low-volume, low-energy, high data rate and can be powered wirelessly. This

IOP Publishing J. Neural Eng. 21 (2024) 066009 Z Xu et al

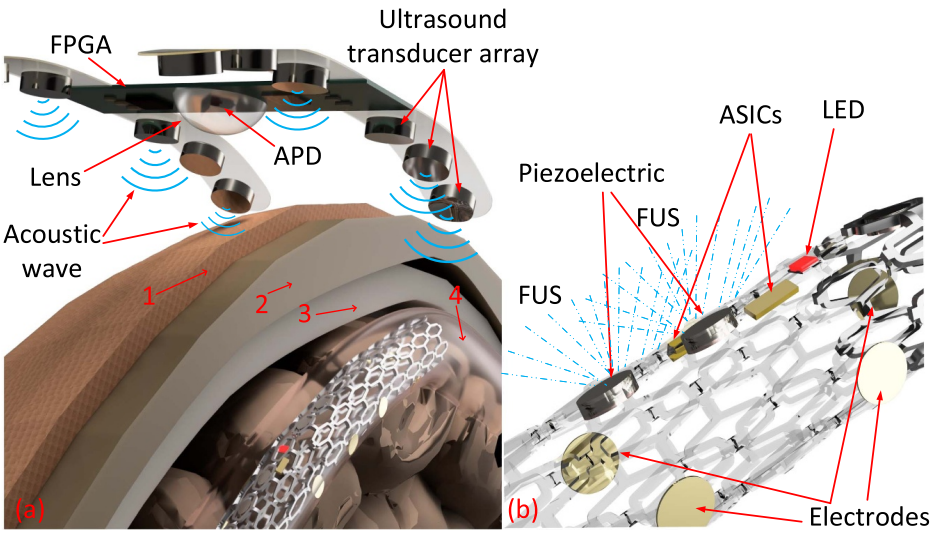

Figure 1. (a) Illustration of the system. In sub-figure (a), the green arrow shows the tissues. (1) Skin tissue, (2) Bone tissue, (3) Dura mater, (4) Superior sagittal sinus. The system will have two parts. An implantable stent and an external device. All electrical components will sit in the stent in the superior sagittal sinus for the implantable part. The external device sits over the scalp and aligns with the implant. In the external device, an avalanche photodiode is used to collect optical signals from the implant, and an Field Programmable Gate Arrays (FPGA) is used to decode the optical data. The ultrasound transducer array in the external device will generate focused ultrasound that delivers energy to the stent. Sub-figure (b) shows the stent with functional components. The sensing electrodes are on the stent for sensing electrical signals from the cortex. Three piezoelectrics sit in the stent to convert energy from FUS to power the circuit. The optical transmitter, an 810 nm wavelength light-emitting diode (LED) (shown in red), sits in a space within the stent. Two application-specific integrated circuits (ASICs) with control and sensing circuits, energy harvesting and power management circuit and LED driver sit in other spaces within the stents.

solution includes an optical data telemetry module that uses a single light-emitting diode (LED) as the transducer. With a simplified circuit design, the data telemetry module can transmit data at a high bit rate while consuming low power and occupying a minimal area. Our experiments showed that we can achieve 5 Mbit/s telemetry data rate and consume less than 4 mW of power with 7 mm bone and 10 mm soft tissues (fat, muscle and skin) between the transmitter and the receiver. The result indicates that the proposed module can transmit neural recording from a 32-channel electrode array with each channel sampled at 9.7 kHz with 16-bit resolution. The proposed solution includes a piezoelectric energy harvesting unit with multiple small piezoelectric power harvesters attached to the stent. Our simulation result showed we could harvest a maximum of 3 mW from one piezoelectric before the delivered acoustic pressure reaches the safety limit. With six or more piezoelectrics, we can easily have more than a 10 mW power budget to supply all the sensing, data telemetry, and potential stimulation circuits. Figure 1 shows the conceptual design of the proposed module working with an eBCIs. In the implant part, three small piezoelectric harvesters are embedded in the stent to power the circuits. An 810 nm wavelength LED sits in the stent as the transducer for data telemetry. Two small application-specific integrated circuits (ASICs) embedded in the stent are the sensing, control, data communication, and power management circuits. In figure 1, above the head is the internal structure of the concept external device for the implant. It will be attached over the head using a headphone-like fixture. This fixture is designed to maintain the external device in a relatively fixed position on the head. During the implantation surgery, the position of the implant is precisely determined, and a CT scan may be required to establish the optimal initial attachment point for the external device. The headphone-like fixture uses the two ear as the reference point for the location, and the cross bar of the headphone-like structure is used to decide the cross-section position of the external device. This fixture can help the external device sit on the head with a relative fixed position. Once the external device is attached, an algorithm will be employed to adjust the phase of the ultrasound transducers within the array. This adjustment allows the system to scan and focus the ultrasound energy, ensuring maximum energy delivery to the implant site. This scan and re-focus algorithm will compensate for the rough alignment of the external device as no precise fixed position for the external device.

Benefiting from the small size of the piezoelectric components and the LED, the proposed module has a transducer volume of less than 2 mm^3 (One LED and

IOP Publishing J. Neural Eng. 21 (2024) 066009 Z Xu et al

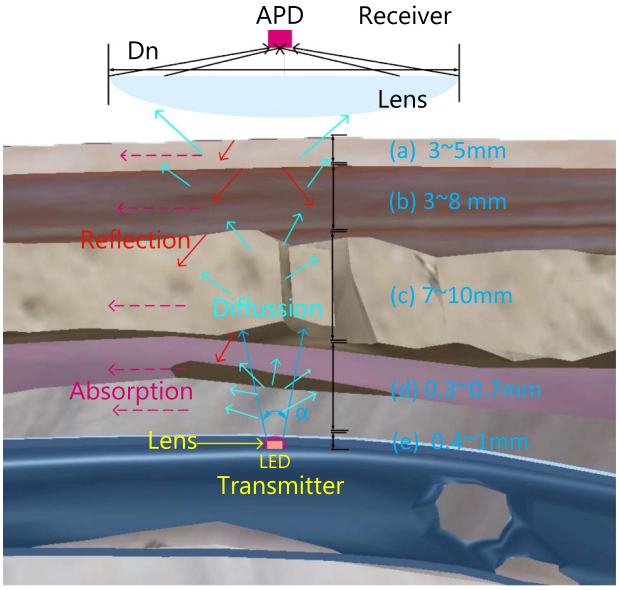

Figure 2. (a) Skin, (b) Connective tissue, Galea aponeurotica, Loose areolar connective tissue, Periosteum, (c) Skull, (d) Dura Mater, (e) Superior sagittal sinus Wall. Dn is the diameter of the lens. Alpha is the emitting angle of the LED, which the emitting lens can control. The arrows represent the diffusion (blue), reflection (red), and absorption effect (pink).

One piezoelectric). The module has significant potential for miniaturization ability. The proof-of-concept testing board created in this work uses discrete components, and the total volume is less than 14 mm^3 (excluding printed circuit board (PCB)), indicating that with future ASIC development, the volume of the module can be smaller than 4.5 mm^3. The entire module can be easily embedded into a stent with this volume.

To validate the proposed design, we did analysis, simulation, and proof-of-concept experiments according to the following parameters of success:

3.1. Optical channel analysis

Research has shown that wavelengths between 750 nm and 850 nm possess optimal optical properties for penetrating all tissue layers of the human head [39, 40]. Technologies such as functional near-infrared spectroscopy (fNIRS), which require light to pass through tissues from the outside to the brain, commonly use wavelengths around 800 nm [41]. Based on this evidence, we chose 810 nm for our data telemetry to leverage this optimal transmission window. In the passage of 810 nm wavelength light through the human head's layers, distinct optical behaviors are observed (see figure 2). The Superior sagittal sinus wall, characterized by a thin endothelial lining, shows low absorption and diffusion at this wavelength, with reflection influenced by refractive index differences between blood and adjacent tissues. The Dura Mater, a dense collagen and elastin membrane, exhibits moderate absorption and high diffusion, with reflection arising from refractive index disparities. The skull, comprising cortical and trabecular bone, has low absorption, moderate diffusion due to its porous structure, and reflection at tissue interfaces. Connective tissue, rich in collagen, elastin, and proteoglycans, demonstrates low absorption and moderate diffusion, with reflection at tissue boundaries. The skin, with its epidermal melanin and dermal blood vessels, shows moderate absorption and high diffusion, with reflection at the interfaces of its layers. Overall, the optical properties at 810 nm involve varying absorption, diffusion, and reflection, primarily influenced by blood, melanin, and water absorption, the fibrous nature of tissues, and structural complexities facilitating light scattering and reflection at tissue interfaces.

3.2. System design

Figure 3 shows the system's block diagram and the device's conceptual design. To eliminate the need for a long cable connecting the brain to the chest, our plan involves integrating energy harvesting, sensing, control, power management, and communication modules directly within the stent itself. An external device will be positioned over the implant site outside the body for seamless communication and power delivery. To accommodate the stent's dimensions, we propose utilizing two ASICs to house

IOP Publishing J. Neural Eng. 21 (2024) 066009 Z Xu et al

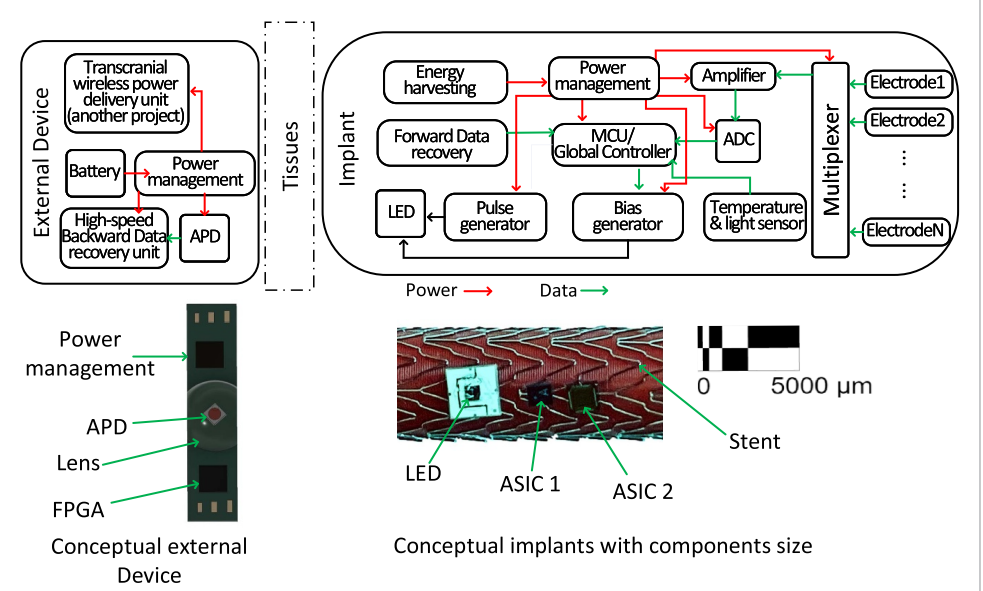

Figure 3. System block diagram. The top left corner shows the blocks in the external device. The data recovery will be implemented on FPGA and the wireless power delivery unit will be described in another work. The upper right part shows the blocks in the implant. The lower right part shows the potential components' size with an actual stent. The LED is a commercially available one and has a big substrate. We need a customized smaller substrate to meet our purpose.

the required circuitry. The first ASIC will encompass the global controller and sensing circuitry, including a multiplexer, amplifier, ADC, and temperature sensor. The second ASIC will contain the energy harvesting, power management, bias, and pulse generator circuits. By making the circuit into two smaller ASICs, the chips can be more easily adapted to fit the constrained dimensions of the stent and minimize the impair to the surrounding tissue or blood flow, which provides more flexibility in component placement and optimizes the use of the stent's internal space. Separating power-intensive components (such as energy harvesting and power management circuits) from sensitive analog components (like amplifiers and ADCs) can reduce the risk of noise interference and improve signal integrity. This can result in higher accuracy and better overall performance of the implant. The external device comprises three primary units: a data receiver unit, a wireless power delivery unit, and a power and battery management unit. Given its exceptional sensitivity and high-speed performance, we use an avalanche photodiode (APD) as the optical data receiver. An field programmable gate arrays (FPGA) is used in our bench experiment for data recovery due to its flexibility and processing capabilities, which far exceed our needs. The power management unit will be responsible for battery management, supplying the bias voltage required for the APD, and providing power to the FPGA.

3.3. System powering plan

The proposed solution for powering the implant in the brain incorporates an external transducer array and an array of minute piezoelectric materials embedded within the stent itself. The transducer array, situated externally over the head, is meticulously engineered to generate focused ultrasound waves. These waves are specifically directed toward the stent's location within the brain, ensuring precision in energy delivery. The transducer array comprises numerous individual transducers, each of which can be controlled independently. This allows for fine-tuning the ultrasound beam in terms of intensity, focus, and direction, ensuring that the energy is delivered accurately to the stent while minimizing exposure to the surrounding brain tissue. The stent, positioned within a blood vessel in the brain, is designed to be minimally invasive while providing the necessary support to the vessel. Embedded within the stent are small piezoelectric materials, which have the capability to convert the acoustic energy from the ultrasound waves into electrical energy. A lead-free potassium-sodium niobate with high piezoelectric coefficient d_{33} is employed [42]. These materials are selected for their high energy conversion efficiency and biocompatibility, ensuring that they function effectively within the body without inducing adverse reactions. The piezoelectric materials are connected to the energy harvesting circuit, which converts the harvested elec-

IOP Publishing J. Neural Eng. 21 (2024) 066009 Z Xu et al

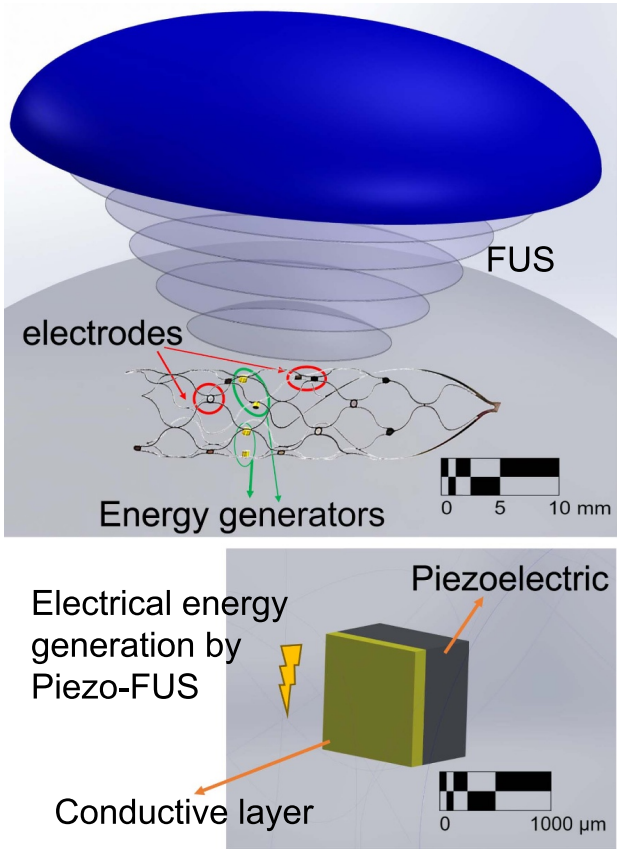

Figure 4. The structure of the piezoelectric harvester Illustrating the process of electrical energy generation using Piezo-FUS: A focused ultrasound beam (blue ellipse) targets a stent embedded with a thin layer of piezoelectric material (highlighted in orange). Upon interaction with the ultrasound, the piezoelectric layer converts the acoustic energy into electrical energy, represented by the lightning bolt symbol.

trical energy into a stable power supply for the other circuits.

The FUS is generated by a group of ultrasound generators in the external unit. To ensure the safety of the ultrasound energy, we not only set intensity limits for each of the ultrasound generators but also carefully control the intensity of the FUS waves to prevent any potential damage to the surrounding brain tissue. Additionally, we plan to use the telemetry channel to include feedback mechanisms, which can let the external unit dynamically adjust the output power, ensuring that the energy delivery and conversion processes are operating efficiently and safely.

Overall, this solution provides a novel method of powering endovascular implants in the brain, utilizing the synergy between FUS and piezoelectric materials to create a self-sufficient system that enhances patient monitoring and intervention capabilities while adhering to stringent safety standards.

Figure 4 shows the structure of piezoelectric elements that we proposed in this work. The piezoelectric material surface is covered by a metallic conductive layer and an electrode connection with the stent. The existence of multiple piezoelectric elements ensures a constant and high-power generation.

Figure 5 visually represents the modeling and simulation process of focused ultrasound propagation through the human brain. Part (a) displays real computed tomography (CT) scan images from the Visible Human Project, processed using the iSEG tool [43], providing a detailed cross-sectional view of the human head with various layers and anatomical details. This initial simulation uses ultrasound waves with an initial pressure of $P_0 = 30$ kPa and a frequency of $f = 1$ MHz.

Part (b) presents a modeled representation of the human head created with Sim4Life [44], along with a single spherical focused ultrasound transducer,

IOP Publishing J. Neural Eng. 21 (2024) 066009 Z Xu et al

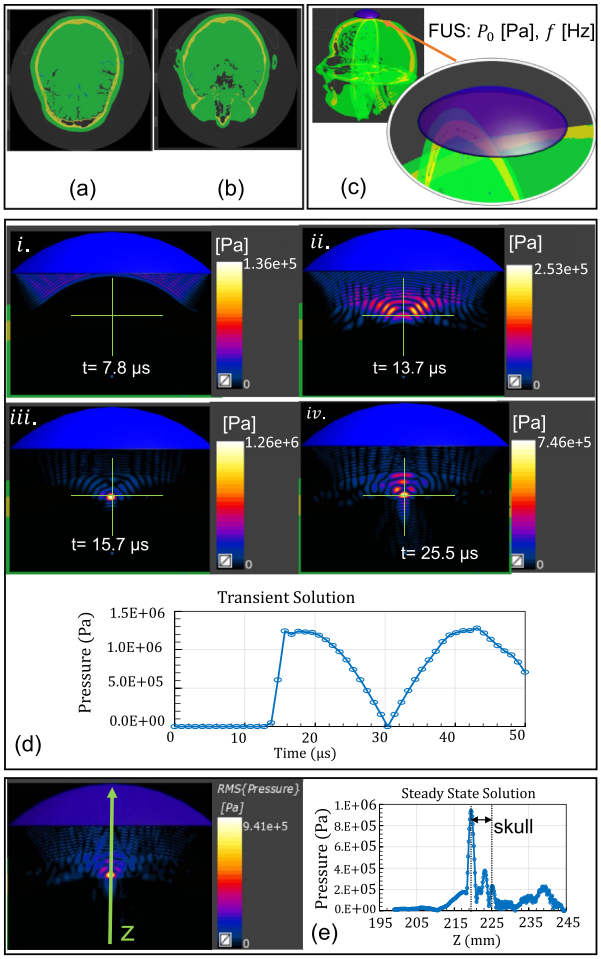

Figure 5. Modelled focused ultrasound/brain, (a) real CT (computed tomography) scan images, (b) modelled human head and a single spherical focused ultrasound transducer, (c) P_0 acoustic wave propagation through the head by the transient solution and the transient acoustic pressure at the scalp, and (d) the steady state solution of acoustic pressure and the acoustic pressure at the focal line.

highlighting the positioning and biological interaction. This transducer generates the focused ultrasound waves used in the simulation.

In part (c), the figure illustrates the dynamics of acoustic wave propagation through the head, showcasing the transient solution and demonstrating how these waves rapidly change over time. It also presents the transient acoustic pressure experienced at the scalp, providing insight into the intensity of the waves as they initially interact with the head.

Finally, part (d) depicts the steady-state solution, capturing the point where the acoustic waves stabilize and no longer change significantly over time. The acoustic pressure along the focal line is displayed, indicating the precise pressure within the targeted region of the brain where the ultrasound is most concentrated. The steady-state acoustic pressure along the Z-axis, shown in figure 5(d), clearly demonstrates the effect of the skull bone on the acoustic pressure concentration; therefore, it is expected that the critical temperature rise occurs at the skull.

Overall, this comprehensive figure offers a holistic view of how focused ultrasound interacts with and propagates through the intricate structures of the human head and brain.

Acoustic-thermal analysis is carried out to meet the long-term thermal safety criteria. Transient ultrasound-thermal analysis for $P_0 =$ 30 kPa and $f =$1 MHz case is shown in figure 6(a)–(d). Due to the acoustic pressure concentration on the skull, the skull temperature rises to the critical temperature. Multiple ultrasound parameters variations are set with the limitation of temperature rise below 2° C. The temperature rise for all frequencies is always

IOP Publishing J. Neural Eng. 21 (2024) 066009 Z Xu et al

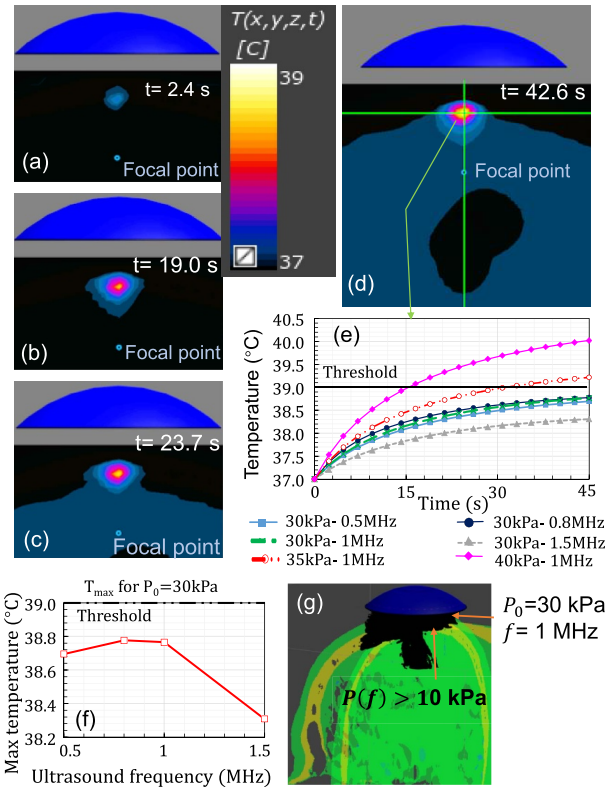

Figure 6. Ultrasound-thermal analysis (a)–(d) The transient temperature contours over time with $P_0 = 30$ kPa and $f = 1$ MHz, (e) temperature at the top of the skull over time for different acoustic settings, (f) maximum temperature versus ultrasound frequency, and (g) The steady-state iso-volume pressure > 10 kPa inside the brain.

below 2° C for $P_0 = 30$ kPa; thus, the acoustic pressure is used for the safe ultrasound.

3.4. Experiment setup

In order to evaluate the design and performance of the telemetry module and its associated system, we manufactured custom PCBs featuring discrete components for experimental purposes. Using 3D printing technology, we created holders to securely position the PCBs and the biological tissue samples during testing. These 3D-printed holders facilitated optimal optical alignment and precise control over distance and potential misalignment settings.

The tissue samples were freshly obtained bovine skin, complete with subcutaneous tissue and bone. All the tissue samples were purchased from the local Supermarket. The 3D-printed frame was used to maintain a firm grip on the tissue samples throughout the experiment. A depiction of the prepared tissue samples is provided in figure 7.

3.5. Testing protocol

To confirm the effectiveness of data transmission via the prototype device, we established a comprehensive testing protocol outlined as follows: Initially, we generate a sequence of random numbers using a random number generator. To this sequence, we add a 32-bit prefix as a starting indicator for data transmission. This prefix consists of four repeats of an 8-bit fixed pattern, which helps align the signal for decoding at the receiver's end. Following this, the combination of random numbers and the prefix is encoded using either pulse-density modulation or pulse-width modulation, depending on the test iteration and the data transmission speed being tested. We use an Analog Discovery 2 (AD2), a FPGA multi-function instrument device from DIGILENT and its application programming interface (API) to create a signal with binary voltage levels, simulating the digital control and data transmission circuits of our proposed system. The output signal from the AD2 is then connected to a custom testing board designed to include our optical pulse generator circuits built from individual components. In response to the data sent, the board's LED emits optical pulses, marking the completion of the transmission test sequence. At the receiving end, an avalanche photodiode captures the optical pulses and converts them into electrical signals. These signals

IOP Publishing J. Neural Eng. 21 (2024) 066009 Z Xu et al

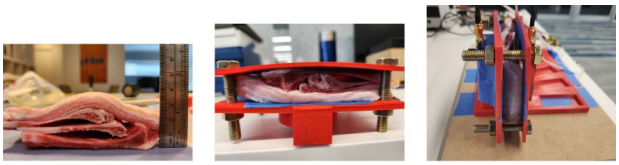

(a) (b) (c)

Figure 7. This figure shows the tissue we used for the experiment. (a) The tissues and their thickness. The top layer is skin tissue with subcutaneous fat. The lower three layers are bones. During the experiments, we stack different layers of bones to get different thicknesses of bone. (b) We use a 3D-printed frame to hold the tissues and use screws to put pressure to make the tissue firmly connected. (c) The experiment setup with tissues in between. The middle is the tissues. The left side is the receiver PCB and the right side is the transmitter.

are then amplified by a trans-impedance amplifier, followed by a cascaded operational amplifier, and fed into another AD2 unit. In this second AD2, the analog-to-digital converter (ADC) converts the analog signals into digital format, making them ready for transfer to a personal computer (PC). This PC uses an adaptive peak-searching algorithm to identify the pulses. After finding the peaks, the algorithm decodes the signal into a binary sequence based on set pulse-density thresholds. The software begins by searching for the start indicator. Due to the lack of synchronization between sending and receiving, a single 8-bit pattern is used as the search criterion. Once a matching pattern is found, the data following the last bit of the prefix is extracted and shortened to 1520 bits. The software then compares this 1520-bit sequence with the originally transmitted data to calculate the Bit Error Rate (BER). Subsequently, the receiving PC signals the transmitting PC to generate a new set of random numbers for the next test. A comprehensive testing setup was deployed to evaluate the BER at specified transmission speeds accurately. This setup can create random images, encode them using the described method, and then decode them to conduct a thorough bit-level comparison between the sent and received image data, counting the total erroneous bits found. To establish a dependable BER metric, this testing protocol was performed continuously for 24 h at each set transmission speed. The tests were carried out indoors with ambient lighting kept around 200 Lux, without direct sunlight exposure, and without using any environmental light shielding during the BER tests, to ensure the system's effectiveness under typical operating conditions without direct sunlight.

Figure 8 shows the testing protocol and how we verify the data transmission has been successful. This testing protocol ensures a comprehensive evaluation of the prototype device's data transfer capabilities, considering synchronization, signal decoding, and error rate analysis. The power consumption is measured by connecting a voltage source to the power management part directly and measuring the input current, so the power consumption already includes the power consumption of the power management unit, LED driver and the driver for data.

To test the power harvesting plan, we combined COMSOL [45] and Sim4Life simulation software [44] to test the harvested energy under the safety limit. Figure 9(a) shows the model parameters and piezoelectric element characteristics. Figure 9(b) illustrates two primary results. The ultrasound frequency plays a vital role in piezoelectric energy generation as it affects the mechanical stress in the piezoelectric. The stent orientation is crucial as it affects the ultrasound-solid interactions. To address the effects of misalignment of the external device and the implant. in our system design and evaluation we implemented multiple piezoelectric elements (1 to 6) in the implantable energy harvester within the stent. This multi-element configuration not only meet the size limit, but also offers advantages against misalignment. By using an array of piezoelectric elements, the energy harvesting is distributed over a small area, not a single point. This means that even if some elements are not perfectly aligned due to misalignment, other elements can compensate, ensuring consistent power delivery. We conducted simulations to evaluate the impact of angular misalignments between the transmitter and receiver. we analysed misalignment angles shows in figure 9 ranging from 0° to 5° in both azimuthal and elevation planes.

4. Result

We did data transfer experiments using the protocol described in figure 8. The result is shown in table 1.

From the result, we can find that the data transfer efficiency is higher when using pulse width modulation. Still, pulse width modulation (PWM) requires more precision timing to ensure the optical pulses can be decoded at the receiver side. When we use pulse-density modulation, we can relax more on timing and simplify the driver circuit for data.

Figure 10 shows the power harvesting result of the proposed power harvesting plan. We can see that a single piezoelectric generates the maximum power

IOP Publishing J. Neural Eng. 21 (2024) 066009 Z Xu et al

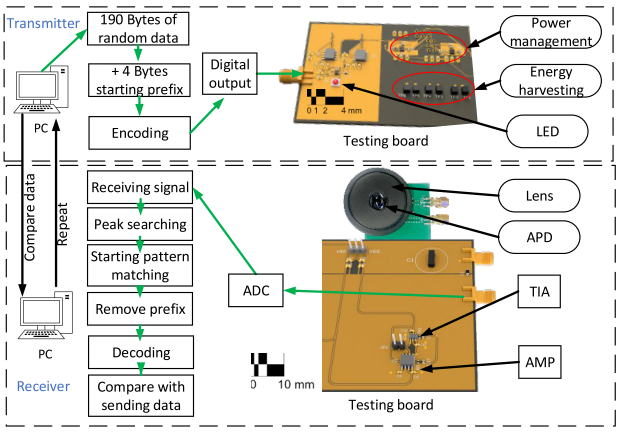

Figure 8. The upper portion of the diagram represents the transmitter. A computer running a program generates 190 bytes of random data at a time, limited by the buffer size of the digital input/ output (I/O) device. The program then adds a 4-byte prefix consisting of repeating fixed data to indicate the beginning of the transmission. The data is subsequently encoded into a pulse signal using either pulse width or pulse-density modulation. A digital I/O device generates the pulse and sends it to the testing board, which in turn produces optical pulses based on the input pulse signal. The lower portion of the diagram represents the receiver. Our testing board includes an analog front-end that converts the received optical pulses into electrical signals. An ADC digitizes the signal and sends it to a computer. Depending on the modulation scheme used, the program on the computer performs different operations. For pulse-density modulation, it conducts peak searching and marks the pulses on the timeline. For pulse width modulation, it uses a duty cycle searching and labeling algorithm to determine the pulse width. Once the signal is converted into binary format, the program searches for the repeated prefix pattern. When an entire segment of the prefix is matched, the program considers this as the starting point of the data and removes the prefix accordingly. After decoding, the program compares the recovered signal with the original transmitted data to verify the data transfer and calculate the data error rate.

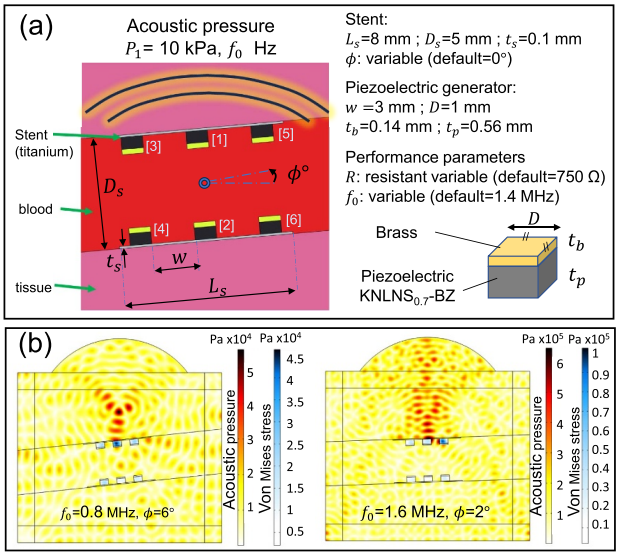

Figure 9. The acoustic-electro-mechanical simulation of energy harvesting system, (a) model parameters of piezoelectric generators, biomedical tissues, and acoustic pressure, (b) acoustic pressure in the tissue surrounding the piezoelectric generators and Von Mises stress on the piezoelectric generators for two settings.

of 3.0 mW, and with the six elements, the sum of power output is 10.0 mW. With rotated piezoelectric elements, a high power output can be generated by tuning the frequency of FUS waves. These results illustrate the tunding of the frequency and placement of the FUS transducer for each piezoelectric; we can get the sum of the maximum single piezoelectric and reach a high level of power generation.

Figure 11 presents the results of the bit error rate (BER) test conducted at transmission speeds of

IOP Publishing J. Neural Eng. 21 (2024) 066009 Z Xu et al

Table 1. Testing results for pulse width modulation (PWM) and pulse-density modulation (PDM).

Data rate (Mbit/s)	Tissue	Modul-ation	Power consumption (mW)	Efficiency (nJ/bit)
0.5	Bone (5 mm) + Skin (7 mm)	PWM	1.1	2.3
1	Bone (5 mm) + Skin (7 mm)	PWM	1.3	1.3
2	Bone (5 mm) + Skin (7 mm)	PWM	1.8	0.9
5	Bone (5 mm) + Skin (7 mm)	PWM	2.7	0.54
1	Bone (5 mm) + Skin (7 mm)	PDM	1.4	1.4
3	Bone (5 mm) + Skin (7 mm)	PDM	2.7	0.9
2	Bone (8 mm) + Skin (7 mm)	PWM	2.1	1.05
5	Bone (8 mm) + Skin (7 mm)	PWM	3.4	0.68
3	Bone (8 mm) + Skin (7 mm)	PDM	2.4	0.8
2	Bone (10 mm) + Skin (7 mm)	PWM	2.6	1.3
5	Bone (10 mm) + Skin (7 mm)	PWM	3.8	0.76
3	Bone (10 mm) + Skin (7 mm)	PDM	2.9	0.96

5 Mbps and 3 Mbps, utilizing 10 mm bone and 7 mm skin as mediums. The figure illustrates the setup used for the BER assessment, including the real-time generation of a random image for testing purposes. Analysis of the data reveals that, at a transmission speed of 5 Mbps with PWM, the BER was maintained below $1.09e^{-8}$. Conversely, employing a transmission speed of 3 Mbps with pulse density modulation (PDM) resulted in a BER below $1.62e^{-9}$. The duration of the BER assessment exceeded 24 h, during which more than 400 Gb of data were transmitted. The use of fresh tissue in these experiments imposed a limitation on the duration of the BER test due to the continuous dehydration of the tissue, which affects its optical and electrical properties. Observations from the test indicate that the BER exhibited fluctuations that appeared to follow a discernible pattern, potentially linked to variations in environmental lighting. However, due to the constrained timeframe of the experiment, a definitive correlation between environmental lighting conditions and BER fluctuations could not be established.

5. Discussion

The wireless and leadless power and data system proposed in this work represents a transformative advancement for eBCIs, addressing critical power and data transmission challenges in current eBCIs designs. The most notable contribution is the elimination of the long, cumbersome cable that traditionally runs from the brain to the chest. Removing this cable significantly reduces the risk of blood flow obstruction and vessel damage, which is especially beneficial for vulnerable populations. Pediatric patients, in particular, benefit from this solution as it eliminates the need to accommodate body growth by adjusting cable length.

A key advantage of the proposed system lies in its enhanced data transfer capabilities within the extremely limited on-site space. While existing communication methods such as near-field, far-field, and ultra-wideband can offer higher data transmission speeds with lower power consumption, their transmitters and antennas are too large to fit within a stent. Other methods, like ultrasound backscatter and body area communication, have compact transmitters that can fit inside a stent but fail to meet the bandwidth requirements for high-fidelity endovascular electrocorticography (ECoG) data transmission. Our system, however, achieves a data transfer rate exceeding 2 Mbit/s, marking a significant improvement that enables real-time transmission of detailed ECoG data, crucial for effective monitoring and intervention.

Regarding power transfer, the system provides efficient and safe energy delivery to the implant site. However, ensuring consistent and reliable wireless power transfer *in vivo* remains a significant challenge due to attenuation caused by variable environments of tissue, bone, and blood. This is a well-known issue in similar systems, and while our solution shows promise, extensive real-world testing will be necessary to confirm that it can perform in complex, variable biological environments as effectively as in controlled simulations.

Another concern regarding power transfer is its suitability for long-term applications. For FUS power delivery, an acoustic couplant is necessary for the external FUS device to effectively transmit energy to the proposed ECoG system. Traditional couplants, such as ultrasound gels, can dry out over time, require frequent reapplication, and may cause skin irritation or discomfort during extended use. These factors could limit the practicality and patient compliance for continuous or long-term applications. To address this challenge, future research should investigate the use of solid-state biocompatible couplants such as hydrogels, hydrophilic polymers, and 3D-printed rubber material [46, 47]s for the FUS device.

Another significant technical challenge is achieving hermetic packaging in the system's design. The telemetry module needs an optical window within its packaging while seamlessly integrating into an

IOP Publishing J. Neural Eng. 21 (2024) 066009 Z Xu et al

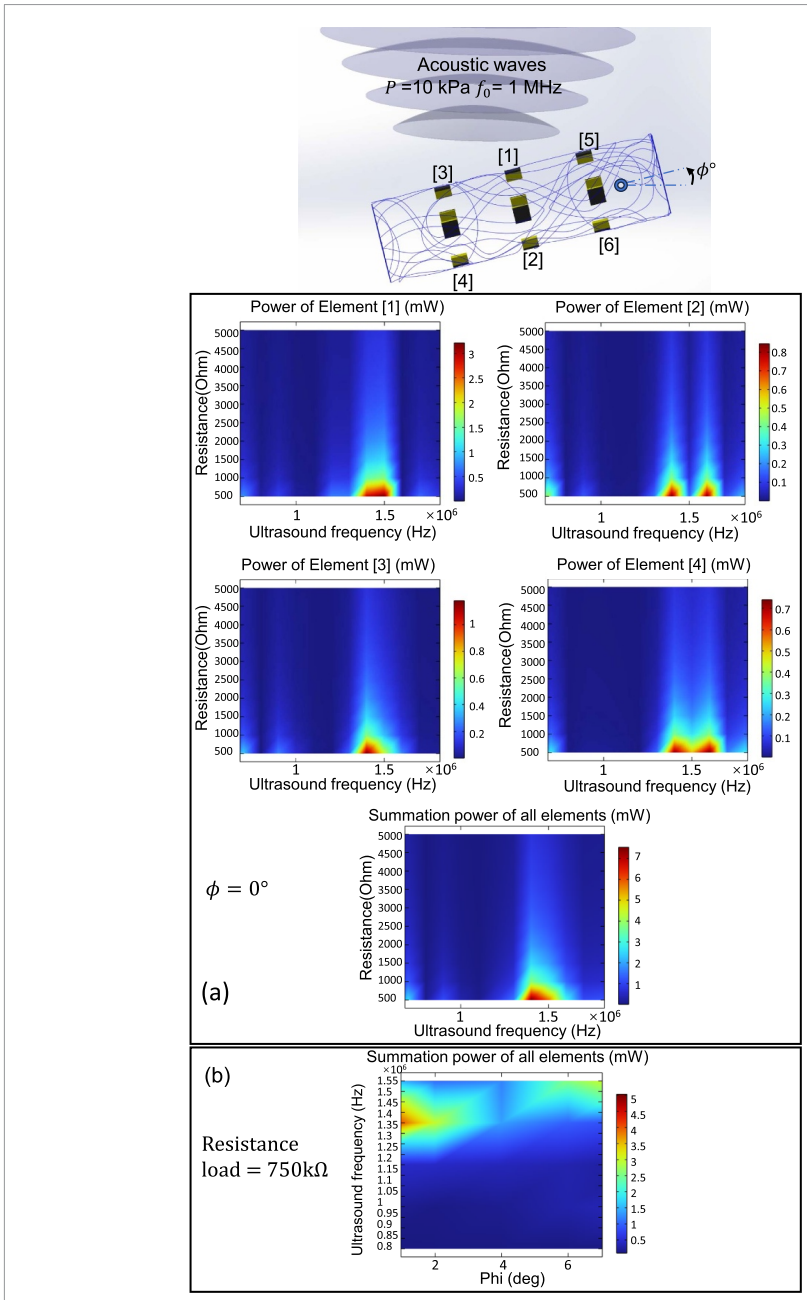

Figure 10. Simulation of piezoelectric power generation with FUS acoustic pressure, (a) piezoelectric power output from element number [1] to [4], and power summation for all elements. Power comparison versus ultrasound frequency and resistance load connection, and (b) the effect of stent-system orientation on the power output.

endovascular stent. As medical devices become more compact, their designs and manufacturing processes become increasingly intricate, which can impact reliability, durability, and overall system performance. This complexity underscores the importance of thorough testing and multiple design iterations to ensure optimal outcomes.

Biocompatibility is also a major concern. While removing the long cable reduces certain risks, introducing new electronic components and materials directly into critical regions like the bloodstream or brain tissue presents new challenges. There is potential for tissue reactions, unforeseen long-term effects, and other adverse events arising from the body's

IOP Publishing J. Neural Eng. 21 (2024) 066009 Z Xu et al

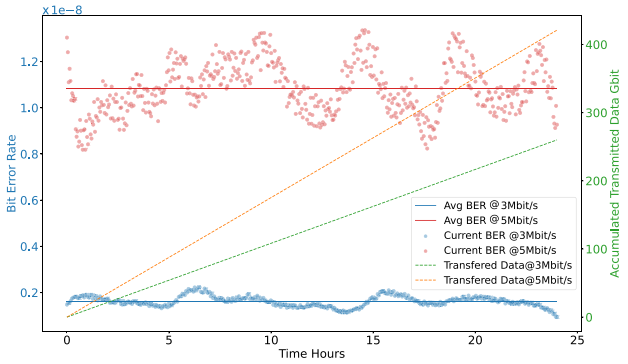

Figure 11. The diagram delineates the setup and outcomes of the bit error rate (BER) testing procedure. The horizontal axis (*X*-axis) indicates the duration of testing, with each evaluation extending over 24 h. The representation includes red dots and a corresponding red line, which illustrate the real-time BER measurements and the overall BER outcome, respectively, for a 5 Mbit/s transfer rate. Similarly, blue dots and a solid blue line depict the real-time BER observations and cumulative results for a 3 Mbit/s transfer rate. Additionally, the orange and green lines signify the total volume of data transmitted during the BER assessment, amounting to 260 Gbit for the 3 Mbit/s rate and 421 Gbit for the 5 Mbit/s rate. We recoreded a video(Link) that also portrays the experimental arrangement, featuring the real-time decoded random image on the computer screen. Positioned at the left is the AD2 device serving as the receiver, while the right showcases the AD2 device functioning as the transmitter. Central to the setup is the tissue sample utilized for testing purposes.

interaction with foreign materials. Rigorous biocompatibility testing of newly introduced materials or design changes is essential to prevent potential complications and ensure patient safety.

Furthermore, although software simulations and modeling provide invaluable insights, they may only partially replicate real-world scenarios. Human physiology and tissue responses are complex, and the device's behavior under actual human conditions might present unanticipated challenges that simulations need to account for. Consequently, extensive in-vivo testing and post-implantation monitoring are crucial to validate the system's performance and safety in real-world settings.

Finally, the leadless power and data solution for eBCIs offers a promising direction that addresses many drawbacks of current systems. However, it also introduces new challenges that require careful consideration, rigorous testing, and continuous monitoring to ensure its viability, safety, and efficacy in practical applications.

6. Conclusion

In conclusion, this paper presents a novel optical wireless telemetry module designed for integration within a smart stent, aiming to overcome the limitations of current eBCIs such as the Stentrode™. By eliminating the need for a long wire connecting the stent electrodes to the encapsulated electronics, the proposed module enhances the eBCIs' applicability for patients with weak blood vessels or susceptible vasculature and addresses the challenges associated with pediatric applications. The telemetry module, which can transfer data at maximum 5 Mbit/s and operate with less than 3 mW power consumption, demonstrates its potential through proof-of-concept experiments using discrete components and fresh bovine bone, muscle, and skin tissue. Future developments of ASICs will further refine the optical telemetry module's performance and pave the way for more versatile, safer, and less invasive eBCIs, ultimately transforming the landscape of neuroscience, engineering, and medical devices.

Data availability statement

All data that support the findings of this study are included within the article (and any supplementary files).

Acknowledgments

The authors acknowledge the financial support from the Australian Research Council under Project DP230100019. The authors also acknowledge the support provided by the Sim4Life software support team.

ORCID iDs

Zhangyu Xu https://orcid.org/0000-0002-1536-2499
Majid Khazaee https://orcid.org/0000-0002-8257-2699
Nhan Duy Truong https://orcid.org/0000-0003-4350-8026
Arman Ahnood https://orcid.org/0000-0002-0253-7579
Omid Kavehei https://orcid.org/0000-0002-2753-5553

IOP Publishing J. Neural Eng. 21 (2024) 066009 Z Xu et al

References

[1] Oxley T J *et al* 2016 Minimally invasive endovascular stent-electrode array for high-fidelity, chronic recordings of cortical neural activity *Nat. Biotechnol.* **34** 320–7

[2] Soldozy S, Young S, Kumar J S, Capek S, Felbaum D R, Jean W C, Park M S and Syed H R 2020 A systematic review of endovascular stent-electrode arrays, a minimally invasive approach to brain-machine interfaces *Neurosurg. Focus* **49** E3

[3] Ibrahim Mahmood A, Kamel Gharghan S, Eldosoky M A and Soliman A M 2022 Near-field wireless power transfer used in biomedical implants: a comprehensive review *IET Power Electron.* **15** 1936–55

[4] Oxley T J *et al* 2021 Motor neuroprosthesis implanted with neurointerventional surgery improves capacity for activities of daily living tasks in severe paralysis: first in-human experience *J. Neurointerv. Surg.* **13** 102–8

[5] Brannigan J F M, Fry A, Opie N L, Campbell B C V, Mitchell P J and Oxley T J 2023 Endovascular brain-computer interfaces in poststroke paralysis *Stroke* **55** 474–83

[6] Majidi S, Harel N, Escalon M, Sawyer A, Lapinska M, Rogers A, Nogueira R, Weber D and Putrino D 2023 Endovascular brain-computer interface to restore motor control for the command of digital devices in patients with severe quadriparesis *Neurology* **100**

[7] Opie N L, Ronayne S M, Rind G S, Yoo P E and Oxley T J 2020 Mechanical suitability of an endovascular brain-computer interface *2020 8th Int. Winter Conf. on Brain-Computer Interface (BCI)* (IEEE) pp 1–6

[8] Oxley T 2022 Long-term safety of a fully implanted endovascular brain-computer interface for severe paralysis *Arch. Phys. Med. Rehabil.* **103** e53

[9] Mitchell P *et al* 2023 Assessment of safety of a fully implanted endovascular brain-computer interface for severe paralysis in 4 patients: the stentrode with thought-controlled digital switch (switch) study *JAMA Neurol.* **80** 270–8

[10] Fry A, Breyman E, LaGrassa E, Oxley T and Putrino D 2023 *Ethical Considerations of Endovascular Brain–Computer Interfaces* (Springer) pp 43–63

[11] Sanjeev S and Karpawich P P 2006 Superior vena cava and innominate vein dimensions in growing children: an aid for interventional devices and transvenous leads *Pediatr. Cardiol.* **27** 414–9

[12] Sun L R, Harrar D, Drocton G, Castillo-Pinto C, Gailloud P and Pearl M S 2021 Endovascular therapy for acute stroke in children: age and size technical limitations *J. Neurointerv. Surg.* **13** 794–8

[13] Nelson B D, Karipott S S, Wang Y and Ong K G 2020 Wireless technologies for implantable devices *Sensors* **20** 4604

[14] Hamami M G M and Ismail Z H 2022 Review of machine learning techniques for eeg based brain computer interface *Arch. Comput. Methods Eng.* **29** 1–20

[15] Javad Karimi M, Schmid A and Dehollain C 2021 Wireless power and data transmission for implanted devices via inductive links: a systematic review *IEEE Sens. J.* **21** 7145–61

[16] Yoo S, Lee J, Joo H, Sunwoo S-H, Kim S and Kim D-H 2021 Wireless power transfer and telemetry for implantable bioelectronics *Adv. Healthcare Mater.* **10** 2100614

[17] Kanaan A I and Sabaawi A M A 2021 Implantable wireless systems: a review of potentials and challenges *Antenna Systems* (IntechOpen) (https://doi.org/10.5772/intechopen.99064)

[18] Hu X yu, lu Yin W, Du F, Zhang C, Xiao P and Li G 2024 Biomedical applications and challenges of in-body implantable antenna for implantable medical devices: a review *AEU - Int. J. Electron. Commun.* **174** 155053

[19] Zhang J, Das R, Zhao J, Mirzai N, Mercer J and Heidari H 2022 Battery-free and wireless technologies for cardiovascular implantable medical devices *Adv. Mater. Technol.* **7** 2101086

[20] Kim H-J and Ho J S 2022 Wireless interfaces for brain neurotechnologies *Phil. Trans. R. Soc.* A **380** 20210020

[21] Iqbal A, Al-Hasan M, Mabrouk I B and Denidni T A 2022 Wireless powering and telemetry of deep-body ingestible bioelectronic capsule *IEEE Trans. Antennas Propag.* **70** 9819–30

[22] Roy S, Azad A N M W, Baidya S, Alam M K and Khan F 2022 Powering solutions for biomedical sensors and implants inside the human body: a comprehensive review on energy harvesting units, energy storage and wireless power transfer techniques *IEEE Trans. Power Electron.* **37** 12237–63

[23] Khan A, Joshi R, Kumar Sharma M, Ganguly A, Parashar P, Wang T-W, Lee S, Kao F-C and Lin Z-H 2024 Piezoelectric and triboelectric nanogenerators: Promising technologies for self-powered implantable biomedical devices *Nano Energy* **119** 109051

[24] Xu Z, Duy Truong N D, Nikpour A and Kavehei O 2023 A miniaturized and low-energy subcutaneous optical telemetry module for neurotechnology *J. Neural Eng.* **20** 036017

[25] Drakopoulou S, Varkevisser F, Sohail L, Aqamolaei M, Costa T L and Spyropoulos G D 2023 Hybrid neuroelectronics: towards a solution-centric way of thinking about complex problems in neurostimulation tools *Front. Electron.* **4** 1250655

[26] Tanskanen J M A, Ahtiainen A and Hyttinen J A K 2020 Toward closed-loop electrical stimulation of neuronal systems: a review *Bioelectricity* **2** 328–47

[27] Upendra B, Panigrahi B, Singh K and Sabareesh G R 2024 Recent advancements in piezoelectric energy harvesting for implantable medical devices *J. Intell. Mater. Syst. Struct.* **35** 129–55

[28] Sezer N and Koç M 2021 A comprehensive review on the state-of-the-art of piezoelectric energy harvesting *Nano Energy* **80** 105567

[29] Azimi S, Golabchi A, Nekookar A, Rabbani S, Amiri M H, Asadi K and Abolhasani M M 2021 Self-powered cardiac pacemaker by piezoelectric polymer nanogenerator implant *Nano Energy* **83** 105781

[30] Li H, Liu J, Li K and Liu Y 2021 A review of recent studies on piezoelectric pumps and their applications *Mech. Syst. Signal Process.* **151** 107393

[31] Ilik B, Koyuncuoğlu A, Sukas ozlem şardan and Külah H 2018 Thin film piezoelectric acoustic transducer for fully implantable cochlear implants *Sens. Actuators* A **280** 38–46

[32] Turner B L, Senevirathne S, Kilgour K, McArt D, Biggs M, Menegatti S and Daniele M A 2021 Ultrasound-powered implants: a critical review of piezoelectric material selection and applications *Adv. Healthcare Mater.* **10** 2100986

[33] Basaeri H, Christensen D B and Roundy S 2016 A review of acoustic power transfer for bio-medical implants *Smart Mater. Struct.* **25** 123001

[34] Haq M 2018 Application of piezo transducers in biomedical science for health monitoring and energy harvesting problems *Mater. Res. Express* **6** 022002

[35] Radziemski L and Makin I R S 2016 *In vivo* demonstration of ultrasound power delivery to charge implanted medical devices via acute and survival porcine studies *Ultrasonics* **64** 1–9

[36] Wan X *et al* 2022 Hybrid-piezoelectret based highly efficient ultrasonic energy harvester for implantable electronics *Adv. Funct. Mater.* **32** 2200589

[37] Bansal S, Choi C, Hardwick J, Bagchi B, Tiwari M K and Subramanian S 2023 Transmissive labyrinthine acoustic metamaterial-based holography for extraordinary energy harvesting *Adv. Eng. Mater.* **25** 2201117

[38] Zhang T *et al* 2022 Piezoelectric ultrasound energy–harvesting device for deep brain stimulation and analgesia applications *Sci. Adv.* **8** eabk0159

[39] Firbank M, Hiraoka M, Essenpreis M and Delpy D T 1993 Measurement of the optical properties of the skull in the wavelength range 650-950 nm *Phys. Med. Biol.* **38** 503

[40] Sawosz P et al 2016 Human skull translucency: post mortem studies *Biomed. Opt. Express* **7** 5010–20
[41] Jeong E, Seo M and Kim K-S 2022 Guide for wavelength selection of leds for fnirs systems *2022 22nd Int. Conf. on Control, Automation and Systems (ICCAS)* pp 1819–22
[42] Zhang B, Wu J, Cheng X, Wang X, Xiao D, Zhu J, Wang X and Lou X 2013 Lead-free piezoelectrics based on potassium–sodium niobate with giant d_33 *ACS Appl. Mater. Interfaces* **5** 7718–25
[43] Ackerman M J 1998 The visible human project *Proc. IEEE* **86** 504–11
[44] Zurich MedTech Sim4Life V7.4 Sim4life and computable human phantoms(Zurich MedTech AG Zurich)
[45] COMSOL Multiphysics 1998 Introduction to comsol multiphysics® COMSOL Multiphysics, Burlington, MA, 32 (Accessed 9 February 2018)
[46] Chen L, Zeng G, Guo D, Liu J, Zhang X, Lin S and Zhang K 2021 Soft elastic hydrogel couplants for ultrasonography *Mater. Sci. Eng.* C **119** 111609
[47] Gao W, Chen Y and Liu W 2023 Research and optimum selection of coupling agent materials in ultrasonic measurement *J. Mater. Res. Technol.* **26** 1006–15